



An ultracold high-flux source for
matter-wave interferometry in microgravity

Von der Fakultät für Mathematik und Naturwissenschaften
der Carl von Ossietzky Universität Oldenburg
zur Erlangung des Grades und Titels eines
Doktors der Naturwissenschaften (Dr. rer. nat.)

angenommene Dissertation

von

Herrn M.Sc. Tammo Sterneke

geboren am 02.11.1984 in Nordhorn

1. Gutachter: Prof. Dr. Claus Lämmerzahl
2. Gutachter: Prof. Dr. Christoph Lienau
3. Gutachter: Prof. Dr. Kai Bongs

Tag der Disputation: 12.02.2018

Atom interferometry has a wide range of applications, for example in the fields of gravimetry, gradiometry and inertial sensing. It can also be used to measure fundamental constants and atomic properties or to test general relativity. All these measurements benefit from a long free fall time of the atoms within the experiment, which is difficult to realize in earthbound setups. The experiment described in this work can create Bose-Einstein condensates of almost 10^5 rubidium atoms at a repetition rate exceeding 1 Hz and is compact, robust and mobile. This combination facilitates an operation in a drop tower and allows for extended free fall times of the atomic ensemble within the experiment. A free evolution time of 2.7 s is demonstrated, which equals the current record [1]. The experiment provides a flux of up to $2.5 \cdot 10^5$ condensed atoms per second. This is the highest flux achieved by a mobile source and is competitive with the best overall. It is designed to ultimately enable dual species light-pulse atom interferometry capable of testing, for example, the universality of free fall.

Any precision measurement using atom interferometry requires an excellent level of control over the source. This is discussed and demonstrated in this work. Critical parameters in this context are the magnetic field environment, the control over the position and the velocity of the atomic ensemble as well as its velocity spread and also vibrations of the experiment. All these points are systematically and thoroughly investigated. The magnetic field can be controlled to a mG precision. Its gradient is measured by time of flight imaging and the implications for precision measurements are discussed. In this context, an adiabatic rapid passage is required. It is analyzed in depth and realized experimentally. The individual contributions that are responsible for a center of mass motion of the atomic ensemble are characterized. A reduction of this velocity of an untrapped atomic ensemble to a few micrometer per second is achieved. The limitations for a further reduction are discussed in this thesis.

A crucial requirement for precision atom interferometry in general and ultralong free evolution times in particular is the realization of an ultrasmall velocity spread. This spread can be reduced by magnetic lensing. So far, a kinetic temperature as low as 1 nK has been observed by this scheme [2]. Typical lens configurations are anisotropic such that they are capable of collimating the ensemble in one or two spatial dimensions only. This constraint can be relaxed by multiple magnetic lensing in analogy to optics, but such a matter-wave telescope is more difficult to adjust compared to a single lens. A different strategy is demonstrated in this work. A quadrupole mode collective excitation of the Bose-Einstein condensate within the release trap is used to collimate the third spatial dimension. This direction is almost unaffected by the single magnetic lens, which is chosen to be axially symmetric to collimate the condensate in the other two dimensions. The origin of collective excitations is explained. Their time dependence is simulated numerically and confirmed experimentally. This thorough understanding allows for a tuning of the collective excitation and to match it to the particular lens configuration. A velocity spread of $140 \mu\text{m/s}$ equivalent to a kinetic temperature of 70 pK is realized, which is the coldest ever observed. Finally, a road map towards realizing fK kinetic temperatures is derived and discussed.

Atominterferometrie findet in vielen Bereichen Anwendung, z.B. in der Gravimetrie, der Gradiometrie oder in der Messung von Rotationen. Mit ihr können auch Naturkonstanten sowie atomare Eigenschaften gemessen oder die allgemeine Relativitätstheorie getestet werden. All diese Messungen profitieren von einer langen Freifallzeit der Atome innerhalb des Experiments, welche in erdgebundenen Aufbauten nur schwer zu realisieren ist. Das in dieser Arbeit beschriebene Experiment kann Bose-Einstein Kondensate mit annähernd 10^5 Rubidium Atomen bei einer Repetitionsrate von über 1 Hz erzeugen und ist dabei kompakt, robust und mobil. Diese Kombination ermöglicht es, das Experiment in einem Fallturm zu betreiben. Damit wird eine verlängerte Freifallzeit des atomaren Ensembles innerhalb des Experiments möglich. Eine freie Expansionszeit von 2.7 s wird gezeigt, was den aktuellen Rekord einstellt [1]. Das Experiment liefert einen Fluss von $2.5 \cdot 10^5$ kondensierten Atomen pro Sekunde. Das ist der höchste jemals von einer mobilen Quelle erzeugte Fluss und er konkurriert mit den besten Quellen überhaupt. Das Experiment wurde darauf ausgelegt, in Zukunft zwei-Spezies Lichtpuls-Atominterferometrie zu ermöglichen um z.B. die Universalität des freien Falls zu überprüfen.

Die Grundvoraussetzung für jede Präzisionsmessung mittels Atominterferometrie ist ein hervorragendes Maß an Kontrolle über die Quelle. Das wird in dieser Arbeit diskutiert und demonstriert. Kritische Faktoren sind diesbezüglich die magnetische Feldumgebung, die Kontrolle über Position und Geschwindigkeit der Atome sowie ihre Geschwindigkeitsstreuung und auch Vibrationen des Experiments. Diese Punkte werden systematisch und gründlich analysiert. Das Magnetfeld kann mit einer Präzision von einem mG kontrolliert werden. Dessen Gradient wird über eine Zeitreihe gemessen. Die Auswirkungen auf Präzisionsmessungen werden diskutiert. In diesem Zusammenhang ist eine adiabatische schnelle Passage erforderlich. Sie wird im Detail analysiert und experimentell realisiert. Die einzelnen Beiträge, die zu einer Schwerpunktsbewegung des atomaren Ensembles führen, werden charakterisiert. Diese Geschwindigkeit des ungefangenen Ensembles kann auf wenige Mikrometer pro Sekunde reduziert werden. Die Einschränkungen bezüglich einer weiteren Verringerung werden in dieser Arbeit diskutiert.

Ein kritischer Parameter für Präzisionsatominterferometrie im Allgemeinen und die Realisierung von sehr langen freien Expansionszeiten im Besonderen ist eine extrem schmale Geschwindigkeitsverteilung. Die Geschwindigkeitsstreuung kann durch eine magnetische Linse reduziert werden. Hiermit konnte bislang eine kinetische Temperatur von 1 nK beobachtet werden [2]. Typische Linsenkonfigurationen sind anisotrop und ermöglichen somit nur eine Kollimation in bis zu zwei Raumdimensionen. Diese Einschränkung kann, analog zur Optik, mit mehreren magnetischen Linsen gelockert werden. Es ist jedoch viel schwieriger, ein solches Materiewellenteleskop zu justieren als nur eine einfache Linse. Eine alternative Strategie wird in dieser Arbeit gezeigt. Mit einer kollektiven Quadrupolanregung des Bose-Einstein Kondensats innerhalb der Falle kann eine Kollimation in der dritten Raumdimension erzielt werden. Diese Richtung wird von einer einzelnen magnetischen Linse kaum beeinflusst, sodass die Linse axialsymmetrisch gewählt wird um eine Kollimation in den anderen zwei Dimensionen zu erzielen. Der Ursprung von kollektiven Anregungen wird erklärt. Ihre Zeitabhängigkeit wird numerisch

simuliert und experimentell bestätigt. Dieses tiefgreifende Verständnis erlaubt es, die kollektive Anregung auf die spezielle Linsenkonfiguration anzupassen. Es werden Geschwindigkeitsstreuungen von $140 \mu\text{m/s}$ realisiert. Das entspricht einer kinetischen Temperatur von nur 70 pK und stellt den aktuellen Rekord dar. Zum Schluss wird eine Strategie zur Erzeugung von kinetischen Temperaturen im fK Bereich entwickelt und diskutiert.

Contents

| | | |
|----------|---|------------|
| 1 | Introduction | 9 |
| 1.1 | Principle of light-pulse atom interferometry | 9 |
| 1.2 | Comparison of reduced gravity environments | 12 |
| 1.3 | Constraints and procedures in the drop tower | 15 |
| 2 | The QUANTUS-2 experiment | 19 |
| 2.1 | Experimental setup | 19 |
| 2.2 | Fast BEC preparation | 44 |
| 2.3 | Experimental sequence and performance | 47 |
| 3 | Magnetic field control | 53 |
| 3.1 | Homogeneous magnetic fields | 53 |
| 3.2 | Switching dynamics | 55 |
| 3.3 | Customizing current ramps | 56 |
| 3.4 | Magnetic gradient fields | 58 |
| 3.4.1 | Ground-based measurements | 59 |
| 3.4.2 | Measurements in microgravity | 60 |
| 4 | Adiabatic rapid passage | 67 |
| 4.1 | Adiabatic rapid passage in a two-level system | 67 |
| 4.2 | Properties of the ^{87}Rb $F = 2$ hyperfine manifold | 72 |
| 4.3 | Relevant experimental parameters and techniques | 79 |
| 4.4 | Adiabatic rapid passage in ^{87}Rb | 89 |
| 5 | Center of mass motion | 105 |
| 5.1 | Measured center of mass motion | 105 |
| 5.2 | Systematic effects on the center of mass motion | 110 |
| 5.2.1 | Centrifugal and Coriolis force | 111 |
| 5.2.2 | Magnetic dipole force | 115 |
| 5.2.3 | Electric dipole force | 115 |
| 5.2.4 | Detection pseudo force | 118 |
| 5.2.5 | Residual air drag | 120 |
| 5.2.6 | Corrected center of mass motion | 123 |
| 5.2.7 | Summary | 125 |

| | | |
|------------------------------|--|------------|
| 5.3 | Reduction of the center of mass motion | 125 |
| 5.3.1 | Center of mass motion by dipole oscillations | 126 |
| 5.3.2 | Center of mass motion by trap switch-off | 131 |
| 5.3.3 | Miscellaneous contributions to center of mass motion | 133 |
| 6 | Magnetic lensing | 141 |
| 6.1 | Free expansion | 141 |
| 6.2 | Concept of magnetic lensing | 146 |
| 6.3 | Collective modes | 151 |
| 6.3.1 | Excitation of collective modes | 157 |
| 6.3.2 | Quadrupole mode excitations for magnetic lensing | 162 |
| 6.4 | Experimental realization of magnetic lensing | 164 |
| 6.4.1 | SC-BC-lens | 164 |
| 6.4.2 | BC-lens | 168 |
| 7 | Summary and discussion | 177 |
| Appendices | | |
| A | SC-BC-lens | 185 |
| A.1 | Detection 1 view | 185 |
| A.2 | Detection 2 view (right cloud) | 188 |
| B | BC-lens | 190 |
| B.1 | Data set in $m_F = 2$ | 190 |
| B.1.1 | Detection 1 view | 190 |
| B.2 | Data set in $m_F = 0$ (Set B) | 192 |
| B.2.1 | Detection 1 view | 192 |
| B.2.2 | Detection 2 view (left cloud) | 194 |
| B.2.3 | Detection 2 view (right cloud) | 196 |
| B.3 | Data set in $m_F = 0$ (Set C) | 198 |
| B.3.1 | Detection 1 view | 198 |
| C | Characteristic data | 200 |
| C.1 | Rubidium data | 200 |
| C.2 | Trap frequencies | 201 |
| D | Appendix to ARP | 202 |
| D.1 | Derivation of the dressed-state Hamiltonian | 202 |
| D.2 | Power series of systematic shifts | 206 |
| D.3 | ARP code | 206 |
| Bibliography | | 207 |
| Glossary and acronyms | | 228 |

Chapter 1

Introduction

Matter-wave interferometry is a wide field comprising interferometry with electrons, ions, neutrons, atoms and molecules [3–5]. Atom interferometry provides valuable contributions to the measurement of fundamental constants, such as the fine structure constant α [6, 7] and the gravitational constant G [8–11], or the measurement of atomic properties such as the electric polarizability [12, 13]. Furthermore, atom interferometers can be used to test general relativity. There exist proposals to detect gravitational waves [14–16] and first tests of Einstein’s equivalence principle (EEP) have been performed [17–23]. Typically, these experiments test the universality of free fall (UFF), which is one of the three pillars of the EEP. The remaining two are the local Lorentz invariance and the local position invariance. Tests with quantum objects are invaluable because they probe the boundary between quantum mechanics and general relativity. So far, all non-gravitational interactions have been unified in a quantum field theory, but their unification with gravity remains an unresolved issue. A test of the superposition principle on macroscopic scales is an active field of research in this respect. Interference effects have been proven for large molecules [24] and for matter waves containing 10^5 atoms [25]. In the latter example the wave packets have been separated by more than half a meter and for more than one second. These scales can be considered macroscopic. Beyond these fundamental tests, atom interferometers can be used for practical applications, too, such as gravimeters [26–34], gradiometers [8, 35, 36] and gyroscopes [37–43]. Miniaturized and portable versions can have promising future applications in geophysics, metrology and inertial navigation [36, 44–46]. Recently, a great interest in a commercialization of such devices emerged. The European Union, for example, has launched a billion euro flagship program to boost the development of quantum technology in general and quantum sensors in particular [47, 48]. First cold atom based devices are commercially available already [49–51].

1.1 Principle of light-pulse atom interferometry

In a Bragg pulse atom interferometer, different momentum states are coupled by counterpropagating laser beams with frequencies ω_1 and ω_2 . Integer multiples of $\hbar k_{\text{eff}}$ can be transferred, where $k_{\text{eff}} = k_1 + k_2$ is the effective wave number of the two

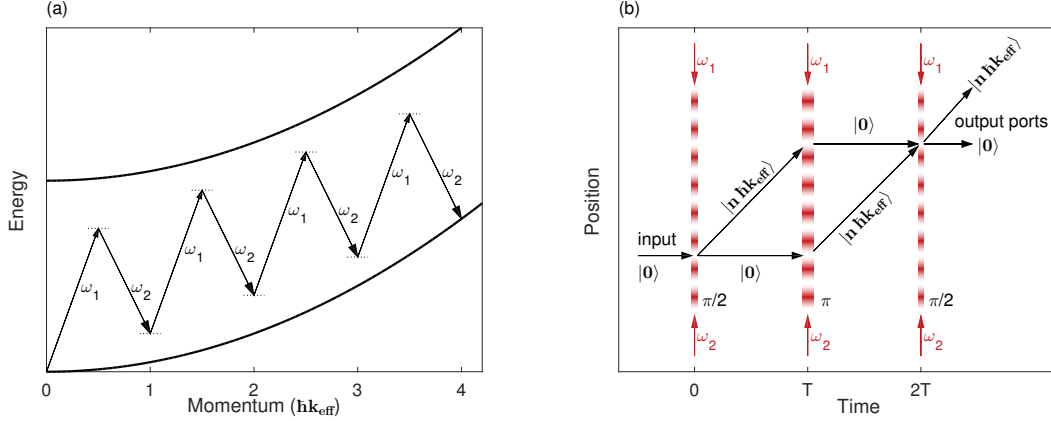


Figure 1.1: (a) shows the energies and momenta involved in a fourth order Bragg diffraction process using counterpropagating laser beams with frequencies ω_1 and ω_2 , respectively. Bragg diffraction preserves the internal atomic state (lower solid line). A Mach-Zehnder n -th order Bragg pulse atom interferometer is depicted in (b). The pulses at a time of 0 , T and $2T$ couple the momentum states $|0\rangle$ and $|n\hbar k_{\text{eff}}\rangle$. The interaction time with the light defines the phase of the Rabi oscillation between these states. A phase of $\pi/2$ realizes a beamsplitter pulse and a phase of π corresponds to a mirror pulse inverting the momentum states.

laser beams. Their relative frequency defines the Bragg order, that is, the particular momentum states involved in this Rabi oscillation. Figure 1.1(a) exemplarily depicts the energy levels involved in a fourth order Bragg diffraction process. An allowed optical transition must exist between two internal states (parabolas). The intermediate momentum states are out of resonance because of the quadratic dispersion relation. Bragg diffraction preserves the internal state of the atoms. In contrast, a coupling of different internal states is called Raman diffraction. Depending on the interaction time with the light, these pulses can create a coherent superposition of the coupled momentum states ($\pi/2$ -pulse) or invert them (π -pulse). Different interferometer geometries can be formed depending on the pulse sequence. For example, a $\pi/2$ - π - $\pi/2$ sequence forms a Mach-Zehnder interferometer, which is shown in Fig. 1.1(b). The time in between these pulses is the pulse separation time T . After the interferometer, the output ports separate in space due to their different momentum. Their relative population constitutes the measurement signal of the atom interferometer. This signal oscillates with the relative phase that the two wave packets accumulate along their paths. The dominant contribution is the local laser phase imprinted on the atoms, which makes such an atom interferometer susceptible to laser wave front distortions and curvatures. A uniform acceleration would be expected to affect both paths equally, but the Doppler shift gives rise to a nonzero phase difference. The resulting sensitivity to accelerations is proportional to the Bragg order and scales quadratically with T [52]. An ultrasmall velocity spread of the atomic ensemble, defined as its root mean square velocity, is required for several reasons. First of all, it is the prerequisite for the realization of a long free expansion time because of the decreasing atomic density. Non-planar laser wave fronts can entail even tighter

constraints. In addition, a narrow momentum width of the atomic ensemble along the interferometry axis allows for an efficient transfer of many photon momenta [53]. Hence, the ultrasmall velocity spread can enhance the sensitivity of an atom interferometer and is essential for high precision measurements.

Such an atom interferometer requires a source of ultracold atoms. This source should provide a high flux for a good repetition rate and therefore reduced statistical errors. The experiment described in this work is such a source. It is compact, but performs on par with lab-sized experiments and sets the benchmark for transportable ones. The necessary reduction of the velocity spread involves cooling the atoms below the critical temperature for the creation of a Bose-Einstein condensate (BEC). The condensed phase is not required for itself, but its properties facilitate the subsequent realization of an ultrasmall velocity spread as discussed in this work.

The QUANTUS collaboration (QUANTengase Unter Schwerelosigkeit) aims at space-based precision measurements with matter waves in order to benefit from the extended free fall times. Most prominent among these measurements is a test of the UFF. Its violation is parametrized by the Eötvös ratio

$$\eta_{A,B} = 2 \frac{g_A - g_B}{g_A + g_B}, \quad (1.1)$$

where $g_{A,B}$ is the gravitational acceleration of the respective test body. These test bodies can be two different atomic species, both of which realize their own interferometer at the same time and the same initial position. Classical tests by lunar laser ranging [54] and torsion balances [55] have an accuracy of approximately 10^{-13} in $\eta_{A,B}$. They found no violation. Tests with quantum objects can have an increased sensitivity to UFF violations and provide better constraints at the same level of precision [56]. The best precision with an atom interferometer is on the 10^{-9} level using different energy eigenstates of ^{87}Rb [57]. Even though no violation has been found, better tests are required for tighter constraints on theories beyond the standard model [58, 59].

In contrast to classical test masses, atoms are equal, irrespective of the particular experiment, research group and location. This makes them a good candidate for tests of fundamental physics. Still, atom interferometry is sensitive to a long list of systematic effects in addition to the wave front issue mentioned above. Schubert et al. [60] have analyzed them in detail for a test of the UFF and the gravitational redshift on a satellite using a simultaneous ^{85}Rb - ^{87}Rb interferometer. This satellite mission is called STE-QUEST (Space-Time Explorer and QUantum Equivalence principle Space Test) and was proposed within the Cosmic Vision program of the European Space Agency [61]. In late 2013, the mission was not selected because of a limited budget and due to an insufficient technology readiness level (TRL) [62]. The control over the atomic ensembles is critical in this respect. If their initial positions for the interferometer differ along its sensitive axis, which is aligned in the direction of gravity, the earth's gravity gradient will result in a different acceleration of the two atomic species. This difference is a systematic error, because it is a bias on $\eta_{A,B}$. The same holds true for a different initial velocity in this direction. The remaining directions are less critical, but not irrelevant. For example, a velocity in

a direction orthogonal to the interferometer axis can lead to a Coriolis acceleration in the sensitive direction, because the satellite has a nonzero rotation rate. Aside from that, magnetic field gradients need to be considered. Their effect can be minimized by preparing the atoms in a non-magnetic state. Still, the quadratic Zeeman shift is responsible for a bias acceleration. Vibrations of the experimental setup can be problematic, too, because the beam pairs in Fig. 1.1(b) are generated by retroreflecting one beam at a mirror. A vibrating mirror shifts the laser wave fronts and has a direct impact on the interferometer phase. STE-QUEST aimed at a target accuracy of $2 \cdot 10^{-15}$ with $2T = 10$ s. This requires a velocity spread below $82 \mu\text{m/s}$ and a magnetic field gradient smaller than $83 \mu\text{G/m}$ at a residual magnetic field of 1 mG . The spatial overlap of the two atomic clouds needs to be better than 1.1 nm and their relative velocities must be smaller than 0.31 nm/s [60]. These constraints are very ambitious. They give an impression on the high level of control over the atomic ensemble required for ultimate precision measurements. This example shows that a source for atom interferometry must fulfill more than only a high flux of cold atoms. The magnetic field environment is critical and the center of mass motion of the atomic ensemble must be reproducible and tunable. For a satellite mission, the source must also be compact and energy efficient.

1.2 Comparison of reduced gravity environments

Since the atoms are subject to the gravitational acceleration, there are two different approaches for realizing a long time of flight (TOF), which is the prerequisite for a long interaction time within the interferometer. The first one is to build the experiment very large and let the atoms fall freely within the experiment's vacuum chamber. This approach is realized by the 10 m towers in Stanford, USA [63], Hanover, Germany [56] and Wuhan, China [64]. All of them use an atomic fountain to double the free fall time to approximately 2.7 s. The advantages are a high repetition rate and good accessibility for adjustments as well as upgrades. A severe disadvantage is its limited scalability to very long TOFs, because the vacuum chamber and the magnetic shield around have to grow quadratically with the desired TOF. For this reason, the QUANTUS collaboration follows a different approach. It is to let the whole experiment fall along with the freely falling atoms. In this case the experiment needs to be operated on a suitable platform. These platforms are often referred to as microgravity¹ platforms.

There exist several platforms suitable for providing reduced gravity environments for scientific payloads. The most commonly used ones are the Airbus ZERO-G, the International Space Station (ISS), the drop tower in Bremen and sounding rockets. Also a dedicated satellite is possible. These platforms differ a lot in the vibrational environment, available time of reduced gravity and in the operational requirements. The vibrational environment is characterized by the power spectral density (PSD) of the vibrations. It is the figure of merit for rating the microgravity quality and is compared in Fig. 1.2 for the different platforms.

¹This can be a misnomer, as will be shown below.

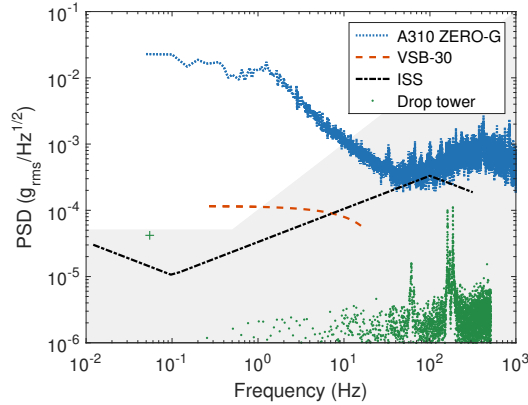


Figure 1.2: Comparison of the PSD of the vibrations on different platforms offering a reduced gravity environment: Novespace A310 ZERO-G (dotted blue line) [23], VSB-30 sounding rocket (dashed orange line) [65], International Space Station (dash-dotted black line) [66] and the drop tower in Bremen [catapult, averaged over 8 s] (green dots) [67]. The DC component (green plus sign) was inferred from air drag measurements. The shaded area indicates the requirements for STE-QUEST as a reference [60]. A gravitational acceleration of $g = 9.81 \text{ ms}^{-2}$ was assumed.

The Novespace A310 ZERO-G is the former German government aircraft (‘Chancellor Airbus’) and successor of the A300 ZERO-G. It provides easy access to reduced gravity for comparably large payloads (200 m^3) by parabolic flights. The microgravity quality is rather poor, as characterized by the dotted blue line in Fig. 1.2. It has been measured by Barrett et al. [23] during the ICE (Interférométrie atomique à sources Cohérentes pour l’Espace) campaigns. One parabola lasts for 20 s and typically 30 repetitions can be conducted in each campaign.

Sounding rockets, for example a VSB-30, provide an interesting platform. The available time of reduced gravity is on the order of 6 minutes. Unfortunately, the only available vibration spectrum is very limited in the frequency domain and had to be derived from [65]. It was measured on the TEXUS-44 mission. The PSD is shown as the dashed orange line in Fig. 1.2. The scientific payload can be altered in between two launches, provided the experiment survives the flight. Still, a re-qualification for the next flight might be necessary. For this reason, the accessibility is rather moderate.

The ISS’s vibrational environment is nonuniform and depends on the current activities on the ISS [68]. Unfortunately, NASA is very reserved concerning the publication of vibration spectra. Therefore the ‘microgravity requirements’ for the ISS published by NASA serve as a reference [66]. They are shown as the dash-dotted black line. NASA claims that these conditions should be satisfied for at least 50% of the payload for 180 days/year (compensation of atmospheric drag). The accessibility to a scientific payload on the ISS is very limited. Maintenance has to be performed by astronauts and replacement parts are not readily available.

The last vibration spectrum shown as the green dots in Fig. 1.2 is from the drop tower at the Center of Applied Space Technology and Microgravity (ZARM) in

Bremen [67]. An evacuated, 110 m high steel tube is installed within this tower. Capsules carrying the scientific payload can be dropped from the top of the tower or catapulted up from the bottom. The corresponding free fall times are 4.72 s and approximately 9 s. The PSD was calculated from the last 7.9 s of a catapult flight on June 15th, 2007. During the first second of this 8.9 s long flight, strong vibrations were allowed to damp out. Their frequencies depend on the resonances defined by the mass distribution of the scientific payload. The residual peaks around 100 Hz are such resonances. Their oscillation amplitude decreases with time. The DC component of the PSD refers to a time constant of $2 \cdot 9$ s. The measurement could not properly resolve this component. Hence, this value (green plus sign) had to be derived from the air drag analysis discussed in Section 5.2 assuming a residual pressure of 20 Pa within the drop tower. When the capsule is dropped instead of catapulted, the PSD can be different. The accessibility to experiments operated on this platform is very good. Small upgrades can even be made in between two drops on the same day.

A representative vibration spectrum of a satellite cannot be shown. However, the PSD can be expected to be better than the one of the ISS. Despite this, the scientific payload is practically inaccessible. Smaller malfunctions can immediately entail a failure of the entire mission. For this reason, extensive studies on other platforms are inevitable prior to embarking a complex experiment on a satellite. The acceptable PSD for STE-QUEST is shown by the shaded area in Fig. 1.2. This can serve as a reference on how large a PSD can be tolerated. The drop tower and the ISS fulfill this criterion.

Sometimes the PSD is distilled into a single number quantifying the strength of vibrations, even though spectral information is lost. This number is called the overall g_{rms} value. It is given by

$$g_{\text{rms (overall)}} = \sqrt{\int_0^{f_{\text{co}}} [PSD(f)]^2 df}, \quad (1.2)$$

where f_{co} is a cutoff frequency. Table 1.1 lists the overall g_{rms} values for two different cutoff frequencies and gives an overview over the relevant figures of merit. Vibrational data cannot be stated for all entries, as mentioned above. The available consecutive time of reduced gravity depends on the mass of the experiment for the catapult mode of the drop tower as well as for sounding rockets. This is simply because heavier payloads cannot be equally accelerated by the catapult or rocket, respectively.

The vibration levels of the A310 ZERO-G are too high for most quantum sensors aiming at high precision. However, the remaining four platforms in Table 1.1 indicate a reasonable path of development of such experiments, which is aimed at by the QUANTUS collaboration to develop the required technologies and methods. Despite its rather short consecutive time of microgravity, the drop tower in Bremen offers an excellent accessibility to the experiment. Lessons learned can be quickly and easily implemented into the experiment. For this reason, the first BEC and the first atom interferometer in microgravity have been realized by the QUANTUS-1 experiment (Q-1) on this platform [2, 69]. The successor QUANTUS-2 (Q-2), which

| | ZERO-G | Drop Tower | VSB-30 | ISS | Satellite |
|--|--------|------------|-----------|-------|-----------|
| Consecutive time of reduced gravity | 20 s | 9.3 s | 6 min | 30 d | >> 30 d |
| $g_{\text{rms}}(f_{\text{co}} = 16 \text{ Hz})$ (μg) | 22 816 | 6 | 350 | 411 | - |
| $g_{\text{rms}}(f_{\text{co}} = 200 \text{ Hz})$ (μg) | 23 950 | 162 | - | 3 807 | - |
| Availability (per year) | 4 h | 1.3 h | 0.7 h | 180 d | 365 d |
| Accessibility | + | ++ | \ominus | - | -- |

Table 1.1: Comparison of different platforms offering a reduced gravity environment: Novespace A310 ZERO-G (assuming 80 hours in 20 years) [23, 75], drop tower in Bremen (assuming two catapult flights per working day)², VSB-30 sounding rocket (assuming 7 campaigns/year) [65], International Space Station [66] and a satellite. The cutoff frequency f_{co} refers to Eq. (1.2).

is described in this work, provides a significantly increased flux and is designed as a dual species atom interferometer for ^{87}Rb and any of the natural potassium isotopes. Q-2 can exploit the full potential of the drop tower by using the catapult mode. The subsequent steps towards a UFF test in space are three sounding rocket missions called MAIUS (MAteriewellen Interferometrie Unter Schwerelosigkeit). The first of them was launched on January 23rd, 2017 and created the first BEC in space. The MAIUS missions aim at performing atom interferometry with condensed atoms in space taking advantage of the extended time of free fall [70–72]. These missions draw heavily on the results of Q-2 and push the TRL level further. The next step is to use the ISS, which is targeted by the Cold Atom Lab (CAL) [73]. Later on, a cold atom experiment called BEC-CAL should be operated on the ISS, too. This project is a joint cooperation of NASA and DLR. BEC-CAL is supposed to be able to test more than only the UFF. There exist further proposals for satellite missions, but none of them is funded yet [46, 74].

1.3 Constraints and procedures in the drop tower

Any experiment that should be operated in free fall within the drop tower in Bremen needs to fit into a capsule as shown in Fig. 1.3. The tower is evacuated to a pressure of 10-20 Pa, but the capsules are sealed to maintain an air pressure of one atmosphere. This is required, among others, for cooling of electronics. The capsules come in different lengths. Fig. 1.3 shows the Q-2 experiment in a small drop capsule, which is approximately 2 m long and 0.8 m in diameter. The longer capsules can accommodate larger experiments, for example Q-1, but only the small ones can be converted into catapult capsules. For this reason, a small capsule is chosen for Q-2 despite the increased effort of miniaturization. The conversion of such a small capsule into a catapult capsule comprises an exchange of the nose cone and the top cover only and is thus a minor change.

²Alternatively, three drops are possible per working day.



Figure 1.3: Drop capsule with the Q-2 experiment hanging inside the drop tower in Bremen next to the deceleration container, which is situated on the left side of the picture.

The accelerating force of the catapult is transmitted by a piston the capsule rests on. After the free fall, the capsule is decelerated by polystyrene pellets within the deceleration container on the left in Fig. 1.3. Depending on the operational mode – catapult or drop – this container swings into position after the accelerated capsule has passed by or simply rests beneath the drop tube.

The available free fall time is quite constant in drop mode. Small variations are on the order of 20 ms and are due to a different level of polystyrene pellets in the deceleration container. In catapult mode, the time primarily depends on the capsule’s mass and the accelerating force of the catapult. The latter cannot be increased a lot, ultimately limited by the deceleration phase of the catapult’s piston [67]. In consequence, only capsules with a maximum mass of 400 kg can take advantage of the full 9.3 s of microgravity. Q-2 weighs 463.5 kg and can reach 9.0 s.

Figure 1.4 shows the forces acting on the Q-2 capsule during the acceleration phase of 280 ms (a) and the slightly shorter deceleration phase (b). The peak deceleration reaches $35g$ and is even higher for lighter capsules. Negative accelerations of $-2g$ occur because of transient elastic deformations during the launch. Experiments have to be built robust enough to endure these forces. The impact velocity of 42.9 m/s is smaller than the initial velocity of 45.4 m/s because of the height of the deceleration container. The number of experiments per day is currently limited by the evacuation and venting of the tower lasting 1.5 and 0.5 hours, respectively. During the evacuation phase the capsule is connected to water cooling with a cooling power of 2.3 kW at 20 °C and three DC power supplies via an umbilical providing $28\text{ V} \cdot [10 + 10 + 100]\text{ A} = 3360\text{ W}$ [76]. In flight, the capsule is supplied by batteries,

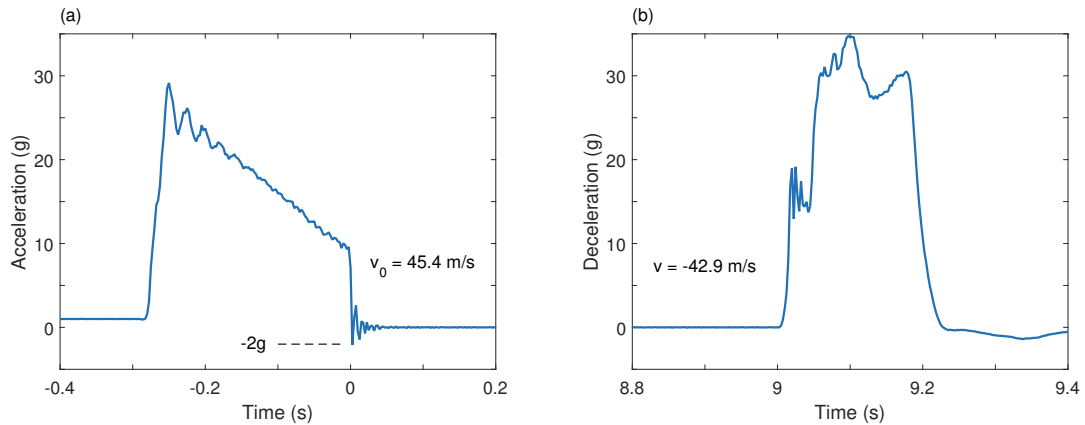


Figure 1.4: (a) Capsule acceleration during a catapult launch in the drop tower in Bremen. (b) Deceleration of the same capsule when diving into the deceleration container filled with polystyrene pellets. Both plots belong to the same data set measured by an inertial measurement unit on board the QUANTUS-2 capsule. The microgravity time was 9.0s and the capsule mass amounted to 463.5 kg. It was accelerated upwards to $v_0 = 45.4 \text{ ms}^{-1}$ and finally hit the container with 42.9 ms^{-1} downwards.

which were buffered by the DC power lines before. The standard battery platform provided by the drop tower has got an available energy of $24 \text{ V} \cdot 25 \text{ Ah} = 600 \text{ Wh}$ for the scientific payload and is buffered by one of the 10 A power lines. WiFi connection to the capsule is given at (almost) all times.

Outline

The next chapter starts with a description of the experimental setup. Afterwards, the strategy for a fast generation of large BECs is explained. The concluding part of that chapter discusses an example experimental sequence and compares the performance of the Q-2 experiment with the state of the art. Chapter 3 characterizes the magnetic field environment as seen by the atoms and shows how it can be manipulated. Chapter 4 is devoted to the adiabatic rapid passage, which is used to prepare the BEC in the non-magnetic substate. The center of mass motion and methods to control it are the subject of Chapter 5. A detailed analysis of the associated systematic effects is presented, which is essential for understanding the bias accelerations in an atom interferometer. Chapter 6 investigates the magnetic lens, which is a method to reduce the velocity spread. Collective excitations of the BEC play an important role in this context. They are discussed in depth. Different experimental realizations of a magnetic lens are shown. Finally, the thesis concludes with a discussion and an outlook.

Chapter 2

The QUANTUS-2 experiment

The first section introduces the experimental setup and its most important features. Section 2.2, in turn, deals with the fast generation of Bose-Einstein condensates, starting with the properties of a thermal ensemble in a magnetic trap. This treatment is based on [77] and [78]. The final section presents the structure of a typical experimental sequence in the drop tower and discusses the differences when operating the experiment in the lab rather than in microgravity. The Q-2 performance benchmark figures are presented in this context, too.

Q-2 was drafted by Waldemar Herr [79], who also built the vacuum chamber and the atom chip together with Jan Rudolph [80]. The subsequent work was a joint team effort by them, Christoph Grzeschik [81], Alexander Grote [82] and the author, who joined the team after the assembly of the vacuum chamber, but before the first atoms were trapped within the experiment. Contributions by the author alone are the power concept with the battery platform and the supervision of the drop tower qualification process of the experiment. Operation, maintenance and upgrades of the experiment have been performed by the team consisting of J. Rudolph, C. Grzeschik, A. Grote, Christian Deppner (later on) and the author with additional support by W. Herr. Temporarily, Dennis Becker and Manuel Popp contributed, too.

2.1 Experimental setup

The buildup of the Q-2 experiment took several years. Even after the successful first drop on July 18th, 2014 the setup was steadily evolving. These changes have been performed for different reasons, for example to improve the reliability of the experiment in the drop tower or to gain more information from the drops. Hence, there is nothing like *the* Q-2 experiment. Nevertheless, upgrades have not been performed within a consecutive series of drops in order to keep the data sets consistent. The setup presented in this work is the status by the end of 2016. The differing previous state of the experiment is highlighted whenever it is important for comprehension or if it can affect the interpretation of experimental data. An image of Q-2 is shown in Fig. 2.1. The overall capsule mass was 463.5 kg for the single catapult campaign and 453 kg for all drop campaigns. The upgrades are typically a replacement of other components and hardly change the mass.

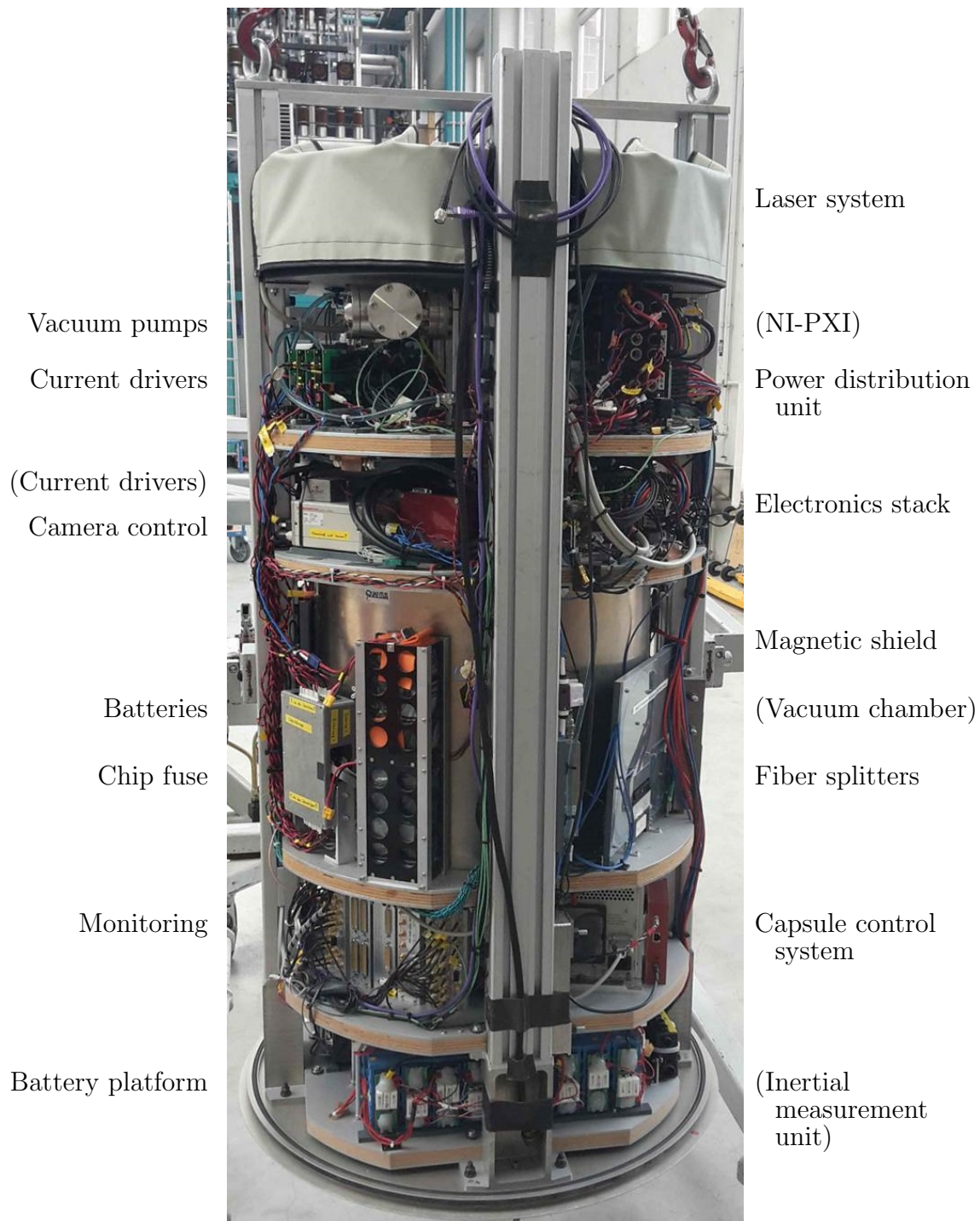


Figure 2.1: The QUANTUS-2 experiment with laser system, National Instruments (NI)-PXI, power distribution unit, electronics stack, mumetal magnetic shield with vacuum chamber inside, optical fiber splitters, capsule control system, inertial measurement unit, vacuum pumps, current drivers, camera control and acquisition hardware, batteries for current drivers, chip fuse, monitoring of status parameters (battery voltages etc.) and a battery platform. Items in parentheses are installed on the respective platform, but are not visible in the image.

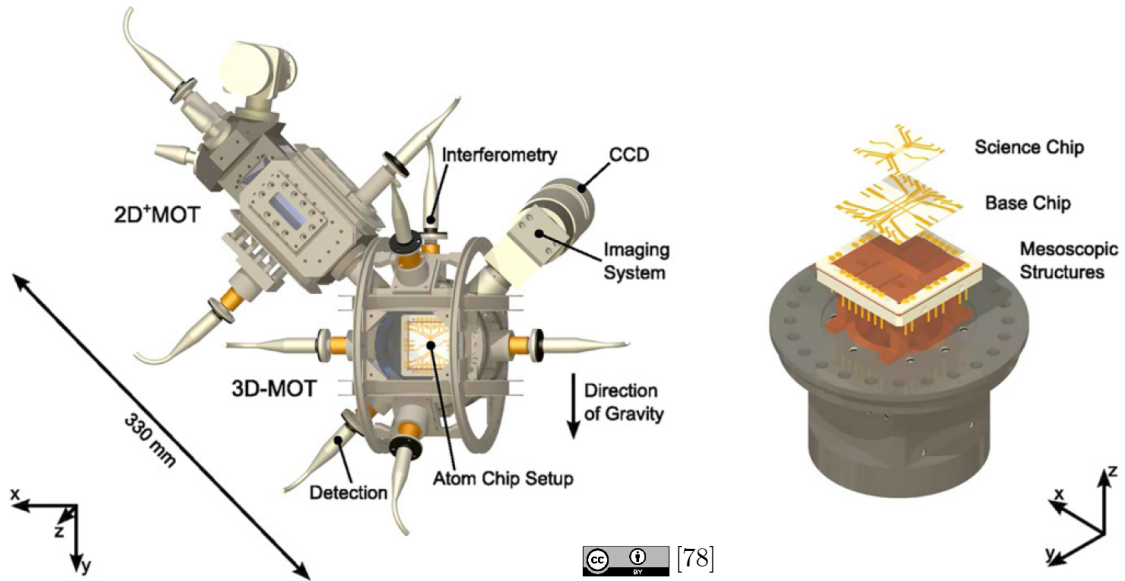


Figure 2.2: Vacuum system of the QUANTUS-2 experiment comprising a chamber for a 2D⁺-MOT and a science chamber. A set of four coils in racetrack configuration is attached to the 2D⁺-MOT chamber. Three Helmholtz coils are wrapped around the science chamber. One detection system is shown (fiber-based collimator for detection laser beam, imaging system and CCD). The detection light passes a three-layer atom chip setup (science chip, base chip and mesoscopic structures), which is shown in the right part of the image. Further fiber-based collimators are attached to the vacuum chamber and provide collimated light for magneto-optical trapping and atom interferometry.

Vacuum system

The Q-2 vacuum system comprises different sections. A rubidium oven is heated to 55°C providing a 2D-MOT chamber (magneto-optical trap) with a sufficient background pressure of ⁸⁷Rb for 2D⁺-MOT operation. A science chamber is connected to the 2D-MOT chamber via a differential pumping stage. Both these chambers are made from titanium and illustrated in Fig. 2.2 as a CAD drawing. Figure 2.3 shows a real image of them. Within the science chamber, ⁸⁷Rb atoms can be trapped either magneto-optically by a 3D-chip-MOT or purely magnetically. The atoms can be detected by two independent detection systems as depicted in Fig. 2.3. The three coil pairs around the science chamber are mounted in Helmholtz configuration. This chamber is connected to a section with three different vacuum pumps [ion getter pump (VinciTech, modified, 5 kV), titanium sublimation pump (VgScienta, SBST110), chemical getter pump (SAES, NEG CapaciTorr C 200 BLD)] and a vacuum sensor (Pfeiffer, IKR270). The typical pressure in this section is $3 \cdot 10^{-11}$ mbar and about three orders of magnitude higher in the oven section due to differential pumping. The ion getter pump and the vacuum sensor require large magnetic fields for operation. For this reason, the pump section is separated from the science chamber as far as possible (≈ 0.6 m). This pump section is partly visible in Fig. 2.1, but not shown in Figs. 2.2 and 2.3.

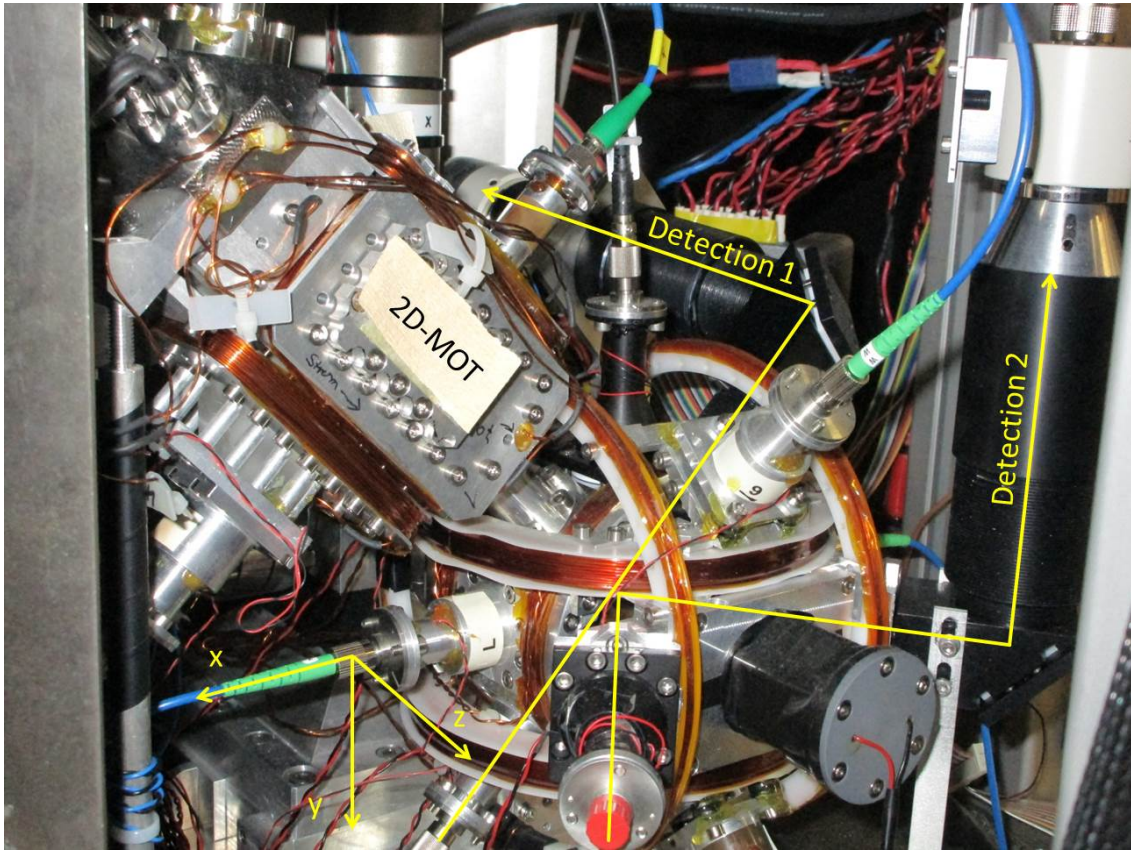


Figure 2.3: The image shows the QUANTUS-2 vacuum system. The light paths for two independent detection systems are highlighted. The Detection 1 system is also shown in the CAD drawing in Fig. 2.2. The light for the Detection 2 system is reflected by the atom chip, which is covered by the corresponding fiber-based collimator.

Trapping of neutral atoms

There are different ways of trapping neutral atoms, for example magneto-optical traps [83], static magnetic traps [84], time-averaged orbiting potential traps [85] and optical dipole traps [86–88]. The Q-2 experiment features magneto-optical trapping for a high flux of precooled atoms followed by high frequency Ioffe-Pritchard (IP) type traps for fast evaporative cooling to quantum degeneracy. This combination facilitates the high repetition rate.

The force on an atom with magnetic dipole moment $\boldsymbol{\mu}$ in a magnetic field \boldsymbol{B} is given by

$$\boldsymbol{F} = \nabla(\boldsymbol{\mu} \cdot \boldsymbol{B}). \quad (2.1)$$

Depending on $\boldsymbol{\mu}$ this force is directed either in the direction of increasing or decreasing magnetic field. Accordingly, the atoms can be either high-field-seekers or low-field-seekers. It can be shown that no local field maximum can exist in a region free of charges and currents [89]. Still, a local field minimum can exist and form a trap for low-field-seekers. In the Q-2 experiment, $^{87}\text{Rb } 5^2\text{S}_{1/2}$ atoms with $F = 2$ are used. The two Zeeman substates $m_F = 2$ and $m_F = 1$ are low-field-seekers and hence

magnetically trappable. The $m_F = -1$ state of the $F = 1$ manifold is trappable, too, but the trapping potential is stronger for the $F = 2, m_F = 2$ substate. A level scheme is shown in Fig. 2.4.

The strength of a trapping potential is characterized by its trap frequency ω . The ideal trap would be isotropic in all three spatial dimensions and harmonic. In fact, real magnetic traps are usually neither of that. The anisotropy is accounted for by introducing three trap frequencies ω_x , ω_y and ω_z for the corresponding spatial dimensions and the anharmonicities are described by the coefficients $L3$ and $L4$. The potential is then given by

$$V(\mathbf{r}) = V_0 + m_{\text{Rb}} \left\{ \frac{\omega_x^2(x - x_0)^2}{2} + \frac{\omega_y^2(y - y_0)^2}{2} + \omega_z^2 \left[\frac{(z - z_0)^2}{2} + \frac{(z - z_0)^3}{3L_3} + \frac{(z - z_0)^4}{4L_4} \right] \right\}. \quad (2.2)$$

The trap center is at (x_0, y_0, z_0) with the trap bottom V_0 . The trap is assumed to be anharmonic in the z direction only. This is a good approximation for the IP traps realized in the Q-2 experiment. It is important that the trap bottom is larger than zero. Otherwise Majorana spin flips would occur leading to a significantly reduced lifetime of the atomic ensemble in the trap [90, 91].

The Atom Chip

The key feature of the Q-2 experiment is a so called atom chip. It comprises three layers of conducting structures mounted within the science chamber as indicated by the right part of Fig. 2.2. A variety of magnetic potentials can be generated by the superposition of their magnetic field with a homogeneous magnetic offset field. The latter is created by three Helmholtz coils for the respective spatial dimensions (x , y and z coil).

The three chip layers are mounted on top of a copper block which serves as a heat sink. It is shown in Fig. 2.5. The bottom layer of the atom chip consists of Kapton isolated copper wires with a conductor diameter of 0.6 mm. They are recessed into the copper mount and referred to as mesoscopic structures. The first one is H-shaped and hence called Meso-H. It can be used to form an IP trap and serves as an example structure to explain the basic concepts of such traps. For a thorough quantitative treatment of magnetic microtraps the reader is referred to [93]. Alas, even such an analysis is insufficient for Q-2, because the supply conductors are not taken into account. Instead, a Biot-Savart simulation is used which accounts for the closest parts of these additional wires, too. This simulation for the full Q-2 atom chip is called the Q-2 chip model and is explained below.

When a current flows through the central wire of the Meso-H in the opposite x direction, a circular magnetic field is created according to the right hand rule. On the z axis, this field is pointing in the y direction and decreases with increasing distance from the wire. When superimposed with a homogeneous magnetic field in the opposite y direction, the resulting magnetic field is zero at a certain distance

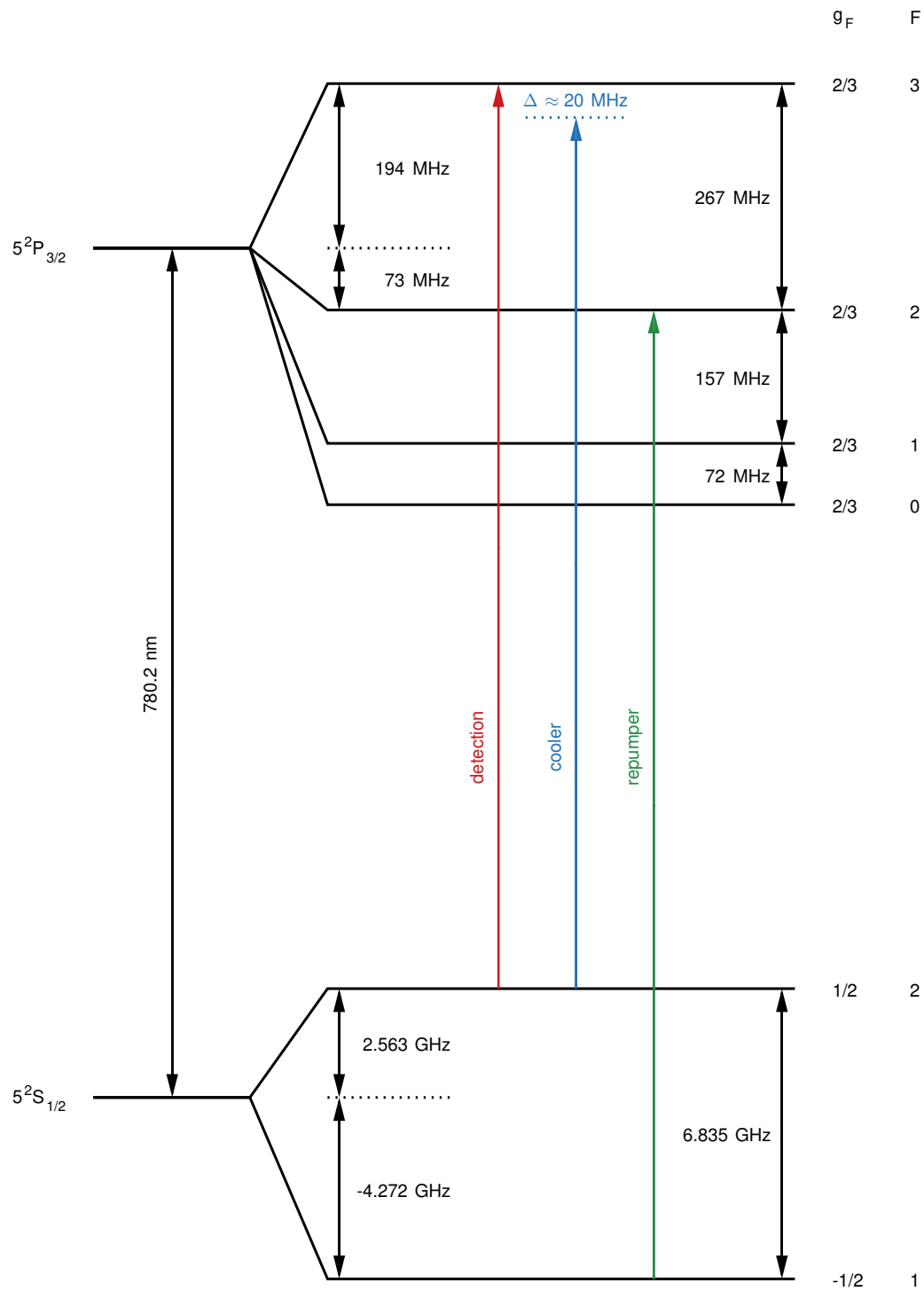


Figure 2.4: Hyperfine structure of the ^{87}Rb D_2 transition with Landé factor g_F and total angular momentum quantum number F . The energy levels are not to scale. The transition used for detection is shown as the red arrow. Transitions used for magneto-optical trapping are the cooling transition (blue arrow), which is detuned by $\Delta \approx 20$ MHz, and the repumping transition (green arrow). Numerical values from [92].

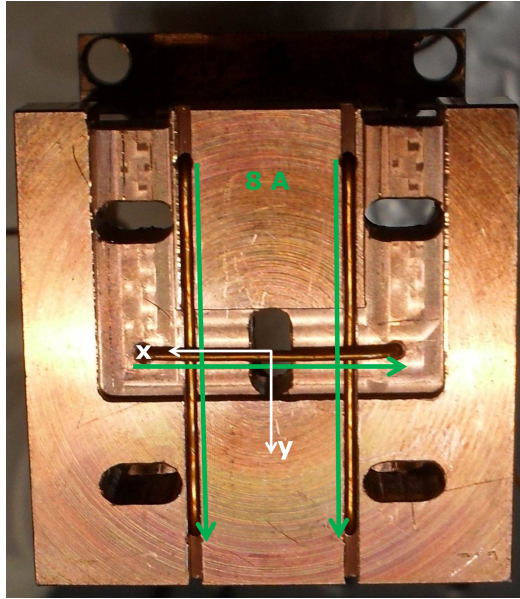


Figure 2.5: Copper chip mount with an edge length of 35 mm. Kapton isolated copper wires are recessed into the bulk material and form an 'H'. The typical current through these wires is 8 A. (Photo source: Waldemar Herr)

depending on the ratio of currents in the Meso-H and the y coil. This is already a two dimensional trap. The trap axis passes through this point of zero field and is parallel to the central wire. Axial confinement is realized by the two parallel wires of the Meso-H resulting in a three dimensional IP trap. Since the y coil is the only indispensable coil it gets an extra name. It is called bias coil and its field is called bias field, accordingly.

The trap can be manipulated in different ways. An increasing bias field at a constant Meso-H current moves the trap center closer to the Meso-H and vice versa. On the other hand, a magnetic offset field in the z direction rotates the trap center around the x axis. Finally, an offset field in the x direction affects the trap bottom. Unfortunately, such traps do not behave well when rescaling all currents by the same factor. In fact, the trap rotates and moves. These effects are quantitatively described by the chip model.

The equipotential surfaces of harmonic traps are ellipsoids. Deviations from this shape can arise from anharmonicities. The trap frequencies predicted by the chip model refer to the eigenvectors of these ellipsoids. In general, they do not coincide with the symmetry axes of the atom chip, but are rotated about the normal to the chip.

In addition to the Meso-H, six U-shaped wires belong to the bottom chip layer, as shown by the left image in Fig. 2.6. In combination with an offset field in the opposite y direction, it creates a magnetic quadrupole field as required for a MOT.

The BC is a 35×35 mm aluminum nitride substrate placed directly on top of the copper mount, as shown by the right image in Fig. 2.6. The electroplated gold structures are $8 \mu\text{m}$ high and can support up to 6 A. They are used to form various

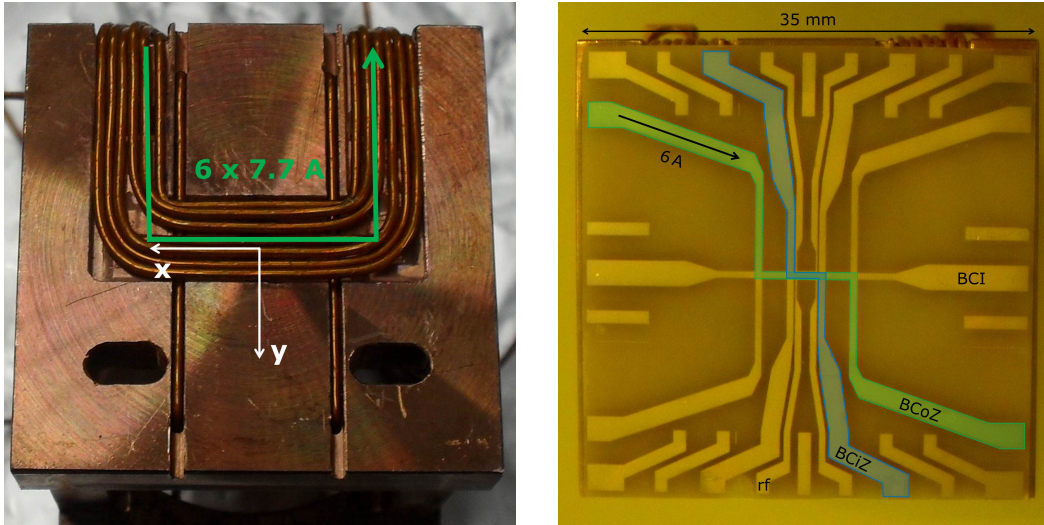


Figure 2.6: (left) Copper chip mount with the mesoscopic chip structures made from Kapton isolated copper wires: Meso-H (see Fig. 2.5) and six wires forming the Meso-U. The typical current through a single Meso-U wire is 7.7 A. (right) Base chip (BC) on top of the mesoscopic structures that are recessed into the chip mount. The BC structures are made from gold and can support up to 6 A (in vacuum). They harness various geometries, for example inner and outer Z-like structures (BCiZ, BCoZ). Two U-shaped radio frequency antennas are close to the central wire (BC-I), but not electrically connected to it. (Photo source: Waldemar Herr)

conductor geometries, for example Z-like. Two of them are shown in the image, that are an inner and an outer Z (BCiZ, BCoZ). Because of the larger trap volume the BCoZ is used for all measurements shown in this work and referred to as BC-Z. H-like structures are possible, too. They are called BCiH and BCoH, accordingly. Unlike the Meso-H, they cannot be fed by a single current driver, because the individual 'wires' are electrically connected. Their width is 0.5 mm at a separation¹ of 2.0 mm in the central region of the BC. In addition to them, there are two (upper and lower) U-shaped radio frequency (rf) antennas close to the central conductor (BC-I). They are required for rf evaporation, for example, and are electrically isolated from the remaining structures.

The third chip layer is the 25×25 mm science chip (SC) placed on top of the BC. It is shown in Fig. 2.7. The conducting structures are similar to the BC, but smaller. They are separated² by 0.5 mm and have a width of 50 μm . These wires can support a current of 2 A. In analogy to the BC, they are called SCoZ, SCiZ, etc. Again, only the SCoZ is used and referred to as SC-Z. Whenever a BC or SC current is given, it is the current through these outer Z-structures. Since optical access for the MOT is limited due to the chip itself, the surface of the SC is coated [OIB Jena] to reach a reflectivity of 97.7% at 45° for a wavelength of 780 nm [80]. The point on this coating and in front of the center of the horizontal SC wire (SC-I) defines the origin

¹The wire centers are $(2.0 + 0.5)$ mm apart.

²The wire centers are $(500 + 50)$ μm apart.

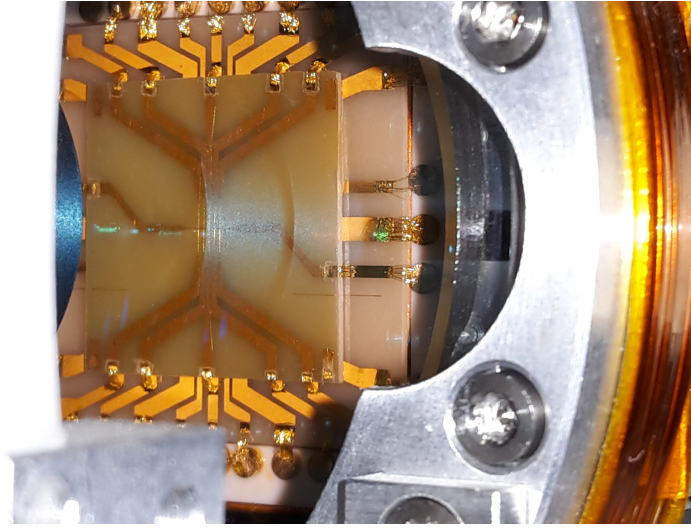


Figure 2.7: Full three layer atom chip setup in the Q-2 experiment. The top layer (science chip) is fully and the intermediate layer (base chip) partially visible. The bottom layer (mesoscopic structures) is completely covered. The titanium to the right is part of the vacuum chamber and wrapped by the z coil (copper wires on the right edge). Gravity points downwards.

of the Q-2 coordinate system. Like in Figs. 2.5 and 2.6, the x axis points towards the left and the y axis points downwards in the direction of gravity. The y axis is parallel to the capsule's symmetry axis, but not coinciding. The z axis points away from the chip as required for a right-handed coordinate system.

Detection of rubidium atoms

The rubidium atoms can be detected by two independent absorption imaging systems. In both of them, a collimated laser beam with an intensity of $I \approx 1$ mW and a $1/e^2$ beam diameter of 7 mm passes the atoms. Their shadow is cast onto a CCD camera with 1344×1024 px [Hamamatsu, C8484-15C]. The pixel size is $6.45 \mu\text{m}$. A magnification of 1.8 is achieved by a telescope with two AR-coated achromatic lenses ($f_1 = 50$ mm [Edmund optics, NT49-957] and $f_2 = 90$ mm [Linos, G322389525]) resulting in a measured resolution of $5.5 \mu\text{m}$ [79]. The detection telescope is mounted such that the atoms are in the focal point of the first lens (f_1) and the camera is in the focal point of the second one. The telescope is bent with a mirror [HR-coated, Linos, G340784000] in between both lenses for geometrical reasons.

The laser beam for the first detection system (Detection 1) propagates along the SC from its bottom left to the top right corner (45° w.r.t. the x and y axis). The beam center is approximately 3 mm away from the chip surface. For comparison, the center of the IP trap is approximately 1 mm in front of the center of the SC. When atoms are released from this trap, they fall downwards and leave the detection zone after a TOF of 22 ms.

The laser beam for the second detection system (Detection 2) propagates in the $y = -0.35(2)$ mm plane and is reflected by the coating on the SC. The angle of

incidence is 37.5° . As a matter of fact, the view in Fig. 2.7 is oriented approximately into this reflected laser beam. There are two images of the cloud on the CCD. One of them is a 'direct image' with the laser beam passing the atoms after reflection on the chip surface. For the second 'reflected image', the laser beam is reflected on the chip surface after passing the atoms. This mirror image is the left cloud in the Detection 2 CCD images presented in this work. It is possible to extract 3D information out of these 2D images provided that both clouds are on the CCD and sufficiently separated. Since the y axis is not projected at an angle of 45° , like in Detection 1, the atoms fall out of the detection zone even more rapidly (after 14 ms TOF). A smaller magnification would increase the available TOF, but deteriorate the resolution.

The laser light for detection can be resonant to the $F = 2 \rightarrow F' = 3$ transition, as shown in Fig. 2.4 by the red arrow, or detuned from this transition. Its natural linewidth is $\Gamma = 2\pi \cdot 6$ MHz [92]. Hence, a detuning δ can be of this order. The scattering of light out of the detection laser beam can be derived from the optical Bloch equations [92]. It is described by the scattering cross section

$$\sigma(\delta, I) = \frac{\sigma_0}{1 + 4(\delta/\Gamma)^2 + I/I_{\text{sat}}}, \quad (2.3)$$

where I is the light intensity, I_{sat} the saturation intensity of the transition and

$$\sigma_0 = \frac{\hbar\omega\Gamma}{2I_{\text{sat}}} \quad (2.4)$$

the on-resonance scattering cross section with the photon frequency ω . The accompanying decrease in intensity is described by Beer's law:

$$\frac{dI}{dz'} = -n(x', y', z')\sigma(\delta, I)I, \quad (2.5)$$

with the atomic density distribution $n(x', y', z')$ and a coordinate system aligned such that the laser beam propagates along the z' direction. The beam profile is implicitly accounted for by $I(x', y')$. Equation (2.5) is a separable differential equation:

$$\frac{1 + 4(\delta/\Gamma)^2 + I/I_{\text{sat}}}{\sigma_0 I} dI = -n(x', y', z') dz'.$$

It can be readily integrated:

$$\frac{1 + 4(\delta/\Gamma)^2}{\sigma_0} \ln(I) + \frac{I}{\sigma_0 I_{\text{sat}}} + c_1 = -\tilde{n}(x', y') + c_2, \quad (2.6)$$

with constants of integration c_1 and c_2 . The two-dimensional atomic density distribution

$$\tilde{n}(x', y') = \int n(x', y', z') dz' \quad (2.7)$$

is the quantity of interest. It can be measured by acquiring three CCD images: An 'atom image' (I_{atoms}) of the laser beam including the shadow cast by the atoms, a 'beam image' (I_{beam}) of the laser beam alone and a 'dark image' (I_{dark}) without

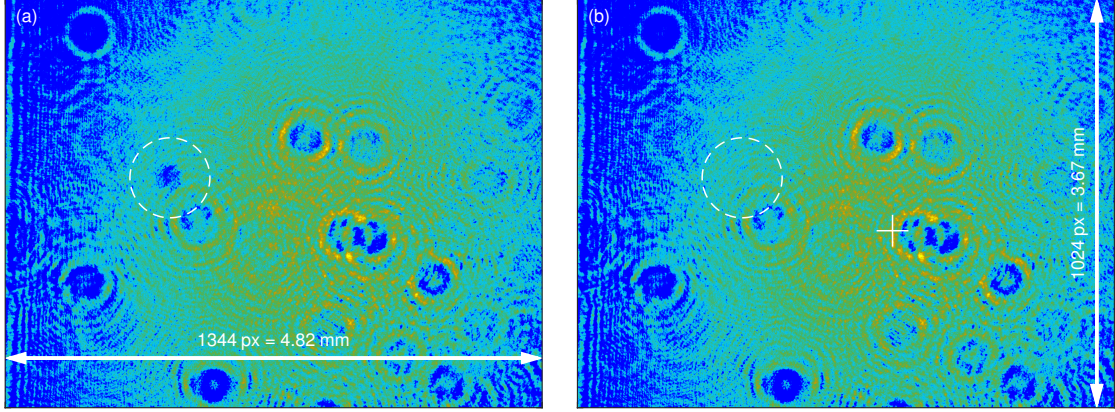


Figure 2.8: CCD images of the laser beam for Detection 1: Yellow regions exhibit a higher intensity than blue ones. The center of the Gaussian beam profile is marked by a white plus sign in (b). Atoms cast a shadow onto the 1344×1024 px large CCD chip as highlighted by the white circle in the atom image (a). The shadow is not present in the beam image (b).

atoms and laser beam to correct for dark counts of the CCD camera. For illustration, an atom image and the corresponding beam image (using Detection 1) are shown in Figs. 2.8(a) and (b), respectively. The atom chip is just to the left of the images and thus not visible. Its diffraction pattern due to the science chip edge, however, is visible (vertical stripes). The remaining airy-like patterns originate from dirt particles in the optical path. They are stable and can be used for a post correction of the camera movement arising from the impact of the capsule into the deceleration container. This movement is on the order of a few micrometers. The beam image is acquired 180 ms after the atom image. This time is required for a camera readout in between two images and is sufficient for the atoms to leave the detection zone. Dark images are acquired on a regular basis, for example once per drop, but not for each set of images individually. Within the exposure time of $40 \mu\text{s}$ a rubidium atom can scatter several hundred photons.

Equation (2.6) can be rewritten in terms of the dark count corrected intensities of the atom and beam image, respectively:

$$\frac{1 + 4(\delta/\Gamma)^2}{\sigma_0} \ln(I_{\text{atoms}} - I_{\text{dark}}) + \frac{I_{\text{atoms}} - I_{\text{dark}}}{\sigma_0 I_{\text{sat}}} + c_1 = -\tilde{n}(x', y') + c_2, \quad (2.8a)$$

$$\frac{1 + 4(\delta/\Gamma)^2}{\sigma_0} \ln(I_{\text{beam}} - I_{\text{dark}}) + \frac{I_{\text{beam}} - I_{\text{dark}}}{\sigma_0 I_{\text{sat}}} + c_1 = c_2, \quad (2.8b)$$

where the atomic density vanishes for the beam image. Subtracting (a) from (b) yields

$$\tilde{n}(x', y') = \frac{1 + 4(\delta/\Gamma)^2}{\sigma_0} \ln\left(\frac{I_{\text{beam}} - I_{\text{dark}}}{I_{\text{atoms}} - I_{\text{dark}}}\right) + \frac{I_{\text{beam}} - I_{\text{atoms}}}{\sigma_0 I_{\text{sat}}}. \quad (2.9)$$

Applying Eq. (2.9) to each pixel of the atom and beam image in Figs. 2.8(a) and (b), respectively, yields the 2D density image in Fig. 2.9. A software package for this



Figure 2.9: Atomic density image resulting from processing the atom and beam image in Fig. 2.8 using Eq. (2.9). The atomic ensemble (yellow region) was detected in microgravity 100 ms after releasing a Bose-Einstein condensate from its trap. The x'_{raw} and y'_{raw} axes show the camera coordinate system of the first detection system (Detection 1) and the red 'x' marks the origin of the Q-2 coordinate system.

image processing was kindly provided by the Q-1 team. The raw camera coordinates x'_{raw} and y'_{raw} are affected by small camera shifts from drop to drop due to the accelerations in the tower. Hence, the coordinates need to be referenced to the atom chip. An overview over the transformations between the different coordinate systems is given below.

The combination of a magnetic offset field co-aligned to the propagation direction of the σ^+ -polarized detection beam realizes a cycling transition. Atoms in $F = 2$, $m_F = 2$ are excited to $F' = 3$, $m_{F'} = 3$ and cannot decay back into any other state but the initial one. Atoms that are initially in any other Zeeman substate of the ground state $F = 2$ manifold are rapidly transferred into the $m_F = 2$ substate after a few transitions. This is possible as long as the magnetic offset field is not too strong such that the frequency shift by the Zeeman effect is on the order of the natural linewidth. The saturation intensity for this cycling transition is $I_{\text{sat}} = 1.67 \text{ mW/cm}^2$ [92]. It can be approximately a factor of two higher if the polarization is not clean. To account for this effect, the effective saturation intensity

$$I_{\text{sat}}^{\text{eff}} = \alpha^* I_{\text{sat}} \quad (2.10)$$

can be introduced according to [94]. The alpha factor is unity for perfectly circularly polarized light and larger otherwise. The scattering cross section transforms accordingly:

$$\sigma_0^{\text{eff}} = \frac{\sigma_0}{\alpha^*}. \quad (2.11)$$

By accounting for this effect, Eq. (2.9) reads:

$$\tilde{n}(x', y') = \alpha^* \frac{1 + 4(\delta/\Gamma)^2}{\sigma_0} \ln \left(\frac{I_{\text{beam}} - I_{\text{dark}}}{I_{\text{atoms}} - I_{\text{dark}}} \right) + \frac{I_{\text{beam}} - I_{\text{atoms}}}{\sigma_0 I_{\text{sat}}}. \quad (2.12)$$

The atom number

$$N = \int \tilde{n}(x', y') dx' dy' \quad (2.13)$$

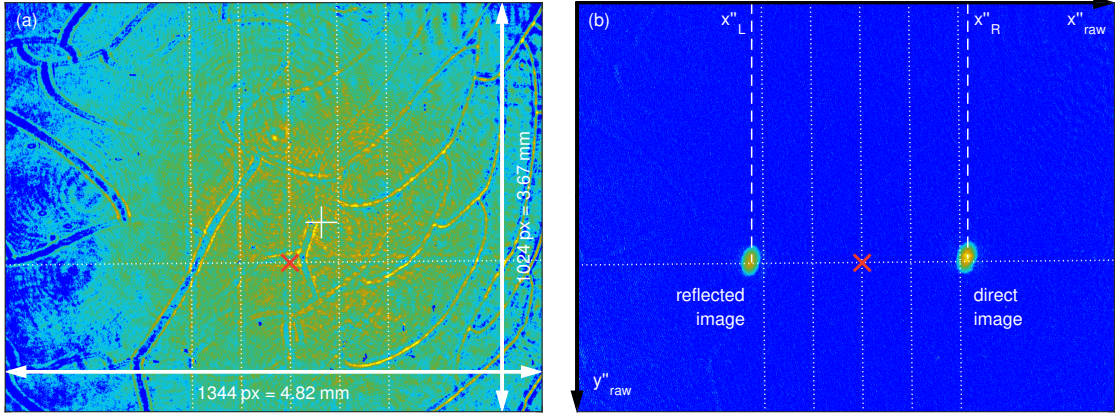


Figure 2.10: (a) Beam image from Detection 2 imaged by a similar detection system as for Detection 1 (see Fig. 2.8). The detection beam center is marked by a white plus. The science chip conductors are faintly visible and highlighted by dotted white lines. Their center defines the origin of the Q-2 coordinate system (red 'x'). (b) Processed density image [Eq. (2.9)] exhibiting two images of the same atomic cloud. For the left cloud, the detection laser beam passes the atoms and is then reflected at the chip surface (reflected image). The remaining light passes the atoms again and a second shadow is cast creating the direct image. The Detection 2 coordinates are labeled x''_{raw} and y''_{raw} with indices L and R. The density image (b) was detected in microgravity 80 ms after releasing a Bose-Einstein condensate from its trap.

can be significantly overestimated by choosing too high a value for α^* . By applying the methods described in [94], this factor was measured to be unity in Q-2:

$$\alpha_{\text{Q-2}}^* = 1. \quad (2.14)$$

Typically, the detection light is on-resonance with the cycling transition. Whenever an atomic cloud is too dense, the light can be detuned to reduce the scattering cross section and hence the optical depth. However, the cloud then behaves as a gradient index lens. For this reason, a detuning is problematic for small clouds, for example BECs after short TOFs.

The images acquired by Detection 2 look different from the ones by Detection 1. Figure 2.10(a) shows such a beam image. Since this beam was reflected by the science chip, its wires are faintly visible. They are highlighted by dotted white lines. Their center is marked by a red 'x' and defines the origin of the Q-2 coordinate system in this plane. These chip wires provide a ruler for a correction of camera shifts and are used for a correction of the raw camera coordinates x''_{raw} and y''_{raw} (in comparison to x'_{raw} and y'_{raw} for Detection 1, where the airy-like patterns are used). Cracks in the high reflective coating of the chip surface are visible, too. Occasionally, they cannot be fully eliminated by the formalism described above. Despite this, valuable 3D information is still available, but at a slightly higher uncertainty in the fitted position. The two images required for this, reflected and direct, can be seen in Fig. 2.10(b). The magnetic field orientation required for the cycling transition is different for Detection 1 and each of the two Detection 2 images. For this reason,

the field can be correctly aligned for only one of the three absorption images at the same time. It is optimized for Detection 1, which is exclusively used to evaluate atom numbers. Detection 2 is used to provide 3D information about the cloud's position and size.

Coordinate systems

The raw camera coordinates are of limited use because of the camera shifts. The beam image has to be compared to a reference beam image, which was used to calibrate the chip model. The necessary corrections are small rotations ($\approx 1^\circ$) and translations (micrometers) of the density image. For definiteness, they are subsumed by $\text{camShift}_{x'}$, $\text{camShift}_{x''}$, etc. In addition, the corrected coordinate system is also shifted by a few mm such that its origin coincides with the origin of the Q-2 coordinate system. The corrected coordinates are x' , y' , x'' and y'' . Their relation to the raw and to the Q-2 coordinate system (x , y and z) is given by Eqs. (2.15) to (2.17):

$$x' = z = x'_{\text{raw}} - \text{camShift}_{x'}, \quad (2.15a)$$

$$y' = (y - x) / \sqrt{2} = y'_{\text{raw}} - \text{camShift}_{y'} - 1.55 \text{ mm}, \quad (2.15b)$$

$$x'' = x''_{\text{raw}} - \text{camShift}_{x''} - 2.53 \text{ mm}, \quad (2.16a)$$

$$y'' = y = y''_{\text{raw}} - \text{camShift}_{y''} - 2.28 \text{ mm}, \quad (2.16b)$$

$$x = (x''_{\text{L}} + x''_{\text{R}}) / 2 = (x''_{\text{L,raw}} + x''_{\text{R,raw}}) / 2 - \text{camShift}_{x''} - 2.53 \text{ mm}, \quad (2.17a)$$

$$y = (y''_{\text{L}} + y''_{\text{R}}) / 2 = (y''_{\text{L,raw}} + y''_{\text{R,raw}}) / 2 - \text{camShift}_{y''} - 2.28 \text{ mm}, \quad (2.17b)$$

$$z = \frac{x''_{\text{R}} - x''_{\text{L}}}{2 \cdot \sin(37.5^\circ)} = \frac{x''_{\text{R,raw}} - x''_{\text{L,raw}}}{2 \cdot \sin(37.5^\circ)} - 72 \text{ } \mu\text{m}, \quad (2.17c)$$

where Eq. (2.17c) is independent of camera translations and the dependence on rotations can be neglected, because its effect is extremely small ($0.2 \text{ } \mu\text{m}$). The offset of $72 \text{ } \mu\text{m}$ is due to the optical coating of the chip defining the $z = 0$ plane for the Detection 2 frame. Equation (2.16) is applicable for both clouds.

In many cases, the data from the first detection system is sufficient. Occasionally, even 3D information can be inferred, for example trap frequencies by means of beat notes on the position data. For a long time, this was the only available detection system. The first drop with the second detection system installed was Drop 119 in August 2015.

The chip model

Magnetic traps can be characterized by a few key properties. The most important ones are their frequencies, anharmonicities and the trap center. Another one is the

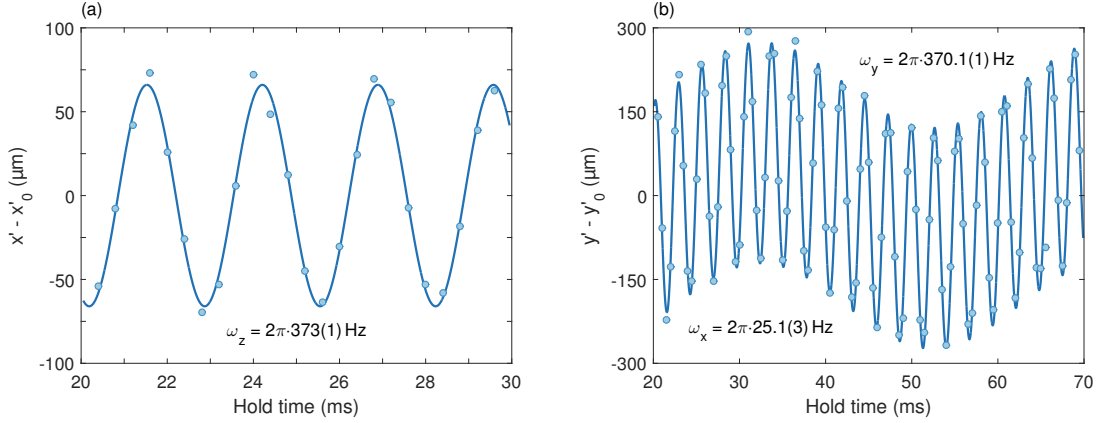


Figure 2.11: Example measurement of the trap frequencies of an IP trap generated by the currents $I_{BC} = 6 \text{ A}$, $I_{SC} = 2 \text{ A}$, $I_y = -1.2 \text{ A}$ and $I_x = I_z = 0$. The positions x' (a) and y' (b) after 11 ms TOF are plotted vs. the hold time within the trap. The centers of oscillation (x'_0 and y'_0) were subtracted from the data. The solid lines are fits giving the trap frequencies ω_x , ω_y and ω_z .

trap bottom, which is proportional to the absolute value of the magnetic field at the trap center. Not all trap configurations can be characterized by ground-based measurements. Shallow traps more than 1 mm away from the chip are deformed too much by the gravitational potential. If it is not compensated, for example optically or magnetically, such traps are accessible in microgravity only. As a matter of fact, these shallow traps are the interesting ones for magnetic lensing. In addition, atom interferometry benefits from the larger separation from the chip, too.

The chip model is a Biot-Savart simulation of all relevant conductors written by Waldemar Herr [79]. It is an invaluable tool predicting the trap properties, especially of the shallow traps that are inaccessible by ground-based measurements. Characterizing them experimentally would consume too much of the valuable microgravity time. This chip model was calibrated by ground-based measurements. Details on the model itself and the calibration process can be found here [79]. An example measurement of trap frequencies is shown in Fig. 2.11. A Bose-Einstein condensate is prepared in the trap of interest (see figure caption). Dipole oscillations are then excited by temporarily displacing the trap. The resulting *in situ* oscillations are very small ($\approx 6 \mu\text{m}$) and hardly detectable. However, the detectable amplitude increases linearly with time after releasing the atoms from the trap. All trap frequencies can then be retrieved from sinusoidal fits to the position data. This procedure is repeated for a variety of trap configurations and is complemented by measurements of the *in situ* position and the trap bottom. The workhorse trap in Q-2 is generated by $I_{BC} = 6 \text{ A}$, $I_{SC} = 2 \text{ A}$, $I_x = 0.5 \text{ A}$ and $I_z = 0$ at different bias currents. The corresponding trap centers and frequencies are shown in Figs. 2.12 and 2.13, respectively. More negative bias currents correspond to steeper traps closer to the chip and vice versa. Gravity also affects the trap properties. Its effect on the trap center can be seen in Fig. 2.12(a) by comparing the solid lines (with gravity) to the dash-dotted

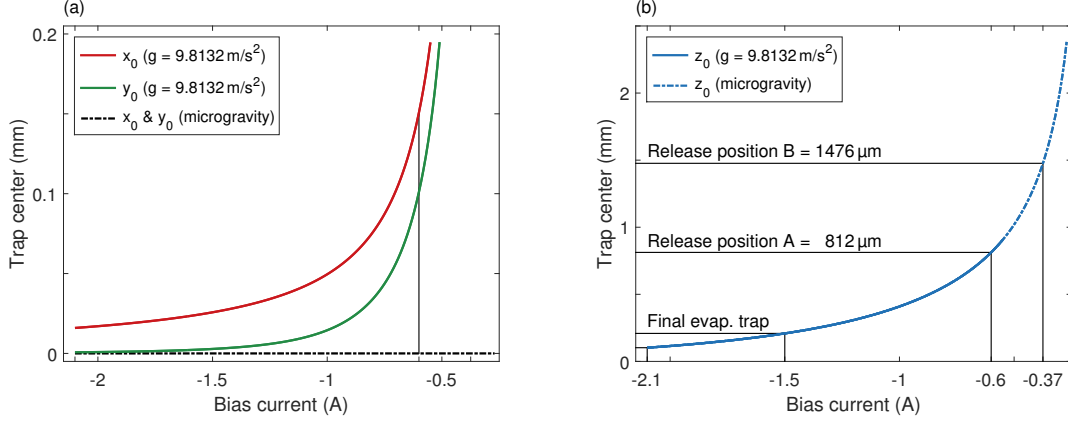


Figure 2.12: Simulated trap centers using the Q-2 chip model for $I_{BC} = 6 \text{ A}$, $I_{SC} = 2 \text{ A}$, $I_x = 0.5 \text{ A}$ and $I_z = 0$. In microgravity (dash-dotted lines), the trap center is on the z axis [$x_0 = y_0 = 0$, dash-dotted black line in (a)], but departs for less negative bias currents, as shown by the solid lines in (a). The bias current $I_y = -0.6 \text{ A}$ is the smallest one used for traps 'with gravity' (lab environment) and is referred to as 'Release position A' at $z = 812 \mu\text{m}$. The trap center's z coordinate differs hardly with or without gravity for larger bias currents. Release position B at $z = 1476 \mu\text{m}$ is possible in a microgravity environment only. At $I_y = -1.5 \text{ A}$ the final phase of evaporative cooling for the creation of a Bose-Einstein condensate is performed.

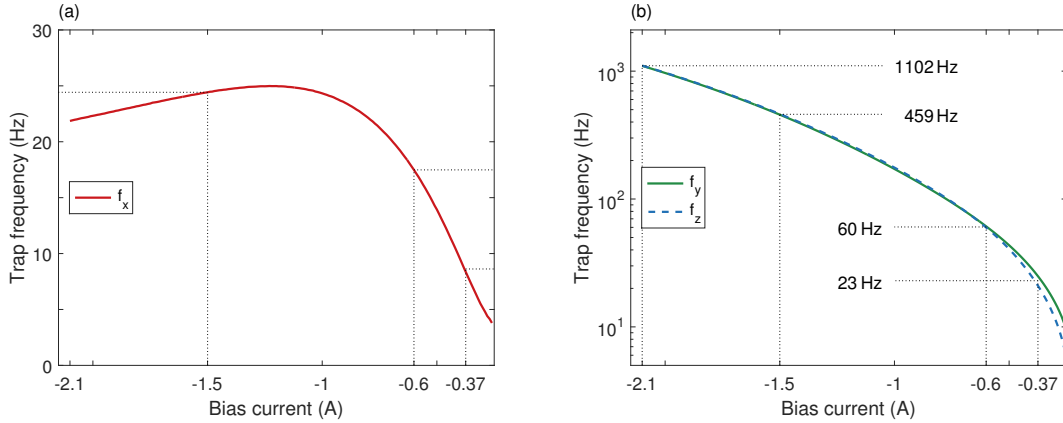


Figure 2.13: Simulated trap frequencies ($f = \omega/2\pi$) in microgravity using the Q-2 chip model. The frequency in the x direction (a) is always smaller than in the y or z direction [solid green and dashed blue line in (b)]. The latter two are very similar to each other. Their geometric mean is given for the particular bias currents shown in Fig. 2.12.

lines (without gravity). The distance from the chip (z_0) hardly differs, but beyond $I_y \approx -0.5$ A traps are possible in microgravity only. Close to this limit, the trap center moves away from the z axis. Release position A – approximately 0.8 mm away from the chip – was used for the first drop campaigns, because it could be tested in the lab. For the later campaigns, release position B at 1.5 mm was used, because the chip model predicts a promising trap for magnetic lensing at this position (see Chapter 6). In both cases, the BEC has to be transferred from its point of creation, that is the final trap for evaporative cooling, to the release position. This transfer is explained in Section 5.3. The release traps corresponding to release positions A and B are referred to as release traps A and B, respectively.

It can be seen in Fig. 2.13 that the trap is anisotropic. The weak trap axis is always pointing approximately in the x direction. The two fast frequencies f_y and f_z are similar or even equal at some specific locations. This holds for other trap configurations as well. High frequency traps are required for a fast creation of BECs, as discussed in Section 2.2. Two traps are successively used for this. The initial one with $I_y = -2.1$ A is 102 μm away from the chip and the final one with $I_y = -1.5$ A is at $z = 209$ μm .

The chip wires are one source of the magnetic field required for the traps. It decreases with the distance from the chip ($1/r$ dependence). The resulting local curvature is responsible for the trap anharmonicity, which is an inevitable property of chip traps. It can, however, be mitigated by choosing traps further away from the chip.

Laser system

The Q-2 laser system provides laser light for cooling, optical pumping, Bragg diffraction and detection of rubidium and (later on) potassium atoms. The lasers were designed and manufactured by the FBH in Berlin and have a footprint of 25×50 mm. A power amplifier (PA) is seeded by a DFB diode as master oscillator (MO). This combination provides 1 W of output power at a wavelength of 780 nm and a linewidth of approximately 1 MHz. More details on these MOPA modules can be found here [95–99]. The laser system has been planned and constructed by the HU-Berlin. So far, only the rubidium part of the laser system was integrated into the Q-2 capsule. Three MOPAs are frequency stabilized by offset locks to a master laser, which is in turn stabilized to the $F = 3 \rightarrow F' = 3/4$ crossover of the ^{85}Rb D_2 transition by frequency modulation spectroscopy. Fast switching (1 μs) and frequency shifting are achieved by acousto-optical modulators (AOMs). Residual light can be completely blocked by mechanical shutters.

The laser system is subdivided into different modules for improved mechanical stability. They are interconnected by polarization maintaining single mode optical fibers. The system is catapult tested: All lasers remain frequency stabilized even during the acceleration and deceleration phases. The light is guided to the vacuum chamber by optical fibers, too. MOT light is split up by fiber splitters. More details on the laser system are described here [81].



Figure 2.14: Customized electronics stack with laser current drivers, temperature controllers, locking electronics, DDS cards for driving AOMs, shutter controllers, communication and power interfaces. All cards have been developed by Thijs Wendrich in Hanover.

Electronics

A substantial amount of electronics is required for the operation of a cold atoms experiment like Q-2. All of it can be bought off the shelf. Nevertheless, these commercially available components are too large to meet the geometrical constraints for the small catapult capsule. For this reason, most of the electronics has been designed from scratch by a project partner (Institute of Quantum Optics, Hanover) and kept as small as possible.

The laser system is controlled by a stack of different cards, each with a size of 10×10 cm. This stack is referred to as T-Stack³ and is shown in Fig. 2.14. The lasers are temperature stabilized using thermoelectric coolers (TECs) to 1 mK precision. Laser currents are provided by two types of current driver cards (200 mA for the MOs and almost 2 A for the PAs⁴). Direct feedback channels from the frequency controller card to the MOs control the laser frequencies. Other cards provide AC-signals for driving the AOMs (80 or 100 MHz), control the mechanical shutters or supply the cooling fans for the electronics itself. Communication is performed at a 50 MHz clock rate using eight address and eight data bits on the T-Bus with a LabView Real Time system on a NI-PXI with a field programmable gate array (FPGA).

Beat signals from the offset lock photodiodes have frequencies of a few GHz. Each of them is amplified by a chain of three Mini-Circuits amplifiers [ZX60-14012L+] and divided by prescalers [Hittite HMC862LP3E] to get below the upper limit of 1.1 GHz for the frequency controller card.

All coil (2D⁺-MOT, x , y and z) and chip currents (Meso-H, Meso-U, BC-Z and SC-Z) are provided by dedicated bipolar current drivers: six commercial drivers

³The design is by Thijs Wendrich, hence the name T-Stack.

⁴Actually, a PA has a separately controllable ridge waveguide (200 mA) and a tapered amplifier (1.7 A).

[HighFinesse (HF) model BSCP 10] and two miniaturized replicas of them (by Manuel Popp [100], 2D coils and Meso-H). It is possible to damage the atom chip and the coils by currents that are too high or requested for too long. To rule out this point of failure, all currents are monitored by additional electronics (chip fuse) and blocked, when preset timeouts (10s) or current limits are exceeded. In addition, it is possible to separate the structures on demand to suppress small offset currents from the current drivers.

Photodiodes are installed within all fiber-based collimators (see also Fig. 2.3). In combination with transimpedance amplifiers, they allow for a continuous monitoring of the laser power within the vacuum chamber.

The experiment needs a start trigger for the experimental sequence when it is operated in the drop tower. This is realized by an accelerometer [Analog Devices ADXL 103, ± 2 g] in combination with a Schmitt trigger. Its low-to-high (high-to-low) level is 0.25 g (0.5 g). This 'micro-g' trigger has a bandwidth of 2.5 kHz. A small constant delay of 6 ms is caused by the previous elastic deformation of the platforms due to gravitation. Hence, a timing jitter of the experimental sequence in the drop tower can be neglected.

Experiment control

All drop and catapult capsules are equipped with a NI-PXI based capsule control system (CCS), which is in turn controlled by an electronic ground support equipment. Both are connected via Ethernet. In the drop tower, signals are transmitted by a WiFi connection. The CCS is located on the second platform (from the bottom, see Fig. 2.1). This pair of computers is used to initiate a drop or a catapult flight and for monitoring of battery voltages and capsule temperatures. The actual experiment is controlled by a NI-PXI-7854R FPGA with LabView Real Time. This computer is located within the capsule. A personal computer outside serves as graphical interface. Experimental sequences are uploaded from here to the FPGA and can then run autonomously. All data, especially the absorption images, are saved on the PXI within the capsule. They are transferred by an ftp protocol to the control PC.

The FPGA is equipped with several analog and digital I/Os. The analog ones have 16 bit resolution within ± 10 V range. This results in a 0.3 mV discretization of control signals, which is equivalent to a current discretization of 0.3 mA (1 A/V).

Figure 2.15 shows the first part of an experimental sequence as seen on the control PC. The sequence is subdivided into blocks of a certain duration. A typical drop sequence consists of approximately 100 blocks. Within them, boolean parameters (triggers) cannot be changed. Analog values, for example currents through the chips or coils, can be either kept constant or changed in time according to an arbitrary, programmable function (ramp). The simplest example is a linear ramp. However, the course of the actual current never equals that of the requested current because of the finite and load dependent step response time of the current drivers. This will be discussed in Sections 3.2 and 3.3.



Figure 2.15: Control interface with the first part of an experimental sequence, which is uploaded to and executed by an FPGA. The columns constitute the smallest logical chunks within a sequence.

Magnetic shielding

The vacuum chamber, except for the pump section, is surrounded by a two-layer magnetic shield. It is made from mumetal⁵ [101], a NiFe alloy, which has a high magnetic permeability. The actual value of the relative permeability μ_r decreases by the production process of the shield and by any subsequent bad mechanical treatment. Published values range from a few thousand to 250,000 [102]. The shield consists of two cylinders with a wall thickness of 2 mm. The outer one is 42 cm high at a radius of 26.5 cm. The inner cylinder is close to the outer one with 3.4 cm radial and 2 cm vertical separation. It has been designed by Thorben Könemann [103] and manufactured by Sekels GmbH. Each cylinder consists of four radial segments and two circular end caps for a good accessibility to the vacuum section within. The shield can be seen in Fig. 2.1 and at the left side in Fig. 2.3. The design has to be a trade off between mass and size budget and the achievable shielding factor

$$S = \frac{B_{\text{ext}}}{B_{\text{int}}}, \quad (2.18)$$

defined as the ratio of the external and internal magnetic field. Indeed, the design is primarily dictated by geometrical constraints. A larger spacing in between both cylinders, for example, would result in an increased shielding factor [104]. Finite element method (FEM) simulations assuming $\mu_r = 30,000$ predict an axial shielding factor of 5,875 (y axis) and radial factors of 12,987 (x axis) and 11,944 (z axis) [103].

The shielding factor for the weak axis (y) was measured by exploiting the position dependence of the IP trap on the bias current [see Fig. 2.12(b)]. An additional 'bias

⁵Registered trademark by Vakuumschmelze GmbH, Hanau, Germany

coil' with a radius of 36 cm is wrapped around the capsule in Helmholtz configuration. Its partially shielded magnetic field is superimposed with the original bias field and shifts the trap. The magnetic field of the y coil can be measured by rf spectroscopy (see Section 4.3). A calculation of this field is not sufficient, because a magnetic shield is expected to enhance all coil fields within [72]. Relating the measured trap shift with the expected one for the outer Helmholtz coil (no magnetic material inside, except the shield to be measured) yields an axial shielding factor of

$$S_{\text{axial}} = 118. \quad (2.19)$$

This is significantly smaller than the predicted factor of 5,875. Actually, such a discrepancy is not unusual for these FEM simulations and they allow for a relative comparison of different shield designs only [105]. The primary reason is the uncertainty in the magnetic permeability of the mumetal. Nevertheless, a passive suppression of external magnetic fields by more than two orders of magnitude is still valuable. The primary sources of magnetic fields and field gradients that need to be suppressed are the ion getter pump within the capsule and weld seams of the drop tower's vacuum tube. The latter field is comparable to that of the earth (≈ 0.5 G), but its orientation and magnitude depends on the position within the drop tube. A measurement of the resulting field fluctuations can be found here [103].

A residual magnetization of the magnetic shield needs to be reduced by a demagnetization procedure. This can be achieved by decaying alternating magnetic fields [102]. Initially, they flip the magnetic domains back and forth, but finally leave them at a random orientation. It is important, that no external field is imprinted on the shield during this procedure. For this reason, only the inner shield is demagnetized by ribbon cables around with the outer shield in place. The magnetic skin depth is

$$\delta = \frac{1}{\sqrt{f_{\text{demag}} \pi \mu_0 \mu_r \sigma}}, \quad (2.20)$$

where μ_0 is the permeability of free space and $\sigma = 1/(0.55 \cdot 10^{-6} \Omega\text{m})$ is the electrical conductivity [102]. A frequency of $f_{\text{demag}} = 50$ Hz is used for the alternating currents. The skin depth should be comparable to or larger than the magnetic shield thickness for the alternating magnetic fields to penetrate the entire material. Since the magnetic permeability is not exactly known, only a rough estimate of the magnetic skin depth is possible. It is equal to the shield's thickness of 2 mm for $\mu_r \approx 1000$. Hence, smaller frequencies for demagnetization could be beneficial. Demagnetization is performed after each assembly of the magnetic shield. Differing magnetic offset fields or gradients were not observed.

Power management

The most sophisticated consumer within the Q-2 experiment is the T-Stack. It requires an abundance of electrical supply lines. Almost all other consumers can be supplied by them, too. The specified T-Stack voltages are integer multiples of a reference range: 3.0...4.2 V. These multiples are +1S, +2S, +4S and +6S, where

| | +3.45 V | ±6.9 V | ±13.8 V | ±21.7 V | 28 V | | | |
|----------------------|---------|--------|---------|---------|------|-----|-----|------|
| CCS | | | | | | | | 2.4 |
| IGP | | | | | 0.4 | | | |
| PXI | | | | | 4.2 | | | |
| Current drivers | | | 1.3 | | | | | |
| Miscellaneous | | 0.8 | | | 0.4 | | | |
| Laser system standby | | 0.5 | 0.7 | | 1.0 | | | |
| T-Stack standby | 1.6 | 1.1 | 0.0 | 0.6 | 0.1 | 0.5 | 1.0 | |
| Lasers + TECs | | 5.5 | 0.1 | 1.5 | | 0.9 | | |
| Potassium (expected) | 1.6 | 7.1 | 0.1 | 2.8 | 0.1 | 2.4 | 1.0 | |
| Total | 3.2 | 14.2 | 1.0 | 6.9 | 0.2 | 9.8 | 2.0 | 2.4 |
| Power | 458 W | | | | | | | 67 W |

Table 2.1: Overview of the Q-2 power demands. The currents (in A) drawn from the various supply lines by the different components [CCS, ion getter pump (IGP), etc.] are listed. The overall power demand is given in the bottom row. The table is subdivided into the capsule’s operational demand (CCS, 67 W) and experiment demand (Q-2, 458 W).

the ‘S’ denotes the serial connection. This specification is clearly guided by the idea that it can be fulfilled by an appropriate set of serially connected lithium ion batteries. All of these supply lines have a common ground defined by the vacuum chamber. The currents drawn from this supply grid by the T-Stack and other consumers are listed in Table 2.1. It is referenced to specific voltages in favor of the $\pm nS$ notation, because some currents are voltage dependent. These consumers, for example the PXI, have internal DC/DC converters and consume a constant power. Others, for example laser current drivers and TECs on the T-Stack, renounce such internal converters in favor of a reduced noise. They have equal input and output currents, which are practically independent of the supply voltage, as long as it is above the minimum voltage required to drive the current through the load. Any excess voltage is converted into heat within the output stage of the respective current driver or TEC. The T-Stack offers the option to pick any of the bipolar supplies to match the demand. Typically, $\pm 2S$ are used for laser current drivers and $\pm 4S$ for TECs.

Most drop tower experiments use the 600 Wh battery provided by the standard drop tower battery platform. Voltages other than 24 V can be generated by appropriate DC/DC converters. Q-2 could be operated for 75 min ($600 \text{ Wh} \cdot 0.95 / 458 \text{ W}$) on this battery, assuming that it is new and the conversion efficiency is 95%. This duration is marginal, since the time span from disconnecting the umbilical within the tower until a reconnection within the lab is about 60 min for a drop and 70 min for a catapult flight. Furthermore, the noise by DC/DC converters should be avoided as far as possible. For these reasons, a designated battery platform is designed for the Q-2 experiment.

Lithium ion batteries have a higher energy density and specific energy because of their high cell voltage compared to lead or nickel batteries, for example. This

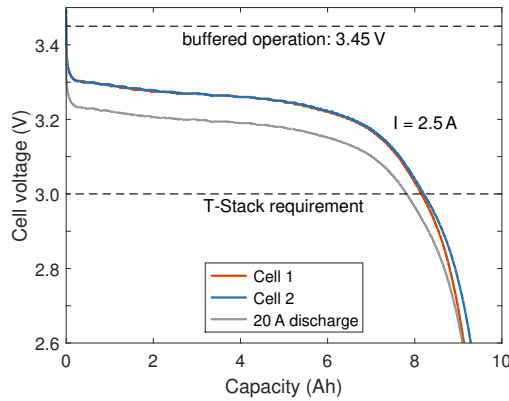
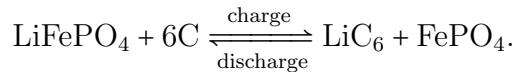


Figure 2.16: Single cell voltages of two lithium iron phosphate (LiFePO_4) batteries connected in series during a discharge at 2.5 A (solid orange and blue lines). The solid gray line shows the expected average single cell voltage when discharging with 20 A (internal resistance is $4 \text{ m}\Omega$). The upper dashed black line shows the per cell voltage for buffering LiFePO_4 batteries. The lower dashed line is the minimum requirement for the T-Stack (see Fig. 2.14).

alleviates the voltage and mass constraints for the rest of the capsule. Lithium ion batteries have, however, some safety issues [106] and need to be guarded by additional electronics, especially for over-voltage protection. Lithium ion batteries with lithium iron phosphate (LiFePO_4) as a cathode material are the safest on the market [107–111]. Therefore, they are used for the Q-2 battery platform. The bare (foil) cells can have an energy density of 240 Wh/l and a specific energy of 130 Wh/kg [112]. The chemical reaction within the cell is [113]:



The single cell voltages of two serially connected (2S) LiFePO_4 batteries during a full discharge at a current of 2.5 A is shown in Fig. 2.16. Their nominal capacity is 10 Ah, but they are not new and were abused by high peak currents prior to this test. At 3.4 V, the batteries are practically full. Further charging would result in a rapid increase of the cell voltage and a reduced battery lifetime. The specified end-of-charge voltage is 3.6 V and the over-voltage protection would completely cut off the charging current if any cell exceeded 3.9 V. In the lab, all batteries are buffered by laboratory power supplies at a voltage of 3.45 V per cell.

After the complementary initial sharp decrease in cell voltage when discharging the battery, the discharge curve is rather flat most of the time. Towards the end, the voltage drops significantly. Below 3 V, the cell is almost empty already. Besides this dependence on the state of charge (SOC), the terminal voltage is a function of the current, too, because of the finite internal resistance [114]. The cells in Fig. 2.16 have an equal internal resistance of $4 \text{ m}\Omega$. The simplest of all battery models, where the voltage drop is proportional to the internal resistance and the drawn current, predicts corresponding voltage drops of 10 mV for the 2.5 A discharge and 80 mV

for a 20 A discharge with respect to open circuit conditions. The expected 20 A discharge curve is shown as the solid gray line. Since no required current is this high, as can be seen in Table 2.1, this battery type fulfills the minimum voltage requirement of the T-Stack (lower dashed black line in Fig. 2.16). There exist several elaborated battery models aiming at calculating the SOC from the terminal voltage [115]. This is rather complicated if the battery is charged or discharged at a variable current. Furthermore, it requires single cell monitoring for a reliable estimate, because serially connected batteries are limited by their weakest cell. This is, however, not implemented in Q-2 yet.

High charge and discharge currents reduce the lifetime of such batteries. Since larger batteries can tolerate a correspondingly larger current, it is sometimes referenced to the battery's capacitance. The 20 A discharge of the 10 Ah battery is equivalent to a so called C-rate of 2. Common notations are 2 C-rate or simply 2 C. All batteries within the Q-2 battery platform are rated to at least 10 C.

If the individual subcells have an equal SOC, they are said to be balanced. Unlike lead batteries, lithium ion batteries cannot balance themselves. Differing SOCs reduce the capacity of the entire battery and further decrease the lifetime, because single cells encounter very high or very low cell voltages more often. This is counteracted by connecting balancers to each cell. Whenever a single cell voltage exceeds a preset value, they draw a current from the cell and discharge it below this threshold. This load current is proportional to the excess voltage within a narrow range of 150 mV above the threshold. The battery management systems (BMS's) used to prevent over- and under-voltages have built in balancers with a balance threshold of 3.6 V and a maximum balance current of 100 mA or below. These modules don't require cooling and can be sealed within a battery pack. This kind of balancers is used for batteries up to 20 Ah. Larger ones are equipped with external, more powerful balancers [Linano PCM-H01S21-L]. They can sink up to 2.1 A at an (adjustable) balance threshold of 3.5 V. This value is ideal for a buffered operation at 3.45 V per cell, because it leaves a symmetric tolerance range of 50 mV for voltage variations due to load changes (the SOC starts to drop below 3.4 V). Furthermore it guarantees high balance currents when exceeding the end-of-charge voltage.

The battery capacities are selected such that the experiment can be operated for three hours and stay idle for at least four hours (lasers off). The battery capacities, BMS's including their current rating and balancer currents are listed in Table 2.2. The supply of the CCS by a separate battery is a requirement imposed by the drop tower operators. In principle, the CCS can be supplied by the +6S battery, too. Some of the blue 40 Ah batteries [CALB SL-FSE] with their balancer modules are visible in Fig. 2.1 on the bottom platform.

Currently, without the potassium laser system, Q-2 is operational on batteries for more than four hours. To keep additional reserves, three batteries (+4S, +6S and the +8S CCS battery) are buffered in the drop tower. In this constellation, three drops per day are possible with only 30 min of charging time in between. This pause is required to prepare the polystyrene pellets within the deceleration container rather than for re-charging. The total energy in all batteries on the battery platform is 2500 Wh.

| | nominal voltage (V) | capacity (Ah) | BMS | balancer current (A) | current rating (A) |
|-----|---------------------|---------------|----------------|----------------------|--------------------|
| +1S | 3.2 | 20 | - | - | N/A |
| +2S | 6.4 | 40 | PCM-L02S20-265 | 2.1 | 20 |
| -2S | -6.4 | 10 | PCB-F2S2 | $\lesssim 0.1$ | 10 |
| +4S | 12.8 | 40 | JPB-S70AB100 | 2.1 | 20 |
| -4S | -12.8 | 10 | PCB-L04S12-4 | $\lesssim 0.1$ | 10 |
| +6S | 19.2 | 40 | JPB-S70AB100 | 2.1 | 20 |
| -6S | -19.2 | 10 | PCB-FH5-9S4 | $\lesssim 0.1$ | 10 |
| +8S | 25.6 | 20 | PCM-L04S12-406 | 0.1 | 12 |

Table 2.2: Overview of Q-2 battery platform with nominal battery voltages (3.2 V per cell), capacities, BMS's, maximum balancer currents and the maximum charge and discharge currents (rating of BMS).

The coil and chip current drivers require an additional supply for the actual load current. The requirement in Table 2.1 refers to the logic supply only. These additional batteries avoid grounding problems and reduce the noise of the current drivers. All connecting cables should be short to keep the inductance of the wires as low as possible [116]. In addition, the batteries would have to be separate from each other if galvanically connected loads, such as two structures on the same atom chip layer, were connected to the current drivers. Even though this is not the case in the current status of the experiment, separate, but interconnected battery packs are installed on the platform right below the current drivers (see Fig. 2.1). They are in $\pm 2S$ configuration for the Meso-U, BC-Z, SC-Z and the z coil and in $\pm 4S$ configuration for all remaining coils (2D, x and y) and the Meso-H.

All electrical power is finally converted into heat. Besides the electrical power given in Table 2.1, the HF current drivers draw a standby current of 0.2 A each. The equivalent power is 18.5 W. The additional power due to the actual load currents in a sequence is negligible in the drop tower, because the number of sequences is small (< 50). The resulting total power is 544 W. For a single drop, the experiment is encapsulated for approximately three hours. Assuming the capsule to be adiabatic with a heat capacity of 1 kJ/kg K and a mass of 453 kg would result in a temperature increase of 13 K. In fact, the heat is not distributed equally and parts of the capsule would heat up more. For this reason, water cooling is installed cooling the platforms and the laser system. The latter is the critical component. A rise in temperature would deteriorate the coupling efficiency of optical fibers. The coolant (primarily water at 20°C) flows through copper cooling elements that are mounted close to heat sources, where possible. The air within the capsule is indirectly cooled by the capsule structure. With this water cooling, the laser system typically heats up by 1 K only (lab-to-drop). The effect on the fiber coupling efficiency is on the few percent level and can be tolerated.

2.2 Fast BEC preparation

After polarization gradient cooling of the atoms released from a 3D-MOT, they are recaptured in a magnetic trap. Typical initial temperatures are on the order of 100 μK after the recapture. Since the thermal energy equivalent $k_B T$ exceeds the excitation quanta of the harmonic traps ($\omega \sim 2\pi \cdot 10^3 \text{ Hz}$) by several orders of magnitude, the discrete energy levels can be described by a density of states:

$$g(\epsilon) = \frac{\epsilon^2}{2\hbar^3\bar{\omega}^3}, \quad (2.21)$$

where

$$\bar{\omega} = \sqrt[3]{\omega_x\omega_y\omega_z} \quad (2.22)$$

is the geometric mean of the three trapping frequencies. The energy levels are populated according to the Bose distribution function

$$f(\epsilon) = \frac{1}{e^{(\epsilon-\mu)/k_B T} - 1}, \quad (2.23)$$

where μ is the chemical potential. The density profile of the atomic cloud is

$$n(\vec{r}) = \frac{N}{(2\pi)^{3/2}\sigma_x\sigma_y\sigma_z} e^{-\frac{x^2}{2\sigma_x^2} - \frac{y^2}{2\sigma_y^2} - \frac{z^2}{2\sigma_z^2}}, \quad (2.24)$$

with the total number of atoms N and the Gaussian widths ($i = x, y, z$)

$$\sigma_i = \sqrt{\frac{k_B T}{m\omega_i^2}}. \quad (2.25)$$

When released from the trap, this anisotropic cloud expands isotropically with the thermal velocity

$$\sigma_v = \sqrt{\frac{2k_B T}{m}} \quad (2.26)$$

according to

$$\sigma_{i,\text{TOF}}(t) = \sqrt{\sigma_i^2 + \sigma_v^2 t^2}. \quad (2.27)$$

The energy distribution of atoms in the (3D) harmonic potential is given by

$$n(\epsilon) = g(\epsilon)f(\epsilon). \quad (2.28)$$

It is plotted in Fig. 2.17. The temperature of the atomic ensemble can be reduced by removing atoms that hold more than the average share of energy. The ensemble rethermalizes after approximately five elastic collisions per atom [117]. This scheme is called evaporative cooling and can be realized by artificially limiting the trap depth to $\eta k_B T$, where η is the truncation parameter. In Q-2, forced evaporation is used. Atoms with an energy exceeding $\eta k_B T$ are coupled to untrapped Zeeman states by rf radiation and repelled from the trapping region. This reduction in temperature inevitably reduces the number of atoms, too.

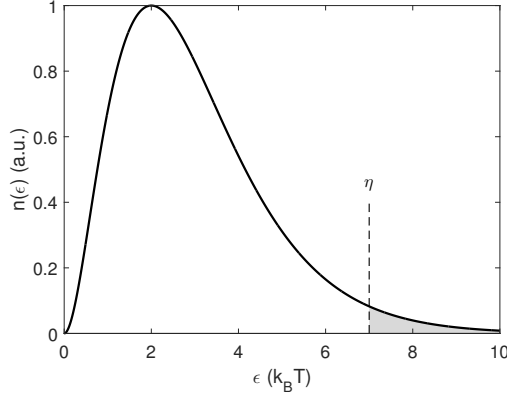


Figure 2.17: Distribution of atoms versus energy in a three dimensional harmonic trap according to Eq. (2.28). The high energy tail (shaded gray) is removed by limiting the trap depth to $\eta k_B T$ using rf radiation.

When the temperature is low enough for the thermal de Broglie wavelength

$$\lambda_T = \sqrt{\frac{2\pi\hbar^2}{mk_B T}} \quad (2.29)$$

to be comparable with the inter-particle separation, a macroscopic occupancy of the trap's ground state occurs. This ensemble of atoms is called BEC or simply condensed cloud in contrast to the thermal cloud at higher temperatures. The figure of merit for the transition to a BEC is the phase space density

$$D = n_0 \lambda_T^3, \quad (2.30)$$

where n_0 is the peak density of the atomic cloud. The phase space density needs to exceed $\zeta(3) \approx 1.202$ in a 3D harmonic potential. The critical temperature T_c for Bose-Einstein condensation depends on the trap frequencies and the number of atoms:

$$k_B T_c = \hbar\bar{\omega} \left(\frac{N}{\zeta(3)} \right)^{1/3} \approx 0.94 \hbar\bar{\omega} N^{1/3}. \quad (2.31)$$

When the temperature is reduced further, the fraction of atoms in the condensed phase increases according to

$$N_0 = N \left[1 - \left(\frac{T}{T_c} \right)^3 \right], \quad (2.32)$$

where N_0 is the number of atoms in the BEC. The critical index depends on the type of trap and its dimensionality. In practice, N_0 is maximized rather than N_0/N . The efficiency of evaporation

$$\gamma = -\frac{d \ln(D)}{d \ln(N)} \quad (2.33)$$

relates the gain in phase space density to the number of atoms lost during the evaporation. This efficiency clearly depends on the truncation parameter: At higher

values fewer atoms are evaporated at a correspondingly higher energy. However, this slows down the cooling rate and increases the time required to reach quantum degeneracy. In fact, the resulting BEC can even be smaller if the lifetime within the trap is too short. Collisions with atoms from the background gas remove rubidium atoms from the trap at a rate Γ_{bg} .

The re-thermalization rate is proportional to the elastic scattering rate

$$\Gamma_{\text{el}} = n_0 \sigma_{\text{scat}} \bar{v}, \quad (2.34)$$

where σ_{scat} is the (s-wave) scattering cross section and

$$\bar{v} = 4 \sqrt{\frac{k_B T}{\pi m}} \quad (2.35)$$

is the average relative velocity between two atoms. Hence, the elastic scattering rate can be increased by increasing the density. This can be achieved by employing high frequency traps [see Eqs. (2.24) and (2.25)]. The desired trap frequency is attained by an adiabatic compression of the trap. When the trap is transformed according to $\bar{\omega} \rightarrow b\bar{\omega}$, temperature, density and elastic scattering rate transform according to:

$$T \rightarrow b^{1/2} T, \quad (2.36a)$$

$$n \rightarrow b^{3/4} n, \quad (2.36b)$$

$$\Gamma_{\text{el}} \rightarrow b \Gamma_{\text{el}}. \quad (2.36c)$$

The phase space density remains unchanged during an adiabatic compression or decompression, as can be seen by comparing (a) and (b) to Eqs. (2.29) and (2.30). Even though the elastic collision rate can be increased significantly by adiabatic compression, the density should not grow as large such that simultaneous collisions of three rubidium atoms set in. These collisions can change the spin and lead to atom loss at a rate $\Gamma_{\text{3-body}} = Ln^2$, where L is a rate constant. The total loss rate then is

$$\Gamma_{\text{loss}} = \Gamma_{\text{bg}} + \Gamma_{\text{3-body}}. \quad (2.37)$$

For this reason, two different traps with $\bar{\omega} = 2\pi \cdot 298 \text{ Hz}$ (initial) and $\bar{\omega} = 2\pi \cdot 173 \text{ Hz}$ (final) are used. The optimum trade-off for the truncation parameter found in Q-2 is $\eta \gtrsim 7$ with $\gamma \approx 3$ for both traps. More details on the efficiency of evaporation can be found here [78].

The condensed phase can be described by a mean field theory. The corresponding Schrödinger equation is called Gross-Pitaevskii equation:

$$i\hbar \frac{\partial}{\partial t} \Phi(\vec{r}, t) = \left[-\frac{\hbar^2}{2m} \Delta + V(\vec{r}) + \frac{4\pi\hbar^2 a}{m} |\Phi(\vec{r}, t)|^2 \right] \Phi(\vec{r}, t), \quad (2.38)$$

where $V(\vec{r})$ is the magnetic trapping potential and $4\pi\hbar^2 a/m$ is the interaction strength with the s-wave scattering length a . Within the trap, the kinetic term is much smaller than the potential and the mean field term. Hence, it can be neglected, which is known as the Thomas-Fermi (TF) approximation. The density

distribution $n(\vec{r})$ of the condensed phase is an inverted parabola⁶, which is bound by zero, with a TF radius of

$$R_i = a_{\text{osc}} \frac{\bar{\omega}}{\omega_i} \left(\frac{15Na}{a_{\text{osc}}} \right)^{1/5} \quad (2.39)$$

for the three spatial dimensions. The oscillator strength

$$a_{\text{osc}} = \sqrt{\frac{\hbar}{m\bar{\omega}}} \quad (2.40)$$

is defined for convenience. The parabolic shape of the condensate is a direct consequence of the dominant mean field term. A single atom in the trap's ground state would see no mean field and its wave function would be Gaussian. In contrast to a thermal cloud [see Eq. (2.25)], the TF radius in one direction also depends on the other trapping frequencies by means of $\bar{\omega}$. This can be understood by considering the increased mean field as a consequence of a higher trapping frequency in any direction. As a matter of fact, this mean field is the driving term responsible for the fast expansion of a BEC when released from its trap. This expansion exceeds the one expected from Heisenberg's uncertainty principle by far and is described in detail in Chapter 6 in the context of magnetic lensing and collective modes. Two closely related terms that quantify the expansion of an atomic ensemble need to be distinguished at this point. The velocity spread is the root mean square velocity of the three dimensional velocity distribution, which is centered around zero for each direction. The expansion rate, on the other hand, is used if the focus is set on the size or its increase in a particular dimension.

2.3 Experimental sequence and performance

An experimental sequence consists of many tiny sub-steps, for example the command to open a mechanical shutter and waiting for this to happen (see also Fig. 2.15). Most of them are not relevant for comprehension. The steps that are relevant are listed in Table 2.3 with the additional non-relevant ones included implicitly. The sequence is an example making use of the full 4.72 s of microgravity that are available in drop mode. Some steps are optional or can be modified, depending on the measurement goal.

Every sequence has to start with loading the 3D-MOT by the 2D⁺-MOT (step 1) at a rate of almost 10⁹ atoms/s. The resulting typical atom numbers are $N \gtrsim 10^8$ after 150 ms and could be increased further by extending the MOT loading phase. However, this also leads to an increased size of the MOT and as a result to a reduced transfer efficiency to the first magnetic trap. As a matter of fact, there would be almost no further increase in the number of condensed atoms. For the same reason, the MOT is also compressed (cMOT) by changing the magnetic field

⁶This is exactly true for harmonic traps only, but a reasonable approximation for the traps in Q-2.

| Stepnumber | Duration (ms) | Stepname |
|------------|---------------|---|
| 1 | 168.0 | MOT loading |
| 2 | 63.3 | compressed MOT |
| 3 | 5.3 | polarization gradient cooling |
| 4 | 1.7 | optical pumping |
| 5 | 25.2 | first magnetic trap |
| 6 | 111.0 | adiabatic compression to initial evaporation trap |
| 7 | 446.0 | initial evaporation phase |
| 8 | 88.7 | adiabatic decompression to final evaporation trap |
| 9 | 500.0 | final evaporation phase |
| 10 | 169.4 | adiabatic decompression to release trap |
| 11 | 80.0 | release & pre-TOF |
| 12 | 2.6 | magnetic lens |
| 13 | 20.0 | delay (eddy currents) |
| 14 | 14.6 | adiabatic rapid passage |
| 15 | 6.0 | Stern-Gerlach separation of states |
| 16 | 2659.4 | maximum additional TOF |
| 17 | 360.1 | detection & camera readout |
| | 4721.3 | total time |

Table 2.3: Overview of the individual steps within an experimental sequence with 2.7 s TOF, which is defined as the time between the magnetic lens (step 12) and detection (last step). The durations of additional actions required for the listed steps are included if appropriate, for example the generation of a homogeneous magnetic field for optical pumping (step 4).

gradient and the detuning of the cooling laser (step 2). Afterwards, the atoms are precooled to approximately $20 \mu\text{K}$ by polarization gradient cooling. In this stage, all Zeeman substates of the $F = 2$ manifold are populated. Optical pumping into the $m_F = 2$ Zeeman substate using the σ^+ -polarized detection light increases the number of atoms in the first magnetic trap by a factor of three compared to no optical pumping. The atom number in this trap is $N \approx 4 \cdot 10^7$.

The first magnetic trap is adiabatically compressed in step 6 to increase the elastic collision rate for a fast evaporation. The evaporation phase (steps 7-9) is also shown in Fig. 2.18. The frequency of the so called rf knife is reduced in six linear ramps from 23.4 MHz to 1.572 MHz. The last two ramps are conducted at a reduced rf amplitude (70% and 2% of the initial value, respectively). After step 9, approximately $3 \cdot 10^5$ condensed atoms are within the final evaporation trap. The total duration up to this point is 1.4 s.

In order to reduce the velocity spread by a magnetic lens in step 12, the positions of atoms and lens have to match. For this reason, the trap is moved to the desired position and is thereby decompressed, too (step 10). The pre-TOF is the time in between the release of the atoms from the trap and the lens. It is the analog to the distance from an optical lens and should be equal to the focal time of the magnetic

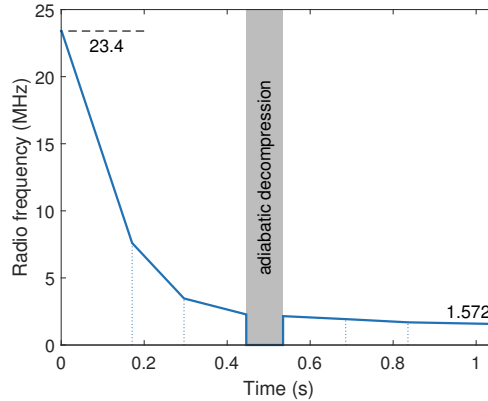


Figure 2.18: The radio frequency for evaporative cooling is ramped down from 23.4 MHz to 1.572 MHz in six linear ramps. In between, the magnetic trap is adiabatically decompressed (shaded gray).

lens to reach a collimated, that is non-expanding, ensemble in an idealized view. If a sequence includes a magnetic lens, the TOF is defined as the time in between the lens and detection. It is 2.7 s in the example sequence (steps 13-16). On the contrary, if no magnetic lens is applied, the TOF is defined as the time in between release and detection. A brief delay of 20 ms (step 13) is inserted directly after the lens to rule out transient forces by decaying eddy currents in combination with a homogenous magnetic field when switching the coils back on.

At the beginning of the TOF in step 14, the atoms can be transferred to the to first order non-magnetic $m_F = 0$ state by an adiabatic rapid passage. The remaining states which are populated because of a non-unity transfer efficiency can be removed by a simple Stern-Gerlach (SG) type experiment: A current of 1 A through the BC-Z is maintained for 3 ms to generate a magnetic gradient field of 590 G/m at release position A or 310 G/m at position B (step 15). The proximity to the chip wires facilitates these large magnetic field gradients. The resulting relative acceleration of the five Zeeman substates of the $F = 2$ hyperfine manifold is 1.9 m/s^2 and 1.0 m/s^2 , respectively. The subsequent free evolution time in step 16 can last up to almost 2.7 s. Finally, the atomic ensemble is detected by absorption imaging. Its duration is ultimately limited by the readout of the atom and beam images ($2 \times 180 \text{ ms}$) rather than the imaging itself ($2 \times 40 \text{ }\mu\text{s}$).

The example sequence in Table 2.3 is illustrated in the bottom of Fig. 2.19. Two full sequences, even though at a reduced TOF, can be accommodated in a single drop, too. This is shown in the top of the figure with the TOF exemplarily chosen to be 200 and 400 ms. In a catapult flight, up to four sequences can be conducted. Alternatively, a single sequence with 7 s TOF is conceivable. It should be noted at this point that there is no difference in the nomenclature between drops and catapult flights in order to keep a successive numbering (Drop 1, 2, ...). The vast majority are actual drops and only Drops 22-30 are catapult flights. The individual absorption images within a drop or catapult flight are labeled with lowercase letters. For example, the second image acquired in Drop 208 is referred to as D208b.

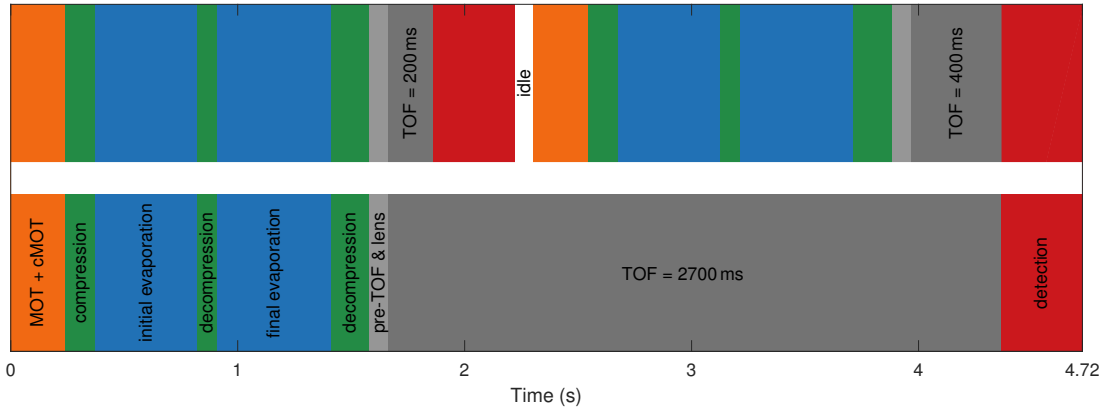


Figure 2.19: Comparison of the experimental sequence in Table 2.3 (bottom time line) to two similar successive sequences with a reduced TOF (top time line). Both require the full 4.72 s of microgravity time that is available in drop mode. The first time-slot (orange, MOT+cMOT) comprises MOT-loading, compressed MOT, polarization gradient cooling and optical pumping (steps 1-4 in Table 2.3). The subsequent green slot (compression) comprises steps 5 and 6. The following ones are the initial phase of evaporative cooling (blue, step 7), adiabatic decompression (green, step 8), the final phase of evaporative cooling to a BEC (blue, step 9), adiabatic decompression to the release trap (green, step 10), release, pre-TOF and magnetic lens (light gray, steps 11 and 12), adiabatic rapid passage, Stern-Gerlach separation of states and a free evolution time (dark gray, steps 13-16) and finally the detection of the atoms (red, step 17). A short idle time (82 ms) in between two sequences is required for technical reasons.

The presented sequences are designed specifically for the drop tower. Since the duration of lab-based sequences is not limited, the time for MOT loading and evaporative cooling could be longer to increase the number of atoms in the BEC. On the other hand, this is not required and reduces the repetition rate. Hence, the sequence up to the BEC in step 9 is not altered in ground-based operation, except for the final radio frequency for measurements with a thermal ensemble.

Two different release traps are used for step 10 [A and B, see Fig. 2.12(b)]. Since release trap B is unable to support the atoms against gravity, only release trap A is suitable for the lab environment. As mentioned earlier, the time in between release and detection is limited due to the gravitational acceleration. The cloud's expansion is not a problem at these timescales. Hence, the application of a magnetic lens is not required in the lab. It would be quite difficult anyway, because the atoms are falling during the application of the lens. For both reasons, a meaningful ground-based characterization of a magnetic lens is not possible.

The experimental sequence can be optimized under different constraints. An optimization for speed yields a BEC with $4 \cdot 10^4$ atoms after 0.85 s (all times without detection). The number of condensed atoms at a 1 Hz rate is $1 \cdot 10^5$ and the maximum overall number is $4 \cdot 10^5$ after 1.6 s. These Q-2 performance benchmarks have been published already [78]. They are shown in Fig. 2.20 by the blue circles [① – ③] in comparison to other experiments capable of creating ^{87}Rb -BECs. The symbols

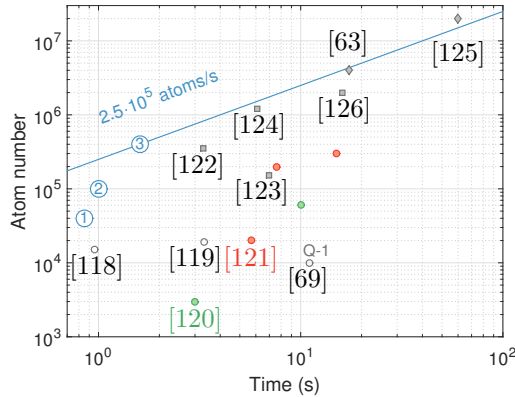


Figure 2.20: Comparison of different machines capable of creating ^{87}Rb -BECs. The three consecutively numbered blue circles show the Q-2 performance for different configurations: optimized for speed ①, for atom number at 1 Hz rate ② and for the highest number of atoms (in the BEC) ③. The symbols indicate the trap type: chip traps (circles), dipole traps (squares) and magnetic (non-chip) traps (diamonds). The open symbols highlight transportable setups, all of which are using chip traps. The colored circles (green and red) are different configurations of the same experiment. The maximum flux of condensed atoms achievable with Q-2 is $2.5 \cdot 10^5$ atoms/s, which is shown as the blue line for comparison.

indicate the type of trap used for evaporative cooling: Chip traps (circles) [69, 118–121], dipole traps (squares) [122–124] and magnetic (non-chip) traps (diamonds) [63, 125] are possible. The two fastest BEC machines (Q-2 and [118]) use chip traps and are portable (open symbols). The two colored sets (green and red) indicate different configurations of the same experiment as given in the respective publication.

Q-2 can produce a flux of $2.5 \cdot 10^5$ condensed atoms per second. This flux is highlighted as the blue line in Fig. 2.20 and is comparable with the best lab-based machines [63, 124–126]. In comparison to Q-1 [69], the repetition rate could be increased by more than a factor of ten and the flux by more than two orders of magnitude.

Some of the steps in Table 2.3 are discussed in the remaining chapters. For example, the adiabatic rapid passage is the subject of Chapter 4. The influence of the release mechanism of the atomic ensemble onto its center of mass motion is explained in Chapter 5. The magnetic lens is finally discussed in Chapter 6. A detailed understanding of the magnetic fields and their control within the Q-2 experiment is required for these chapters. Hence, Chapter 3 is devoted to the magnetic field control within Q-2.

Chapter 3

Magnetic field control

Precision measurements using cold atoms require an excellent control over the magnetic field. A detailed knowledge of the field, its gradient and curvature and also their time dependence are essential for all remaining chapters. The microgravity campaigns with the Q-2 experiment require an extensive use of numerical simulations. Their accuracy depends, among others, on the accuracy at which the magnetic field environment is known. This chapter begins with the characterization of the homogeneous magnetic field by the set of Helmholtz coils (x , y and z) and the offset field at zero current. The switching dynamics of the coil and chip currents is shown in the second section. Afterwards, the customization of the course of the actual current through these structures is demonstrated. This chapter concludes with measurements of the magnetic field gradient and transient forces by changing currents through the coils.

The author contributed significantly to the techniques, measurements and conclusions presented in this chapter. Christian Deppner assisted the measurements on the coil calibration presented in the first section. The work described in Section 3.2 was conducted by Jan Rudolph together with the author. The measurements in microgravity were a joint team effort by Jan Rudolph, Christoph Grzeschik, Alexander Grote, Christian Deppner and the author with additional support by Waldemar Herr. The evaluation of the data presented here and the technique described in Section 3.3 were performed by the author.

3.1 Homogeneous magnetic fields

The magnetic field can be measured by probing the transition frequency between the Zeeman substates in the $F = 2$ ground state manifold. This rf spectroscopy is explained in depth in Section 4.3. The accuracy is approximately 1 mG. Each Helmholtz coil has a fixed conversion factor of current to magnetic field determined by its geometry in combination with the magnetic shield. This conversion factor is independent of the polarity. Still, the current drivers might be gauged unequally imitating unequal conversion factors. This is checked by measuring the magnetic field for a set of positive and negative currents. An example measurement is shown in Fig. 3.1(a) for the z coil revealing a conversion factor of 6.959(1) G/A for positive

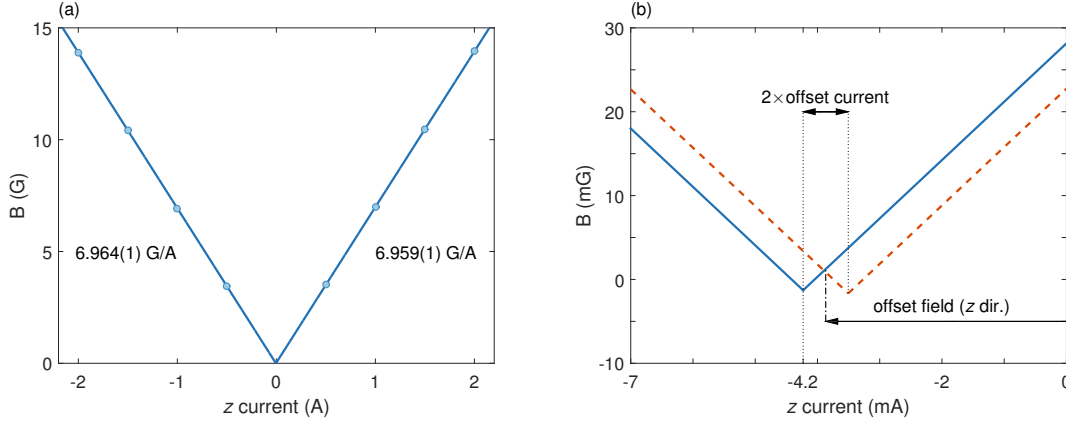


Figure 3.1: (a) The data points show the magnetic field measured by rf spectroscopy at different currents through the z coil. The current to magnetic field conversion factors for positive and negative currents are determined by linear regression (solid line) and given in the figure. (b) shows a magnified view of (a) which is augmented by the same measurement with inverted current driver outputs to discern the offset current ($+0.4(1)$ mA) and the offset field (-3.8 mA \equiv $+27(1)$ mG).

currents and $6.964(1)$ G/A for negative ones by linear regression. As a matter of fact, the conversion factors are slightly different. The uncertainty is on the level of the discretization of the analog outputs controlling the current drivers ($20\text{ V}/2^{16} \approx 0.3\text{ mV} \equiv 0.3\text{ mA}$). No error bars are shown because they are much smaller than the data points themselves. The time between switching the coil current on and the rf spectroscopy is 6.3 ms, which is longer than the settling time of the coils (see next section). In addition, this delay time can also affect the measurement in the presence of strong magnetic field gradients. However, this effect can be neglected here as will be shown below.

The closer look in Fig. 3.1(b) further reveals that both linear fits do not intersect in the origin. A positive minimum in the magnetic field can be caused by residual offset fields in the orthogonal directions (other than z in this case). Since rf spectroscopy is sensitive to the absolute value of B , physically reasonable intersections are bound by zero. Nevertheless, a higher sensitivity to such offset fields can be expected with the probe field co-aligned. This is because the resulting magnetic field is the vector sum of the strong probe field and a small offset field. Co-aligned, the signature of such an offset field is the intersection at a nonzero current. Nonetheless, this is indistinguishable from an offset current of the current driver using the measurement in Fig. 3.1(a) only. For this reason, the same measurement is repeated with an inverted output of the current driver [dashed orange line in Fig. 3.1(b)]. The abscissa refers to the actual current through the coil rather than the current driver output. The blue line is the same as in (a) with its minimum at -4.2 mA. If the current drivers had zero offset current, this minimum would be caused by the offset field only and remain unchanged when inverting outputs. Nonzero offset currents, however, shift the intersection by twice their value. The fitted offset current is $+0.4$ mA, which is again on the level of the discretization of the analog outputs. The offset field in the

| | radius (mm) | I_{\max} (A) | '-' conversion factor (G/A) | '+' conversion factor (G/A) | B_{offset} (mG) |
|----------|-------------|----------------|-----------------------------|-----------------------------|--------------------------|
| x coil | 80 | 5 | 1.926(1) | 1.922(1) | 1(1) |
| y coil | 65 | 2 | 14.307(2) | | -3(2) |
| z coil | 49 | 2 | 6.964(1) | 6.959(1) | 27(1) |

Table 3.1: The table lists the coil radii, the maximum currents without saturation effects, the current-to-field conversion factors for positive and negative currents and the static magnetic offset fields (B_{offset}). The latter three were determined in calibration measurements as exemplarily shown in Fig. 3.1 for the z coil.

z direction is 27(1) mG. In fact, this is the only direction with a significant offset field. The remaining coils (x and y) are characterized by similar measurements. Their results are summarized in Table 3.1. The y direction cannot be probed at the same level of precision because the field is almost parallel to the alternating B vector of the rf field.

3.2 Switching dynamics

The current drivers need a finite time to establish a steady current through a load. Inductive loads such as coils have a longer settling time than ohmic ones (chips). Each coil in combination with the internal capacitance C_i of its HF current driver constitutes a damped RLC-oscillator. Its resonance frequency is given by:

$$f = \frac{1}{2\pi} \sqrt{\left(\frac{1}{L_{\text{coil}}C_i}\right)^2 - \left(\frac{R_{\text{coil}}}{2L_{\text{coil}}}\right)^2}, \quad (3.1)$$

where R_{coil} is the coil's ohmic resistance and L_{coil} the inductance [127]. The current drivers are pure PI-controllers. For this reason they are rather slow and require many periods of the oscillation to stabilize a current. This can be sped up by introducing a bypass for the current which changes the impedance of the load. A single resistor would allow for steady current through the bypass. The correspondingly lower current in the coil can be re-calibrated. It is, however, temperature dependent because the load can heat up and the current ratio changes. This steady current can be blocked by a capacitor. A circuit diagram is shown in Fig. 3.2. The dashed line represents the current driver. All parameters are given in Table 3.2. Both bypass parameters, C_b and R_b , were optimized experimentally to minimize the settling time. For the y coil, one of the two parallel 4.7 μF internal capacitors had to be removed for optimum performance. Numerical simulations of the full circuit show that the bypass reduces the frequency of the oscillation at a significantly increased damping rate. The resulting damping rates exceed the corresponding frequencies by approximately a factor of three.

The resulting switching dynamics of the coils is shown in Fig. 3.3(a). It is the course of the current when changing the control from 1 A to 0 A. The chip currents

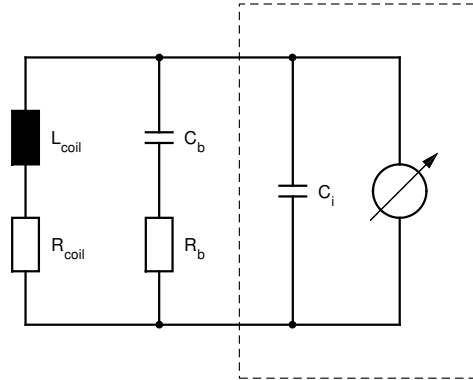


Figure 3.2: The equivalent circuit diagram of a current driver (dashed line) with its internal capacitance C_i and a coil as an external load is shown. The coil is subdivided into its inductance L_{coil} and ohmic resistance R_{coil} . A current bypass comprising a capacitor C_b and a resistor R_b is connected in parallel to the coil.

| | L_{coil} (mH) | R_{coil} (Ω) | C_i (μF) | f_0 (kHz) | C_b (μF) | R_b (Ω) | f (kHz) | δ_{damp} (kHz) |
|----------|---------------------------|-----------------------------------|----------------------------|----------------|----------------------------|-----------------------|--------------|---------------------------------|
| x coil | 0.177 | 0.664 | 9.4 | 3.9 | 30 | 5.7 | 3.2 | 9.4 |
| y coil | 4.676 | 2.862 | 4.7 | 1.1 | 20 | 22.0 | 0.6 | 1.9 |
| z coil | 0.438 | 0.922 | 9.4 | 2.5 | 50 | 2.5 | 0.9 | 3.2 |

Table 3.2: Electrical parameters of the circuit in Fig. 3.2 for the three coils. The ohmic resistance R_{coil} includes the conducting wires to and from the coil. The oscillating frequency of the pure RLC-oscillator (without the bypass) is f_0 . With the bypass it reduces to f and the oscillation is damped at a rate δ_{damp} . The latter two are determined by numerical simulations and f_0 is calculated using Eq. (3.1).

can be changed more rapidly as depicted in (b). An impedance matching is not necessary here. Among the coils, the x coil is the fastest one by virtue of its smallest inductance. Without any limitations on the supply voltage, these so called response functions look the same, independent of the requested change in current. Such systems are called linear. Yet, small differences exist, especially when requesting larger currents. This is due to the finite supply voltage. The maximum currents up to which such nonlinearities are negligible are given in Table 3.1 as I_{max} .

3.3 Customizing current ramps

Within an experimental sequence the coil and chip currents should follow a predetermined course. In some steps, for example MOT loading (see Table 2.3), a 1 ms delay of the current can be neglected. In others, for example the magnetic lens, it is crucial. Such a lens is used as an example in this analysis, but the formalism itself is more general. The lens is a rescaled version of release trap A (see Fig. 2.12), which is switched on and off within 6 ms with an approximately Gaussian shape.

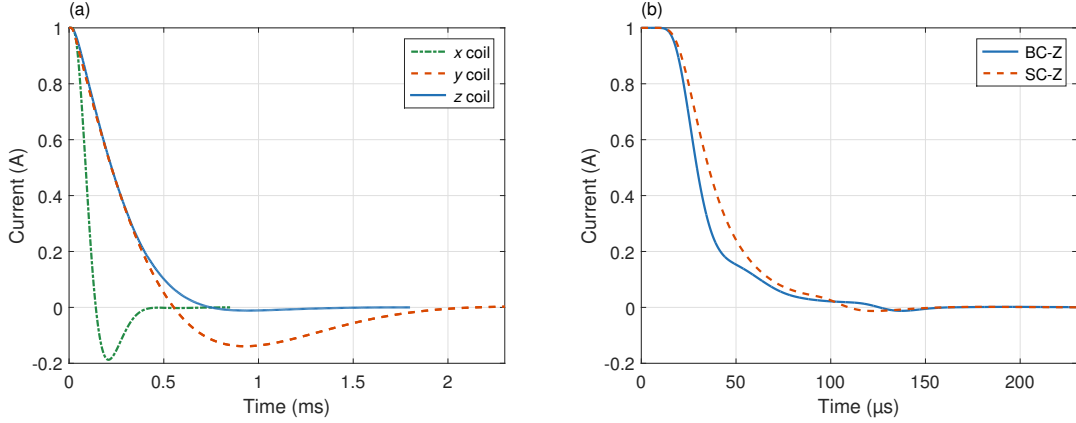


Figure 3.3: Step response of the current to the control step $1 \rightarrow 0$ (at $t = 0$) for the x , y and z coil (a) and the BC-Z and SC-Z (b).

It cannot be exactly Gaussian, because the current needs to start at zero or the previous value, which is encoded by zero in arbitrary units. This desired current is shown as the solid gray line in Fig. 3.4. The goal is to determine precisely the shape of control signals for the current drivers (control ramp), such that the y coil and both chips (BC-Z and SC-Z) respond in their way to produce the desired currents.

In signal processing, the system response to a unit step function is called step function response or simply step response (SR). For practical reasons this is redefined as the step from one to zero in this work (see Fig. 3.3). For the calculation it is useful to introduce the impulse response (IR):

$$IR = \frac{d}{dt}SR, \quad (3.2)$$

which is simply the time derivative of the SR. The system response is then:

$$\text{response} = -\text{control} * IR, \quad (3.3)$$

where the $*$ denotes a convolution. The minus sign is a consequence of the redefinition of the SR. To solve this equation for the control, the Fourier transform is taken:

$$\mathcal{F}\{\text{response}\} = -\mathcal{F}\{\text{control}\} \cdot \mathcal{F}\{IR\} \quad (3.4)$$

and the identity that the Fourier transform of a convolution of two functions is equal to the product of the Fourier transforms of the individual functions is invoked. Rearranging and taking the inverse Fourier transform yields:

$$\text{control} = -\mathcal{F}^{-1}\left\{\frac{\mathcal{F}\{\text{response}\}}{\mathcal{F}\{IR\}}\right\}. \quad (3.5)$$

The response should be equal to the desired curve and can be replaced by it in the equation. The resulting control signal is shown as the dash-dotted black line in Fig. 3.4(a) for the y coil and omitted in (b) because it would be hardly distinguishable from the desired curve. The measured system response to the respective control

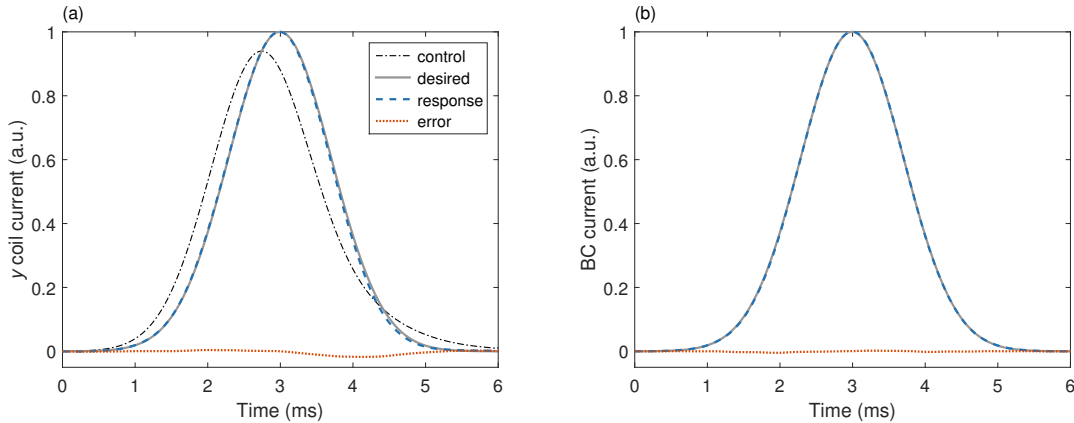


Figure 3.4: The figures show the application of Eq. (3.5) to the y coil (a) and the BC (b) with a quasi-Gaussian shape as a desired response (solid gray line). The calculated control for the y coil is shown as the dash-dotted black line in (a). It is omitted in (b), because it is hardly distinguishable from the desired current itself. The actual response to the respective control is shown as the dashed blue line. It is deviating very little from the desired current, as shown by the error signals (dotted orange lines).

is shown as the dashed blue line. It resembles the desired curve almost perfectly for the BC and SC (not shown). The y coil response deviates by less than 2% (dotted red line) because of small nonlinearities in the system. A higher precision can be achieved by applying Eq. (3.5) to the inverse error signal as the desired response and adding the resulting control as a correction to the initial one.

Equations (3.2) to (3.5) implicitly assume a continuous basis and functions defined on the interval $(-\infty, +\infty)$. Neither is the case in practical applications. In these cases, the Fourier transform becomes discrete and the impulse response must vanish outside of some finite interval.

All control ramps are bound to the domain $[0,1]$ in the experiment control. With this limitation the minimum total ramp time for the y coil to be able to follow such a Gaussian ramp is 3.6 ms. Supply voltage limitations can set in even earlier depending on the desired maximum current.

3.4 Magnetic gradient fields

The job of a Helmholtz coil is to generate a homogeneous magnetic offset field. Even though the atoms are in the center of all Helmholtz coils to a 1 mm precision, which is on the scale of typical position differences within the experimental sequence, there are static magnetic field gradients. Furthermore, also transient accelerations (kicks) arise when a coil current is changed. Both, gradients and kicks, are proportional to the respective coil current, but the proportionality factors are different for the three coils. The first part of this section characterizes these effects in ground-based measurements. In the second part, these results are compared to data taken in microgravity.

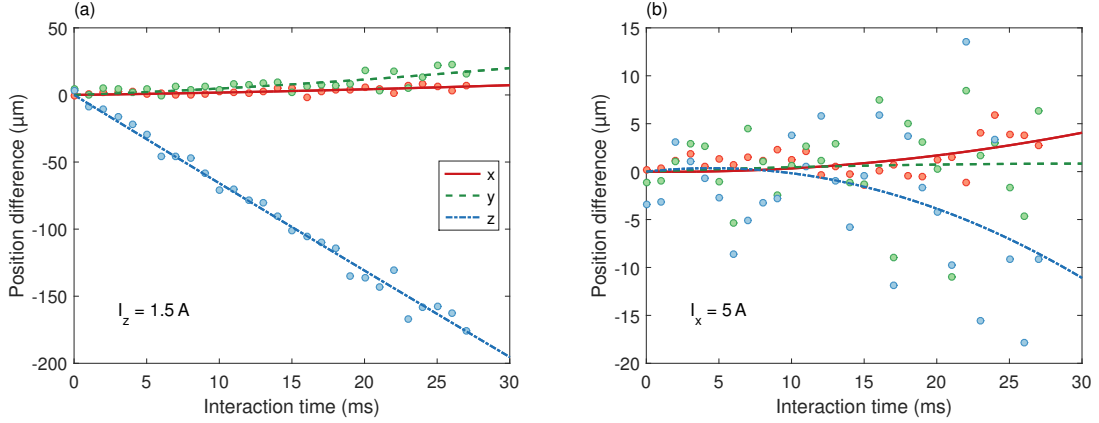


Figure 3.5: Both figures show differential time of flight data (filled circles) to measure the effect of switching a coil current from zero to a specific value, for example $I_z = 1.5 \text{ A}$ in the z coil (a). This current is kept constant for the interaction time. The x coil data points in (b) are plotted with the same color code as in (a). The lines are quadratic fits to the corresponding data points, all of which were acquired with rubidium atoms in the $m_F = 2$ substate.

3.4.1 Ground-based measurements

The ground-based measurement of small kicks or accelerations is difficult, because the sensitivity to these effects scales linearly and quadratically with the available TOF, respectively. In any case, these measurements set upper bounds on such effects. A small increase in sensitivity is achieved by an upward acceleration of the release trap prior to the release. This extends the available TOF to approximately 34 ms with Detection 2, which is required for 3D information. The effects are measured by comparing the position difference of two sets of time of flight data, one of them with the probe field switched on. Two example measurements for the x and z coil are presented in Fig. 3.5. A current of 1.5 A was chosen for the z coil in (a) and $I_x = 5 \text{ A}$ was selected in (b). Both of them result in $B \approx 10 \text{ G}$. Each data point is the average over ten of these differential measurements. The static accelerations and kicks from switching are determined by quadratic fits to the respective data sets. The largest of all effects is the kick of the z coil in the negative z direction, that is towards the chip. In contrast to this, the effect by the x coil is so weak such that it vanishes within a statistical scatter in the atomic position. The y coil has an intermediate effect (not shown). This correlates with the coil radius (see Table 3.1).

All effects are summarized in Table 3.3. The values are normalized to a field strength of 1 G to make them comparable. Most accelerations are smaller than their 1σ uncertainty, which is given in parentheses. The only exceptions are the y direction for y coil currents and the z direction for the x coil. The situation is different for the kicks, where three values are statistically significant. One of them, the z kick of the z coil, can be seen in Fig. 3.5(a). The statistical variations can be reduced by averaging, provided that the system is sufficiently stable. To gain a factor 100, for example, $10 \cdot 100^2 = 10^5$ averages would be required. This would take

| | acceleration (mm/s ² /G) | | | kick (μm/s/G) | | |
|----------|-------------------------------------|-------|-------|---------------|-----------|-----------|
| | a_x | a_y | a_z | $v_{0,x}$ | $v_{0,y}$ | $v_{0,z}$ |
| x coil | 1(1) | 0(2) | -4(3) | -2(8) | 6(23) | 17(34) |
| y coil | 0(1) | -2(1) | -1(1) | 3(3) | 39(8) | -84(10) |
| z coil | 1(1) | 2(2) | 1(3) | 14(9) | 37(20) | -633(28) |

Table 3.3: The fitted accelerations due to a static magnetic field gradient of the three coils are given for the different spatial dimensions. The kick by switching the coil on is listed in the right half of the table. Both are normalized to a homogeneous magnetic field of 1 G corresponding to different coil currents (see Table 3.1). The values refer to rubidium atoms in the $m_F = 2$ substate.

two years for a single coil and produce 20 TB of data, which is clearly not an option.

The coil calibration measurement (see Table 3.1) is valid for a single point within the vacuum chamber only, at which the rf interaction took place. The data in Table 3.3 can be used to estimate the valid range up to which this calibration can be expected to provide a reliable estimate of the magnetic field. The accelerations a_z (a_y) by the x coil (y coil) serve as examples. The expected magnetic field gradients can be estimated as follows [see Eq. (4.30) in Section 4.2]:

$$\left. \frac{\partial B}{\partial z} \right|_{I_x=1 \text{ A}} = -\frac{m}{\mu_B g_F m_F} a_z = -155.61 \frac{\text{G/m}}{\text{m/s}^2} \cdot (-4) \frac{\text{mm}}{\text{G s}^2} \cdot 1.922 \frac{\text{G}}{\text{A}} \cdot 1 \text{ A} \approx 1 \frac{\text{mG}}{\text{mm}},$$

$$\left. \frac{\partial B}{\partial y} \right|_{I_y=1 \text{ A}} = -\frac{m}{\mu_B g_F m_F} a_y = -155.61 \frac{\text{G/m}}{\text{m/s}^2} \cdot (-2) \frac{\text{mm}}{\text{G s}^2} \cdot 14.307 \frac{\text{G}}{\text{A}} \cdot 1 \text{ A} \approx 4 \frac{\text{mG}}{\text{mm}}.$$

Since typical position differences are smaller than 1 mm, this effect is of the same order as the measurement uncertainty of the coil calibration in Table 3.1 and can be neglected for all measurements in this work.

The x coil imprints the smallest kick per Gauss on the atoms. For this reason, it is used to provide a small quantization field during long TOFs and a large one for the adiabatic rapid passage. A delay time of 5 ms between release and coil switching was implemented for the measurements in this section. Other ground-based measurements have shown, that the coil kicks can increase with decreasing delay time. A possible explanation are eddy currents in the copper chip mount, but this could not be proved so far. This is the reason for the delay of 20 ms prior to the adiabatic rapid passage (see Table 2.3).

3.4.2 Measurements in microgravity

Measurements in microgravity are different from ground-based ones because of a possible static background magnetic field gradient superimposed to the one generated by the coils. In the lab, the acceleration due to this static gradient is superimposed with the much stronger gravitational acceleration and is indistinguishable from it. Both these accelerations do not affect the differential ground-based measurement,

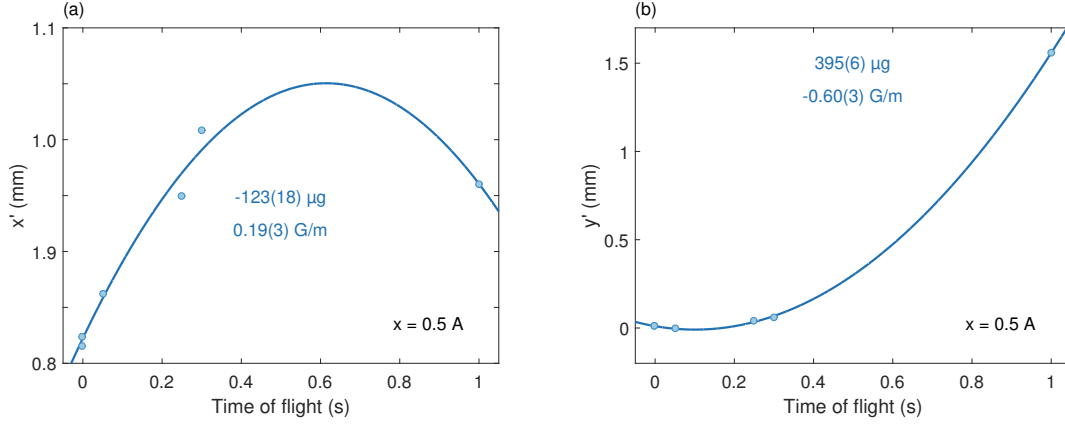


Figure 3.6: The data points (full circles) show the position of a magnetically lensed BEC versus the time of flight after the lens in the Detection 1 coordinate system. The atoms are in the $m_F = 2$ substate at a quantization field of approximately 1 G generated by 0.5 A in the x coil. The acceleration due to the magnetic field gradient is determined by a quadratic fit (solid lines). The given errors are fit uncertainties.

because they are common effects. In microgravity, the acceleration due to the combined background and coil gradient can be fitted with time of flight data of atoms in, for example, the $m_F = 2$ substate.

Figure 3.6 shows such a data set (filled circles) imaged by Detection 1 for a quantization field of $B \approx 1$ G generated by 0.5 A in the x coil. The combined gradients (background + coil) determined by a quadratic fit (solid line) are:

$$\begin{aligned} \left. \frac{\partial B}{\partial x'} \right|_{I_x=0.5 \text{ A}} &= +0.19(3) \frac{\text{G}}{\text{m}}, \\ \left. \frac{\partial B}{\partial y'} \right|_{I_x=0.5 \text{ A}} &= -0.60(3) \frac{\text{G}}{\text{m}}. \end{aligned} \quad (3.6)$$

The images from Detection 2 cannot provide full 3D information, because the left cloud is not within the detection zone for the entire TOF. The y coordinate, however, can be extracted from the right cloud only to a sufficient precision. This data set is shown in Fig. 3.7 with a fitted gradient of 0.15(1) G/m. With this additional information, the three spatial components of the gradient are:

$$\begin{aligned} \left. \frac{\partial B}{\partial x} \right|_{I_x=0.5 \text{ A}} &= 1.00(2) \frac{\text{G}}{\text{m}}, \\ \left. \frac{\partial B}{\partial y} \right|_{I_x=0.5 \text{ A}} &= 0.15(1) \frac{\text{G}}{\text{m}}, \\ \left. \frac{\partial B}{\partial z} \right|_{I_x=0.5 \text{ A}} &= 0.19(3) \frac{\text{G}}{\text{m}}. \end{aligned} \quad (3.7)$$

In order to discern background and coil contributions to this gradient, additional microgravity data are required with a different current in the x coil. The current

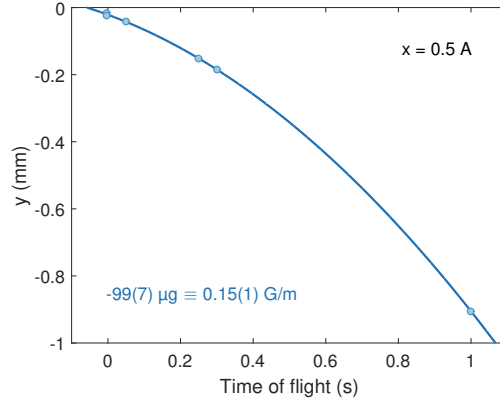


Figure 3.7: The data points were taken simultaneously with the ones in Fig. 3.6, but with Detection 2. The plotted position is the y coordinate determined from the direct image [right cloud, see also Fig. 2.10(b)]. The quadratic fit (solid line) yields a gradient of $0.15(1)$ G/m in this direction.

must be nonzero in order to avoid a random mixing of the five Zeeman substates. Figure 3.8 shows such a data set with $I_x = 0.1$ A and resulting gradients of:

$$\begin{aligned} \left. \frac{\partial B}{\partial x'} \right|_{I_x=0.1 \text{ A}} &= -0.21(3) \frac{\text{G}}{\text{m}}, \\ \left. \frac{\partial B}{\partial y'} \right|_{I_x=0.1 \text{ A}} &= -0.68(2) \frac{\text{G}}{\text{m}}. \end{aligned} \quad (3.8)$$

Information from the second detection system is not available for this data set. For this reason, a comparison is limited to the $x' - y'$ coordinate system. If the measured gradients were exclusively from the background, for example by a residual magnetization of the magnetic shield or sources of magnetic dipole fields within, the measured gradients would be unaffected by the different coil current. On the contrary, if the coil's gradient were the sole cause, the measured gradients would be suppressed by a factor of five according to the current ratio. Neither of this is the case and both sources of magnetic field gradients need to be taken into consideration. In fact, a small x current can even reduce the background gradient in these two directions. At $I_x = 0.3$ A, the gradient in the z direction would vanish, since the coil contribution amounts to approximately one Gauss per meter and ampere. In the language of Table 3.3 this is equivalent to

$$a_z = \frac{\frac{0.19 \frac{\text{G}}{\text{m}} - (-0.21) \frac{\text{G}}{\text{m}}}{0.4 \text{ A} \cdot 1.922 \frac{\text{G}}{\text{A}}}}{-\frac{m}{\mu_B g_F m_F}} = -3.3(3) \frac{\text{mm}}{\text{s}^2 \text{ G}},$$

which is in good agreement to the less accurate ground-based measurement of the accelerations due to the x coil gradient.

In addition to the time of flight data presented above, further information can be extracted from microgravity data if atoms in more than one Zeeman substate are present. For example, a large fraction in the $m_F = 0$ substate and smaller fractions in

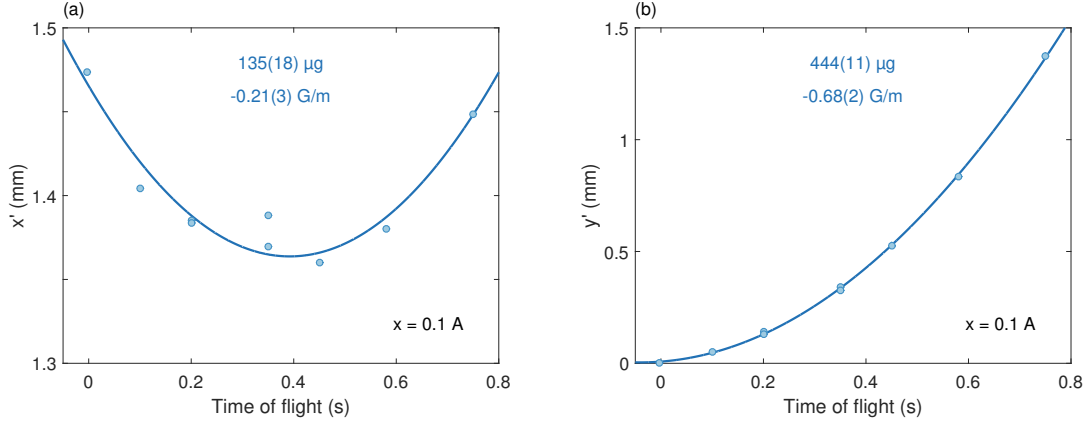


Figure 3.8: The data set is similar to the one in Fig. 3.6, but acquired at a quantization field of 0.2 G. The fitted magnetic field gradients are $-0.21(3)$ G/m in the x' direction and $-0.68(2)$ G/m in the y' direction.

$m_F = \pm 1$ can be prepared by an adiabatic rapid passage (see Chapter 4). These atoms separate in space after a sufficiently long TOF, because the force due to the magnetic field gradient is proportional to the magnetic quantum number. Aside from that, a large magnetic field is required for the passage. This field is realized by $I_x = 5$ A and thus involves the two switching processes $I_x = 0.5$ A \rightarrow 5 A and $I_x = 5$ A \rightarrow 0.5 A if the quantization field during the TOF is generated by $I_x = 0.5$ A. Both of these processes can produce a kick, even though the ground-based measurement could not resolve it. A kick by the switch-on would act on all atoms in the same way because they are still in the $m_F = 2$ substate. The switch-off kick, on the contrary, would be state-selective. In the absence of such a kick, the different Zeeman states separate according to the magnetic field gradient. The angle γ connecting the centers of mass would then depend on the ratio of the gradients:

$$\gamma = \tan^{-1} \left(-\frac{\frac{\partial B}{\partial x'}}{\frac{\partial B}{\partial y'}} \right) = 17(2)^\circ. \quad (3.9)$$

A nonzero coil kick can result in a deviating angle, especially for short TOFs. Furthermore, the separation of the subclouds can differ from the expectation.

Example images by Detection 1 are shown in Fig. 3.9(a) for 0.5 s TOF and in Fig. 3.9(b) for 1 s TOF. The 0.5 s in (a) are already enough to separate the states by 432 μ m. In (b), they are separated even further (1.68 mm). For both images, the quantization field was generated by $I_x = 0.5$ A. The expected angle according to Eq. (3.9) is visualized as the dotted white line in both images. In (a), the actual angle is 29° and deviates significantly from this expectation. The equivalent state-selective kick can be calculated from the data by Newtonian kinematics. With respect to the $m_F = 1$ atoms it is:

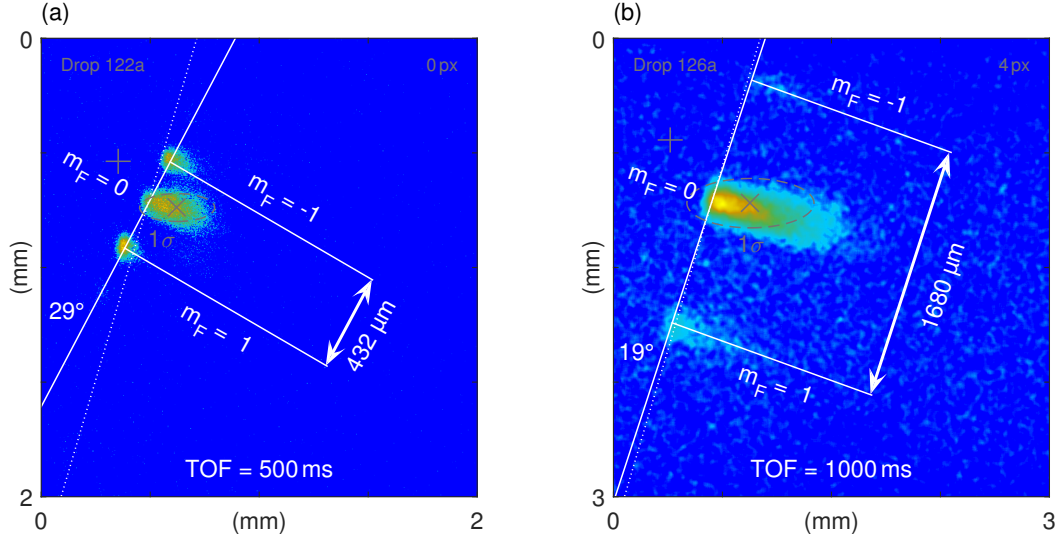


Figure 3.9: Detection 1 absorption images with the largest fraction of the magnetically lensed atoms in the $m_F = 0$ substate and smaller fractions in $m_F = \pm 1$ after a TOF of 0.5 s (a) and 1 s (b). A magnetic field gradient and different initial velocities separate the states by $432 \mu\text{m}$ in (a) and 1.68 mm in (b). The expected angle [see Eq. (3.9)] according to the measured gradient (see Fig. 3.6) is 17° and shown by the dotted white line. The actual angle is 29° in (a) and 19° in (b). The position of the $m_F = 0$ atoms expected from time of flight imaging is marked as the gray 'x' assuming that a ramp-up of the x coil within 1.5 ms makes no kick. The 1σ confidence bound is depicted as the dashed gray ellipse. If the slow ramp-up produced twice the kick in Eq. (3.10) ($m_F = 2$ instead of $m_F = 1$), the expected position is marked as the '+'.

$$\begin{aligned}\Delta v'_x &= \frac{-d \cdot \tan(\gamma)}{2t\sqrt{1 + \tan^2(\gamma)}} - \frac{1}{2}a_{x'}t \approx -79(19) \frac{\mu\text{m}}{\text{s}}, \\ \Delta v'_y &= \frac{d}{2t\sqrt{1 + \tan^2(\gamma)}} - \frac{1}{2}a_{y'}t \approx -59(20) \frac{\mu\text{m}}{\text{s}},\end{aligned}\tag{3.10}$$

where $d = 432(20) \mu\text{m}$ is the distance between the $m_F = \pm 1$ substates in Fig. 3.9(a), $t = 500 \text{ ms} - 27 \text{ ms} = 473 \text{ ms}$ is the remaining TOF after switching the x coil from $I_x = 5 \text{ A} \rightarrow 0.5 \text{ A}$ and the accelerations $a_{x'}$ and $a_{y'}$ are half the fitted values from Fig. 3.6 ($m_F = +1$ instead of $m_F = +2$). The effect on the $m_F = -1$ atoms is just the opposite.

These kicks correspond to $-9 \mu\text{m/s/G}$ in the x' direction and $-7 \mu\text{m/s/G}$ in the y' direction for a comparison with Table 3.3. They lie well within the bounds set up by the ground-based measurement. It must be noted at this point that all these values extracted from Fig. 3.9(a) are based on this single data point. Even though this single shot image has the advantage that common systematics on the center of mass motion drop out, for example the residual air drag in the tower, more data points are required for a reliable estimate. So far, there exists only one similar measurement which is shown in Fig. 3.9(b). Unfortunately, it is very dilute due to the long TOF.

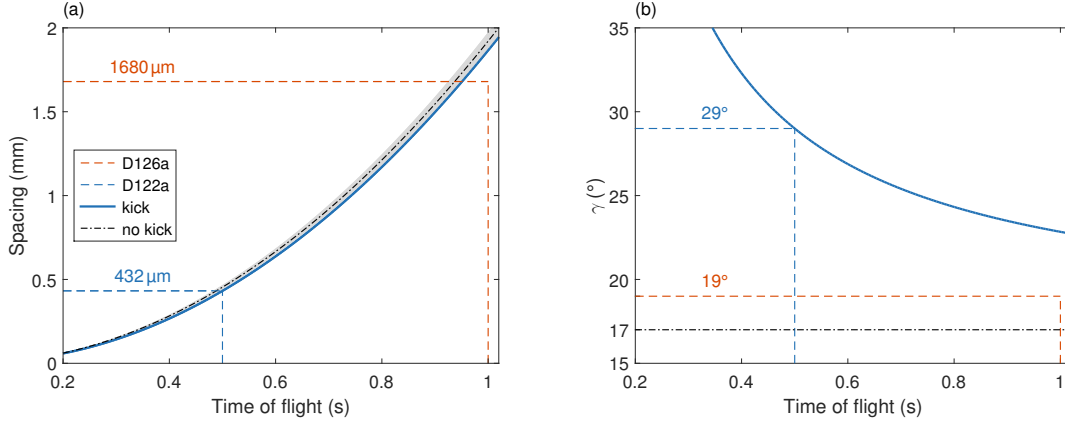


Figure 3.10: Expected coarse of the $m_F = 1$ to -1 spacing (a) and the angle γ of the line connecting the centers of mass of the different Zeeman states (b) is shown with the coil kick estimated from Drop 122a [Fig. 3.9(a), see also Eq. (3.10)]. The corresponding values (dashed blue lines) are highlighted and are met by construction. The values corresponding to Drop 126a [Fig. 3.9(b)] are shown as the dashed orange lines. The expected angle without any kicks is $17(2)^\circ$ and shown by the dash-dotted line in (b). The corresponding expected spacing in (a) is illustrated with its 1σ confidence interval defined by the uncertainty in the gradient (shaded gray).

In addition, the experimental sequence was slightly different such that the switch-off kick is not comparable. The difference was a ramp-down of I_x within 1.5 ms rather than simply switching the current with the step response. It is interesting to see that the measured angle hardly differs from the zero-kick estimate.

The expected course of the spacing d and the angle γ using the estimated kicks from above are shown in Fig. 3.10 (solid blue lines). The measured spacing for 500 ms (dashed blue line) coincides with this expected one by construction. The separation for 1 s TOF (dashed orange line) deviates by approximately $200\ \mu\text{m}$, which is on the order of the uncertainty in the measured value. In the absence of kicks, the spacing would follow the dash-dotted line with the shaded gray area indicating the confidence bound by the gradient measurement. It can be seen that the blue line is almost within this confidence interval, such that the spacing alone is no good probe for the measurement of coil kicks. The angle in (b) tends towards the dash-dotted black line at 17° , which is the expected value in the absence of kicks. At 500 ms, the angle difference is 12° corresponding to 6σ , which is significant.

A potential mitigation strategy to reduce this not sufficiently characterized kick is to linearly ramp the x coil current, for example within 1.5 ms, rather than switching it with the step response. This was actually performed for the switch-on process in Figs. 3.9(a) and (b). If this strategy was sufficient, the position of the $m_F = 0$ atoms should coincide with the position expected from time of flight imaging of the $m_F = 2$ atoms (Fig. 3.6). Assuming that the center of mass velocity of the $m_F = 0$ atoms remains constant after the adiabatic rapid passage, the expected position is shown as the gray 'x' in Figs. 3.9(a) and (b). The 1σ uncertainty from the corresponding fits is shown as the dashed gray ellipse around the expected position. The $m_F = 0$

atoms lie well within this range. If this slow switching had produced the same kicks (without considering sign changes, but including the factor 2 for the different Zeeman substate), the expected position would have been the one marked by the gray '+'. The positions corresponding to the two assumptions are separated by $95\ \mu\text{m}$ corresponding to 4σ . Hence, the slow ramp-up of the x coil might indeed reduce the kick imprinted on the atoms.

Conclusions

In this chapter, all bias coils were characterized in ground-based calibration measurements to a mG precision. In this context, a static magnetic background field of 27 mG was found in the z direction. The dynamics of the magnetic field after requesting a different current depends on the characteristic step response of the respective coil or chip in combination with the current driver. These response functions were measured and a method for making the actual current response match a desired shape was demonstrated. Still the time scales are limited by the characteristic switching time, which is approximately 0.1 ms for the chips and up to 2 ms for the coils.

A static magnetic field gradient was measured in microgravity by tracking the accelerated motion of atoms in the $m_F = 2$ substate. This gradient includes contributions from a static background and the x coil and thus depends on I_x . Within the Detection 1 camera frame (x', y'), the gradient is $(0.19, -0.6)$ G/m for $I_x = 0.5$ A and $(-0.21, -0.68)$ G/m for $I_x = 0.1$ A. The Detection 2 system had been installed within the magnetic shield just before both data sets were acquired. These results prove the existence of a static background magnetic field gradient, because the values are not proportional to I_x . The source of this gradient could not be identified. The gradient due to the coils was measured in a ground-based measurement, too, but the sensitivity was insufficient to gain significantly more information because of the limited TOF. Still, these measurements provide an upper bound on the magnetic field gradients by the coils. The largest acceleration per Gauss was $a_z = -4(3)$ mm/s²/G for the x coil, which corresponds to a gradient per Gauss of $0.6(5)$ G/m/G. This is compatible with the result $a_z = -3.3(3)$ mm/s²/G obtained in microgravity.

Besides the static gradient, all coils are responsible for a transient gradient when the coil current is changed. The resulting velocity change experienced by the atomic ensemble can amount to several mm/s as proven in a ground-based measurement. The largest contribution stems from the z coil. For example, switching it to 1 A results in a velocity change of 4.4 mm/s in the z direction. The transient behavior could be demonstrated in microgravity, too. Here, the ratio of the x' to y' gradient defines the angle at which different Zeeman states separate. A deviation from the expected angle was observed, which can be explained by a transient gradient due to the coil switching process. It was demonstrated for the x coil that this effect might be mitigated by a slow ramp-up. However, this strategy is not necessarily applicable to all coils and must be studied further.

Chapter 4

Adiabatic rapid passage

A population reversal in a two-level system by a chirped electromagnetic pulse is called adiabatic rapid passage (ARP). The first experimental realization was carried out in nuclear magnetic resonance (NMR) [128, 129]. Later on, ARP was successfully applied in other fields as well [130–139]. It is not restricted to a specific range of the electromagnetic spectrum because the required frequency solely depends on the energy difference of the intended transition. For instance, there are realizations using rf [130–133], microwave [132–134] and optical [135–139] pulses. In the scope of cold atoms, ARP can be used to transfer an atomic ensemble into any particular Zeeman state.

Camparo and Frueholz [140] have thoroughly treated ARP for a two-level system in the dressed state formalism. Their results are recalled in the first section and extended where necessary. These results serve as a reference for the application to ^{87}Rb . Furthermore, an in-depth understanding of ARP in a two-level system is helpful when considering more complex systems.

In the second section, relevant properties of the ^{87}Rb $F = 2$ hyperfine manifold are discussed. The previous results are transferred to the dressed rubidium atom. Section 4.3 deals with experimental parameters and procedures. Different realizations of ARPs are shown in Section 4.4. Predictions of the model as well as various limitations are discussed.

All measurements and their analysis presented in this chapter were performed by the author, except for the two images in Fig. 4.23. They were measured by Christian Deppner and Merle Cornelius with support by the author.

4.1 Adiabatic rapid passage in a two-level system

In this section, the adiabatic rapid passage is explained for a simple two-level system coupled to a single quantized field mode at frequency ω_{rf} . Without loss of generality, it is assumed to be in the rf regime, which is the case for all measurements presented in this work. This so called Jaynes-Cummings model [141] has been covered in many textbooks and is not derived here [142–144]. However, the key properties are recalled, because they apply to more complex systems as well.

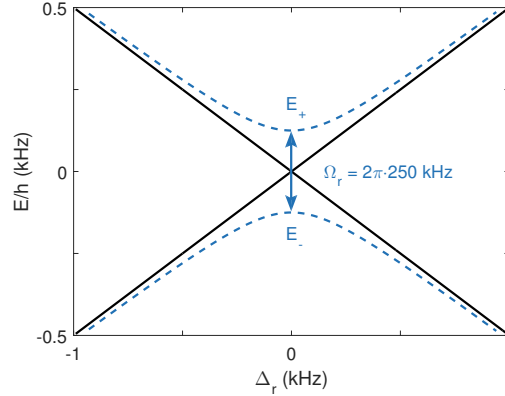


Figure 4.1: Comparison of the dressed-state energy levels (dashed blue lines) to those of an unperturbed system (solid black lines) as a function of the detuning Δ_r . In the unperturbed system, the diabatic states cross at zero detuning. The coupled system exhibits an avoided crossing with a separation $E_+ - E_- = \Omega_r$.

The two levels involved are the excited state $|e\rangle$ and ground state $|g\rangle$ which are separated in energy by $\hbar\omega_{eg}$. These orthonormal eigenstates of the unperturbed system are called diabatic states. The Jaynes-Cummings Hamiltonian for the dressed system is

$$H_{\text{JC}} = \frac{\hbar}{2} \begin{pmatrix} \Delta_r & \Omega_r \\ \Omega_r & -\Delta_r \end{pmatrix}, \quad (4.1)$$

with the Rabi frequency Ω_r and the detuning $\Delta_r = \omega_{\text{rf}} - \omega_{eg}$. This choice in favor of $\omega_{eg} - \omega_{\text{rf}}$ has one advantage: An increase in ω_{rf} increases Δ_r , which is more intuitive. With this definition, the diabatic basis for Eq. (4.1) is¹:

$$|e\rangle = \begin{pmatrix} 1 \\ 0 \end{pmatrix}, \quad |g\rangle = \begin{pmatrix} 0 \\ 1 \end{pmatrix}. \quad (4.2)$$

The eigenvectors of Eq. (4.1) are given by

$$|\phi_{\pm}\rangle = \frac{1}{\sqrt{\Omega_r^2 + (2E_{\pm} - \Delta_r)^2}} \begin{pmatrix} \Omega_r \\ 2E_{\pm} - \Delta_r \end{pmatrix}. \quad (4.3)$$

They are called dressed states (also adiabatic states) and are stationary under H_{JC} with eigenvalues

$$E_{\pm} = \pm \frac{1}{2} \sqrt{\Omega_r^2 + \Delta_r^2}. \quad (4.4)$$

These eigenvalues are shown in Fig. 4.1 for $\Omega_r = 2\pi \cdot 250$ kHz (dashed blue line) in comparison to the unperturbed values (solid black lines).

The energy difference at resonance ($\Delta_r = 0$) is

$$\Delta E(\Delta_r = 0) = E_+ - E_- = \Omega_r. \quad (4.5)$$

¹Both these definitions are arbitrary. Inverting either of them would produce a change of sign in the diagonal elements of H_{JC} .

Here, the dressed states are equal superpositions of the diabatic states

$$|\psi_{\pm}(t)\rangle = \frac{1}{\sqrt{2}}[|g\rangle \pm |e\rangle].$$

In the limit of a large positive or negative detuning, they are essentially equal to the unperturbed states:

$$\begin{aligned} \lim_{\Delta_r \rightarrow -\infty} |\psi_+(t)\rangle &= |e\rangle, & \lim_{\Delta_r \rightarrow +\infty} |\psi_+(t)\rangle &= |g\rangle, \\ \lim_{\Delta_r \rightarrow -\infty} |\psi_-(t)\rangle &= |g\rangle, & \lim_{\Delta_r \rightarrow +\infty} |\psi_-(t)\rangle &= -|e\rangle. \end{aligned} \quad (4.6)$$

The time evolution of a diabatic state under the action of H_{JC} is a Rabi oscillation between the two diabatic states [145]. At $\Delta_r = 0$, its frequency is the resonant Rabi frequency Ω_r while the coefficients of the superposition $|\psi(t)\rangle = c_g |g\rangle + c_e |e\rangle$ oscillate at half the Rabi frequency, equivalent to the off-diagonal elements in H_{JC} . The probability to find the system in, for example, state $|g\rangle$ is

$$p_g = |\langle g|\psi(t)\rangle|^2 = |c_g|^2 = \left| \sin\left(\frac{1}{2}\Omega_r t\right) \right|^2 = \frac{1}{2} [1 - \cos(\Omega_r t)], \quad (4.7)$$

which oscillates with Ω_r . In the off-resonant case, this frequency increases to

$$\Omega'_r = \sqrt{\Omega_r^2 + \Delta_r^2}, \quad (4.8)$$

while the amplitude A decreases from unity to

$$A = \left(\frac{\Omega_r}{\Omega'_r} \right)^2. \quad (4.9)$$

Hence, a full reversal of the atomic state is not possible by Rabi-oscillations in the off-resonant case.

ARP for $|e\rangle \rightarrow |g\rangle$

In the following, ARP is discussed for the passage from initial state $\Psi_i = |e\rangle$ to final state $\Psi_f = |g\rangle$. At an infinitely large negative detuning, the initial state is identical to the upper dressed state [Ψ_+ , see Eq. (4.6)]. When the detuning is increased slowly enough (adiabatically), the system remains in $|\psi_+\rangle$. At an infinitely large positive detuning, this upper dressed state is identical to the ground state, which is the desired final state Ψ_f . However, this simplified recipe neglects adiabatic and decoherence losses. To characterize adiabatic losses, the sweep rate α is introduced as

$$\alpha = \frac{d}{dt} \Delta_r. \quad (4.10)$$

Landau and Zener independently derived an expression for the probability of adiabatic losses [146]:

$$P_{LZ} = \exp\left(-\frac{\pi\Omega_r^2}{2|\alpha|}\right), \quad (4.11)$$

also known as the Landau-Zener formula. The probability for an adiabatic passage through the crossing region is

$$P_{\text{ad}} = 1 - \exp\left(-\frac{\pi\Omega_r^2}{2|\alpha|}\right). \quad (4.12)$$

This gives rise to the so called adiabaticity criterion, which is rather qualitative:

$$|\alpha| \ll \Omega_r^2. \quad (4.13)$$

In any real experiment, Δ_r cannot be swept from or to infinity, but has to take finite initial ($\Delta_{r,i}$) and final ($\Delta_{r,f}$) values. When the perturbation is switched on, the initial state is projected onto the new basis of dressed states. This gives rise to further losses, because the projection of the excited state onto $\phi_-(\Delta_{r,i})$ is nonzero. The complementary probability for the desired dressed state ϕ_+ is

$$P_i = 1 - |\langle\phi_-(\Delta_{r,i})|e\rangle|^2 = |\langle\phi_+(\Delta_{r,i})|e\rangle|^2. \quad (4.14)$$

Since P_i is the overlap integral of the adiabatic with the diabatic state it is simply called initial overlap of states. In an analogous manner, the final overlap can be defined as

$$P_f = |\langle g|\phi_+(\Delta_{r,f})\rangle|^2. \quad (4.15)$$

Decoherence is quantified by the longitudinal (T_1) and transverse (T_2) relaxation time as originally defined by F. Bloch [147]:

$$\begin{aligned} \dot{S}_x &= \frac{1}{T_2} S_x, \\ \dot{S}_y &= \frac{1}{T_2} S_y, \\ \dot{S}_z &= \frac{1}{T_1} S_z, \end{aligned} \quad (4.16)$$

where $S_{x,y,z}$ are the expectation values of the spin components (in the rotating frame). T_1 is also called energy relaxation time, since it depends on magnetic field fluctuations at the Larmor frequency. It is related to spontaneous emission [148]. T_2 is also known as total relaxation time, dephasing time or coherence time and can be defined as

$$\frac{1}{T_2} = \frac{1}{2T_1} + \frac{1}{T_2'}, \quad (4.17)$$

where T_2' is the pure dephasing time resulting from, for instance, dephasing collisions [140]. In the presence of decoherence, Rabi oscillations are damped at the Rabi decay rate. The corresponding Rabi decay time can be different from the intrinsic T_2 in the presence of imperfections in the measuring apparatus, for example, gradients in the magnetic field or the rf amplitude.

T_1 can be measured by inversion recovery [149]. However, it is sufficient to consider T_2 only, because the Zeeman states are stable in the presence of a static magnetic field.

Spin-echos, as first discovered in NMR by E. L. Hahn [150], can be used to measure T_2 . The scheme is called Carr-Purcell sequence [151]: First, a $\pi/2$ -pulse (X) brings

an ensemble of spins into the y direction of the Bloch sphere. After a time $\tau/2n$, a sequence of n π -pulses (X^2) is applied, separated by τ/n . These pulses rotate the spins by 180° around the x direction of the Bloch sphere. Finally, a $\pi/2$ -pulse is applied, when the spin should be measured in the z direction. The overall time of this sequence is τ and the simplest implementation with $n = 1$ is

$$X \frac{\tau}{2} X^2 \frac{\tau}{2} X. \quad (4.18)$$

After the first pulse, all spins can dephase along the x - y plane for the time $\tau/2n$. The time evolution of some of the fluctuations which are slow compared to τ/n can be reversed by X^2 . The spins rephase after another $\tau/2n$ producing the spin-echo. Its amplitude decays as

$$A_{\text{echo}}(t) = A_0 \exp\left(-\frac{t}{T_2}\right). \quad (4.19)$$

Although, if n is chosen too small or if the pulses X and X^2 are not perfect, the echo amplitude will decay faster. Furthermore, there are systematics which are uncompensated for by this Carr-Purcell sequence, for instance, expansion in or motion through a magnetic field gradient by the ensemble of spins. The value for T_2 that is determined by this method can therefore be interpreted as a lower limit to the intrinsic T_2 .

To minimize the effect of decoherence in ARP, the rapidity criterion can be defined as [152]

$$|\alpha| \gg \frac{\Omega_r}{T_2}. \quad (4.20)$$

The probability Π to remain in the same dressed state after the passage can be derived in a formal treatment [140]. Drawing on these results, an approximate solution can be stated:

$$\Pi \simeq \exp\left(-\frac{3\pi\Omega_r}{8|\alpha|T_2}\right). \quad (4.21)$$

Combining Eqs. (4.12), (4.14), (4.15) and (4.21) yields an expression for the ARP efficiency:

$$\eta = P_i P_{\text{ad}} P_f \Pi. \quad (4.22)$$

Rabi cycling is a faster alternative to such a passage by a chirped rf pulse is. It is achieved by a single π -pulse in the case of a two-level system or by a chain of π -pulses at the correct frequencies in systems with more than two levels. However, this scheme is less robust. Any change in Ω_r induces a phase error in the π -pulse. In addition, magnetic field changes cause a corresponding shift of the resonance frequency. This entails a nonzero detuning, which in turn changes frequency [Eq. (4.8)] and amplitude [Eq. (4.9)] of the Rabi oscillation. This is why ARP is generally favored over Rabi cycling. Still, there are occasions in which the extra time matters and Ω_r as well as Δ_r are stable enough. In these cases, Rabi cycling is the better choice.

4.2 Properties of the ^{87}Rb $F = 2$ hyperfine manifold

All Zeeman levels of the ^{87}Rb $5^2\text{S}_{1/2}$ manifold are described by the Breit-Rabi formula for arbitrary magnetic field strengths [153]:

$$E(F = I \pm \frac{1}{2}, m_F, B_{\tilde{z}}) = -\frac{\Delta E_{\text{hfs}}}{2(2I+1)} + g_I \mu_B m_F B_{\tilde{z}} \pm \frac{\Delta E_{\text{hfs}}}{2} \left(1 + \frac{4m_F x}{2I+1} + x^2 \right)^{\frac{1}{2}}, \quad (4.23)$$

where $I = 3/2$ is the nuclear angular momentum, m_F the magnetic quantum number, g_I the nuclear g -factor, μ_B the Bohr magneton, $B_{\tilde{z}}$ the strength of the quantization field with \tilde{z} defined as its direction and ΔE_{hfs} the ground-state hyperfine splitting. The plus sign applies to the (upper) $F = 2$ manifold in the anomalous Zeeman regime while the minus sign refers to $F = 1$. x is defined as

$$x = \frac{(g_J - g_I) \mu_B B_{\tilde{z}}}{\Delta E_{\text{hfs}}}, \quad (4.24)$$

where g_J is the fine structure Landé g -factor of the state $5^2\text{S}_{1/2}$.

The energy levels according to Eq. (4.23) are shown in Fig. 4.2(a). For weak magnetic fields, F is a good quantum number. In the regime of strong magnetic fields, I and J no longer couple to F . This is called the hyperfine Paschen-Back effect.

Inserting the nuclear angular momentum $I = \frac{3}{2}$ into Eq. (4.23) and choosing the + sign for $F = 2$ yields

$$E(F = I + \frac{1}{2}, m_F, B_{\tilde{z}}) = -\frac{\Delta E_{\text{hfs}}}{8} + g_I \mu_B m_F B_{\tilde{z}} + \frac{\Delta E_{\text{hfs}}}{2} (1 + m_F x + x^2)^{\frac{1}{2}}.$$

This equation can be approximated to second order in $B_{\tilde{z}}$ by a Taylor series expansion of the square root at $x = 0$:

$$\begin{aligned} E(F = I + \frac{1}{2}, m_F, B_{\tilde{z}}) &\approx -\frac{\Delta E_{\text{hfs}}}{8} + g_I \mu_B m_F B_{\tilde{z}} + \frac{\Delta E_{\text{hfs}}}{2} \left\{ 1 + \frac{m_F}{2} x \right. \\ &\quad \left. + \frac{1}{2} \left[1 - \left(\frac{m_F}{2} \right)^2 \right] x^2 \right\} \\ &= \frac{3}{8} \Delta E_{\text{hfs}} + g_I \mu_B m_F B_{\tilde{z}} + \frac{\Delta E_{\text{hfs}}}{4} \left\{ m_F x + \left[1 - \left(\frac{m_F}{2} \right)^2 \right] x^2 \right\} \\ &= g_I \mu_B m_F B_{\tilde{z}} + \frac{\Delta E_{\text{hfs}}}{4} [m_F x + Q_{m_F} x^2], \end{aligned}$$

where the point of zero energy has been shifted to get rid of the constant term and the abbreviation

$$Q_{m_F} = 1 - \left(\frac{m_F}{2} \right)^2 \quad (4.25)$$

was introduced. Inserting Eq. (4.24) yields

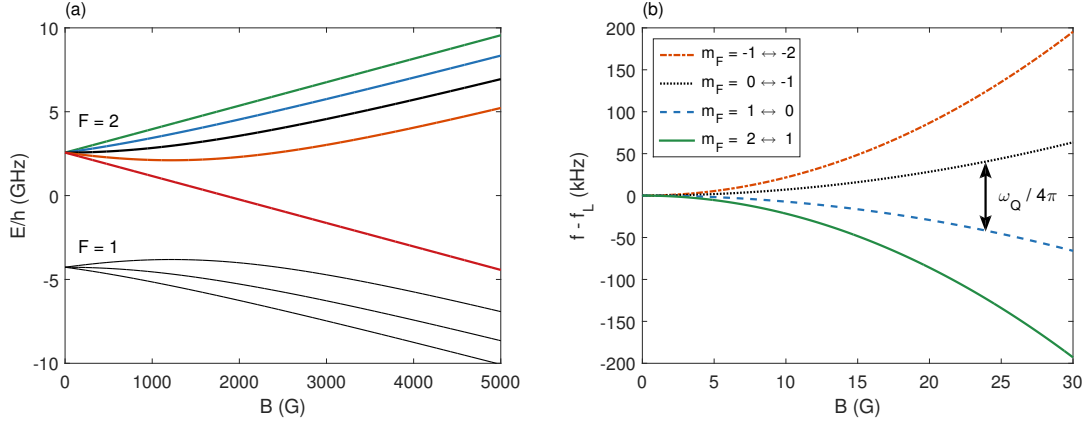


Figure 4.2: (a) Zeeman structure of the two ^{87}Rb $5^2\text{S}_{1/2}$ hyperfine levels. For weak magnetic fields (anomalous Zeeman regime), the sublevels can be described by the magnetic quantum number m_F ranging from $m_F = 2$ (green, top) to $m_F = -2$ (red) for $F = 2$ and from $m_F = -1$ (top) to $m_F = 1$ (bottom) for $F = 1$. In the regime of strong magnetic fields, the states are described by the quantum numbers m_J and m_I (hyperfine Paschen-Back effect). The upmost four states (green to orange) have $m_J = +\frac{1}{2}$ and $m_I = (\frac{3}{2}, \frac{1}{2}, -\frac{1}{2}, -\frac{3}{2})$. The lower four have $m_J = -\frac{1}{2}$ and m_I in reverse order. (b) The transition frequency for neighboring states deviates from the linear dependence on B (hf_L), which is called quadratic Zeeman effect with the quadratic Zeeman shift ω_Q . It is plotted for $F = 2$.

$$\begin{aligned}
 E(F = I + \frac{1}{2}, m_F, B_z) &\approx g_I \mu_B m_F B_z + \frac{\Delta E_{\text{hfs}}}{4} \left\{ m_F \frac{(g_J - g_I) \mu_B B_z}{\Delta E_{\text{hfs}}} \right. \\
 &\quad \left. + Q_{m_F} \left[\frac{(g_J - g_I) \mu_B B_z}{\Delta E_{\text{hfs}}} \right]^2 \right\} \\
 &= g_I \mu_B m_F B_z + \frac{1}{4} m_F (g_J - g_I) \mu_B B_z + \frac{1}{4} Q_{m_F} \frac{(g_J - g_I)^2 \mu_B^2}{\Delta E_{\text{hfs}}} B_z^2 \\
 &= \left(\frac{1}{4} g_J + \frac{3}{4} g_I \right) \mu_B m_F B_z + \frac{1}{4} Q_{m_F} \frac{(g_J - g_I)^2 \mu_B^2}{\Delta E_{\text{hfs}}} B_z^2 \\
 &\approx g_F \mu_B m_F B_z + Q_{m_F} \frac{\mu_B^2 B_z^2}{\Delta E_{\text{hfs}}},
 \end{aligned}$$

where the sum of g-factors in the first term is exactly the definition of g_F for a $5^2\text{S}_{1/2}$ state. The approximation $g_J - g_I \approx 2$ was made for the second term. It can be simplified even further by introducing the linear Zeeman shift

$$\omega_L = \frac{1}{\hbar} g_F \mu_B B_z \quad (4.26)$$

and the quadratic Zeeman shift

$$\omega_Q = \frac{1}{\hbar} \frac{\mu_B^2 B_z^2}{\Delta E_{\text{hfs}}} \quad (4.27)$$

to

$$E \approx \hbar (\omega_L m_F + Q_{m_F} \omega_Q). \quad (4.28)$$

This quadratic dependence is shown in Fig. 4.2(b), where the domain was reduced compared to Fig. 4.2(a). In the linear regime, the transition frequencies between neighboring Zeeman states are described by Eq. (4.26) with $2\pi f_L = \omega_L$. The deviation of this linear dependence is called the quadratic Zeeman effect. The neighboring transitions are separated by $\omega_Q/4\pi$ in the frequency domain. This separation is not just a small undesired perturbation, but *the* essential effect for an adiabatic rapid passage in rubidium.

The quadratic approximation can be applied to a limited range of magnetic fields only. At higher fields, the predicted transition frequencies differ from the actual values too much. In the range plotted in Fig. 4.2(b), the relative error is 2% or below. A field strength of 100 G can be considered critical since the deviations are on the 6% level already. At this level, an extension of the Taylor series expansion to the third order is recommended. This is possible with the same methods as used below, but not required here. The error by the approximation $g_J - g_I \approx 2$ is negligible, since it is on the order of 0.3%.

To avoid confusion, some more words are spent on the quadratic Zeeman effect. Some authors [154, 155] define the quadratic Zeeman shift as the shift of the 0-0 hyperfine (clock) transition, which is just a special case. Hence, the term clock shift is better suited for this. However, there also exists a second type of quadratic Zeeman effect. It is a diamagnetic effect [156, 157] and of no relevance in this work.

The strong linear Zeeman shift facilitates an efficient SG separation of states by the m_F dependent force

$$F_i = -\frac{\partial E}{\partial r_i} = -g_F \mu_B m_F \frac{\partial B}{\partial r_i}, \quad (4.29)$$

in the spatial direction r_i with $i = \{x, y, z\}$. Rearranging this equation allows for the determination of the gradient of the magnetic field's absolute value:

$$\frac{\partial B}{\partial r_i} = -\frac{m_{\text{Rb}}}{g_F \mu_B m_F} a_i, \quad (4.30)$$

where a_i is the acceleration in the i direction and m_{Rb} is the mass of a rubidium atom. The fraction amounts to $155.61 \frac{\text{G/m}}{\text{m/s}^2}$ for $m_F = 2$, which is the relation used in Section 3.4.

Equation (4.28) describes the energy of a state $|m_F\rangle$ in a uniform magnetic field. It can be written as an operator after replacing the m_F by \hat{F}_z . Since $|m_F\rangle$ is an eigenvector of \hat{F}_z , the same holds true for $\hat{Q}_{m_F} |m_F\rangle = Q_{m_F} |m_F\rangle$ by definition [see Eq. (4.25)]:

$$\hat{H}_0 = \hbar (\omega_L \hat{F}_z + \omega_Q \hat{Q}_z). \quad (4.31)$$

The dressed manifold

A coupling of the Zeeman states is realized by applying a resonant or near-resonant rf field, as described in the previous section. The oscillating magnetic field must be perpendicular to the static field B_z in order to have non-vanishing matrix elements.

The common convention is to define the x direction (here \tilde{x}) as the direction of the B -field vector. Adhering to this, the interaction Hamiltonian is

$$\hat{H}_{\text{rf}}(t) = g_F \mu_B B_{\text{rf}} \cos(\omega_{\text{rf}} t) \hat{F}_{\tilde{x}}, \quad (4.32)$$

with the oscillating field amplitude B_{rf} at frequency ω_{rf} . The operator $\hat{F}_{\tilde{x}}$ can be expressed in terms of creation and annihilation operators \hat{F}_{\pm} :

$$\hat{F}_{\tilde{x}} = \frac{1}{2} (\hat{F}_+ + \hat{F}_-), \quad (4.33)$$

with²

$$\hat{F}_{\pm} |m_F\rangle = (\hat{F}_{\tilde{x}} \pm i\hat{F}_{\tilde{y}}) |m_F\rangle = \sqrt{F(F+1) - m_F(m_F \pm 1)} |m_F \pm 1\rangle. \quad (4.34)$$

To find the matrix elements of the time-independent Schrödinger picture Hamiltonian in a proper basis, the Schrödinger equation has to be solved for the overall time-dependent Hamiltonian:

$$i\hbar \frac{\partial}{\partial t} |\Psi(t)\rangle = [\hat{H}_0 + \hat{H}_{\text{rf}}(t)] |\Psi(t)\rangle. \quad (4.35)$$

The solution is a bit lengthy but straightforward. It can be found in Appendix D.1. Choosing the basis

$$|2\rangle = \begin{pmatrix} 1 \\ 0 \\ 0 \\ 0 \\ 0 \end{pmatrix}, \quad \dots \quad |-2\rangle = \begin{pmatrix} 0 \\ 0 \\ 0 \\ 0 \\ 1 \end{pmatrix}, \quad (4.36)$$

the corresponding matrix representation of \hat{H} is

$$\hat{H} = \hbar \begin{pmatrix} -2\Delta_r & \frac{1}{2}\Omega_r & 0 & 0 & 0 \\ \frac{1}{2}\Omega_r & \frac{3}{4}\omega_Q - \Delta_r & \sqrt{\frac{3}{8}}\Omega_r & 0 & 0 \\ 0 & \sqrt{\frac{3}{8}}\Omega_r & \omega_Q & \sqrt{\frac{3}{8}}\Omega_r & 0 \\ 0 & 0 & \sqrt{\frac{3}{8}}\Omega_r & \frac{3}{4}\omega_Q + \Delta_r & \frac{1}{2}\Omega_r \\ 0 & 0 & 0 & \frac{1}{2}\Omega_r & 2\Delta_r \end{pmatrix}, \quad (4.37)$$

with

$$\Delta_r = \omega_{\text{rf}} - \omega_L \quad (4.38)$$

and

$$\Omega_r = \frac{1}{\hbar} g_F \mu_B B_{\text{rf}}. \quad (4.39)$$

²Since this is just a choice of coordinates, it cannot have any physical significance. In fact, all conclusions are the same when choosing, for example, the \tilde{y} direction. The only difference is a phase factor in the off-diagonal matrix elements. These phase factors for the corresponding matrix elements are complex conjugates to each other. This is of course necessary since the Hamiltonian must be Hermitian. Choosing the \tilde{x} direction is convenient since all coupling matrix elements are real.

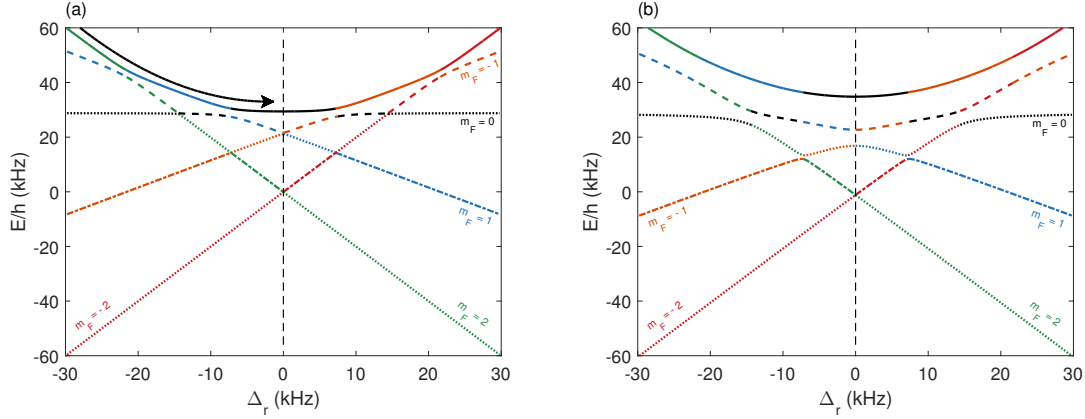


Figure 4.3: Eigenvalues of \hat{H} [see Eq. (4.37)] for $B = 10$ G. The solid line represents the largest eigenvalue (E_5), the dashed line E_4 , etc. The colors indicate the dominating diabatic state in the decomposition of the corresponding dressed state. (a) $\Omega_r = 2\pi \cdot 2.5$ kHz ($\Omega_r/B^2 = 0.025$ kHz/G²); The arrow shows a frequency sweep for ARP in the (upper) dressed state $|\varphi_5\rangle$. (b) $\Omega_r = 2\pi \cdot 10$ kHz ($\Omega_r/B^2 = 0.1$ kHz/G²)

Inspection of Eq. (4.37) immediately reveals some properties of the dressed system. By equating neighboring diagonal elements, the avoided crossings are at $\Delta_r = \pm \frac{3}{4}\omega_Q$ and $\pm \frac{1}{4}\omega_Q$. The Rabi frequency of the ‘outer’ transitions (i.e., $m_F = +2 \leftrightarrow +1$ and $m_F = -2 \leftrightarrow -1$) is $\Omega_{\pm 2, \pm 1} = 2 \cdot \frac{1}{2}\Omega_r = \Omega_r$ [see Eq. (4.7)], but it is higher for the ‘inner’ ones ($\Omega_{\pm 1, 0} = 2 \cdot \sqrt{3/8}\Omega_r = \sqrt{3/2}\Omega_r$). Figure 4.3 shows the solution of the eigenvalue problem

$$\hat{H}|\varphi_n\rangle = E_n|\varphi_n\rangle \quad (4.40)$$

for $B = 10$ G, where $\{\varphi_n\}$ is the dressed state basis. For definiteness, E_5 is defined to be the largest eigenvalue (solid line). The remaining ones follow in decreasing order (dashed line for E_4 etc.). Figure 4.3(a) is calculated for $\Omega_r = 2\pi \cdot 2.5$ kHz and (b) for $\Omega_r = 2\pi \cdot 10$ kHz. The colors indicate which diabatic state dominates the corresponding dressed state decomposition.

Ω_r is directly proportional to the externally applied rf amplitude. Unfortunately, this is not exactly true for the Rabi frequencies of the respective transitions. In fact, they are disturbed by the neighboring crossings for large values of Ω_r/B^2 , violating the previous offhand interpretation of Eq. (4.37). However, symmetry requires $\Omega_{2,1} = \Omega_{-2,-1}$ and $\Omega_{1,0} = \Omega_{-1,0}$ (order of subscripts has no meaning). At $\Omega_r/B^2 = 0.1$ kHz/G², the individual crossings are almost indistinguishable [Fig. 4.3(b)]. Even crossings with $\Delta m_F \neq \pm 1$ become avoided in this regime. Even for smaller Ω_r/B^2 , each crossing is affected by its neighbor in position (detuning) and energy separation (Rabi frequency), as shown in Fig. 4.4.

Although both effects are rather small, they cannot be neglected in general. The numerical algorithm to be discussed in Section 4.4 intrinsically accounts for these effects. Furthermore, the shift is relevant when characterizing the experiment, for instance Ω_r , since the detuning should be much smaller than Ω_r [see Eq. (4.8)]. To give an example, Δ_{error} of the $m_F = 2 \leftrightarrow 1$ crossing in Figs. 4.3(a) and (b) is

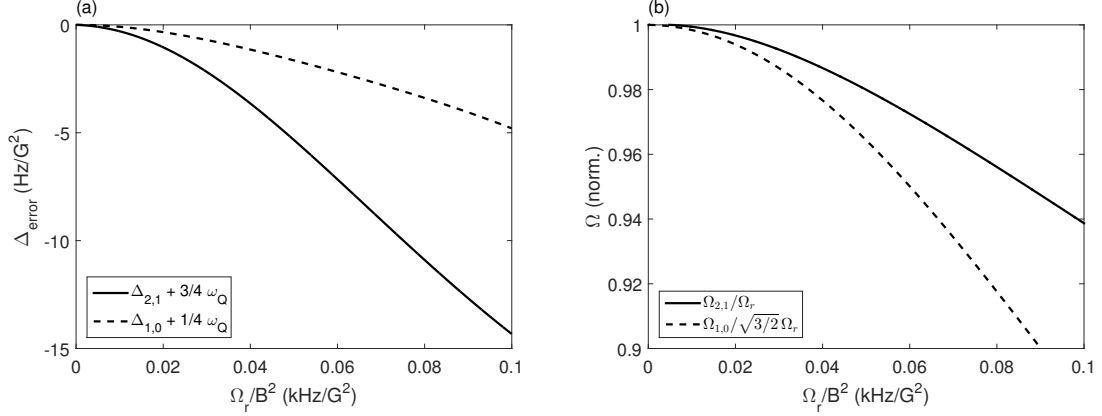


Figure 4.4: Systematic shifts of the crossings $m_F = 2 \leftrightarrow 1$ (solid lines) and $m_F = 1 \leftrightarrow 0$ (dashed lines) – c.f. Fig. 4.3(a) – in detuning (a) and energy separation (b). Negative values of Δ_{error} in (a) signify a shift of the crossings to more negative values of Δ_r . By symmetry, these results apply to the crossings $m_F = -2 \leftrightarrow -1$ and $m_F = -1 \leftrightarrow 0$, too, but with a change of sign in (a).

$-2\pi \cdot 0.2 \text{ kHz}$ and $-2\pi \cdot 1.4 \text{ kHz}$, respectively. The impact of a reduced Rabi frequency [Fig. 4.4(b)] can be anticipated by inspecting Eq. (4.12). A power series of these systematic shifts is given in Appendix D.2. It is valid for $\Omega_r/B^2 \lesssim 0.175 \text{ kHz/G}^2$, where the respective minimum of $E_5 - E_4$ corresponding to crossing $m_F = 1 \leftrightarrow 0$ disappears. Despite the more rapid relative decrease of $\Omega_{1,0}$, it is always larger than $\Omega_{2,1}$.

The contributions of the diabatic states to $|\varphi_5\rangle$ in Figs. 4.3(a) and (b) are shown in Figs. 4.5(a) and (b), respectively. The effect of increasing Ω_r is to broaden the avoided crossing region. This increased overlap reduces the probability to find an atom in the dominating diabatic state. In contrast, an increased magnetic field [Figs. 4.5(c) and (d)] moves the crossings further apart. This increases the maximum probabilities of the ‘inner’ diabatic states ($m_F \neq \pm 2$). In the following, the state $m_F = 0$ is selected as final state P_f for its significantly lower sensitivity to magnetic field gradients. In analogy to Eqs. (4.14) and (4.15), the initial and final overlap are

$$P_i(\Delta_{r,i}, B, \Omega_r) = |\langle \varphi_5 | 2 \rangle|^2 \quad (4.41)$$

and

$$P_f(\Delta_{r,f} = 0, B, \Omega_r) = |\langle 0 | \varphi_5 \rangle|^2. \quad (4.42)$$

Dressed states with the same value of Ω_r/B^2 , but different Ω_r (and B), are similar to each other. They can be mapped into each other by rescaling the abscissa by the ratio of the corresponding Rabi frequencies, which is equal to the square of the ratio of the corresponding magnetic fields. An example of this are Figs. 4.5(a) and (d) with a rescaling factor of four. Both share $\Omega_r/B^2 = 0.025 \text{ kHz/G}^2$ and the same P_f . The comparison with Figs. 4.5(b) and (c) suggests that P_f strictly decreases with Ω_r/B^2 . This is indeed the case, as shown in Fig. 4.6.

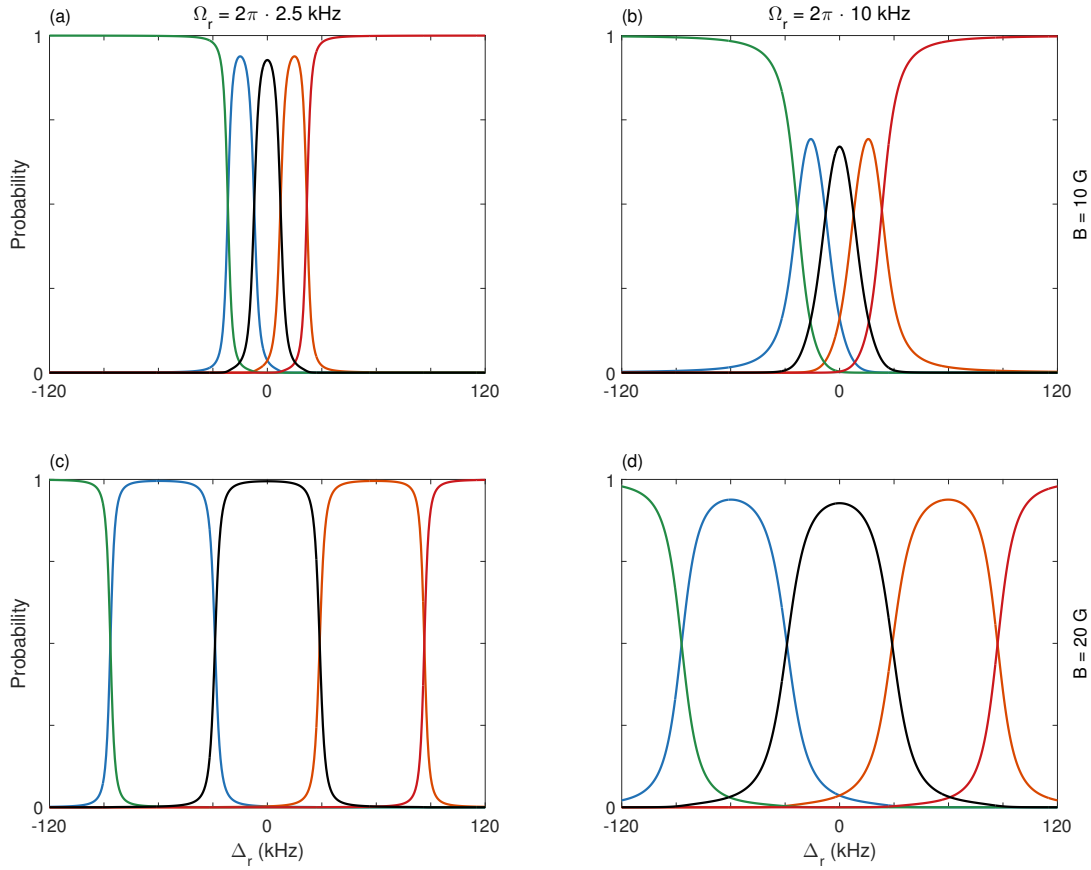


Figure 4.5: Decomposition of the upper dressed state $|\varphi_5\rangle$ in Fig. 4.3 into the diatomic states $\{m_F\}$ for $B = 10$ G (top row) and $B = 20$ G (bottom row). Two different Rabi frequencies are shown for both field strengths: $\Omega_r = 2\pi \cdot 2.5$ kHz (left column) and $\Omega_r = 2\pi \cdot 10$ kHz (right column). The previous color code is maintained, that is, green (left) for $m_F = 2$ to red (right) for $m_F = -2$.

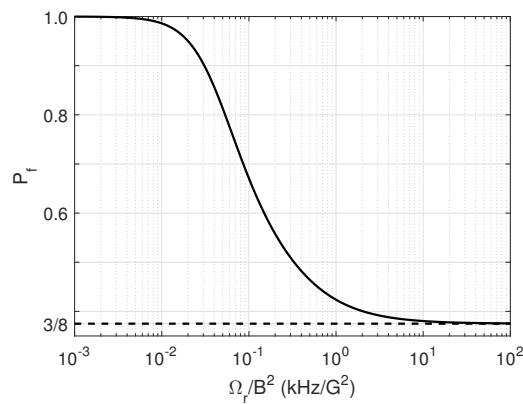


Figure 4.6: The solid line shows the final overlap of states $P_f = |\langle 0|\varphi_5\rangle|^2$ of the energetically highest dressed state $|\varphi_5\rangle$ (see Fig. 4.3) with the diatomic state $|m_F = 0\rangle$. For large Ω_r/B^2 , P_f approaches $3/8$ (dashed line).

From the final overlap point of view, Ω_r/B^2 should be as small as possible. The initial overlap can be adjusted by choosing a sufficiently large (negative) initial detuning $\Delta_{r,i}$ for any value of B and Ω_r . On the other hand, a large magnetic field entails a long sweep time or high sweep rate of the rf chirp due to the larger initial detuning. This deteriorates either Π or P_{ad} . In addition, there are experimental constraints on the available parameter range. The ones relevant to the Q-2 apparatus are discussed in the following section. The ARP is then optimized under these constraints in Section 4.4. However, the results are presented in a way that allows for a direct transfer to other experiments using cold ^{87}Rb atoms. It is not limited to BECs either.

4.3 Relevant experimental parameters and techniques

The magnetic field and the Rabi frequency could be identified as the most critical parameters for ARP. Their time dependence must be known, too, because the passage takes a finite time. Furthermore, the spatial gradient is important, because the atoms can be moving during the ARP. This section introduces the corresponding measurement techniques and investigates these questions. Another important parameter is the transverse relaxation time. A protocol for measuring this time is demonstrated.

Measurement of magnetic fields by rf spectroscopy

The magnetic field as seen by the atoms cannot be measured by external sensors, because access is blocked by the vacuum chamber. Furthermore, some magnetic sensors introduce a field as well. However, the field can be measured using the atoms themselves by rf spectroscopy with a sufficient precision and time resolution (see also Section 3.1). This works for freely falling atoms or atoms being trapped in optical potentials, but obviously not for magnetic ones. Since Q-2 features no optical dipole trap, atoms have to be released from the magnetic trap. After this release, the atoms are accelerated due to earth's gravitational field and leave the detection area after approximately 22 ms TOF. This time is sufficient for switching coils, a brief manipulation of the atoms, optionally a SG experiment to separate the magnetic substates in space and to detect them. Initially, the atoms are in the $m_F = 2$ substate. When applying an rf field resonant to the $m_F = 2 \leftrightarrow 1$ transition for $t_{rf} = \pi/\Omega_{2,1}$, the state $m_F = 2$ is completely depleted (π -pulse). Off resonance, Rabi oscillations occur at reduced amplitude and increased frequency. The magnetic field can then be determined by scanning the frequency, identifying the minimum of the relative population in $m_F = 2$, accounting for the frequency shift shown in Fig. 4.4(a) and invoking Eqs. (4.26) to (4.28). The relative populations n_i depend on B , Ω_r , Δ_r and t_{rf} . An example is shown in Fig. 4.7 probing the magnetic field of the x coil at a current $I_x = 5 \text{ A}$ ($x \equiv \tilde{z}$ in this case) and $t_{rf} = 0.1 \text{ ms}$. The rf amplitude was chosen such that the π -pulse condition is almost ($\approx 0.9\pi$) met. A phase exceeding

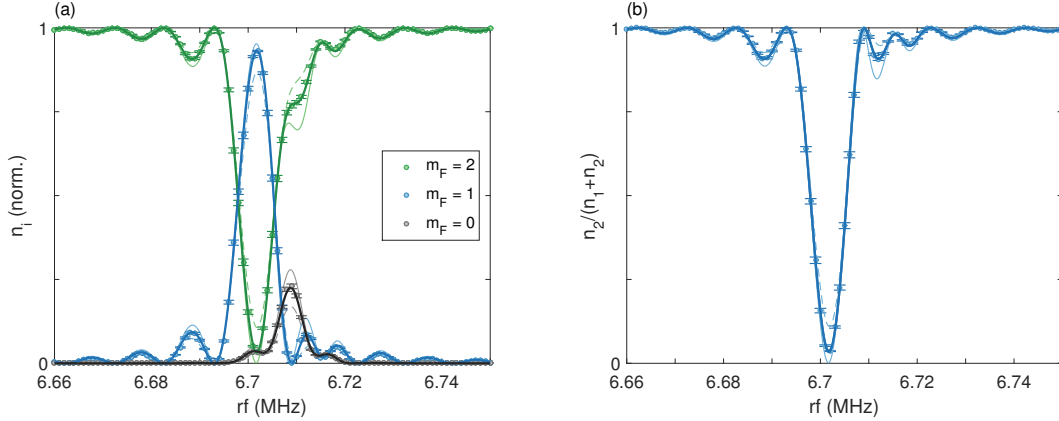


Figure 4.7: rf spectroscopy at $B = 9.61$ G ($I_x = 5$ A, 7.5 ms after switching on the coil) for $t_{\text{rf}} = 0.1$ ms at $\Omega_r \approx 2\pi \cdot 4.5$ kHz. (a) Relative populations n_2 (green), n_1 (blue) and n_0 (black) of the magnetic substates $m_F = 2, 1$ and 0 after the interaction with the rf field. n_{-1} and n_{-2} can be neglected here. Solid thick lines are numerical solutions of the time dependent Schrödinger equation for the complete five-level system with $\Omega_r = 2\pi \cdot 4.5$ kHz. Thin lines are simulations with $\Omega_r = 2\pi \cdot 4$ kHz (dashed) and $\Omega_r = 2\pi \cdot 5$ kHz (solid). (b) Renormalized relative population difference for $m_F = 2$ and 1 only.

π makes the identification of the resonance frequency unnecessarily complicated, because it is no longer at the minimum of n_2 . On the contrary, smaller values exhibit a reduced contrast. Figure 4.7(a) shows data points measured with thermal atoms for the substates $m_F = 2, 1$ and 0 . The population of the remaining two states is below 0.5% and not shown. The solid thick lines show numerical solutions of the time dependent Schrödinger equation using the Hamiltonian from Eq. (4.37) and $\Omega_r = 2\pi \cdot 4.5$ kHz. The solid (dashed) thin lines show the effect of a Rabi frequency that is higher (lower) by $2\pi \cdot 0.5$ kHz. A nice visualization of the Rabi oscillations in this five level system is made available under this <http://bit.ly/2x0LRbI> alias link.

In practice, it is sufficient to consider the substates $m_F = 2$ and 1 only. A renormalized relative population difference can be defined as $n_2/(n_1 + n_2)$ and is shown in Fig. 4.7(b). Its minimum coincides with the minimum of n_2 in Fig. 4.7(a) at 6.7017 MHz. The numerically simulated data had to be shifted by 6.7023 MHz to transform the Δ_r -basis (detunings around zero) into the rf basis, that is, the actual radio frequency [see Eq. (4.38)]. The difference of approximately 0.6 kHz is the Δ_{error} in Fig. 4.4(a) ($\Omega_r/B^2 \approx 0.049$ kHz/G²).

Measurement of the Rabi frequency

The radio frequency is generated by a NI 5421 arbitrary waveform generator (AWG). Its output amplitude depends on the load and is specified to $12 V_{\text{p-p}}$ into a 50Ω load. The actual current through the rf antenna is also affected by its complex impedance that is in turn dependent on the cables, connectors, vacuum feedthrough and finally the antenna itself. Furthermore, the amplitude of the oscillating rf field is highly

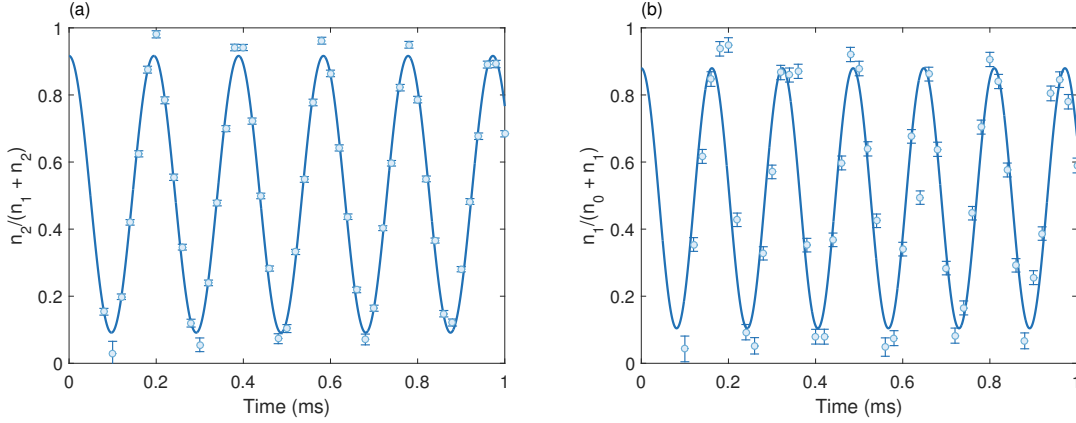


Figure 4.8: Rabi oscillations at $B = 9.61$ G ($I_x = 5$ A) resonant to the (a) $m_F = 2 \leftrightarrow 1$ transition with $\Omega_{2,1} = 2\pi \cdot 5140(5)$ Hz and (b) to the $m_F = 1 \leftrightarrow 0$ transition with $\Omega_{1,0} = 2\pi \cdot 6171(19)$ Hz. For (b), a π -pulse was applied to prepare the atoms in $m_F = 1$. The data points in (a) were averaged ten times. In contrast, no averaging was applied in (b).

position dependent. At least it is proportional to the AWG's output amplitude which can be controlled by the product of two control parameters: a global gain (range: $[0,5]$) and a relative rf amplitude (range: $[0,1]$). The available amplitude is never a real limitation in Q-2. The card is operated at 70% of its maximum output amplitude at the beginning of the evaporative cooling and below afterwards. For ARP and all remaining measurements presented in this chapter, significantly lower values are sufficient. For instance, the data points in Fig. 4.7 were taken at a relative amplitude of 0.09 and the same global gain, which cannot be changed within a measurement sequence. Since these parameters are highly device- and even sequence-specific, the Rabi frequency is used as a figure of merit.

In principle, rf spectroscopy can be used to measure Ω_r as well. However, it is inferior to a simple tracking of Rabi oscillations in precision and measurement effort. An example measurement using Rabi oscillations resonant to the $m_F = 2 \leftrightarrow 1$ transition at $\Omega_{2,1} = 2\pi \cdot 5140(5)$ Hz is shown in Fig. 4.8(a). Accounting for the systematics in Fig. 4.4(b) yields $\Omega_r = 2\pi \cdot 5273(5)$ Hz. Alternatively, the $m_F = 1 \leftrightarrow 0$ transition can be used to measure $\Omega_{1,0}$, yielding $\Omega_r = 2\pi \cdot 5279(16)$ Hz [Fig. 4.8(b)]. Both measurements were performed with the same rf amplitude (0.1 relative amplitude) and their results are consistent. For (b), a π -pulse was necessary to prepare the atoms in the $m_F = 1$ substate. For this reason, the more direct measurement shown in (a) is generally used to determine Ω_r .

In general, the frequency accuracy of a sinusoidal fit can be improved by lengthening the time interval of the measurement. However, this will not be the case if the Rabi or resonance frequency changes with time of flight. As will be shown later, this is actually the case. The alternative is averaging, provided that the system is stable enough. For illustration, the data points in Fig. 4.8(a) were averaged ten times while no averaging was performed in (b). Rabi decay, as can also be anticipated in (a), will be discussed in more detail in due course.

Magnetic field stability

The magnetic field is not stable during the available TOF of 22 ms for several reasons. First of all, the coil's step response to a certain current request [see Fig. 3.3(a)] is an obvious and dominant contribution. This is superimposed with a magnetic field gradient the atoms are falling through. Furthermore, the field can change due to a heating of the experiment (e.g., reference resistors in current drivers) during a long series of measurements. An example of the field dynamics after switching the x coil to 5 A is shown in Fig. 4.9. Each data point is acquired by rf spectroscopy similar to Fig. 4.7(b) at a time resolution of 0.1 ms. Data points were measured 'from left to right' with three averages revealing a systematic drift saturating during the first run (Series 1). Within the first 6 ms after switching on the coil, the variations are even stronger.

A discrimination between switching dynamics and TOF contributions to the resonance drift is possible by delaying the switching of the coil. Still, this information is of no practical interest unless it leads to a plainer time dynamics. Such a compensation is a highly nontrivial affair and would work for one specific configuration and measurement only. Hence it is reasonable to have a look at the actual requirements. For ARP it is sufficient, if at all necessary, to account for the different start and stop frequency as long as the variations are small compared to the sweep rate α . Although a thorough quantitative discussion is reserved for the following section, a brief estimate shall be given here. According to Fig. 4.3(a) the minimum frequency sweep has to be larger than 20 kHz for all Ω_r at this particular magnetic field. Hence, the requirement $201 \text{ Hz/ms} \ll 20 \text{ kHz}/6 \text{ ms}$ is clearly fulfilled in the linear regime ($8 \text{ ms} < t < 14 \text{ ms}$). However, the situation is different at the beginning, when the resonance frequency changes more quickly. For a characterization of the system, for example the decoherence time, Rabi decay time or Rabi frequencies, it is important to maintain $\Delta_r = \text{constant}$ for as long as possible.

In the time interval $7 \text{ ms} < t < 14 \text{ ms}$ the magnetic field is stable up to $\pm 1 \text{ mG}$. This is equivalent to a relative stability of the magnetic field and thus the resonance frequency on the low 10^{-4} -level, but its variations are on the same order of magnitude as Ω_r . Hence, the detuning has to be kept constant by sweeping the radio frequency along with the resonance frequency. With this strategy, the stability of the magnetic field is sufficient.

Ω_r versus time of flight

During the free fall of an atomic ensemble, its distance to the rf antenna changes. For this reason, the amplitude of the rf field and accordingly Ω_r change, too. Its time dependence can be measured by tracking resonant Rabi oscillations for a long enough time ($m_F = 2 \leftrightarrow 1$). For this purpose, the results from the previous measurement can be exploited by switching the x coil in the same way. The rf is linearly swept along with the resonance as shown by the black line in Fig. 4.9. Warm-up is realized by performing 30 averages and neglecting the first ten, disregarding a similar number (≈ 2400) of data points as in Series 1. Figure 4.10 shows the results using BECs.

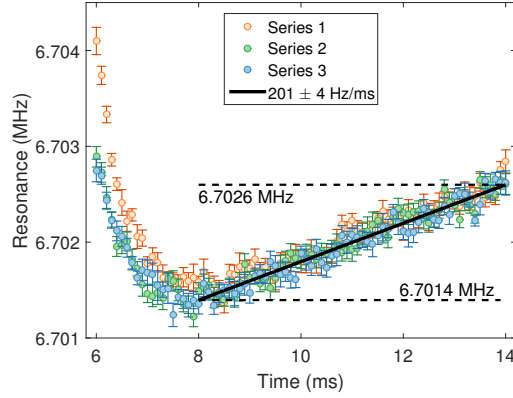


Figure 4.9: Resonance frequency of the $m_F = 2 \leftrightarrow 1$ transition as a function of the time after switching the x coil to 5 A. Three measurement series were performed, each starting at 6 ms. Between 8 and 14 ms the resonance frequency changes linearly with time at a rate of $201(4)$ Hz/ms.

The most prominent feature is the decreasing amplitude. This Rabi decay is rather linear than exponential. The latter would be expected if pure T_2 dephasing was the cause. This can be understood by inspecting Eq. (4.19) and interpreting the Rabi oscillation as a consecutive chain of π -pulses in a spin-echo measurement. A possible cause of the observed decay is a spatial gradient in the rf amplitude. The atoms' free fall would map this into a time dependent Rabi frequency $\Omega_r(t)$. The spatial gradient and its relation to Rabi decay will be discussed in more detail below.

Knowing $\Omega_r(t)$ is of particular importance for many of the following measurements. It can be extracted by fitting the data to a sinusoid of, in this case, linearly increasing frequency and decreasing amplitude. Quadratic terms were not necessary, even though they might be expected due to the accelerated motion of the atomic ensemble. The outcome of this fit is

$$\Omega_{2,1}(t) = 2\pi \cdot [4465(4) \text{ Hz} + 82(1) \text{ Hz/ms} \cdot (t - 8 \text{ ms})], \quad (4.43)$$

where the errors are the fit uncertainty and t is the time after switching the x coil to 5 A. This time t is equivalent to the TOF, because the coil was switched on immediately after release of the atoms from the trap.

The ratio $\Omega_{2,1}(t)/\Omega_r(t)$ is not constant, because it depends on Ω_r [see Fig. 4.4(b)]. However, these corrections can be neglected here and the ratio is assumed to be 0.98 for all t , resulting in

$$\Omega_r(t) = 2\pi \cdot [4556(5) \text{ Hz} + 83(1) \text{ Hz/ms} \cdot (t - 8 \text{ ms})]. \quad (4.44)$$

Although extensive care was taken to assure that the resonance condition is fulfilled during the entire scan, the center of the Rabi oscillation is found at $0.427(3)$ and not 0.5. A mismatch of 1.85 kHz would be necessary to explain this in terms of a detuning. If this were the case, Ω_r would be overestimated by 8%. Such a detuning

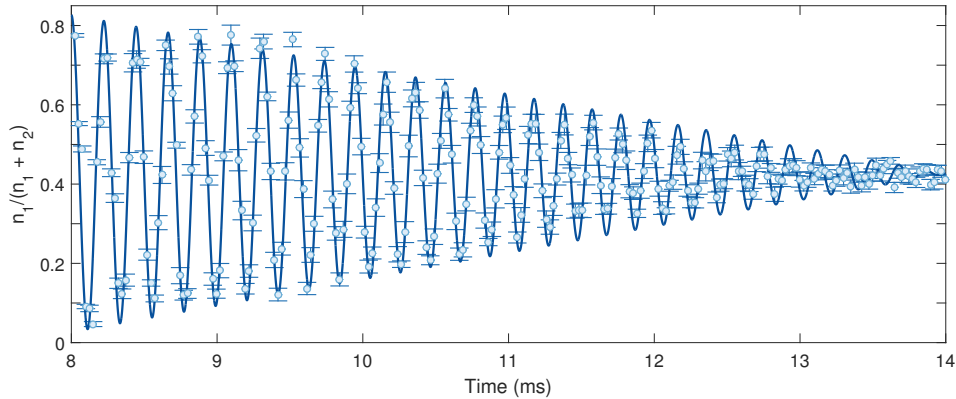


Figure 4.10: Rabi oscillations ($m_F = 2 \leftrightarrow 1$) with the rf set to the linearly increasing resonance frequency as shown by the solid black line in Fig. 4.9. The solid blue line in this figure shows a fit with a linearly increasing frequency and linearly decreasing amplitude to measure the time dependence of the Rabi frequency.

is in considerable disagreement with other measurements (e.g., Fig. 4.8) and can be ruled out by Fig. 4.9. A possible explanation for the observed shift might be magnetic field fluctuations in a frequency range close to the Rabi frequency, which would be hardly resolvable by the methods shown before.

Measurement of T_2 using spin-echos

This part is devoted to giving an estimate of the transverse coherence time T_2 using the spin-echo method described in the previous section. The limiting factor is the accuracy and stability of the rf pulses for spin-manipulation (π and $\pi/2$). For this reason, $n = 1$ is chosen as the simplest possible case. Obviously, not all fluctuations are removed by this scheme. Hence, the resulting estimate on T_2 has to be interpreted as a lower limit.

Again, advantage is taken of the linear part between 8 and 14 ms found in Fig. 4.9, since all pulses have to be on-resonance. Six τ -values $\{1, 2, 3, 4, 5, 6\}$ ms are used for the measurement with the π -pulse being applied at $\tau/2$. At the end, a $\pi/2$ -pulse is required to transform back into the measurement basis. Unlike in NMR, the echo does not ‘automatically’ appear. Since these pulses limit the accuracy, the final pulse is replaced by a short Rabi scan. Its contrast is a more robust measure for the echo amplitude. The results over fifteen averages after a warm-up are shown in Fig. 4.11 by the blue data points. For direct comparison, a reference measurement is performed omitting the π -pulse (orange data points). The solid lines are sinusoidal fits of the respective data sets.

The effect of the refocusing pulse is clearly visible for $\tau = \{1, 2, 3\}$ ms, even though the contrast has hardly decayed during the first millisecond. It is interesting to inspect the last two subplots: The contrast increases again. This is a clear evidence for n being chosen too small. Furthermore, Carr and Purcell [151] have shown that in the case of convection through a magnetic field gradient within liquid NMR

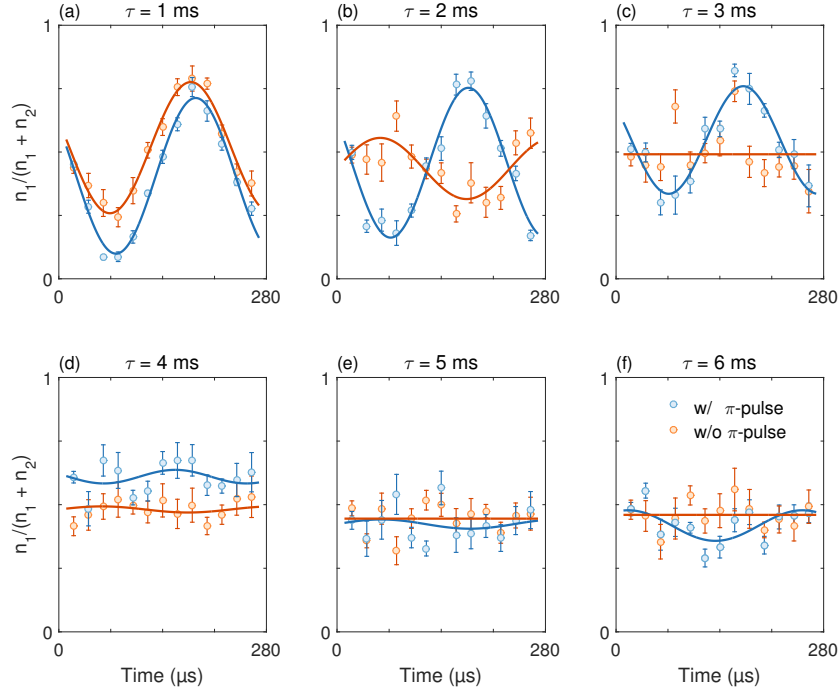


Figure 4.11: Comparison of the renormalized relative population difference ($n_1/(n_1+n_2)$) after a spin-echo measurement with $n = 1$ (blue points) to the same measurement without the π -pulse at $\tau/2$ (orange points). The contrast of the final Rabi oscillation, as fitted by the respective solid lines, is taken as the echo amplitude for Fig. 4.12. The six subplots show the data for $\tau = \{1, 2, \dots, 6\}$ ms.

samples, odd-numbered echos are partially suppressed. Drawing the parallel to the free fall through such a gradient, these results are applicable to Q-2 as well, despite the acceleration. Hence, using $n = 2$ might be worth trying.

By definition, the maximum possible contrast is unity. In practice, it can be defined as the contrast of a plain Rabi oscillation as shown in Fig. 4.8(a). It is 0.83(2) in that case. This value is taken as the echo amplitude at $t = 0$. Figure 4.12 shows this reference echo amplitude (black point) together with the fit results of Fig. 4.11 using the same color-code. The finite length of the rf interaction is accounted for by an offset of 0.13 ms between the data points and the corresponding values of τ . The black point is common to both data sets. It is considered in the exponential fits using the model defined by Eq. (4.19). The solid orange line as well as the dashed blue line include all data points of the respective set. A better estimate of T_2 is found when neglecting the last three data points (solid blue line) of the blue set. This can be justified with the previously mentioned problems using $n = 1$ and the fact that the result has to be interpreted as a lower limit anyway. Hence, the result of this measurement is

$$T_2 \geq 5 \text{ ms.}$$

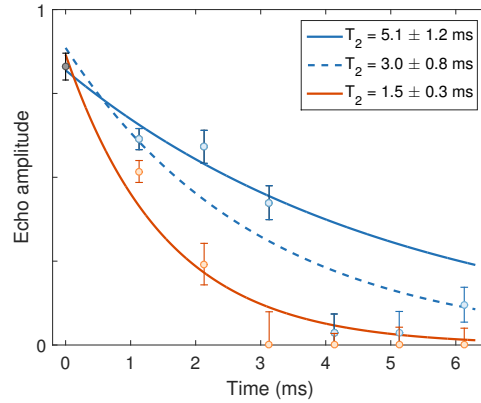


Figure 4.12: Spin-echo amplitudes from Fig. 4.11 defined as the fitted contrast of the respective final Rabi oscillation (blue points). The orange points represent the reference measurement without the π -pulse at $\tau/2$. The black point at $t = 0$ is a reference contrast of 0.83 common to both data sets. The difference between abscissa- and τ values (0.13 ms) accounts for the finite pulse lengths. Solid lines are exponential fits [see Eq. (4.19)] of the single black and all orange data points (orange line) or all blue data points (dashed blue line). For the solid blue line, the last three (blue) data points were neglected.

Measurement of rf gradients

The Rabi decay in Fig. 4.10 was previously explained with a gradient of the rf amplitude, but no proof or further explanation was given so far. This is rectified using thermal atoms now. They are more sensitive to spatial gradients due to the larger size of the atomic ensemble. The atoms are coupled to an rf field at 6.702 MHz for $10 \text{ ms} \leq t \leq 10.5 \text{ ms}$ after release. The same quantization field is used as before ($I_x = 5 \text{ A}$, c.f. Fig. 4.9). State separation is accomplished by a subsequent SG experiment. The final rf cut of evaporative cooling is chosen such that the substates are still separable in the remaining TOF but as large as possible (1.69 MHz instead of 1.572 MHz for an almost pure BEC). This measurement is performed for 1001 equally spaced values of the relative rf amplitude between 0 and 1. Since the frequency error nonlinearly depends on this amplitude, it cannot be compensated for during the measurement. Its relative effect is small for large rf amplitudes and tolerated for small ones.

In the case of a spatially homogeneous amplitude, all atoms undergo collective Rabi oscillations at the same frequency, amplitude and phase. In the presence of spatial gradients, different points in the cloud have a different Rabi frequency. This leads to a dephasing across the atomic ensemble as illustrated by Fig. 4.13. Initially, at $\Omega_{2,1} = 0$, all atoms are in the substate $m_F = 2$ (top leftmost subimage). The density profile is purely Gaussian, as shown in the integrated column density plot below the absorption image. The dashed black line is an imaginary dividing rule between the two substates. An integration of the normalized density profile over the part right of the line yields $n_2/(n_1 + n_2)$. During the first two Rabi cycles, corresponding to $\Omega_{2,1} \leq 2\pi \cdot 4 \text{ kHz}$, a reduced contrast is observed because of the large detuning ($\approx 1 \text{ kHz}$) relative to $\Omega_{2,1}$. At larger Rabi frequencies, for example,

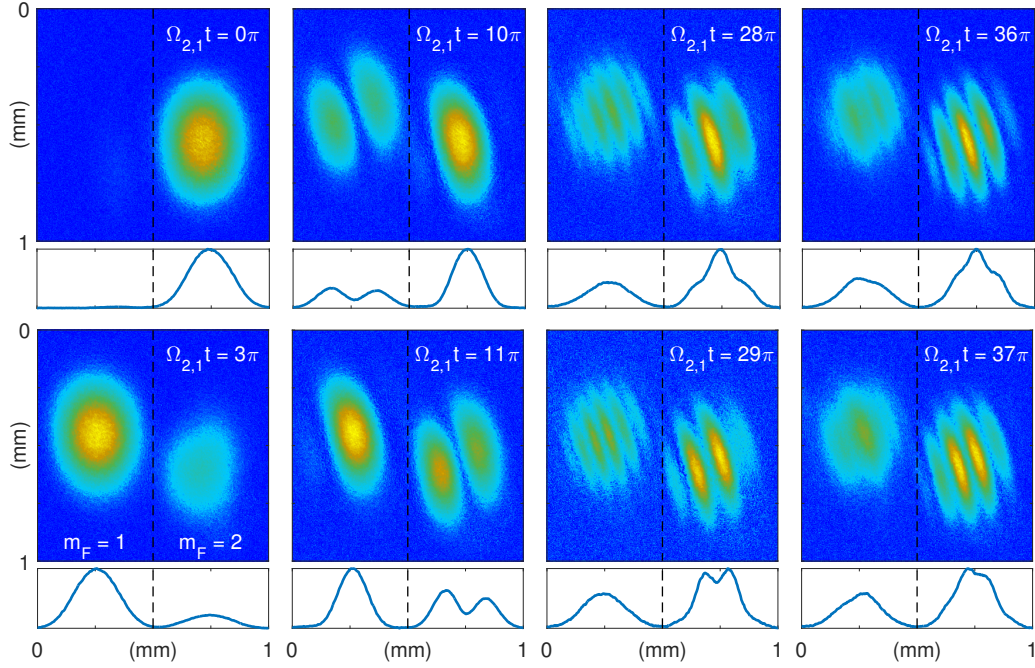


Figure 4.13: Absorption images of the $m_F = 2$ and 1 substates of a thermal cloud after coupling to an rf field for 0.5 ms. The images were measured with different rf amplitudes. The Rabi phase $\Omega_{2,1}t$ at the cloud center (same for both substates) is shown. The dashed black lines show an imaginary dividing rule between the substates. The smaller plots show the integrated column density of the respective absorption images. These density profiles are renormalized by $n_1 + n_2$.

at $\Omega_{2,1}t = 10\pi$ (second subplot in top row), the central part of both clouds has undergone five complete Rabi cycles. However, the two subclouds in $m_F = 1$ reveal a slightly different phase at off-center positions. The stripe moves from the bottom left of the cloud to the top right when increasing the Rabi frequency. Hence, the top right part lags in phase while the bottom left is ahead. In the image right below, the phase has evolved by another π . The dominant fraction should be in $m_F = 1$ now, but the density profiles already show the significantly reduced contrast of the renormalized relative population difference.

When the phase difference across the cloud exceeds 2π , more than one stripe is visible. The separation between two adjacent minima within the $m_F = 2$ cloud is a measure for the spatial gradient of the Rabi frequency. The spatial frequency within the $m_F = 1$ cloud is higher, which is evident in the third column of Fig. 4.13. This is because of the three more substates ($m_F = 0, -1, -2$) being off-resonantly coupled. In fact, all substates are populated at high Rabi phases (not shown). It should be stated very clearly at this point, that the observed structure is no interference.

The observed stripes are actually three dimensional slices. It is in no way obvious that they are visible at all. The detection axis has to be parallel to the slices. Orthogonally detected, the structure would be invisible. Still, this orientation is not a coincidence, because the detection axis is parallel to the chip surface. Since the rf source is part of the atom chip, the rf amplitude is expected to decline with

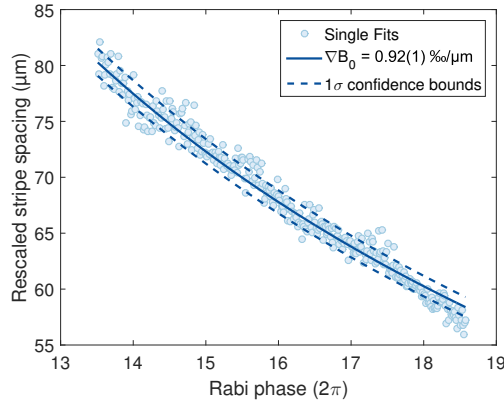


Figure 4.14: The data points show the stripe spacing as a function of the Rabi phase within the $m_F = 2$ cloud as exemplarily illustrated in the rightmost four subfigures of Fig. 4.13. The values are rescaled to account for the expansion between rf interaction and detection. (solid line) Fitted stripe spacing corresponding to a relative rf gradient of $\nabla B_0 = 0.92\text{‰}/\mu\text{m}$. (dashed lines) Confidence bounds (1σ) of fit.

increasing distance from the chip, that is located at the left of the absorption images.

The stripes are inclined by approximately 18° ($\pm 2^\circ$) towards the left. During the rf interaction the atoms are at $y \approx 240\ \mu\text{m}$ and $z = 807\ \mu\text{m}$ in capsule coordinates. The falling distance during the 0.5 ms of rf interaction is $\Delta y \approx 50\ \mu\text{m}$. Hence, the atoms are approximately on the same height as the horizontal part of the lower rf-U (inverted ‘U’). Having said that, the inclination of the stripes indicates that the effective rf source is below. The reason could be the remaining conductors of the rf-U, for instance, the vertical parts. Actually, the vacuum chamber itself and the magnetic shielding around might have an effect on the near-field structure of the rf amplitude as well ($\lambda \approx 45\ \text{m}$ at 6.7 MHz). The rightmost four images in Fig. 4.13 also exhibit a small curvature. The radius is approximately 2 mm and in reasonable agreement with the distance to the BC-layer of the atom chip.

The stripe pattern is imprinted onto the cloud during the rf interaction. The average Gaussian width is $\sigma_{\text{rf}} = 53\ \mu\text{m}$ at this time. Until detection, the cloud has expanded further to $\sigma_{\text{det}} = 94\ \mu\text{m}$. To extract the rf gradient from the stripe spacing, it has to be multiplied by the size ratio $\sigma_{\text{rf}}/\sigma_{\text{det}}$. This rescaled stripe spacing is shown in Fig. 4.14. The single data points represent fits of a sinusoidally modulated Gaussian to the density profile of the rotated absorption images (such that the stripes are vertically aligned).

Since the total phase at cloud center is known, the rf gradient can be fitted to the data points. It is $\nabla B_0 = 0.92(1)\text{‰}/\mu\text{m}$ and shown by the solid line. The dashed lines show the 1σ confidence bounds of the fit.

The practical use of the gradient’s precise value is rather limited, because it is valid for only one specific position within the vacuum chamber. Nevertheless, the gain is twofold. First of all, it provides at least a rough estimate of the Rabi frequency at positions inaccessible in ground-based measurements. This is a valuable information in microgravity campaigns. Second, it can be used to explain the Rabi

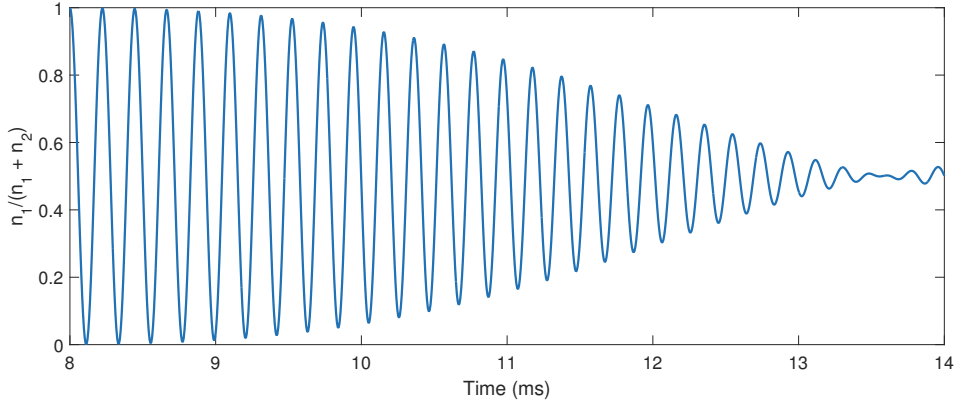


Figure 4.15: Simulation of the Rabi decay in Fig. 4.10 assuming a relative rf gradient of $\nabla B_0 = 0.92\ \%/ \mu\text{m}$ as the sole cause.

decay measured in precisely this region of space, for example, the one in Fig. 4.10. The BEC had been released from an $\omega_y \approx \omega_z \approx 2\pi \cdot 60\ \text{Hz}$ trap (strong axes). The resulting expansion can be linearly approximated for this purpose. The Thomas-Fermi radius increases from $16.7\ \mu\text{m}$ to $29.2\ \mu\text{m}$ within the 6 ms of scan time. Stripes, like the ones in Fig. 4.13, are not visible in the absorption images of a BEC because they cannot be resolved by the detection system. When taking into account this time dependent cloud size in combination with $\Omega_{2,1}(t)$ and ∇B_0 , the expected renormalized relative population difference can be calculated as a cloud average. The result is shown in Fig. 4.15. Its envelope is indeed strikingly similar to the data in Fig. 4.10, except for the reduced initial contrast. Hence, the primary cause of this decay is not decoherence. However, this does not exclude smaller contributions of correspondingly larger values of T_2 . It should be mentioned in this context, that the expected exponential (resonant) Rabi decay constant is $2T_2$. This can be understood because transverse decoherence is only effective in the $x - y$ plane of the Bloch sphere.

4.4 Adiabatic rapid passage in ^{87}Rb

An adiabatic rapid passage can be realized between any two Zeeman states of a hyperfine manifold, but the $m_F = 2 \rightarrow 0$ transfer, which was visualized by the black arrow in Fig. 4.3(a), is of special interest as explained above. A big difference compared to ARP in a two-level system is the passage through two avoided crossings. The accompanying adiabatic losses are well understood by means of the dressed state Hamiltonian and the Landau-Zener formula. These losses are confirmed by reverse rf sweeps in the first subsection. These measurements also give rise to an alternative scheme for ARP compared to the conventional one mentioned above. Afterwards, a model function for the ARP efficiency is defined which summarizes all loss channels. Temporarily, the decoherence rate $1/T_2$ will be assumed to vanish, which effectively eliminates the rapidity criterion. The implications for the ARP efficiency in Q-2 are discussed. These predictions are compared to experimental results from ground-

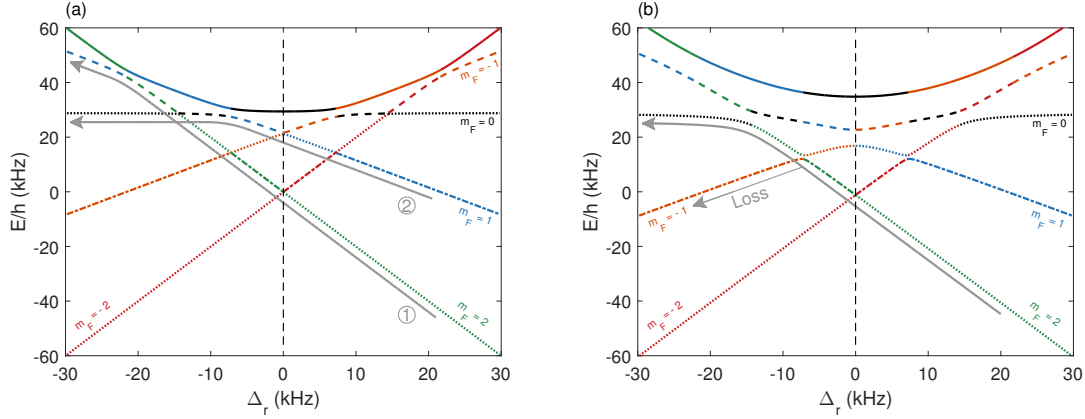


Figure 4.16: Reprint of Fig. 4.3 to illustrate reverse ARP. In (a) reverse ARP is performed by two successive sweeps first from $m_F = 2 \rightarrow 1$ ① and then from $m_F = 1 \rightarrow 0$ ②. At higher Rabi frequencies, for example at $\Omega_r = 10$ kHz in (b), compared to $\Omega_r = 2.5$ kHz in (a), a direct sweep from $m_F = 2 \rightarrow 0$ is possible. Losses can occur at each crossing and are exemplarily highlighted for the $m_F = 2 \leftrightarrow -1$ crossing in (b).

based measurements and are applied to measurements in microgravity. The effect of a finite T_2 is discussed and quantified. Finally, a mitigation strategy for transverse decoherence is presented.

Landau-Zener losses and reverse ARP

The dressed energy eigenstates in Fig. 4.3 also allow for reverse rf sweeps, that is, from positive to negative detunings, as illustrated in Fig. 4.16(a). This reverse passage starts in $\Psi_i = |2\rangle$ and transiently ends in $\Psi_i = |1\rangle$. Afterwards, it has to be repeated with $\Psi_i = |1\rangle$ to finally end up in $\Psi_i = |0\rangle$. Its advantage is the better final overlap P_f , which is indeed the dominant limitation for the conventional ARP. In a reverse ARP, P_f can be increased simply by sweeping further.

The losses due to the passage through an avoided crossing region are quantified by the Landau-Zener formula [see Eq. (4.11)]. It was stated for a two-level system where the Rabi frequency is identical to the separation of the dressed energy eigenstates (the factor \hbar is omitted here). In the five-level system, Ω_r has to be substituted in Eq. (4.11) by the corresponding minimum energy differences $\Omega_{i,j}$ at the crossings $m_F = i \leftrightarrow j$. $\Omega_{i,j}$ are the observable Rabi flopping frequencies while Ω_r is the value in the Hamiltonian. At low rf amplitudes, the only nonzero values of $\Omega_{i,j}$ are those with $\Delta m_F = 1$. However, this limitation breaks down for higher rf amplitudes. It is shown in Fig. 4.16(b) with clearly visible $\Omega_{2,0}$, $\Omega_{1,-1}$ and $\Omega_{0,-2}$. Thus, an adiabatic passage is possible at each of the ten crossings of the manifold. In this regime, a direct reverse passage from $m_F = 2 \rightarrow 0$ is feasible, as illustrated by the thick gray arrow in Fig. 4.16(b).

The Landau-Zener losses occurring at the crossings relevant for reverse ARP when sweeping with $\alpha = -2\pi \cdot 25$ kHz/ms at $B = 9.61$ G are shown in Fig. 4.17. The rf sweep started at $\Delta_r = 2\pi \cdot 50$ kHz, in other words, sufficiently far away from the $m_F = 2 \leftrightarrow -2$

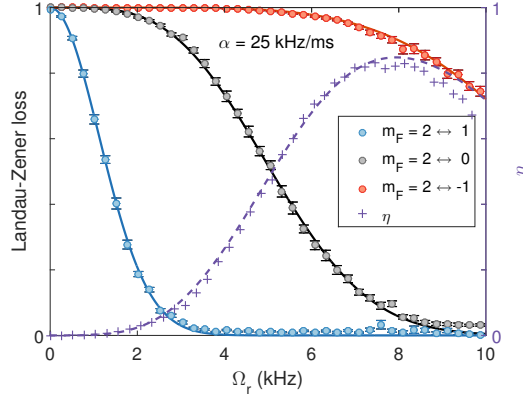


Figure 4.17: Landau-Zener losses at the crossings of the $m_F = 2$ substate (in diabatic notation) with $m_F = 1$ (blue), $m_F = 0$ (black) and $m_F = -1$ (orange) when sweeping the detuning from $\Delta_{r,i} = +2\pi \cdot 50$ kHz to $\Delta_{r,f} = -2\pi \cdot 75$ kHz within 5 ms ($\alpha = 2\pi \cdot 25$ kHz/ms). The solid lines are numerical calculations using the previously measured $\Omega_r(t)$. Purple ‘+’-signs show the fraction in $m_F = 0$ after the passage (η , right axis). The dashed purple line shows the expected η according to the calculated Landau-Zener losses.

crossing, and subsequently passed the crossings with all other substates. It finally ended at $\Delta_r = -2\pi \cdot 75$ kHz approximately $2\pi \cdot 55$ kHz to the left of the $m_F = 2 \leftrightarrow 1$ crossing.

Initially, all atoms are in $\Psi_i = |2\rangle = |\varphi_1\rangle$. After passing the first crossing ($2 \leftrightarrow -2$), they are almost completely lost into $|\varphi_2\rangle$ (dash-dotted line) for $\Omega_r \leq 2\pi \cdot 10$ kHz. The tiny fraction remaining in $|\varphi_1\rangle$ (lower dotted line) will end up in $m_F = -2$ after the sweep. The atoms in $|\varphi_2\rangle$ are then available to probe the next crossing ($2 \leftrightarrow -1$) and so forth.

The solid lines in Fig. 4.17 are no fits, but calculated from the Landau-Zener formula. The corresponding Rabi frequencies $\Omega_{i,j}$ were obtained by diagonalizing the Hamiltonian and determining the respective local minimum energy differences at the previously measured $\Omega_r(t)$. For crossings with $\Delta m_F \neq 1$, the value of α has to be adapted accordingly, because the time derivative of the energy difference is the figure of merit [146]. It is equal to the rf sweep rate for $\Delta m_F = 1$ only.

For the first part of the reverse ARP outlined before [① in Fig. 4.16(a)], it is required to have almost full losses at all crossings except at $m_F = 2 \leftrightarrow 1$, where the losses should be close to zero. As shown in Fig. 4.17, there is no Ω_r satisfying this condition. In fact, the relation of the $\Omega_{i,j}$ is such that a reverse ARP can be done directly at $\Omega_r = 2\pi \cdot 8$ kHz, although with a moderate efficiency of approximately 80% only. The purple plus signs show the measured fraction in $m_F = 0$ after the passage. The dashed purple line is the expected reverse ARP efficiency according to the calculated Landau-Zener losses.

In a conventional ARP, the passage has to be adiabatic with respect to the $m_F = 2 \leftrightarrow 1$ crossing. The adiabaticity criterion is then automatically fulfilled for the $m_F = 1 \leftrightarrow 0$ crossing, because $\Omega_{1,0} > \Omega_{2,1}$. The rapidity criterion is exclusively determined by decoherence, which is neglected momentarily. In contrast, the

relations are more complex in reverse ARP. The passage has to be adiabatic with respect to the $m_F = 2 \leftrightarrow 0$ crossing, but also rapid with respect to $m_F = 2 \leftrightarrow -1$. This interplay is unsatisfactorily fulfilled in the example shown. Moreover, it is qualitatively unchanged in a wide range of magnetic fields and sweep rates. The advantage of reverse ARP is its immunity against magnetic field changes, because the sweep range can be extended to account for such fluctuations or uncertainties.

The ARP model and its numerical solutions

Equation (4.22) can be applied to ^{87}Rb now. P_{ad} splits up into two factors for the individual crossings. The respective Rabi frequencies $\Omega_{2,1}$ and $\Omega_{1,0}$ shown in Fig. 4.4(b) have to be used in Eq. (4.12). They are a function of Ω_r/B^2 alone. The final overlap P_f [see Eq. (4.42)] was shown in Fig. 4.6 to depend solely on Ω_r/B^2 , too. Unfortunately, the initial overlap does not scale like this and the matrix element in Eq. (4.41) has to be calculated numerically. Assuming $\Pi = 1$, the total ARP efficiency is:

$$\eta(\Delta_{r,i}, B, \Omega_r, \alpha) = |\langle \varphi_5 | 2 \rangle|^2 \left[1 - \exp\left(-\frac{\pi\Omega_{2,1}^2}{2|\alpha|}\right) \right] \left[1 - \exp\left(-\frac{\pi\Omega_{1,0}^2}{2|\alpha|}\right) \right] P_f(\Omega_r/B^2), \quad (4.45)$$

with $\varphi_5(\Delta_{r,i}, \Omega_r, B)$ and $\Omega_{i,j}(\Omega_r/B^2)$. The sweep rate α [see Eq. (4.10)] simplifies to

$$\alpha = \Delta_{r,i}/\tau, \quad (4.46)$$

because $\Delta_{r,f} = 0$. τ is the total sweep time of the ARP. Hence, the problem is four-dimensional. The function in this form has no maximum. For each set of values there exists another set with larger B and τ and a higher efficiency. To find useful solutions, the parameter space is restricted to fixed values of B and τ . The now existing maximum of η is then found by a numerical gradient ascent method. The code can be downloaded under the link printed in Appendix D.3. There exist no local maxima besides the global one.

If decoherence is to be accounted for in the model, the right hand side of Eq. (4.45) has to be multiplied by Π [see Eq. (4.21)] after applying it to the current problem with two crossings involved:

$$\Pi(B, \Omega_r, \alpha) = \exp\left(-\frac{3\pi\Omega_{2,1}}{8|\alpha|T_2}\right) \cdot \exp\left(-\frac{3\pi\Omega_{1,0}}{8|\alpha|T_2}\right). \quad (4.47)$$

This does not change the dimensionality of the problem, because T_2 is no parameter. Still, the peak efficiency is reached at a finite τ for a given B .

Figure 4.18(a) shows the maximum possible ARP efficiency for magnetic fields ranging from 5 G to 30 G and a set of four different ARP times. Every point in this plot has its own $\Delta_{r,i}$ and Ω_r found by the gradient ascent method to maximize η . They are shown in Figs. 4.18(c) and (d). The initial detuning is dominated by the quadratic Zeeman shift of the $m_F = 2 \leftrightarrow 1$ crossing. Deviations from this parabolic shape are of the order of the Rabi frequency and not visible in the plot. It is obvious

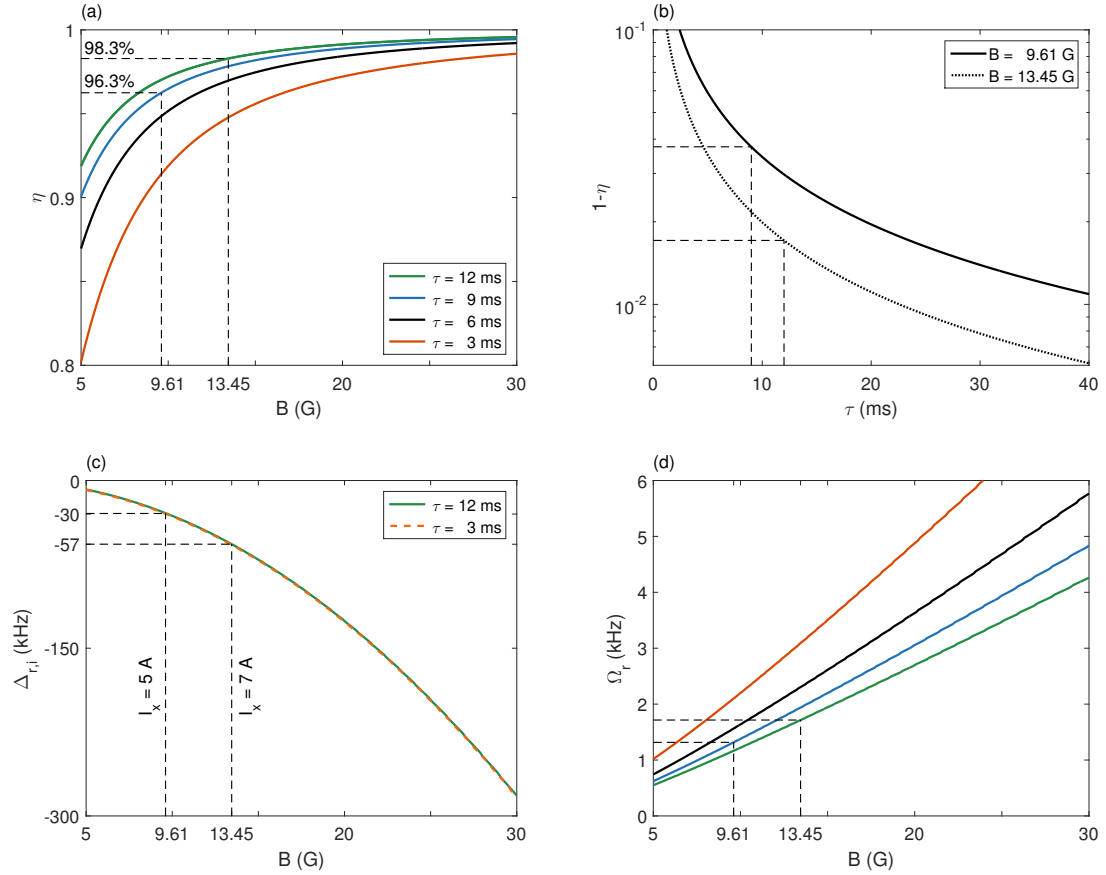


Figure 4.18: (a) Numerical simulations of the maximum possible ARP efficiency η as a function of the magnetic field for ARP times $\tau = 12$ ms (green), 9 ms (blue), 6 ms (black) and 3 ms (orange). Two parameter sets are highlighted by dashed black lines. They are $\tau = 9$ ms at $B = 9.61$ G ($I_x = 5$ A) and $\tau = 12$ ms at $B = 13.45$ G ($I_x = 7$ A). Their corresponding efficiency is 96.3% and 98.3%, respectively. (b) Dependence of $1 - \eta$ on τ for fixed B . Initial detuning $\Delta_{r,i}$ (c) and Rabi frequency Ω_r (d) corresponding to the optimum efficiency values in (a).

that the efficiency can be increased using longer τ in the absence of decoherence. The necessary Rabi frequency for comparable or even reduced adiabatic losses is lower, which improves P_f . Figure 4.18(b) shows examples for $B = 9.61$ G and $B = 13.45$ G, corresponding to $I_x = 5$ A and $I_x = 7$ A, respectively. The dependence on B is not that obvious. On the one hand a larger magnetic field increases the separation between the two central crossings (upper dressed state). On the other hand, the sweep range has to be extended. This in turn requires higher Rabi frequencies that counteract the acquired increase of P_f in return. It turns out that the net effect of a larger field is still positive. Hence, as far as the ARP efficiency is concerned and decoherence is neglected, B and τ should be as large as possible.

For ARP in Q-2, $I_x = 5$ A is chosen ($B = 9.61$ G). This is the maximum current which can be generated reproducibly on batteries. Both remaining coils imprint a large momentum on the atomic ensemble when the current is switched (see Fig. 3.5

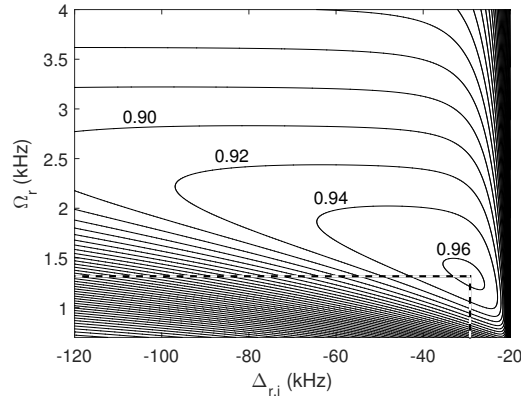


Figure 4.19: Contour lines of ARP efficiency η as a function of detuning $\Delta_{r,i}$ and Rabi frequency Ω_r . The plotted values are numerical solutions of Eq. (4.45) for $B = 9.61$ G and $\tau = 9$ ms. The maximum efficiency is 96.25% for $\Delta_{r,i} = -2\pi \cdot 29.24$ kHz and $\Omega_r = 2\pi \cdot 1.315$ kHz (dashed line).

and Table 3.3). This alone makes them second choice. The y coil alone would not be usable anyway, because it is aligned in parallel to the oscillating magnetic field vector dressing the states. (A combination of x and y coil is possible though.) The time τ is chosen to be 9 ms. For these values, the efficiency in the vicinity of the maximum (96.3%) is shown in Fig. 4.19. It can be seen that the drop in η is more severe for too small Ω_r than it is for a too large one.

Experimental realization of ARP

The same set of parameters ($B, \tau, \Delta_{r,i}, \Omega_r$) as in Fig. 4.19 is used for an experimental realization of ARP. The transient states during ARP as well as the initial and final state are illustrated in Fig. 4.20. This surface plot visualizes the optical and hence atomic density. The magnetic substates were separated by a SG experiment, as before. The transient states are produced by adjusting the final detuning after the $\tau = 9$ ms frequency sweep. Since absorption imaging is destructive, the five rows were measured with different, newly created samples. All subimages are individually normalized. By a proper choice of the final detuning, any substate can be selected. Superpositions between neighboring states are possible, too. However, the parameter set is chosen such that it optimizes the transfer efficiency to $m_F = 0$. The bottom row of Fig. 4.20 exhibits approximately 91% in this state. The substates $m_F = -1, 1$ and 2 are only faintly populated. The $m_F = -2$ state is not populated at all during this measurement. The actual efficiency of 91% is slightly worse than the theoretically predicted value of 96%. Clearly, Ω_r is the parameter that is easiest to miss. Nevertheless, also a mutual shift of initial and final detuning can occur, for example, by a heating up of the experiment as shown in Fig. 4.9. In this case, an imbalance towards one of the neighboring substates were visible. This is not the case in Fig. 4.20.

The impact of a mismatched Rabi frequency is worth further attention because of

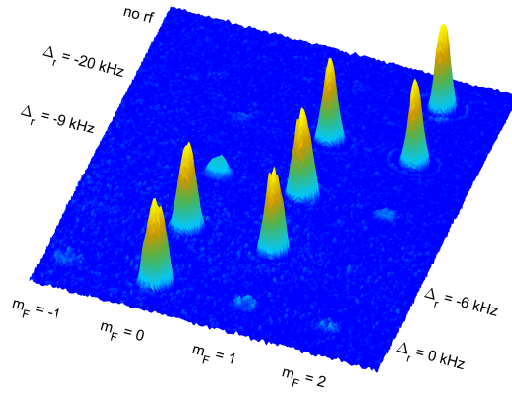


Figure 4.20: Normalized absorption images after a 9 ms ARP at $B = 9.61$ G. Without rf interaction, all atoms remain in $m_F = 2$ (top right cloud). The three middle rows show the intermediate states produced by adjusting the final detuning. The bottom row shows the final state after the ARP with $\eta \approx 91\%$. To reduce detection noise, a Gaussian filter ($\sigma = 1$ px) was applied to the absorption images.

its position-dependence (see Fig. 4.14). For this purpose, η is measured for different rf amplitudes. It is compared to the expected values in Fig. 4.21(a) (solid blue line). The efficiency peaks at $\Omega_r = 2\pi \cdot 1.3$ kHz (dashed black line), as predicted. Yet still, the measured η is systematically below the model's prediction for all Ω_r in the vicinity of the optimum. Hence, a mere mismatch of Ω_r is not responsible for the reduced efficiency. The ARP model [see Eq. (4.45)] assumes a constant Ω_r , which is only an idealized assumption [see Eq. (4.44)]. The solid blue line already takes into account this time variation by adapting the Rabi frequency for each factor. For instance, P_f is calculated using the Rabi frequency at the end of the ARP. The resulting deviation is 0.5% only and not shown in Fig. 4.21(a). The drift of the resonance frequency (see Fig. 4.9) effectively reduces the sweep rate by $2\pi \cdot 0.2$ kHz/ms (6%), because the crossings are passed at 8.5 ms (first) and 12.5 ms (second). The effect on η is a 0.2% increase and can be neglected.

It is worth discussing the different contributions to the loss $(1 - \eta)$ on this measurement, as shown in Fig. 4.21(b). The solid line corresponds to the solid line in Fig. 4.21(a) while the straight dotted lines indicate the loss at constant Rabi frequency. It is no surprise that the Landau-Zener losses are dominated by the first crossing ($m_F = 2 \leftrightarrow 1$) because of its smaller Rabi frequency. The initial overlap is negligible, provided that $\Delta_{r,i}$ is correctly met. At peak efficiency, the total loss is dominated by P_f (dashed orange line). This is also true for Rabi frequencies above the optimum value. These findings can be directly transferred to the bottom row of Fig. 4.20. The small fraction in $m_F = 2$ originates from the Landau-Zener loss at the first crossing. In contrast, the fractions in $m_F = \pm 1$ are due to P_f .

Hence, clear signatures of a mismatched Rabi frequency can be stated: For Ω_r too low, a significant fraction remains in $m_F = 2$ while $m_F = \pm 1$ are not populated at all. Too high values of Ω_r manifest themselves in the opposite effect. However, this is only true as long as no mutual shift of $\Delta_{r,i}$ and $\Delta_{r,f}$ occurs. If the rf sweep starts too close to the first crossing, a large fraction will be projected into $|\varphi_4\rangle$ instead of $|\varphi_5\rangle$.

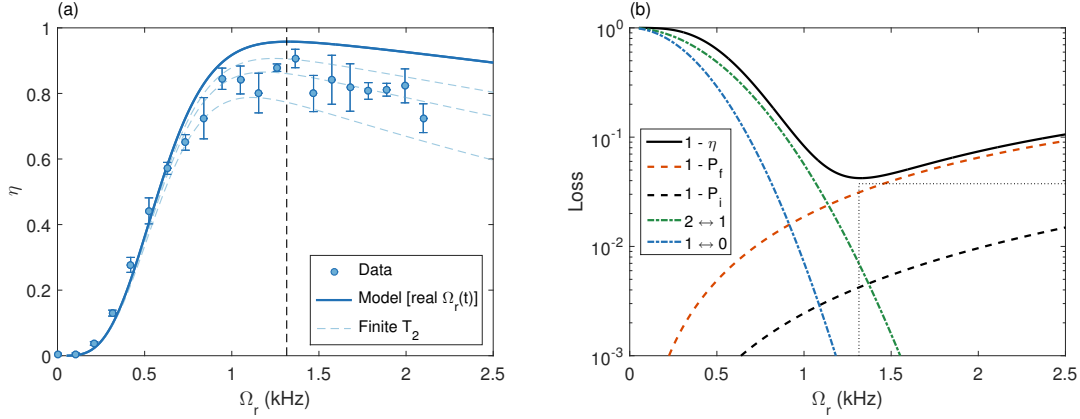


Figure 4.21: (a) Experimental realization of ARP with $\Delta_{r,i} = -2\pi \cdot 29.2$ kHz. The measured ARP efficiency η (blue circles) is compared to the theoretically expected values [Eq. (4.45)] for different Rabi frequencies Ω_r (solid blue line peaking at 95.8%). The dashed lines take into account finite values of T_2 (top to bottom: 19 ms, 10 ms and 5 ms). (b) Contributions to the total loss ($1-\eta$) when accounting for the time dependence of Ω_r (solid black line) and assuming $1/T_2 = 0$. The dash-dotted lines are the Landau-Zener contributions to the total loss. The dashed lines show the share of the initial (P_i) and final (P_f) overlap in $1 - \eta$. The dotted lines highlight the peak efficiency at constant (and optimum) Ω_r . The deviation is approximately 0.5 percentage points. All other curves in (a) and (b) take into account the actual course of Ω_r [see Eq. (4.44)].

After the ARP this fraction will end up in $m_F = 2$ for correct or too low Ω_r . Since the rf sweep would end at $\Delta_{r,f} > 0$, too, the decomposition of $|\varphi_5\rangle$ contains larger contributions from $m_F = -1$ than from $m_F = +1$. In contrast, if the sweep starts too far away from the crossing, the decomposition of $|\varphi_5\rangle$ will be shifted towards $m_F = +1$ after the ARP. The initial overlap is practically perfect in this case, that is, no increased fraction in $m_F = 2$ is observed (besides the Landau-Zener loss). Combinations of both mismatches can be ambiguous. There exist further possible causes for the efficiency being worse than expected. First of all, measured values always scatter about their mean, whatever the cause. If the value to be measured is subject to an upper bound, such as η , scatter will in fact reduce the mean value. The two key parameters that can be subject to scatter and would affect η are B and Ω_r . Both are expected to vary from shot to shot. Even a small relative change in the magnetic field on the 10^{-4} level results in a detuning error on the order of $2\pi \cdot 1$ kHz. The rf amplitude by itself can be expected to be very reproducible. Aside from that, a position scatter of the atomic ensemble in the presence of rf gradients results in a scatter of Ω_r . The expected variations are on the order of 0.5% and negligible in this case, because even a change of 10% in Ω_r would not change the efficiency by this much (see Fig. 4.21). Furthermore, the observability of Rabi oscillations over 1 ms at approximately constant amplitude (Fig. 4.8) sets tight limits on possible variations of B and Ω_r . In fact, a Gaussian distribution of Δ_r with $\sigma = 2\pi \cdot 1$ kHz can be considered as an upper limit to these variations, provided that Ω_r is constant. Yet, the detrimental effect of this variation on η is below 1%.

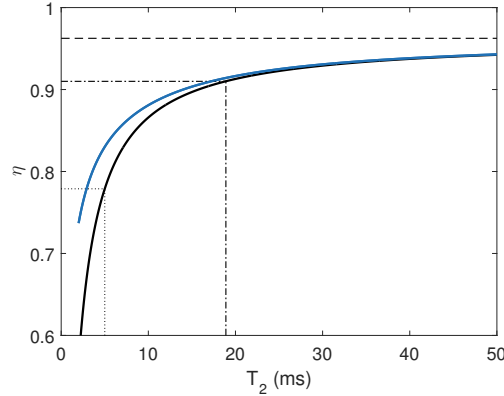


Figure 4.22: ARP efficiency η vs. transverse coherence time T_2 when using the optimum set of parameters in absence of decoherence for $\tau = 9$ ms and $B = 9.61$ G (solid black line). The dashed line indicates the limiting efficiency for $T_2 \rightarrow \infty$. The dotted and dash-dotted lines highlight $T_2 = 5$ ms and 19 ms, respectively. The solid blue line is the peak efficiency when using the set of parameters optimized for the respective value of T_2 .

Of course, there may also be mundane technical reasons. For example, the number of discrete steps (100) used for the synthesis of the linear frequency ramp. It was checked and no correlation with the ARP efficiency was found.

So far, all conceivable technical, systematic and statistical causes for the reduced efficiency could be ruled out – except for a finite transverse coherence time. In the spin-echo measurement it could be shown to be at least 5 ms. The measurement of rf gradients suggested that it is even longer, but no reliable estimate was possible. For this reason, the effect of different values of T_2 is shown and compared to the data. Two specific values are of particular interest. The first one is $T_2 = 5$ ms as the lower limit. Also the smallest value consistent with the 91% efficiency observed in Figs. 4.20 and 4.21(a) is considered. It is $T_2 = 19$ ms. Their effect is shown by the blue dash-dotted lines in Fig. 4.21(a) besides an intermediate value of $T_2 = 10$ ms. The latter shows a reasonable agreement with the data. A characteristic feature is the steeper decrease towards higher Ω_r compared to the model without decoherence.

The effect of a finite T_2 on η at the optimum set of parameters in absence of decoherence is shown in Fig. 4.22 by the solid black line. The dashed line indicates the limiting case of $1/T_2 = 0$. The dotted and dash-dotted lines highlight the previously mentioned values of $T_2 = 5$ ms and 19 ms, respectively.

In principle, the ARP efficiency can be optimized for a given transverse coherence time. The resulting optimum Rabi frequency is higher and the rf sweep needs to start further detuned from the first crossing. Also the optimum sweep time τ becomes finite. As a matter of fact, the ARP time has to be shorter than this value anyway (in Q-2). The result of such an optimization, that is, including Eq. (4.47), is shown by the solid blue line. A direct comparison reveals that there is only little to gain for coherence times longer than 10 ms. However, all of these results apply to the scenario of an approximately constant rf amplitude. The possible gain of utilizing an actively controlled Rabi frequency is discussed at the end of this section.

ARP in microgravity

After the thorough characterization of ARP on ground it should be utilized in microgravity now. This might seem trivial because the presence of a gravitational force itself has no influence on ARP. On the other hand, the atomic ensemble is (intentionally) further away from the chip in microgravity. These positions cannot be probed directly in ground-based measurements, because the traps are too shallow. Probing them in flight would be a waste of valuable microgravity time. Hence, the difficulty is to derive an estimate for Ω_r and B .

The magnetic field gradient was measured to be -0.21 G/m in the z direction [see Fig. 3.8(b)]. Since the ground-based vs. microgravity position difference for release trap B is less than 1 mm, the expected change in resonance frequency is -0.1 kHz only. This can be neglected, because the nearest crossings are at $\Delta_r \approx \pm 7$ kHz.

The derivation of a new relative rf amplitude producing the same Rabi frequency at the microgravity position is more complex. One possibility is to turn the capsule around by approximately 90° and then try to let the new atomic trajectory pass by the microgravity position. The atoms would then fall to the right instead of downwards in the absorption images. This alone would be quite arduous, but still possible with Q-2. In addition, the entire experimental sequence would have to be re-optimized for the new direction of gravity. Using thermal atoms with a correspondingly less critical experimental sequence is not an option. A separation of the Zeeman states would then no longer be possible in the reduced magnetic field gradient further away from the atom chip. Invoking the measurement on rf gradients is an alternative. By linear extrapolation the Rabi frequency is expected to decrease to approximately 45% compared to the ground-based measurement. However, this value might well be too small, because the rf amplitude cannot change linearly all over the chamber. It is most likely no $1/r$ dependence either, because the rf antenna is not a single straight wire. Nevertheless, an underestimation of the actual Rabi frequency at the microgravity position is less critical than an overestimation (see Fig. 4.21).

A realization of ARP in microgravity is shown in Fig. 4.23 for two different TOFs after the application of a magnetic lens. A SG experiment accelerates the Zeeman states to a relative velocity of $1.81(2)$ mm/s in the horizontal (x') direction. The SG field is effective in this direction only. The inclination of the imaginary interconnecting line is caused by an acceleration of the magnetic substates in the remaining static magnetic field gradient. For this reason, the inclination is larger after 460 ms compared to 350 ms.

The optimum relative rf amplitude in the ground-based measurement is 0.0255 and is extrapolated to $0.0255/0.45 = 0.0567$ for use in microgravity. In both cases, the Rabi frequency should be $\Omega_r = 2\pi \cdot 1315$ Hz. Its gradient across a cloud with $R_{TF} \approx 130$ μm would result in deviations of Ω_r on the order of $\pm 12\%$ assuming the previously measured value of 0.92 $\text{\%}/\mu\text{m}$. The actual deviations can be expected to be smaller because of the reduced gradient further away from the chip. Yet, even $\pm 12\%$ were tolerable. The two examples in Fig. 4.23 show the best (a) and the worst (b) efficiency of the measurement series (different TOFs after the same lens)

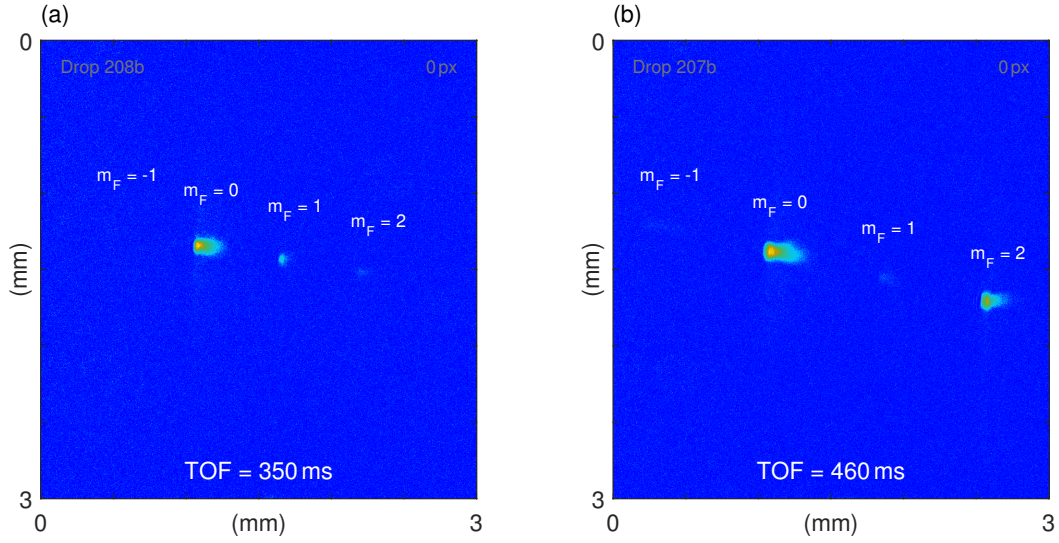


Figure 4.23: Both images show the Zeeman states after an adiabatic rapid passage in microgravity ($m_F = -2$ not populated). The states separate with $1.81(2)$ mm/s (SG). The indicated TOF starts after the application of a magnetic lens and includes 38.3 ms for ARP and a SG experiment. The ARP efficiency is 85% (a) and 72% (b).

to illustrate the shot-to-shot variations. Without a SG experiment, it would take about 500 ms for the magnetic substates to separate in the static magnetic gradient field.

Optimization of ARP under a variable rf amplitude

All previous calculations assumed a constant Rabi frequency. In this final part, the expected efficiency gain when allowing Ω_r to change linearly with time is discussed. With this degree of freedom, a mitigation strategy for transverse decoherence in ARP can be proposed.

It was shown in Fig. 4.21(b) that P_f is the limiting factor for ARP in the absence of decoherence. This loss channel can be eliminated by adiabatically undressing the states after the ARP. Ideally, all atoms in $|\varphi_5\rangle$ will finally end up in $|m_F = 0\rangle$. Of course, a linear ramp-down of the rf amplitude is not necessarily adiabatic, let alone optimal. Nevertheless, any continuous function can be approximated by linear parts to arbitrary precision if required. Figure 4.24 shows solutions of the time dependent Schrödinger equation for a linear rampdown from $\Omega_r = 2\pi \cdot 10$ kHz to zero at $B = 9.61$ G and $\Delta_r = 0$ with the initial state $|\varphi_5\rangle$. This Rabi frequency is already rather high compared to B ($\Omega_r/B^2 \approx 0.1$ kHz/G²). The corresponding energy eigenstates were shown in Fig. 4.3(b). There exist four distinct avoided crossings of $|\varphi_5\rangle$ up to $\Omega_r/B^2 \approx 0.175$ kHz/G². Actually, the ARP model [see Eq. (4.45)] cannot be expected to make correct predictions in this regime. Even 0.1 kHz/G² seem to be quite ambitious, because the individual crossings are hardly distinguishable. However, the solutions in Fig. 4.24 were calculated with the full Hamiltonian [see

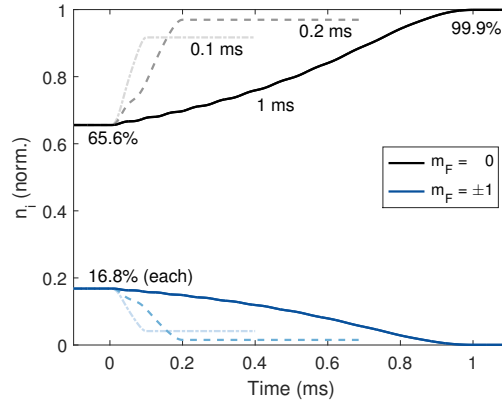


Figure 4.24: Contributions of diabatic states $m_F = 0$ (black lines, top) and $m_F = \pm 1$ (blue lines, bottom) to $|\varphi_5\rangle$ during a linear rampdown of the Rabi frequency from $\Omega_r = 2\pi \cdot 10$ kHz to zero within 1 ms (solid lines), 0.2 ms (dashed lines) and 0.1 ms (dash-dotted lines). The data are numerical solutions of the time dependent Schrödinger equation at $B = 9.61$ G.

Eq. (4.37)]. They are no approximations. In this rather extreme scenario, P_f would be 65.6% and can be increased to 99.9% by a linear rampdown of the rf amplitude within 1 ms, as shown by the solid black line. The solid blue line shows the corresponding contributions of the neighboring diabatic states to $|\varphi_5\rangle$. The combined contributions of $m_F = \pm 2$ add up to 0.8% (initially) and are not shown. For a significantly shorter ramp time, for instance, 0.1 ms (dash-dotted lines) or 0.2 ms (dashed lines), the rampdown is apparently not adiabatic. This would entail a reduced final fraction in $m_F = 0$. At a lower initial Rabi frequency, the rampdown can only be more efficient. For this reason, a linear rampdown within 1 ms is a robust protocol that can be used for smaller Ω_r , too. A division into partial ramps is not required. This additional time is wisely invested, even if the remaining ARP time needs to be reduced accordingly. Nevertheless, Q-2 defies an experimental verification. The measured efficiency hardly improves. However, this is in good agreement with the hypothesis, that the dominant loss channel is decoherence rather than the final overlap of states.

Since P_i has almost no effect [Fig. 4.21(b)] and P_f can be eliminated by a rampdown of the rf amplitude, a self-evident mitigation strategy for decoherence in ARP is to minimize the remaining losses at the two crossings. For example, the combined passage efficiency at the first crossing reads

$$\left[1 - \exp\left(-\frac{\pi\Omega_{2,1}^2}{2|\alpha|}\right) \right] \cdot \exp\left(-\frac{3\pi\Omega_{2,1}}{8|\alpha|T_2}\right).$$

It depends on two free parameters only, none of which is the ARP time τ . The magnetic field indirectly contributes by setting an upper limit to Ω_r – and hence $\Omega_{2,1}$ – as well as influencing the latter by the systematic shift shown in Fig. 4.4(b). Ideally, the fraction in the first exponential should be as large as possible and vice versa for the second one. A large sweep rate can be chosen to compensate for a short T_2 . The correspondingly larger Landau-Zener loss can easily be circumvented

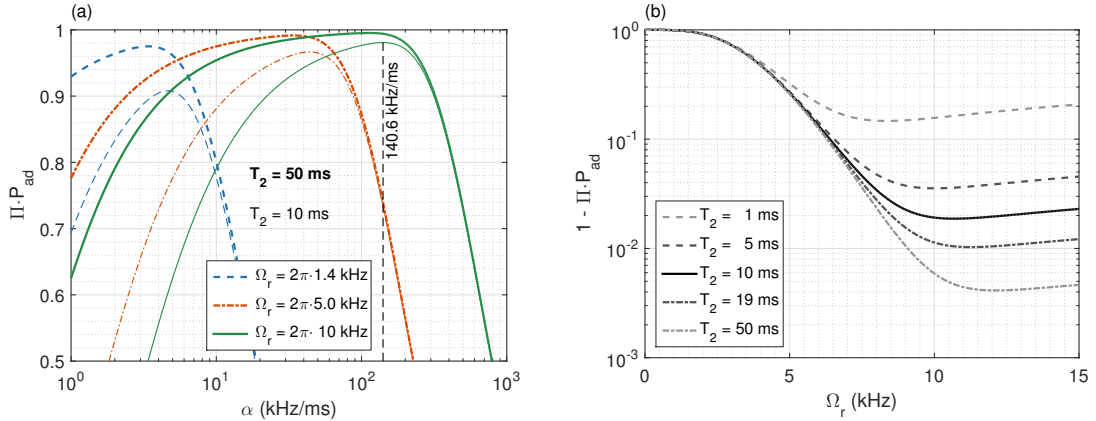


Figure 4.25: (a) Passage efficiency when considering the overall decoherence (Π) and adiabatic (P_{ad}) losses at both crossings ($m_F = 2 \leftrightarrow 1$ and $m_F = 1 \leftrightarrow 0$) for three different Rabi frequencies Ω_r and for the transverse coherence times $T_2 = 50$ ms (thick lines) as well as $T_2 = 10$ ms (thin lines). The vertical dashed line highlights the optimum sweep rate $\alpha = 2\pi \cdot 140.6$ kHz/ms at $\Omega_r = 2\pi \cdot 10$ kHz and $T_2 = 10$ ms. (b) Passage losses vs. Rabi frequency at this optimum α for different values of T_2 .

by an appropriate increase in Rabi frequency. This does not completely compromise the reduction of the second fraction due to the quadratic dependence on $\Omega_{2,1}$ in the first term. Unfortunately, there is no analytic solution to this equation. It is clear that this expression can be arbitrarily close to unity, as long as sweep rate and Rabi frequency can be increased further. In fact, Ω_r is the crucial point. At $B = 9.61$ G, the upper limit is $\Omega_r \approx 2\pi \cdot 10$ kHz (0.1 kHz/G 2). In Q-2, the magnetic field for ARP should not be increased further, as discussed before, even though the maximum Rabi frequency quadratically depends on B .

Under these constraints, the overall passage efficiency for both crossings is shown in Fig. 4.25(a) as a function of the sweep rate for three different Rabi frequencies (plotted in blue, red and green). The efficiency corresponding to each of them is plotted once for $T_2 = 50$ ms (thick lines) and for $T_2 = 10$ ms (thin lines). The efficiencies for $T_2 = 10$ ms are always worse and their optimum is found at an increased sweep rate, as expected. The overall optimum efficiency is reached at the maximum Rabi frequency that may be used and a specific sweep rate. This in turn depends on T_2 , which is not known to a satisfactory precision. However, it will not be shorter than 10 ms [see Fig. 4.21(a)]. With this set of parameters ($B = 9.61$ G, $\Omega_r = 2\pi \cdot 10$ kHz, $T_2 = 10$ ms) and with $\alpha = 2\pi \cdot 140.6$ kHz/ms, an efficiency of 98% is possible. If the transverse coherence time were longer, the efficiency would be better.

It was stated before that these results are independent of τ . This will be true only if τ is long enough for the sweep to start sufficiently far detuned ($\Delta_{r,i} = -|\alpha|\tau$) for the condition $P_1 \approx 1$ to be satisfied. Luckily, this condition is easily fulfilled. For instance, with $\tau = 1.43$ ms the sweep starts at $\Delta_{r,i} = -2\pi \cdot 200.6$ kHz with $P_1 = 99.9\%$.

It is worth analyzing the dependence of this peak efficiency on Ω_r , because it is not exactly known in microgravity. Figure 4.25(b) shows the passage losses as a

function of Ω_r for various T_2 . All curves are calculated with the same optimum sweep rate derived above. Like in conventional ARP at constant Ω_r , this passage is more sensitive to Ω_r being too low rather than too high. In fact, even the optimum value is at a slightly higher Rabi frequency compared to the one assumed to optimize α in Fig. 4.25(a). The reason is that Ω_r could not be optimized, but had to be fixed at the rather arbitrary upper bound. Still, no sharp decrease of the efficiency will occur if this upper limit is exceeded. The model will simply start to fail making correct quantitative predictions. Therefore, it is indeed reasonable to choose Ω_r slightly too large rather than too small.

Conclusions

In this chapter, different schemes for ARP were discussed in great detail. The best efficiencies are possible when the Rabi frequency can be actively controlled, for example, by linearly decreasing the rf amplitude in the end. With this technique, a mitigation strategy for decoherence in ARP was proposed. The expected efficiency is 98% with $T_2 = 10$ ms. For a constant Rabi frequency, the conventional ARP was analyzed in great detail and supported by experimental data. In this case, the efficiency benefits from a longer sweep time while a larger magnetic field is advantageous in both cases. It was also shown that ARP is more sensitive to a Rabi frequency that is too low rather than too high. Reverse ARP was briefly discussed as an alternative to the conventional one. It is less susceptible to smaller magnetic fields and larger field fluctuations than the conventional one. However, the tolerance on mismatched Rabi frequencies is lower. Even the maximum possible efficiency is smaller within the given experimental limitations. For this reason, conventional ARP is favored over reverse ARP in Q-2. Nevertheless, reverse ARP is an alternative for experiments featuring lower and especially less stable magnetic fields, where a reliable final detuning is an issue.

The advantage of a highly efficient ARP in Q-2 is twofold. Clearly, more atoms in the desired $m_F = 0$ substate as the input state for an atom interferometer are beneficial. Furthermore, if the remaining magnetic substates were no longer detectable, there would be no need to separate them after the ARP. This would allow for an analysis of a magnetic lens even for short TOFs. Of course, the magnetic gradient could be increased to speed up the separation of states, too. Yet, this would also affect the $m_F = 0$ state because of the quadratic Zeeman shift. In the example shown in Fig. 4.23, the SG experiment accelerates the $m_F = 0$ atoms by approximately $2.4 \mu\text{m/s}$ within 3 ms.

Other experiments suffering from much higher magnetic gradient fields might have to apply the ARP several times. For example, to transfer the atoms into the $m_F = 0$ state right after release and only transiently transfer back into $m_F = 2$ to apply the magnetic lens. This protocol benefits from an ARP efficiency close to unity to a great extent.

In principle, the detuning can be changed either by chirping the rf pulse or by changing the magnetic field. For the latter, the switching dynamics of the coils can be exploited or the current through the coils is changed as a function of time. Hence it may be called ‘coil ARP’, too, even though it is in no way different to the conventional one. The disadvantage, however, is the significantly reduced flexibility due to the rather slow step response of the coil current. With this scheme, efficiencies of up to 80% could be demonstrated (not shown), similar to reverse ARP.

Much effort was spent on modeling, characterizing and optimizing the conventional ARP. Owing to this, efficiencies of up to 91% could be demonstrated on ground and up to 85% in microgravity. The mitigation strategy for decoherence in ARP could not be tested so far.

Chapter 5

Center of mass motion

According to Newton's first law, every object retains its state of motion in an inertial reference frame, unless a force is acting upon the object. In the scope of this chapter, the object is the BEC and all forces are taken to act on its center of mass (COM). The analysis is performed within the drop capsule's reference frame, which is not inertial. Three data sets were acquired in microgravity. They are presented in the first section and are the basis for a detailed discussion of systematic effects on the center of mass motion (COMM) in Section 5.2. These effects can lead to real or fictitious forces on the atoms within the capsule's reference frame. The microgravity environment is essential for this analysis, because all these forces are small compared to gravity, but they can be measured on long time scales. This chapter concludes with strategies for reducing the COMM as required for precision sensors.

All data points presented in this chapter were measured in microgravity by Christoph Grzeschik, Alexander Grote, Christian Deppner and the author with additional support by Waldemar Herr. Jan Rudolph and Merle Cornelius were part of the team, too, but not for the entire measurement time. Decisions regarding the experimental sequence were made by the team. The data analysis, numerical simulations and the analysis of systematic effects were conducted by the author.

5.1 Measured center of mass motion

The COMM is measured by time of flight imaging. This involves creating at least two atomic ensembles in the same way and detecting them after different TOFs. This method is prone to a velocity scatter of the atoms. For this reason, two alternatives are studied, both involving the detection of the same atomic ensemble for several times at a significantly reduced intensity in the detection laser beam. The advantage is the same initial state for all images. The first alternative aims at a direct measurement of the COMM by choosing the time intervals in between the images such that the displacement due to this COMM exceeds the increasing cloud diameter. In this way, separate clouds will be visible on the same density image if the camera is not read out in between. However, the detection process heats the atoms resulting in an increased expansion rate. Hence, this method cannot work for small COM velocities. Still, the readout time for the camera can be reduced by binning

or a sub-image readout to circumvent this problem. Nevertheless, the heating limits the available time span for this scheme to approximately 100 ms. Furthermore, the choice of an appropriate magnetic quantization field is problematic, because it may not be changed within the TOF due to the coil kicks, which would falsify the COMM measurement. Therefore, the field can be maintained either in the configuration for detection or in any desired configuration, for example with $I_x = 0.1$ A. Both these options have significant disadvantages, because the method would be either limited to a certain high-field and high-gradient configuration or no information on the number of atoms could be extracted, if the condition for the cycling transition is not met. In summary, this alternative is impractical for detecting small COM velocities and leads to systematic rather than statistical errors.

The second alternative aims at an indirect measurement of the *in situ* dipole oscillations. This is only a single aspect leading to COMM, but needs to be treated separately anyway. If the atoms are imaged many times over exactly one or many cycles of the oscillation, the density distribution in the absorption image will resemble the classical probability distribution of a harmonic oscillator with maxima at the turning points. This method works well for *in situ* oscillation amplitudes exceeding $50\ \mu\text{m}$, which is far above the target accuracy of approximately one micrometer. However, this alternative can still be used to suppress large dipole oscillations, as will be explained below. In summary, both alternatives have the incentive of requiring fewer drops, but they are not precise enough for measuring the center of mass velocities presented in this work.

Three independent data sets on the COMM of magnetically lensed atoms are presented in Fig. 5.1. A different lens was used for each of these sets (A, B and C). Set A was lensed with the 'SC-BC Gaussian lens' taken as an example in Section 3.3. The remaining two sets were lensed by a pure BC 'box lens', where the BC current was simply switched on for 2.64 ms, while the bias coil was kept constant at $I_y \approx -75$ mA. The difference between Set B and C is the value of the BC current, which is 1.8 A for Set B and 1.828 A for C. This primarily results in a different position of the lens trap and thus a different COM velocity. The details of these lenses are not relevant in this section. They are discussed in Chapter 6 on magnetic lensing.

After the respective lens, the atoms were transferred to the $m_F = 0$ substate. The COMM is expected to be uniform in the absence of forces. For definiteness, the COM is taken as the first moment of the integrated density profile of an absorption density image¹. The resulting uncertainty in the position is much smaller than the data points. The motion is approximately uniform for the x' direction (left column in Fig. 5.1), but accelerated in the positive y' direction (right column). It is a downward acceleration of the atoms with respect to the capsule due to a residual air drag in the drop tower, as will be shown in the next section. The initial velocities are on the order of a few hundred $\mu\text{m/s}$. The dominant contributions originate from the particular experimental sequence as will be explained in the remainder of this section.

¹A glance to Appendices A and B gives an impression of these absorption images. In these appendices, they are compared to the results of a numerical simulation, which is explained in the next chapter.

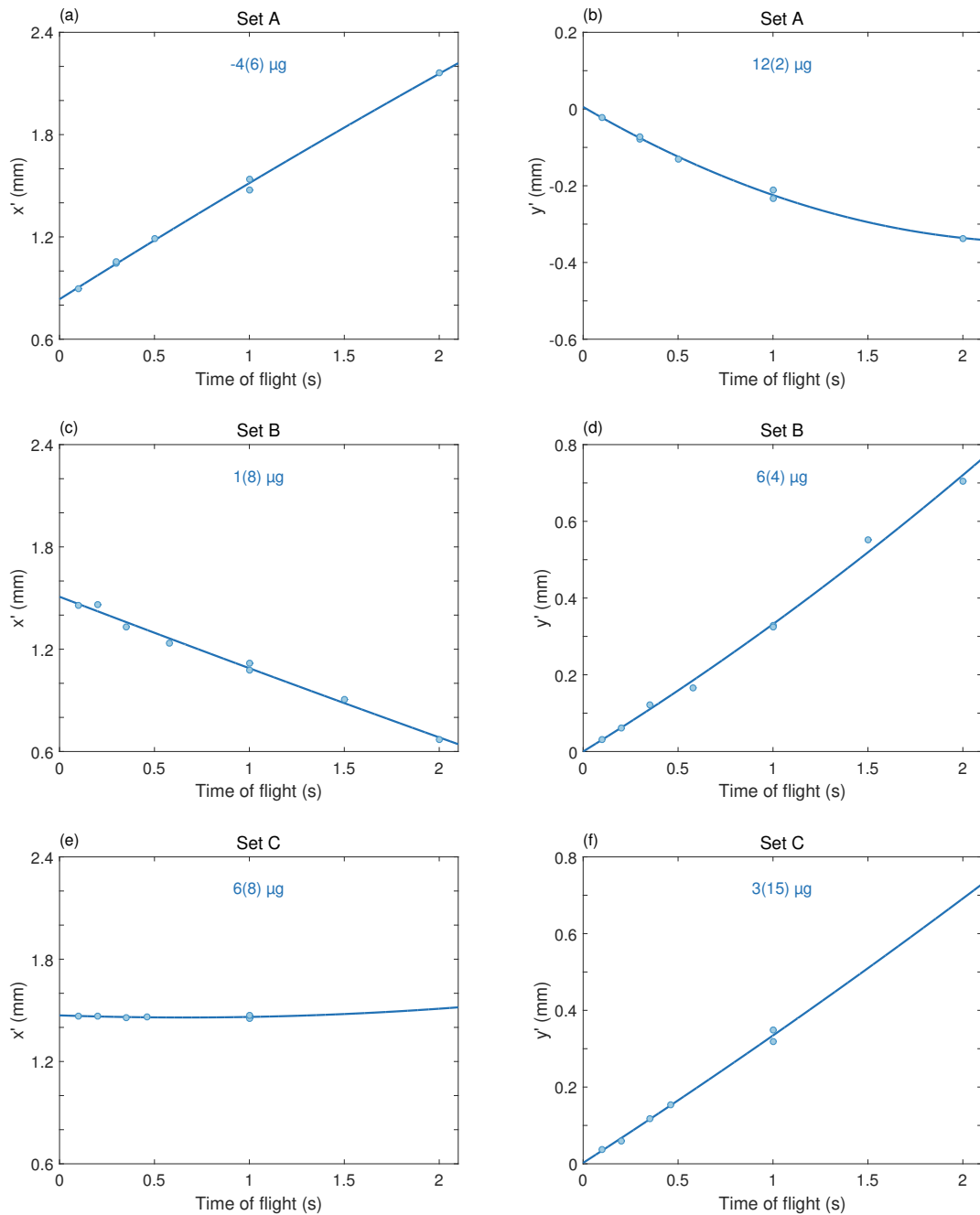


Figure 5.1: The figures show the measured x' (left column) and y' (right column) COM coordinates of three data sets (A, B and C) of magnetically lensed atoms after different TOFs. The solid blue line is a quadratic fit to the respective data sets. The fitted residual accelerations are given in each subfigure.

The BEC can be assumed to be at rest in the final evaporation trap. In between this point and the end of the ARP, from where on the atoms are almost insensitive to magnetic gradient fields, every step within the experimental sequence (see Table 2.3) has a significant effect on the center of mass motion. The first one is the transfer of the BEC to its release position. As an example, the transfer to release position A as used for Set A is discussed in more detail. In principle, this transfer can be performed slow enough such that no dipole oscillations are excited. Still, the finite drop tower height limits the time that can be invested into this adiabatic decompression. The course of the y coil control responsible for the trap motion is parametrized by a sigmoid function:

$$\text{control}(\tilde{t}) = 1 - \frac{\frac{1}{1+e^{-s/2}} - \frac{1}{1+e^{s(1/2-\tilde{t})}}}{\frac{1}{1+e^{-s/2}} - \frac{1}{1+e^{s/2}}}, \quad (5.1)$$

where \tilde{t} is a normalized time on the domain $[0,1]$ and $s \in [0, \infty)$ is a parameter defining the shape of the control ramp. It starts at zero for $\tilde{t} = 0$ and terminates at unity for $\tilde{t} = 1$. The two extreme cases $s = 0$ and $s \rightarrow \infty$ correspond to a linear ramp and a unit step function with the step at $\tilde{t} = 0.5$, respectively. For Set A, the trap is moved within a duration of 250 ms to position A using $s = 10$, which is rather smooth in the beginning and at the end. This time is much longer than the coil's settling time. Hence, the step response can be neglected in this case. The ramp duration was chosen such that no dipole oscillations are detectable in ground-based measurements, that is, with TOFs ≤ 22 ms. Yet, small *in situ* oscillations are easily detectable after a longer TOF. The maximum kinetic energy $m_{\text{Rb}}v_{\text{max}}^2/2$ the atoms can acquire due to dipole oscillations equals the maximum potential energy in the trap. Using Eq. (2.2) and limiting the analysis to the z direction of a purely harmonic trap:

$$\frac{1}{2}m_{\text{Rb}}\omega_z^2\Delta z^2 = \frac{1}{2}m_{\text{Rb}}v_{\text{max}}^2,$$

where Δz is the amplitude of the *in situ* oscillation, yields

$$v_{\text{max}} = \omega_z\Delta z. \quad (5.2)$$

Figure 5.2 shows microgravity data detected after 100 ms TOF. The hold time within the release trap was varied in order to measure residual dipole oscillations. The COM positions are shown in (a) and (c) for the two detection coordinates x' and y' , respectively. In (a), an after-TOF oscillation amplitude of $51(6) \mu\text{m}$ at a frequency of $60.4(3) \text{ Hz}$ is detected. It agrees well with the predicted value of $2\pi \cdot 59.8 \text{ Hz}$ by the chip model. According to Eq. (5.2), the measured amplitude corresponds to an *in situ* amplitude of $1.3 \mu\text{m}$, which is neglected in the fit. The hold time needs to be chosen such that the resulting COMM is minimal. This corresponds to the turning point of the *in situ* oscillation and to the center of the after-TOF oscillation. A mismatch can lead to a COMM of up to 0.5 mm/s . In the y' direction, no oscillation can be seen. The data set shows more than just the residual oscillation amplitude. Since absorption imaging is destructive, as explained above, every data point was acquired using a newly created BEC. Many drops were required because only two such data points can be taken in a single drop. Nevertheless, an oscillation can be

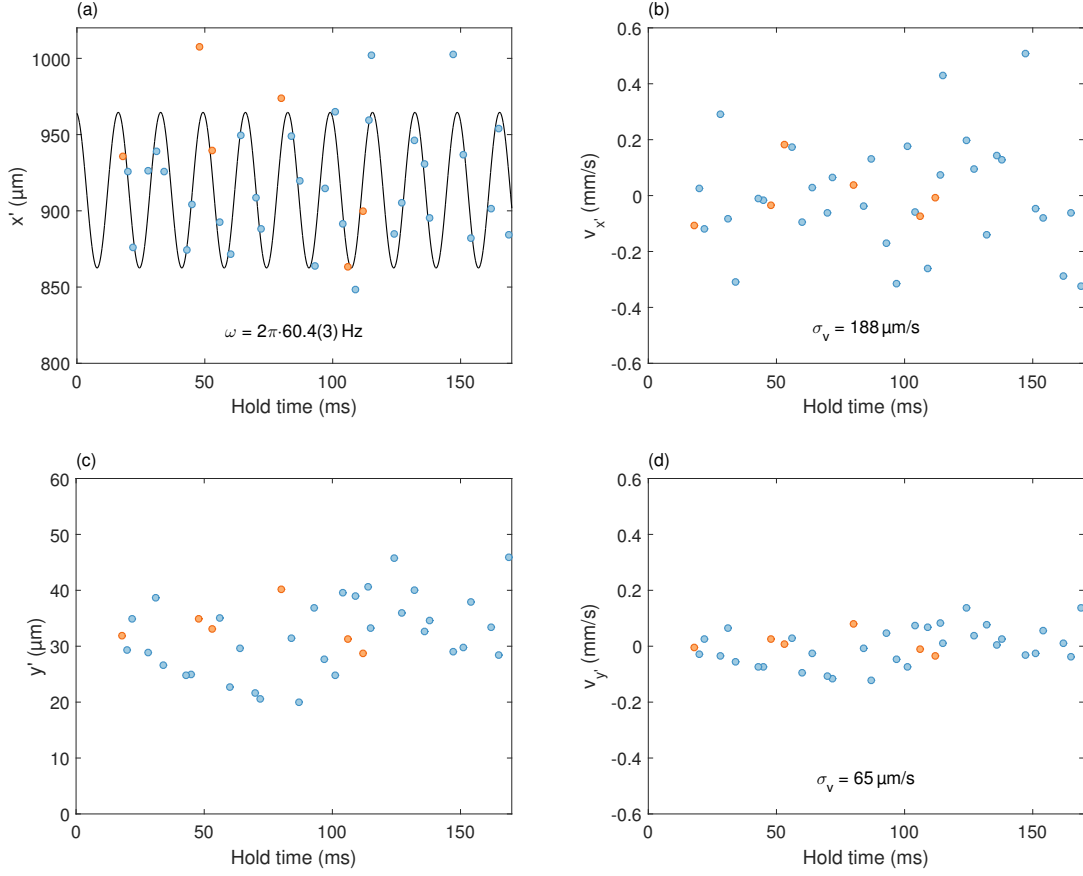


Figure 5.2: The filled circles in (a) and (c) are the center of mass positions (x' and y') measured in microgravity after 100 ms TOF for various hold times in the release trap. The blue (orange) points were measured in drop (catapult) mode. The solid black line in (a) is a sinusoidal fit of the x' coordinate of both data sets. The fitted frequency is $\omega = 2\pi \cdot 60.4(3)$ Hz. The scatter in the velocity after the release is shown in (b) and (d) for the two respective directions. The combined standard deviation is $188 \mu\text{m/s}$ in the x' direction and $65 \mu\text{m/s}$ in the y' direction.

detected in the x' direction. This means that it is phase coherent from drop to drop. If this were not the case, the dipole oscillation would manifest itself in an increased scatter of the atomic position after TOF and the control over the COMM would be much more complicated.

The scatter in position after such a long TOF is dominated by the scatter in the COM velocity after release. This velocity scatter is calculated from the data in Figs. 5.2(a) and (c) and is shown in (b) and (d), respectively. For (b), the fitted dipole oscillation was subtracted from the data. The standard deviation of the velocities is a measure for this velocity scatter. It is $\sigma_v = 188 \mu\text{m/s}$ in the x' direction and $\sigma_v = 65 \mu\text{m/s}$ in the y' direction. This scatter can be reduced by magnetic lensing, as will be shown below.

The orange data points in Fig. 5.2 were taken during different catapult flights in contrast to the blue ones (drop mode). Unfortunately, the data yield per flight

in catapult mode is worse than in drop mode, because of dust particles within the vacuum chamber². They are visible to the naked eye and fly through the chamber during a catapult flight due to elastic deformations in the acceleration phase. This spoils many images. The scatter in the y' direction is significantly larger for the first out of four data points during a catapult flight (not shown). These data points are neglected, too. The remaining data points, however, are comparable in phase and oscillation amplitude to those in drop mode. Aside from that, the scatter seems to be reduced in catapult mode, even though the data set is too small for a definitive statement.

After the transfer of the atoms to the release position and holding them for a certain time, as explained above, the atoms are released from the trap. The typical timescale for this release is on the order of 1 ms, limited by the step response of the bias coil. If both, this coil and the chips in use (BC and SC), were simply switched off with the step response function, the chip currents would decrease much faster than the coil current. In turn, the trap center would move rapidly towards the chip leading to a transient acceleration of the atomic ensemble. This effect is investigated further in Section 5.3 together with a mitigation strategy.

In the free expansion phase prior to the magnetic lens (pre-TOF), the atoms are in the $m_F = 2$ substate and hence susceptible to magnetic field gradients, as discussed in Section 3.4. The lens itself can accelerate the atoms, too: First of all by the on and off switching processes and also if the atoms are displaced from the center of the lens.

Finally, the atoms are transferred to the $m_F = 0$ substate by the ARP. The high magnetic field, which is advantageous for an efficient ARP, can change the COMM by the coil switching process, as discussed in Section 3.4. All these effects must be either reduced or compensated when aiming at a reduction of the center of mass motion.

5.2 Systematic effects on the center of mass motion

The total force on the atoms within the capsule's reference frame is the vector sum of Coriolis and centrifugal force, the force by the residual air drag, magnetic and electric dipole force and a detection pseudo force arising when imaging dilute and highly asymmetric clouds:

$$\vec{F}_{\text{total}} = \vec{F}_{\text{centrifugal}} + \vec{F}_{\text{Coriolis}} + \vec{F}_{\text{magnetic}} + \vec{F}_{\text{electric}} + \vec{F}_{\text{pseudo}} + \vec{F}_{\text{air drag}}. \quad (5.3)$$

These forces are discussed in the following. It should be mentioned that the air drag is acting on the drop capsule rather than the atoms. $\vec{F}_{\text{air drag}}$, on the other hand, is defined as the resulting fictitious force on the atoms within this non-inertial frame.

²The cleaning of the vacuum chamber requires breaking the vacuum. This is a very lengthy procedure due to the required baking out phase afterwards. This was postponed in order to collect data in microgravity that are valuable for the MAIUS-1 mission.

5.2.1 Centrifugal and Coriolis force

The freely falling capsule can rotate about its center of mass, which does not coincide with the origin of the Q-2 coordinate system S_{Q-2} . Its position vector with respect to the capsule's center of mass system S_C is

$$\vec{R} = \begin{pmatrix} -47(2) \\ 138(10) \\ 54(2) \end{pmatrix} \text{ mm.} \quad (5.4)$$

Hence, the capsule's center of mass is approximately 14 cm above the chip center and axially separated by 7 cm. The position of the COM of the atomic ensemble with respect to S_{Q-2} is given by \vec{r} . If the capsule is rotating with angular frequency $\vec{\omega}$, this will give rise to the centrifugal force [158]

$$\vec{F}_{\text{centrifugal}} = -m_{\text{Rb}} \vec{\omega} \times [\vec{\omega} \times (\vec{R} + \vec{r})] = -m_{\text{Rb}} \vec{\omega} \times (\vec{\omega} \times \vec{R}) - m_{\text{Rb}} \vec{\omega} \times (\vec{\omega} \times \vec{r}). \quad (5.5)$$

This is equivalent to the acceleration

$$\vec{a}_{\text{centrifugal}} = \frac{d^2 \vec{r}}{dt^2} = -\vec{\omega} \times (\vec{\omega} \times \vec{R}) - \vec{\omega} \times (\vec{\omega} \times \vec{r}), \quad (5.6)$$

which is given instead of the force for a more compact notation. The centrifugal acceleration depends on the capsule's rotation rate and the atomic position with respect to the capsule's center of mass, but not on the atomic velocity. On the other hand, the Coriolis acceleration [158]

$$\vec{a}_{\text{Coriolis}} = -2\vec{\omega} \times \frac{d\vec{r}}{dt} \quad (5.7)$$

depends on the atomic velocity and on $\vec{\omega}$, but not on the atomic position.

The capsule's rotation rate can be measured with an inertial measurement unit (IMU). The three components of $\vec{\omega}$ are shown in Fig. 5.3(a) for all drops with the IMU embarked on Q-2. The nine catapult flights (Drops 22 to 30) are highlighted by the shaded gray area in the figure. The rotation rates are significantly higher in catapult mode. The largest of all components is about the capsule's symmetry axis (green circles). A rotation about this axis is inevitable due to the manufacturing process of the piston accelerating the capsule and is partially desired in order to stabilize the capsule against tilting [67]. The measured tilt rate is shown by the gray circles and integrates up to approximately 5° over an entire catapult flight.

The axial rotation rate is practically zero in drop mode. Aside from that, it is noticeable that the tilt rate is much lower in the second half of the data set. Modifications of the experimental setup are unlikely to be the cause, since even a removal of 3 kg of balance weights in the stringers in between the first two sets of drops (34-54 and 63-86) did not have any detectable effect on the rotation rates. As a matter of fact, drop campaigns often involve many drops within one or a few weeks. In effect, the weather can be similar within a campaign and significantly different in another one. Indeed, a correlation with the ambient temperature can be seen, as

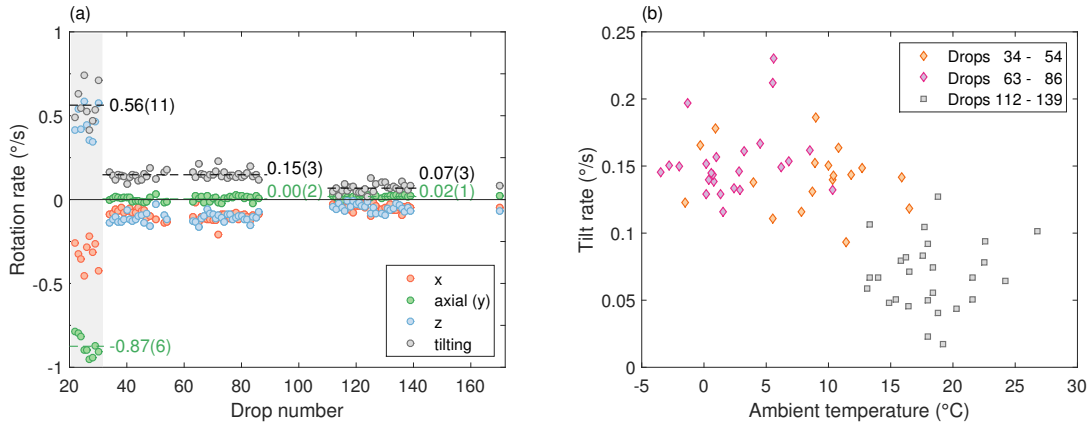


Figure 5.3: The circles in (a) show the measured rotation rates about the capsule’s x (red), y (green) and z axis (blue) and the combined tilt rate (gray) of the capsule’s symmetry axis. Drop numbers 22-30 represent catapult flights and are highlighted by the shaded gray area. The correlation of the tilt rate with the ambient temperature (official Bremen airport temperature) is shown in (b).

shown in Fig. 5.3(b). The ambient temperature was taken as the officially reported Bremen airport temperature at the time of the respective drop [159]. Of course, such a correlation is no evidence for causality³. However, it is at least conceivable, since the temperature could have an effect on the release mechanism of the capsule. It provides a hint on how the rotation rates might be reduced in case they are too high for some experiment.

The scattering of the rotation rates is to some extent due to the wind leading to an oscillation of the drop tower. In fact, the outer tower and the inner steel tube form two oscillators coupled at the bottom with relative amplitudes on the order of 30 cm (at the top of the tower) on stormy days. A capsule hanging at the top forms a pendulum driven by the tower oscillation. The resulting capsule oscillations can be measured by the IMU. An example on such a stormy day is shown in Fig. 5.4(a). The peak rotation rates are about $0.1^\circ/\text{s}$ at a frequency of 0.34 Hz, as shown by the power spectral density in (b). As a consequence, the capsule’s rotation rate can change by this amount depending on the release time. This leads to a scatter in the tilt rate because the release time is chosen independently from the phase of this oscillation.

The effect of the centrifugal acceleration on the COM of the atoms is shown in Fig. 5.5. The average rotation rates of all catapult flights [see Fig. 5.3(a)] are used for (a) and the respective average rates of the first two drop mode subsets for (b). The centrifugal displacement is shown for all three spatial directions and for the projection onto the Detection 1 camera frame (x' and y'). The largest accelerations ($\sim 3 \mu\text{g}$) can be expected within this frame leading to displacements that would be easily detectable with the free evolution times explored so far. In drop mode, the displacements are significantly smaller. Indeed, the displacement in the y' direction

³Just like the spurious relationship between the storks and the number of births in a country.

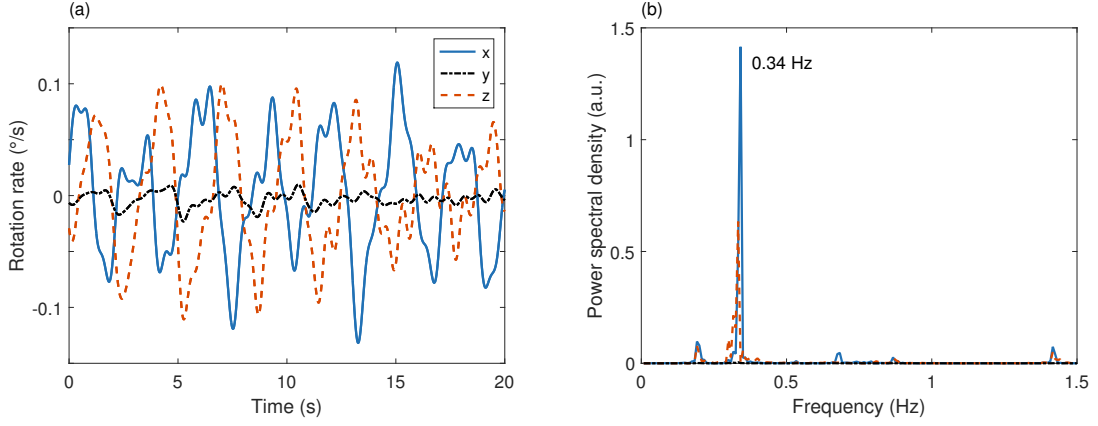


Figure 5.4: (a) The rotation rates of a drop capsule hanging in the top of the drop tower on a stormy day are plotted with respect to the Q-2 coordinate system. The dominant frequency of the oscillation is 0.34 Hz, as can be seen by the power spectral density (b) of the data in (a).

after 2 s TOF is smaller than $2 \mu\text{m}$. This is undetectable with the measurements in Fig. 5.1. Hence, the centrifugal force can be neglected in drop mode, but not in catapult mode (unless the TOF is small).

The calculation of the Coriolis displacement requires the knowledge of the atomic COM velocity. As an example, the COM velocity $\vec{v} = (-0.28, 0.04, -0.37) \text{ mm/s}$ is used. It is realistic, as will be shown below. With the same values for $\vec{\omega}$ as in Fig. 5.5, the resulting Coriolis displacement is plotted in Fig. 5.6(a) for catapult operation and in (b) for the drop mode. Again, the resulting accelerations are extremely small in drop mode and can be neglected. The Coriolis accelerations in catapult mode are smaller than the centrifugal accelerations, but cannot be neglected at long TOFs either. Both accelerations can add up or counteract each other, depending on the direction of the atomic motion.

The range of atomic COM positions varies by less than 2 mm. This is small compared to R . Hence, the centrifugal force can be assumed to be independent of the experimental sequence. The centrifugal acceleration is then

$$\vec{a}_{\text{centrifugal,catapult}} = \begin{pmatrix} -2.38 \\ 2.45 \\ 2.99 \end{pmatrix} \mu\text{g} \quad (5.8)$$

in catapult mode and

$$\vec{a}_{\text{centrifugal,drop}} \lesssim \begin{pmatrix} -0.03 \\ 0.09 \\ 0.03 \end{pmatrix} \mu\text{g} \quad (5.9)$$

in drop mode, where the \lesssim sign is stated because the (larger) average $\vec{\omega}$ of the first set of drops was used. The corresponding absolute values are:

$$\begin{aligned} a_{\text{centrifugal,catapult}} &= 4.5 \mu\text{g}, \\ a_{\text{centrifugal,drop}} &\lesssim 0.1 \mu\text{g}, \end{aligned} \quad (5.10)$$

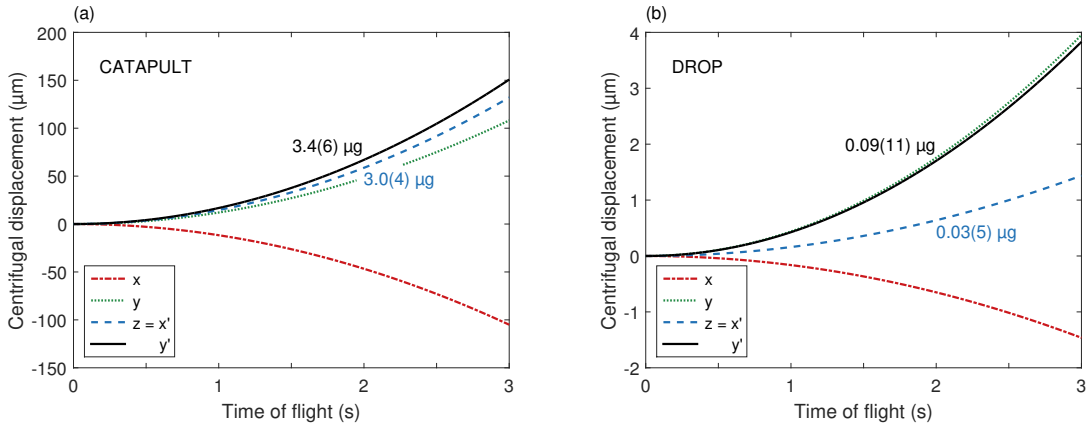


Figure 5.5: The displacement of the atomic COM position due to the centrifugal force is shown for the catapault mode (a) and the drop mode (b) for the different spatial directions and their projection onto the Detection 1 coordinate system. The corresponding accelerations within this frame are given in the figures.

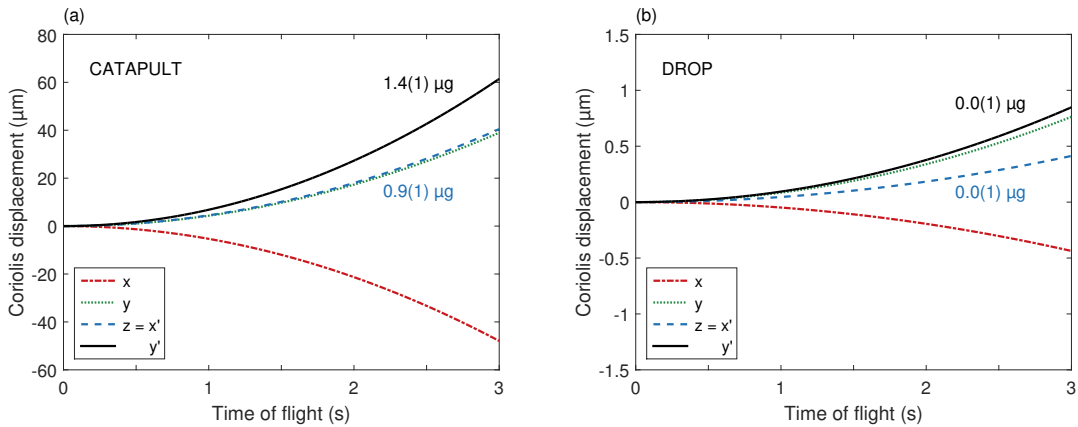


Figure 5.6: The displacement of the atomic COM position due to the Coriolis force assuming an atomic velocity of $\vec{v} = (-0.28, 0.04, -0.37)$ mm/s (as measured in Fig. 5.13) is shown for the catapault mode (a) and the drop mode (b) for the different spatial directions and their projection onto the Detection 1 coordinate system. The corresponding accelerations within this frame are given in the figures.

for future reference. Such an estimate is not possible for the Coriolis acceleration because of the dependence on the atomic velocity. However, an upper bound can be given by assuming $\vec{v} \perp \vec{\omega}$ and $v = 1$ mm/s, which is higher than all velocities observed in Fig. 5.1:

$$\begin{aligned} a_{\text{Coriolis,catapult}} &< 3.7 \mu\text{g}, \\ a_{\text{Coriolis,drop}} &< 0.5 \mu\text{g}. \end{aligned} \quad (5.11)$$

The maximum of all TOFs explored in catapult mode is 100 ms with Coriolis and centrifugal displacements well below $1 \mu\text{m}$. The accelerations in drop mode are small enough such that they can be neglected, too. In fact, they are below the fit uncertainties in Fig. 5.1.

5.2.2 Magnetic dipole force

It was shown in Section 4.2 that the energy of the $m_F = 0$ substate depends quadratically on the magnetic field (quadratic Zeeman shift). For convenience, this dependency is reprinted here [see Eqs. (4.27) and (4.28)]:

$$E(F = I + \frac{1}{2}, m_F = 0, B) \approx \frac{\mu_B^2 B^2}{\Delta E_{\text{hfs}}}.$$

The resulting force is

$$\vec{F}_{\text{magnetic}} = -\nabla E = -\sum_{i=1}^3 \frac{\partial E}{\partial B} \frac{\partial B}{\partial r_i} \hat{e}_i \approx -2 \frac{\mu_B^2 B}{\Delta E_{\text{hfs}}} \sum_{i=1}^3 \frac{\partial B}{\partial r_i} \hat{e}_i, \quad (5.12)$$

where the r_i are the coordinates x , y and z with the corresponding unit vectors \hat{e}_i . In other words, the magnetic force is proportional to B and its gradient. Both of them were measured in Section 3.4 using the $m_F = 2$ substate. The calculated acceleration of the $m_F = 0$ substate in the y' direction for the data sets in Fig. 5.1 is shown in Fig. 5.7. This particular direction is chosen for its largest component of the magnetic field gradient within the Detection 1 frame. Furthermore, it is of special interest for the air drag discussion below. The gradient in the x direction can be as large as 1 G/m [see Eq. (3.7)] leading to an acceleration of $0.3 \mu\text{g}$. Data Set A was taken with a quantization field of $B \approx 1$ G using $I_x = 0.5$ A. The resulting effect on the atomic trajectory is shown by the solid blue line. For Data Sets B and C, $I_x = 0.1$ A was used resulting in a much smaller acceleration (dashed black line). The effects are small, but known to a relative uncertainty of less than 3% for all data sets. Hence, all data points in Fig. 5.1 can be corrected for this effect, which is performed at the end of this section.

5.2.3 Electric dipole force

Characterizing the magnetic forces acting on the $m_F = 0$ atoms was easy. The magnetic environment could be measured using the $m_F = 2$ state allowing for a direct calculation of the actual forces. This situation is fundamentally different for electric dipole forces, since all available (stable) states of rubidium have the same

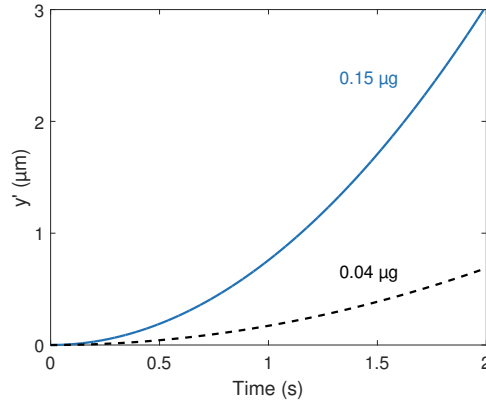


Figure 5.7: The solid blue line shows the accelerated motion of $m_F = 0$ atoms along the y' direction caused by the magnetic field gradient in Eq. (3.6) and the quantization field $B \approx 1$ G generated by $I_x = 0.5$ A. The dashed black line depicts the trajectory for $I_x = 0.1$ A and the corresponding gradients in Eq. (3.8).

electrostatic polarizability α_0 . As a matter of fact, the alkali atoms even have the highest polarizability of all atomic species by virtue of their single valence electron. The potential energy of an atom placed in an electric field E is reduced according to

$$H_E = -\frac{1}{2}\alpha_0 E^2, \quad (5.13)$$

because the induced electric dipole moment is aligned in parallel to the electric field [92]. Within the magnetic shield, no large accumulation of charges is expected. Still, there are actively controlled components, for example the camera head, photodiodes, coils and chips. This active control involves different electric potentials within these components. If they have a nonzero capacitance, spatially separated charges will accumulate. This leads to an electric field, which is approximated as a pure dipole field.

The largest capacities can be found in the capacitors of electric circuits. In a simplified view, they consist of many parallel plate capacitors at a very small separation that are folded many times. The remaining electric dipole field is practically zero. Still, even two parallel wire elements of length l have a capacitance given by

$$C = \pi\epsilon_0 \frac{l}{\ln\left(\frac{d}{2R_{\text{wire}}}\right)}, \quad (5.14)$$

where R_{wire} is the wire radius and d their separation [160]. Assuming $d \gg l$, the two wire elements can be treated as point charges. Their electric dipole moment is

$$\vec{p} = Q\vec{d}, \quad (5.15)$$

with charge $Q = CU$, where U is the potential difference between the two wire elements. The resulting electric field is [161]

$$\vec{E}(\vec{r}) = \frac{1}{4\pi\epsilon_0} \left[\frac{3(\vec{p} \cdot \hat{r}) \cdot \hat{r} - \vec{p}}{r^3} \right], \quad (5.16)$$

where $\vec{r} = r \cdot \hat{r}$ is the position vector relative to the dipole center. Squaring this equation yields

$$\begin{aligned} E^2(\vec{r}) &= (4\pi\epsilon_0 r^3)^{-2} [9(\vec{p} \cdot \hat{r})^2 r^2 - 6(\vec{p} \cdot \hat{r})^2 + p^2], \\ &= (4\pi\epsilon_0 r^3)^{-2} [3(\vec{p} \cdot \hat{r})^2 + p^2]. \end{aligned} \quad (5.17)$$

The electric field is strongest for $\vec{p} \parallel \hat{r}$:

$$E^2(r) \leq (4\pi\epsilon_0 r^3)^{-2} [4p^2] = \frac{p^2}{4\pi^2\epsilon_0^2 r^6}. \quad (5.18)$$

Inserting this into Eq. (5.13) and taking the negative gradient yields an upper limit for the electric force on the atoms:

$$|\vec{F}_{\text{electric}}| \leq \frac{3\alpha_0 p^2}{4\pi^2\epsilon_0^2 r^7}, \quad (5.19)$$

which is directed towards the dipole. To give an estimate on the order of magnitude of the effect, a simple example is calculated. The electric dipole moment of two parallel wire elements of length $l = 1$ cm, wire radius $R_{\text{wire}} = 0.25$ mm and potential difference $U = 12$ V is shown in Fig. 5.8(a) as a function of the wire separation. The electric dipole moment ranges from 10^{-14} to 10^{-13} Cm. Such a wire geometry is not particularly unlikely. See, for example, the black and the red wire in the bottom right of Fig. 2.3, even though these particular wires are connected to a photodiode in photovoltaic mode such that $U \approx 0$.

The electric dipole force on rubidium atoms for three different electric dipole moments is shown in Fig. 5.8(b). In all cases, the acceleration is much smaller than $1 \mu\text{g}$, which was about the fit uncertainty of the acceleration by time of flight imaging in Fig. 5.1. In fact, the electric dipole moment may even be two orders of magnitude larger still without being able to detect the effect of such dipole forces at the current level of precision. Actually, no configuration within the Q-2 shield could be identified that could be responsible for $p = 10^{-15}$ Cm or even above (not even close). Hence, electric dipole forces can be neglected for all measurements within this work.

It must be noted, that the assumption $d \gg l$ is not strictly fulfilled in the left part of Fig. 5.8(a). In addition, (b) is invalid for points in between the wires or close to them, because a point-like dipole is assumed for Eq. (5.17).

It is interesting to compare the estimates with the target accuracy of typical proposed EEP test missions, for example STE-QUEST. Relative accelerations between different atoms should be measured on the $2 \cdot 10^{-15}$ level in $\eta_{\text{A,B}}$ [62]. This level is shown as the dashed black line in Fig. 5.8(b). The force, but not the acceleration, is equal for different isotopes of the same atomic species, such that the relative acceleration is largely suppressed. For the case of potassium and rubidium, on the other hand, it is only slightly suppressed because of their similar polarizabilities ($\alpha_{0,\text{K}} = 43.4 \text{ cm}^3$ vs. $\alpha_{0,\text{Rb}} = 47.3 \text{ cm}^3$) [162], but different mass numbers. However, it is not hard to build the experiment such that electric dipole forces can be ruled out completely as a source of systematic errors.

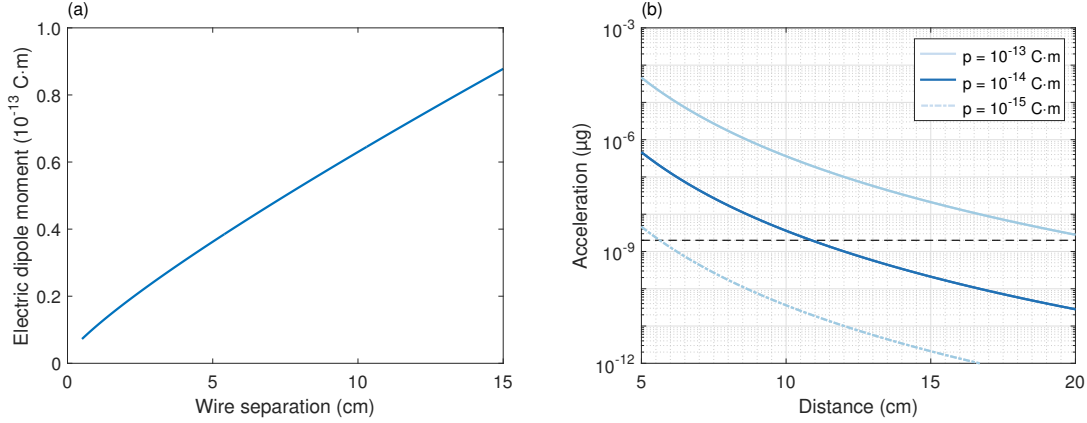


Figure 5.8: (a) Electric dipole moment of two wires of radius 0.25 mm and length 1 cm as a function of their separation. A potential difference of 12 V between the wires is assumed. (b) shows the acceleration of ^{87}Rb atoms due to the electric dipole field by various dipoles. The dashed black line shows the STE-QUEST target accuracy as a reference [62].

5.2.4 Detection pseudo force

There is another source of systematic errors arising when imaging dilute and highly asymmetric clouds. The asymmetry is caused by magnetic lensing with anharmonic magnetic traps. This 1D effect is calculated for the two lens types (SC-BC and pure BC). The small difference between Set B and C can be neglected here. The magnetic potential in the z direction is plotted in Fig. 5.9 for both lenses (blue line). Equal scales are chosen for comparison. The Gaussian ramp used for the SC-BC-lens is irrelevant for this discussion. It can be assumed that both lenses are simply switched on and off again. The parabolic approximation to the atomic density distribution for 10^5 atoms after the respective pre-TOF of 33 ms (SC-BC-lens) and 80 ms (BC-lens) is depicted as the black line. The relative atomic velocity is approximately proportional to the distance from the COM of the cloud, which is assumed to coincide with the lens trap center z_0 . A harmonic lens of the correct duration would stop the expansion without any further effects leading to a collimated ensemble. However, the lenses are not harmonic and the anharmonicities defined by Eq. (2.2) are

$$\begin{aligned} L_{3,\text{SC-BC}} &= -1/2.87 \text{ mm}, \\ L_{4,\text{SC-BC}} &= 1/3.28 \text{ mm}^2 \end{aligned} \quad (5.20)$$

and

$$\begin{aligned} L_{3,\text{BC}} &= -1/1.18 \text{ mm}, \\ L_{4,\text{BC}} &= 1/0.31 \text{ mm}^2. \end{aligned} \quad (5.21)$$

The L_3 -asymmetry in the magnetic potential is strongest and profoundly visible for the SC-BC-lens. This steeper increase towards the left, that is towards the chip, leads to an overcompensation of the relative atomic velocity. The opposite is the case for points to the right of the trap center. Atoms at the very left of the cloud fly through it and can separate from the COM again during the subsequent TOF.

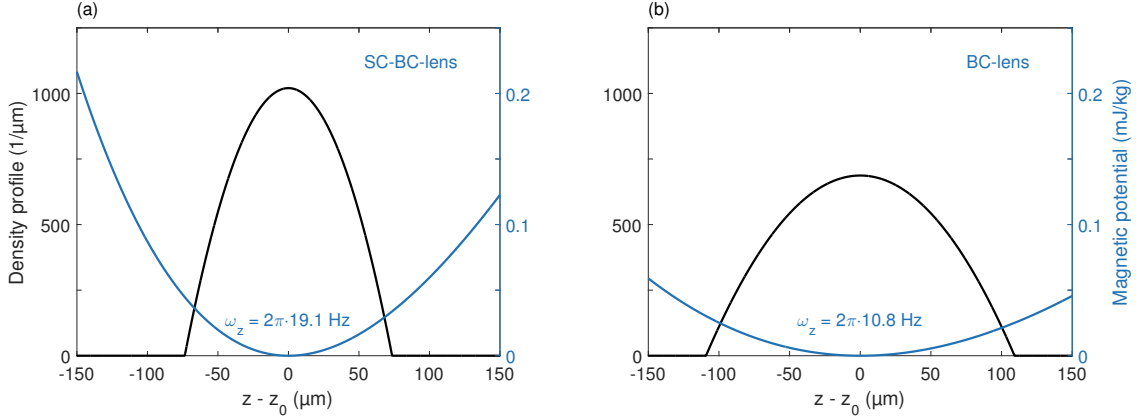


Figure 5.9: The magnetic lens potential (blue line) with its center at $z = z_0$ is shown for the SC-BC-lens (a) and the pure BC-lens (b). The 1D atomic density distribution for 10^5 atoms after the respective pre-TOF is shown as the black line. The frequencies of the lens traps are given in the figures.

The resulting density profiles after 2 s TOF are exemplarily shown in Fig. 5.10(a). The tail away from the chip is more pronounced for the SC-BC-lens, as expected. If all atoms were detectable, the L_3 -anharmonicity would merely result in a changed COM velocity:

$$\begin{aligned}\Delta v_{L_3, \text{SC-BC}} &= 188 \frac{\mu\text{m}}{\text{s}}, \\ \Delta v_{L_3, \text{BC}} &= 67 \frac{\mu\text{m}}{\text{s}}.\end{aligned}\tag{5.22}$$

However, the detection noise is superimposed with the atomic density signal and shrouds the atoms in the far end of the tail. Actually, these atoms have the strongest effect on the COM position due to their largest separation from it. If, for example, the detection threshold were at a density of $10/\mu\text{m}$, atoms in the shaded gray area in Fig. 5.10(a) would remain undetected. The threshold was roughly estimated from measured absorption images. In (b), the resulting effect on a measured COM (solid lines) is shown in comparison to the true COM (dashed lines). The deviation can be described by an increasing pseudo acceleration, which is significantly stronger for the SC-BC-lens. The values given in the figure depend on the chosen threshold value. Whether or not this pseudo acceleration is an issue can be seen by inspection of the x' coordinate of the COM, because this is the direction in which the tail is predominantly oriented. Hence, the largest effect can be expected in Fig. 5.1(a). Indeed, the fitted acceleration is rather negative, in contrast to sets B and C, but the uncertainty is larger than the value.

If the cloud and lens center do not coincide, the tail can be oriented at an angle to the z axis allowing for a pseudo acceleration in the y' direction. This was the case in Set A with a component of a_{pseudo} directed in the negative y' direction opposing the measured acceleration. Hence, this effect cannot be responsible for an over-estimation of the air drag, which is the last systematic effect in this discussion.

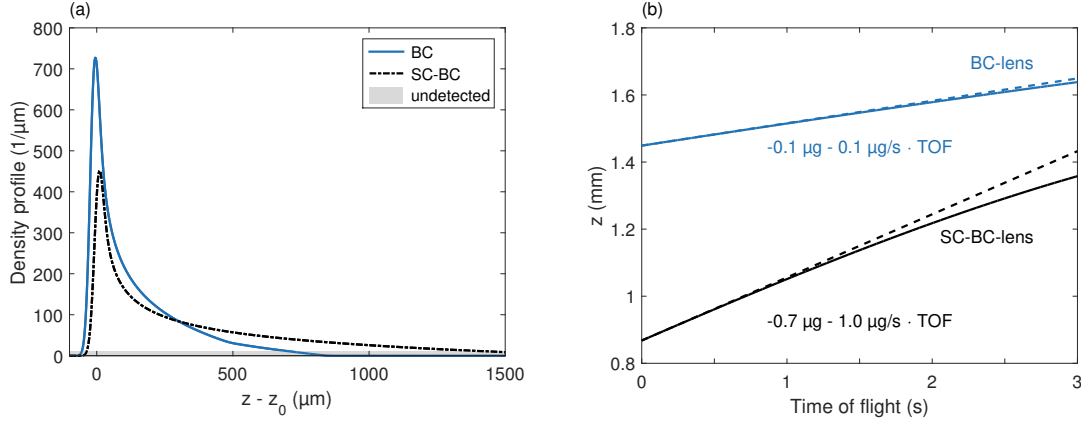


Figure 5.10: (a) shows the atomic density distributions from Fig. 5.9 after 2 s TOF. The shaded gray area at the very bottom depicts the roughly estimated detection threshold. The center of mass motion due to the L_3 anharmonicity is plotted in (b) as the dashed lines. The undetected atoms within the tail in (a) lead to a pseudo acceleration towards the chip, which is depicted by the solid lines. The pseudo acceleration is increasing with TOF and given in (b).

5.2.5 Residual air drag

The drop tower is evacuated to a pressure of 10-20 Pa. Still, this residual air impedes the free fall of the drop capsule such that it lags the free fall of the atomic ensemble within. The resulting differential velocity can be derived from [163] and is below 1 mm/s. Compared to the impact velocity of 46.3 m/s it can be treated as a small perturbation. The fictitious force on the atoms ($F_{\text{air drag}}$) within this accelerated frame is of equal magnitude, but opposite direction compared to the drag force on the capsule:

$$F_{\text{air drag}}^{\text{capsule}} = -F_{\text{air drag}} = -\frac{1}{2}c_d A \rho v_c^2, \quad (5.23)$$

where c_d is the drag coefficient, ρ the density of the remaining air, $A \approx \pi \cdot (0.4 \text{ m})^2 \approx 0.5 \text{ m}^2$ is the circular cross section of the drop capsule and v_c its velocity. Higher order contributions resulting in a small reduction of $F_{\text{air drag}}^{\text{capsule}}$ due to the reduced velocity by the drag itself are neglected, such that

$$v_c = gt \quad (5.24)$$

is assumed for all calculations. The drag coefficient depends on the Reynolds number and therefore on v_c [164]. Selig et al. have measured the residual acceleration in the drop tower with the SuperSTAR accelerometer [165] used for the GRACE mission [166] in order to test accelerometers for the MICROSCOPE mission [167]. They have shown that the residual acceleration has components that are both, quadratic and linear in the velocity. The latter one is known as Stokes friction, which is responsible for the velocity dependence of the drag coefficient:

$$c_d(v_c) \approx c_1 + \frac{c_2}{v_c}, \quad (5.25)$$

with constants c_1 and c_2 . The corresponding acceleration of the atoms can then be written as

$$a_{\text{air drag}} = a_S t + a_T t^2, \quad (5.26)$$

where $a_S t$ is the acceleration due to Stokes friction and

$$a_T = \frac{1}{2m} c_1 A \rho g^2 \quad (5.27)$$

parametrizes the acceleration due to turbulent drag (form drag). The following values can be fitted to the MICROSCOPE data [168]:

$$c_1 = 0.406(82) \quad (5.28)$$

and

$$a_S = 1.2(1) \cdot 10^{-5} \frac{\text{m/s}^2}{\text{s}}, \quad (5.29)$$

where the latter is rescaled to the mass of the Q-2 capsule (453 kg) and referenced to a temperature of 273 K. The temperature dependence is

$$a_S(T) = a_S(273 \text{ K}) \sqrt{\frac{T}{273 \text{ K}}}. \quad (5.30)$$

The following discussion assumes the drop mode for illustration. An adaptation to the catapult case is straightforward. In free fall, the air drag acceleration [Eq. (5.26)] of the capsule is upwards. While the atoms are trapped, they are co-accelerated with the capsule. After release at $t = t_1$ they accumulate the relative downward velocity

$$\begin{aligned} \Delta v_{\text{atoms}}(t, t_1) &= \int_{t_1}^t (a_S t' + a_T t'^2) dt' \\ &= \frac{a_S}{2} (t^2 - t_1^2) + \frac{a_T}{3} (t^3 - t_1^3), \end{aligned} \quad (5.31)$$

valid for $t_1 < t < 4.72 \text{ s}$. The resulting position difference at $t = t_2$ is

$$\begin{aligned} \Delta y_{\text{atoms}}(t_1, t_2) &= \int_{t_1}^{t_2} \Delta v_{\text{atoms}}(t, t_1) dt \\ &= \frac{a_S}{2} \left(\frac{t^3}{3} - t_1^2 t \right) + \frac{a_T}{3} \left(\frac{t^4}{4} - t_1^3 t \right) \Big|_{t_1}^{t_2} \\ &= \frac{a_S}{6} (t_2^3 - 3t_1^2 t_2 + 2t_1^3) + \frac{a_T}{12} (t_2^4 - 4t_1^3 t_2 + 3t_1^4). \end{aligned} \quad (5.32)$$

The MICROSCOPE data sets have been acquired during ten catapult flights. The measured acceleration traces suffer from the onset of noise and/or oscillations in many cases. In addition, the sensor was operated beyond the specified measurement range [165] and no information on the sensor calibration is available. Still, it is the only direct measurement of the residual air drag in the drop tower and was performed with a similar – but not equal – capsule as for Q-2. A compensation of exactly the effect calculated by Eqs. (5.27) to (5.30) and (5.32) leads to an underestimation of

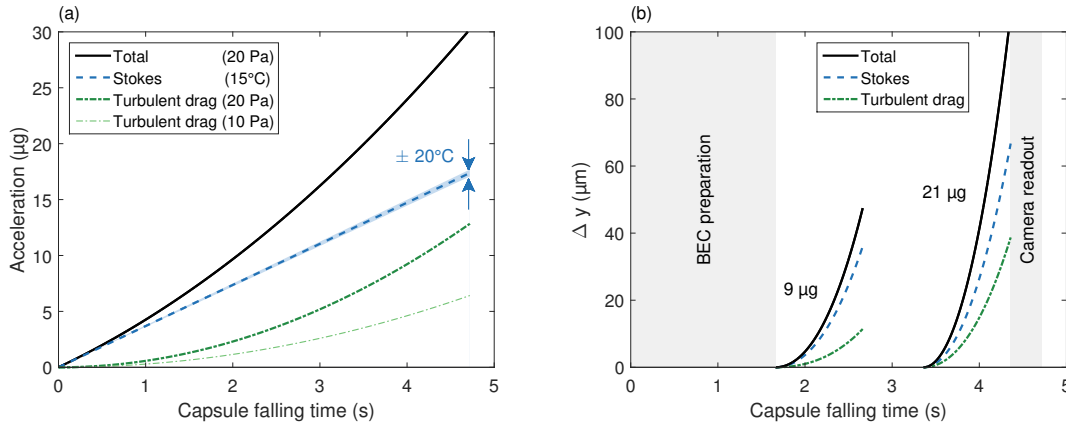


Figure 5.11: (a) shows the Stokes (dashed blue line) and the turbulent drag (thick dash-dotted green line) contributions to the total air drag (solid black line) at a tower pressure of 20 Pa. The turbulent drag at 10 Pa is shown by the thin dash-dotted green line. The shaded blue area visualizes the temperature dependence of the Stokes drag. (b) shows the different contributions to the atomic displacement Δy during 1 s TOF for two different start times. The respective average total accelerations are $9 \mu\text{g}$ and $20 \mu\text{g}$. The available TOF range is limited by the BEC preparation, the camera readout and the available total time in free fall.

$a_{\text{air drag}}$ measured by time of flight imaging (Fig. 5.1). The effect by the magnetic field gradient was corrected before this analysis. The residual accelerations differ from zero by approximately two standard deviations. It was shown above that other systematics affecting the atomic COMM are below the $1 \mu\text{g}$ -level. They cannot be responsible for the discrepancy. Systematic differences are the typical tower pressure, which was approximately 5 Pa lower for the MICROSCOPE flights than for Q-2 and the slightly different capsule. It cannot be ruled out that these systematics may account for the observed discrepancy. Further uncertainties are the actual pressure distribution within the tower and possibly convection, which would be time dependent. The issue with the sensor range might falsify the MICROSCOPE data, too, even though no saturation effects are visible. The detection pseudo force would contribute to an acceleration primarily in the x' direction, as discussed above.

The time of flight data from Fig. 5.1 do not allow to discern Stokes and turbulent drag. Therefore, the MICROSCOPE results are used, but rescaled by a factor of 2.1(8), which minimizes the residual accelerations in the y' direction. The resulting contributions to $a_{\text{air drag}}$ are depicted in Fig. 5.11(a) with linearly increasing a_S (dashed blue line) and quadratically increasing a_T (dash-dotted green lines). The Stokes friction is independent of pressure, but depends on the temperature according to Eq. (5.30). The effect is very small, as illustrated by the shaded blue area equivalent to temperature variations of $\pm 20^\circ\text{C}$. The turbulent drag, on the contrary, is proportional to the pressure, but independent of temperature. It is depicted by the dash-dotted green lines for tower pressures of 10 Pa and 20 Pa, respectively. The total air drag at 20 Pa is shown by the solid black line. In Fig. 5.11(b) the atomic displacement during 1 s time of flight is shown for the earliest possible case (left) and

the latest possible case (right). The left one is representative for a typical sequence with a TOF exceeding 600 ms. Even though the trajectory is not parabolic [see Eq. (5.32)], an average acceleration can be stated. It is of interest because this is precisely what fits to time of flight data would deliver. These average accelerations are much larger than those by the other systematics.

5.2.6 Corrected center of mass motion

It could be shown that most of the forces in Eq. (5.3) can be neglected, except for the air drag. $\vec{F}_{\text{magnetic}}$ is not neglected either, because it is well known for all data points, even though its contribution is smaller than a few micrometer. The data points from Fig. 5.1 are corrected for these two effects and shown in Fig. 5.12 as the full circles. The sole air drag effect, including the factor of 2.1, is visualized in Fig. 5.12(b), (d) and (f) by the comparison of the open circles to the filled ones. Two different model functions are fitted to the corrected data sets, a linear (dashed black line) and a quadratic one (solid blue line). The residual accelerations and the corresponding fit uncertainties are given in the figures. No acceleration differs from zero by more than one standard deviation. Again, all data points are weighted with $1/\sqrt{\text{TOF}}$. The results of the linear fits are given in Table 5.1 along with the residual accelerations from the quadratic fits. The accuracy at which the COM velocity can be determined is limited by the velocity scatter. The corresponding fit uncertainties of Set A can be compared with the velocity scatter in Fig. 5.2, because both data sets originate from the same release trap (release position A). The lens suppresses the velocity scatter by a factor of ten in this case.

All three data sets are limited to the Detection 1 coordinate system, in which the y' coordinate is a superposition of x and y [see Eq. (2.15)]. In order to determine the components of the COMM in these two directions, Data Set B is augmented by data acquired with Detection 2. This set is shown in Fig. 5.13. Again, the open circles are the raw data without air drag correction, which is effective in the y direction only. The fitted components of the COM velocity were used to estimate the Coriolis force above. The z component is $-0.37(2)$ mm/s and can be directly compared to $v_{x'} = -0.41(2)$ mm/s from Table 5.1. The values are similar, but not equal. This is not surprising, because the two data sets were measured in different drops. Even though the experimental sequence is equal, the atomic positions still scatter. The COMM in the y' direction can be reconstructed from the x and y fits in Fig. 5.13(a):

$$v_{y'} = \frac{0.04(4) \text{ mm/s} - (-0.28(1) \text{ mm/s})}{\sqrt{2}} = 0.23(3) \text{ mm/s},$$

which is slightly smaller than the $0.29(1)$ mm/s found with Set B in Fig. 5.12(d). Nevertheless, it can be seen from Fig. 5.13(a) that the largest component of the y' COMM is in the negative x direction, which is the one with the largest magnetic field gradient (see Section 3.4). This relation is discussed in Section 5.3. Still, the largest of all Cartesian velocity components in Set B is v_z and the total center of mass speed is $v_{\text{COM}} = 0.47(2)$ mm/s.

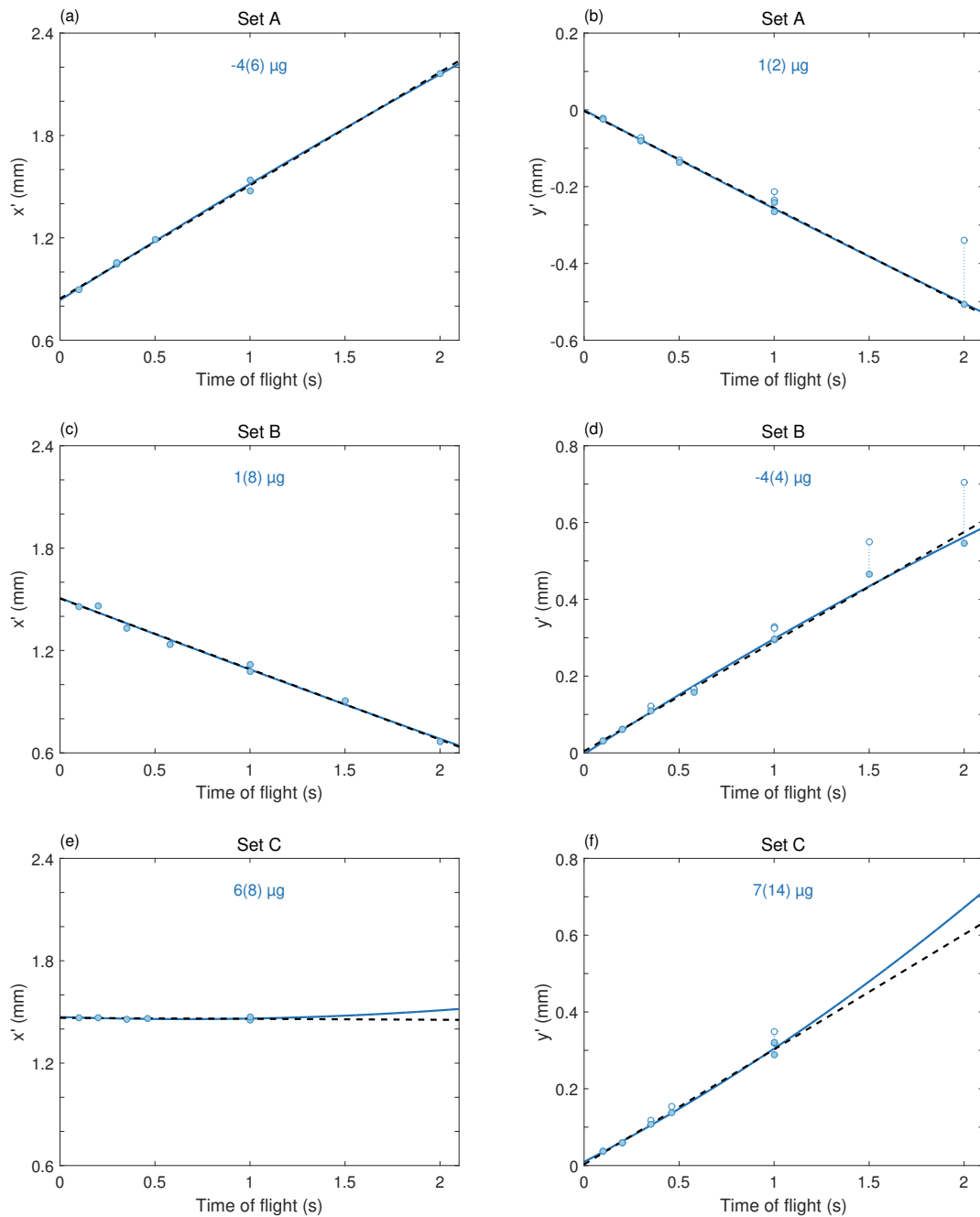


Figure 5.12: The figures show the corrected x' (left column) and y' (right column) COM coordinates of three data sets (A, B and C) of magnetically lensed atoms after different TOFs (see also Fig. 5.1). The open circles highlight the air drag correction, applicable to the y' direction only. The data in (a) and the open circles in (b) differ from the data points in Fig. 5.1 only due to the effect of $\vec{F}_{\text{magnetic}}$, which is hardly visible. The dashed black (solid blue) line is a linear (quadratic) fit to the respective data sets. The fitted residual accelerations are given in each subfigure.

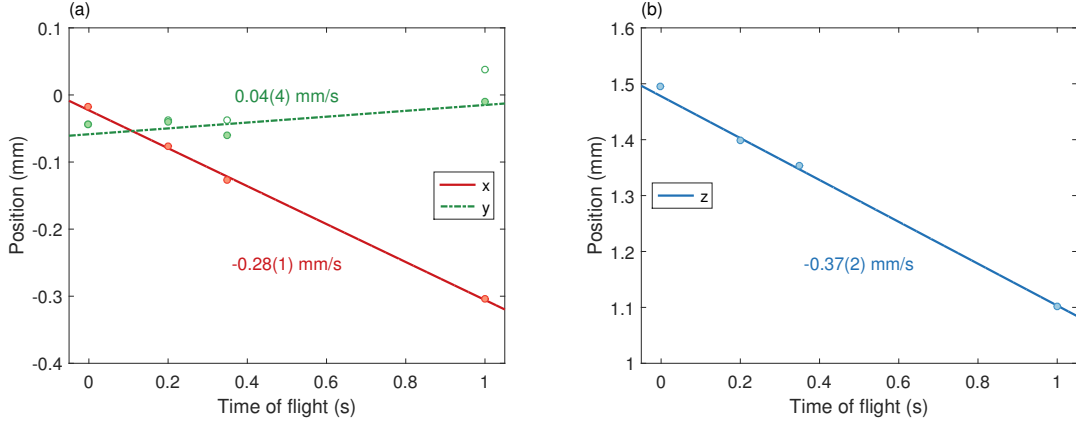


Figure 5.13: Center of mass positions measured with Detection 2 and the same experimental sequence that led to Data Set B in Table 5.1. The lines are linear fits to the respective data points. Open circles show the y coordinate without air drag correction.

| | lens type | x'_0 (μm) | y'_0 (μm) | $v_{x'}$ ($\mu\text{m/s}$) | $v_{y'}$ ($\mu\text{m/s}$) | $a_{x'}$ (μg) | $a_{y'}$ (μg) |
|-------|-----------|--------------------------|--------------------------|------------------------------|------------------------------|----------------------------|----------------------------|
| Set A | SC-BC | 844(13) | -3(5) | 664(18) | -252(7) | -4(6) | 1(2) |
| Set B | BC | 1505(16) | 4(8) | -414(20) | 286(10) | 1(8) | -4(4) |
| Set C | BC | 1465(4) | 3(7) | -6(9) | 300(14) | 6(8) | 7(14) |

Table 5.1: Overview of the fit results of Fig. 5.12 for the three data sets (A, B and C). The initial positions (at zero TOF) x'_0 and y'_0 as well as the initial velocities $v_{x'}$ and $v_{y'}$ come from the linear fit (dashed black lines in Fig. 5.12). The residual accelerations $a_{x'}$ and $a_{y'}$ are obtained from the quadratic fit.

5.2.7 Summary

Various forces within the Q-2 experiment leading to an acceleration of ^{87}Rb atoms in the $m_F = 0$ substate of the the $F = 2$ hyperfine manifold were discussed. The corresponding accelerations are summarized in Table 5.2. The Coriolis and centrifugal force refer to the drop mode and the air drag force to the maximum acceleration prior to the latest possible detection time ($\approx 4.4\text{s}$) at a tower pressure of 20 Pa. The detection pseudo force is a rough estimate for the BC-lens. The most significant acceleration is due to the residual air drag.

5.3 Reduction of the center of mass motion

There are a lot of contributions to the center of mass motion as described above. Some of them are negligible. Others need to be taken into account, but cannot be controlled well enough. For example the air drag and magnetic field gradients. The latter can be changed slightly by a different quantization field, but this makes no real difference. It would be better to identify the source and eliminate this gradient. However, this involves measuring the magnetic field within a partially opened magnetic shield, which is not comparable to a closed shield. A complete

| | |
|------------------------|---------------------------|
| Centrifugal force | $a < 0.1 \mu\text{g}$ |
| Coriolis force | $a < 0.5 \mu\text{g}$ |
| Magnetic dipole force | $a \leq 0.3 \mu\text{g}$ |
| Electric dipole force | $a \ll 0.1 \mu\text{g}$ |
| Air drag force | $a_y \leq 30 \mu\text{g}$ |
| Detection pseudo force | $a_z < 0.5 \mu\text{g}$ |

Table 5.2: Overview of accelerations of $m_F = 0$ atoms due to various forces in drop mode at a tower pressure of 20 Pa. The last entry refers to atoms after the BC-lens.

removal of the shield would require to disassemble the vacuum chamber. In fact, it is even conceivable that the magnetic shield itself is the source of the observed gradient. On the contrary, there are many options to control the COMM by properly adjusting the experimental sequence. They are discussed within this concluding part of the chapter.

5.3.1 Center of mass motion by dipole oscillations

The dipole oscillations within the release trap depend exclusively on the decompression phase of the final evaporation trap to either of the two release traps (A or B). The control options are the time within which the bias current is reduced and the shape of the control ramp. The primary direction of the dipole oscillation is along the z axis, because this is the direction in which the trap is moved. Actually, a small residual dipole oscillations can be useful, because the COMM can be tuned by changing the hold time within the trap prior to the release. However, it is more difficult to suppress rather than excite dipole oscillations. For this reason a complete suppression of the dipole oscillation is aimed at.

Three different strategies are presented. The first one is to gently ramp the bias current within 250 ms from -1.5 A to -0.6 A (release position A) using an $s = 10$ sigmoid [Eq. (5.1)]. This strategy is used for the SC-BC lens. The pure BC lens is further away from the chip (position B). This requires either a much longer sigmoid ramp or a different strategy. One possibility is to ramp out fast (75 ms), which leads to large oscillation amplitudes, and to rapidly move the trap center to the atom's COM when they are at the turning point of the oscillation. This strategy is reminiscent of quickly moving a load suspended by a rope on a crane. Hence it is referred to as 'crane trick'. The third strategy is to design the control ramp for the bias coil such that the atoms are at rest after the ramp. This is called shortcut to adiabaticity (STA).

Numerical simulations of the atomic COM trajectory are conducted as follows: Spatial gradients of the magnetic potential at the current position are calculated using the chip model. The new position is then determined by Verlet's algorithm [169] in its velocity form [170]. The atomic velocity is deduced by simple differentiation. The COM oscillations after a TOF can be directly calculated from this velocity. A contribution of the oscillating *in situ* position is negligible for all measurements presented in this context.

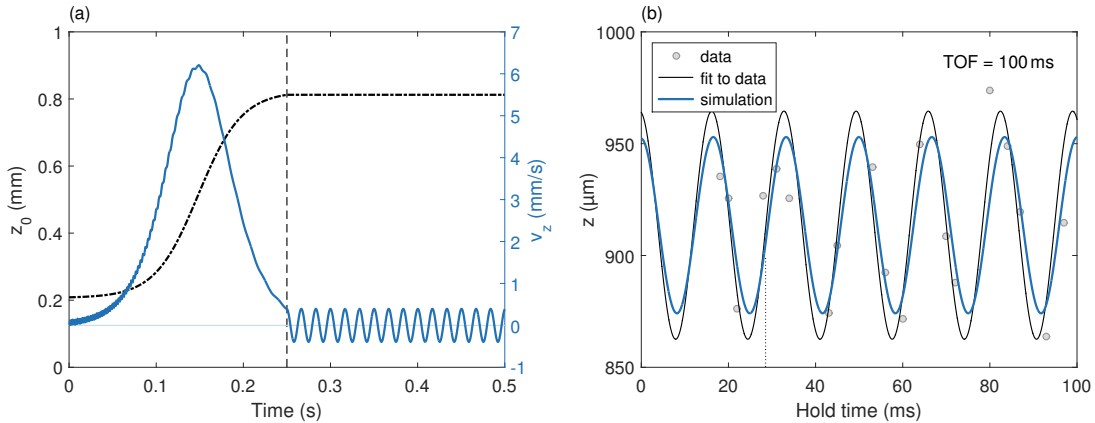


Figure 5.14: (a) Simulated trap center z_0 when decompressing the final evaporation trap within 250 ms to release trap A using an $s = 10$ sigmoid control ramp [see Eq. (5.1)] for the y coil (dash-dotted black line). The end of this ramp is highlighted by a vertical dashed black line. Subsequently, the trap center is held constant for another 250 ms to illustrate *in situ* oscillations as shown by the velocity v_z (solid blue line). (b) The expected position after 100 ms TOF due to this oscillation is shown by the solid thick blue line as a function of the hold time, which starts after the ramp in (a). The results from Fig. 5.2(a) are shown for comparison (gray points and solid thin black line). The release time used for magnetic lensing is 28.52 ms and highlighted by the dotted black line.

Strategy 1: slow sigmoid ramp

The simulation results for the 250 ms sigmoid ramp are presented in Fig. 5.14. The dash-dotted black line in (a) is the z coordinate of the trap center (z_0), starting at 209 μm . After the ramp it is held constant at 812 μm in order to simulate the resulting *in situ* dipole oscillations. The COM velocity in the z direction (v_z) is plotted as the solid blue line (right axis). It peaks at about 6 mm/s. For comparison, the average velocity required for transport is $(812 - 209)/250 \mu\text{m}/\text{ms} \approx 2.4 \text{ mm/s}$. At the end of the ramp, highlighted as the vertical dashed line, v_z is nonzero. This leads to the dipole oscillation. The abscissa of the velocity plot is indicated as the solid light blue line. The rapid oscillation in the beginning is no numerical artifact. It has, however, practically no influence on the final state. Oscillations in the other directions are smaller by more than two orders of magnitude and are neglected.

The resulting dipole oscillation after 100 ms TOF is shown in Fig. 5.14(b) as the solid blue line. It is compared to the fit to the measured data in Fig. 5.2(a) [solid black line], which has a slightly larger amplitude [51(6) μm vs. 39 μm]. The simulated trap frequency ($2\pi \cdot 59.83 \text{ Hz}$) is 1% smaller than the one fitted to the data [$2\pi \cdot 60.4(3) \text{ Hz}$]. The predicted initial phase of the oscillation is in excellent agreement with the measured one. The center of the after-TOF oscillation, however, cannot be predicted in this context. It is shifted by 102 μm to the fitted value of 914 μm for comparison.

The turning points of the *in situ* oscillation correspond to the center of the after-TOF oscillation and vice versa. The measured after-TOF amplitude corresponds to

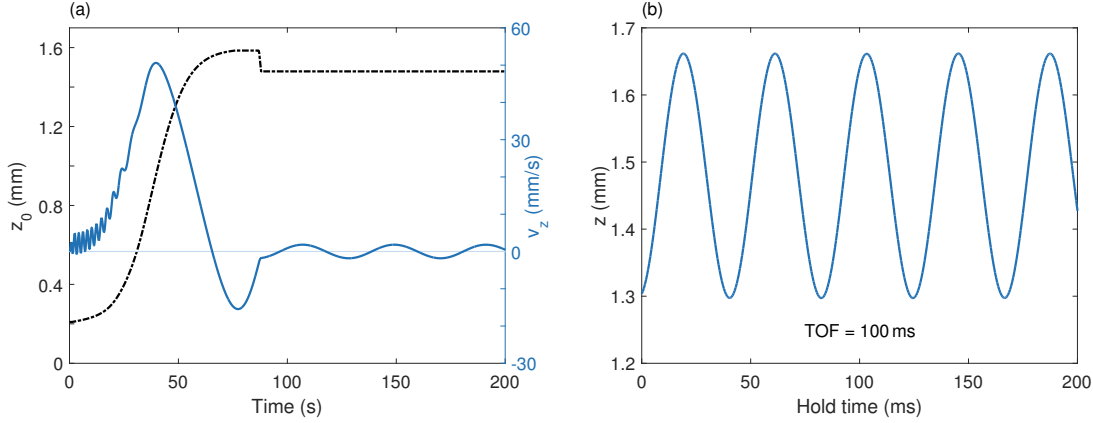


Figure 5.15: (a) Simulated trap center z_0 (dash-dotted black line) and velocity v_z (solid blue line) during trap decompression (75 ms), crane trick delay t_{ct} (11 ms), crane trick (1 ms) and subsequent hold time. (b) shows the simulated after-TOF oscillation about release position B as a function of the hold time after the crane trick.

peak *in situ* velocities of $\pm 51 \mu\text{m}/100 \text{ ms} \approx \pm 0.5 \text{ mm/s}$. This is the range in which the COM velocity in the z direction can be tuned by varying the hold time prior to release from trap A. Larger amplitudes are not necessarily helpful because of the increased sensitivity to an uncertainty in the phase of the oscillation. For the SC-BC lens a hold time of 28.52 ms is used, as depicted by the dotted line in Fig. 5.14(b).

Strategy 2: 'crane trick'

Moving the atoms to release position B requires a longer decompression time or a higher average velocity. For the crane trick the trap is moved within 75 ms to a position even beyond release position B, as shown by the dash-dotted line in Fig. 5.15(a). This very fast method leads to a peak velocity of approximately 50 mm/s and a large dipole oscillation. It is large enough to be resolvable by the *in situ* multi detection scheme described above. This measurement can also be performed after the trap had been moved by suddenly switching the SC current from 2 A to some smaller value⁴. The choice of the SC for switching is arbitrary. Alternatively, the BC current (6 A) could be reduced. The y coil is not used because it is much slower. The resulting shift of the trap affects the oscillation amplitude. Its change depends on the time of the SC switching (t_{ct} in ms) and the final current (I_{ct} in A) after this crane trick. The chip model allows for educated guesses and a model function for the expected oscillation amplitude can be derived [171]:

$$A_{\text{osc}} = \text{offset} + \sqrt{102403 \cdot (I_{ct}^0 - I_{ct})^2 + 44094.8 \cdot \sin[0.0667964 \cdot (t_{ct}^0 - t_{ct})^2]}, \quad (5.33)$$

where the offset accounts for the finite resolution of the imaging system. The measurement is repeated for different values of I_{ct} and t_{ct} . By least squares, the experimentally optimized values for the crane trick are $I_{ct}^0 = 1.68(2) \text{ A}$ after a hold time

⁴Larger values are not possible, because the SC is limited to 2 A.

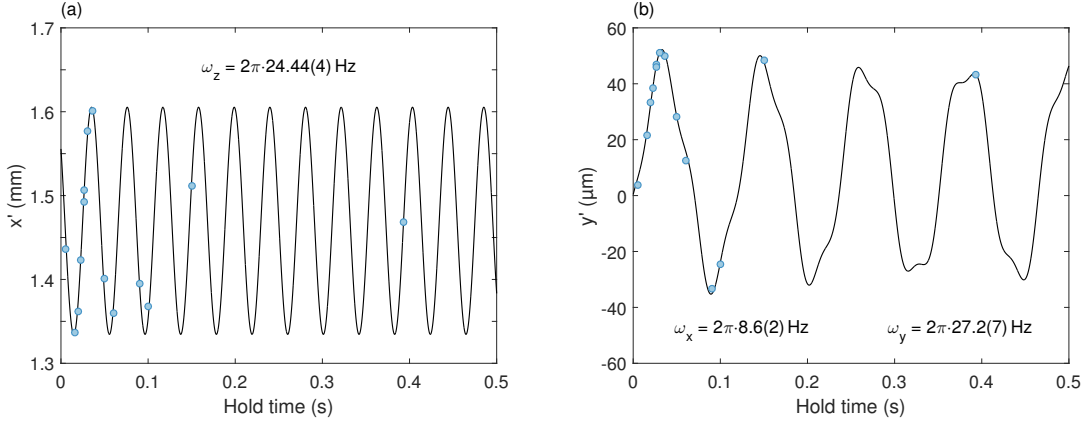


Figure 5.16: (a) Shows the measured x' positions after the crane trick and 100 ms TOF (blue circles) as a function of the hold time [see Fig. 5.15(b)]. A sinusoidal fit at a frequency of $\omega_z = 2\pi \cdot 24.44(4)$ Hz is shown as the solid black line. (b) Shows the corresponding y' positions of the same data points. The fitted curve is a beat note of the frequencies $\omega_x = 2\pi \cdot 8.6(2)$ Hz and $\omega_y = 2\pi \cdot 27.2(7)$ Hz.

of $t_{\text{ct}}^0 = 11.0(2)$ ms. These values were used for the simulation in Fig. 5.15. The estimated standard error of A_{osc} is $\sigma_A \approx 10 \mu\text{m}$ for the uncertainties $\sigma_I = 20$ mA and $\sigma_t = 0.2$ ms. This value for σ_A maps to an uncertainty of 0.15 mm for the after-TOF amplitude, which is approximately the simulated amplitude shown in Fig. 5.15(b).

The measured after-TOF oscillation for the optimized crane trick parameters is shown in Fig. 5.16. Indeed, the measured x' amplitude is of the same order, too. The accuracy of the crane trick is limited by the measurement of the *in situ* oscillation amplitude. Still, a second crane trick based on the knowledge of the residual oscillation can reduce it further. Nevertheless, this would be more complicated because the residual oscillation is three dimensional, as can be inferred from the y' oscillation in Fig. 5.16(b). In this direction a superposition of the x and y oscillation can be seen. The fitted after-TOF amplitudes are $A_x = 39(2) \mu\text{m}$ and $A_y = 6(1) \mu\text{m}$. Hence, the x component dominates. The chip model predicts trap frequencies of $\omega = 2\pi \cdot (8.3, 26.5, 23.8)$ Hz in this trap. The measured ones (see Fig. 5.16) are approximately 3% higher.

Strategy 3: STA

The last strategy for minimizing the residual dipole oscillations within the release trap is to design a ramp shape for the bias coil with the following constraints:

1. trap center and atomic COM coincide at the beginning and at the end of the ramp,
2. the atomic COMM is zero at the beginning and at the end of the ramp,
3. the ramp shape is smooth compared to the y coil's step response function.

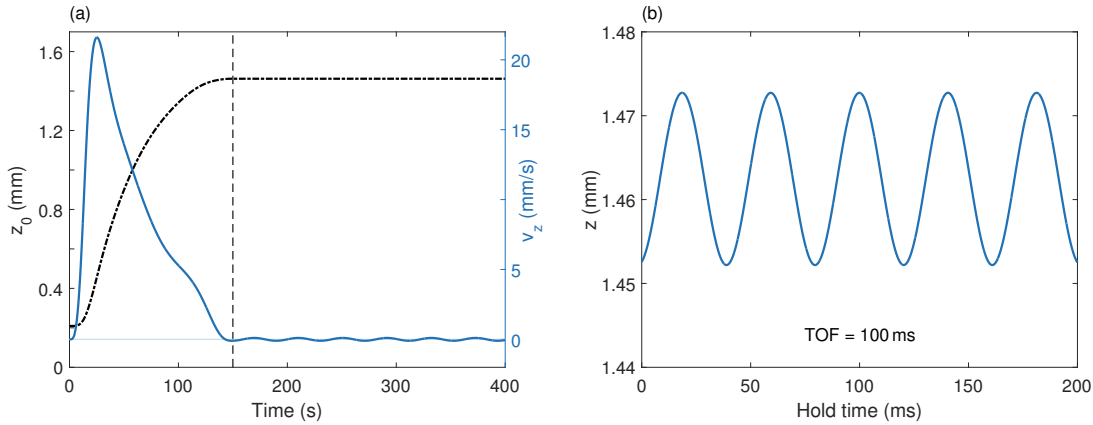


Figure 5.17: (a) shows the simulated trap center z_0 (dash-dotted black line) and the velocity v_z (solid blue line) when decompressing to release trap B with a 150 ms y coil ramp designed to minimize residual oscillations. The corresponding oscillation after 100 ms TOF is depicted in (b). The hold time starts at the end of the ramp, which is indicated by the vertical dashed black line in (a).

The last constraint in combination with the matching centers at the beginning is a necessary condition for the existence of a control function for the bias coil which can produce such a ramp for the bias current. This STA approach takes into account the rapidly decreasing trap frequency during the ramp, too. The ramp was calculated for a duration of 150 ms by Robin Corgier (Institute of Quantum Optics, Hanover). Much faster shortcuts would be possible, but this duration is chosen in view of strong collective excitations after the 75 ms ramp for the previous strategy. The course of the trap center and that of v_z are plotted in Fig. 5.17(a). In the beginning the atoms are rapidly accelerated up to a velocity exceeding 20 mm/s. Afterwards, for the major fraction of the ramp time, the atoms are continuously decelerated to zero. Actually, there should be no residual oscillation by construction. The simulated after-TOF amplitude of approximately 10 μm [Fig. 5.17(b)] arises from the fact that an analytical model function had to be fitted to the chip model for the STA calculations resulting in small deviations. In fact, the measured x' oscillation is yet larger, as can be seen in Fig. 5.18(a). The oscillation in the y' direction (b) is much smaller than for x' . It is not possible to fit a beat note to these data points. All fitted frequencies agree reasonably well with $\omega_B = 2\pi \cdot (9.1, 27.9, 24.6)$ Hz as predicted by the chip model. The after-TOF x' -amplitude is 74(10) μm corresponding to a tuning range of ± 0.7 mm/s. A hold time of 18.46 ms (vertical dotted line) is chosen for the BC lens as explained below.

Summary

In principle, all three strategies can be applied for moving the atoms to the desired release position. Despite its smallest residual oscillation, the sigmoid ramp is only useful for spatially short transfers. The crane trick protocol is the quickest one, but it heavily excites collective modes of the trapped condensate, as will be explained in

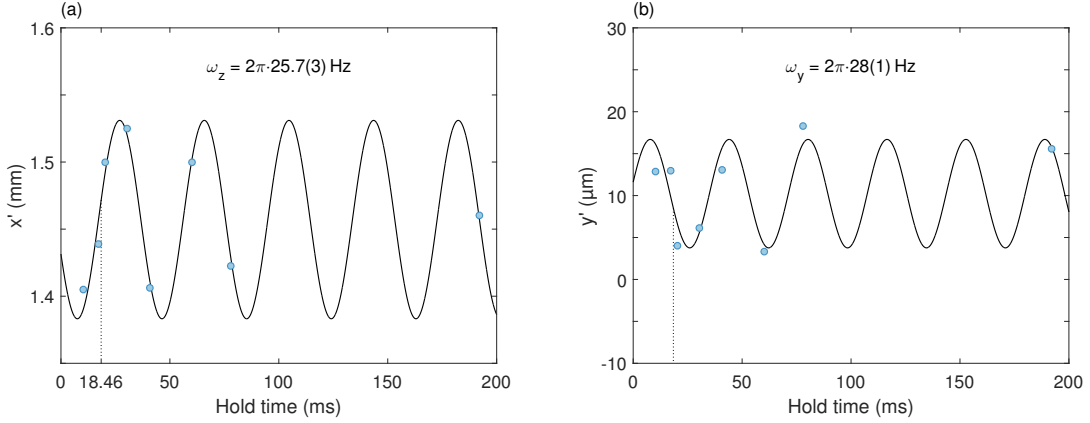


Figure 5.18: (blue circles) Measured x' (a) and y' (b) positions with 100 ms TOF are shown as a function of the hold time after the trap decompression in Fig. 5.17(a). Sinusoidal fits to the data are plotted as the solid black lines and yield $\omega_z = 2\pi \cdot 25.7(3)$ Hz and $\omega_y = 2\pi \cdot 28(1)$ Hz, respectively. The hold time chosen for magnetic lensing is 18.46 ms. It is depicted as the dotted black line.

the next chapter. Furthermore, the residual y' oscillation is difficult to handle. The STA ramp excites collective modes, too, but not equally strong. Therefore it is used for the transfer to release position B. In fact, this particular excitation can even be useful for the magnetic lens. The crane trick is not used at all for magnetic lensing primarily because of these too strong collective modes. All measured residual x' oscillations could be reduced further by a small crane trick. However, neither this nor the deliberate excitation of a dipole oscillation is required for COMM tuning.

5.3.2 Center of mass motion by trap switch-off

The chip currents can be changed more rapidly than the coil currents, as discussed in Section 3.2. For illustration, the first part of the step response function for the chips and the bias coil (see also Fig. 3.3) are replotted in Fig. 5.19(a). This mismatch causes the trap to move towards the chip with the trapped atoms co-accelerated. This acceleration depends on the trap frequency and is stronger for the high frequency traps at larger bias currents closer to the chip. This kick imprinted on the atoms is simulated with the help of the chip model. The standard configuration with $I_{BC} = 6$ A and $I_{SC} = 2$ A is used for two different x coil currents (0.1 A and 0.5 A). The predicted kick is plotted as a function of the bias current in Fig. 5.19(b), confirming the qualitative argument above. It can be seen that the x current hardly affects this kick. The difference with vs. without gravity is even smaller (not shown). The plotted curves were simulated for microgravity conditions.

It is interesting to analyze three particular points. If the atoms were released from the final evaporation trap by simply switching off all currents, the predicted kick at, for example, $I_x = 0.5$ A would be -7.43 mm/s. At the standard lab TOF of 22 ms, this corresponds to a displacement of 163 μ m towards the chip. Since the

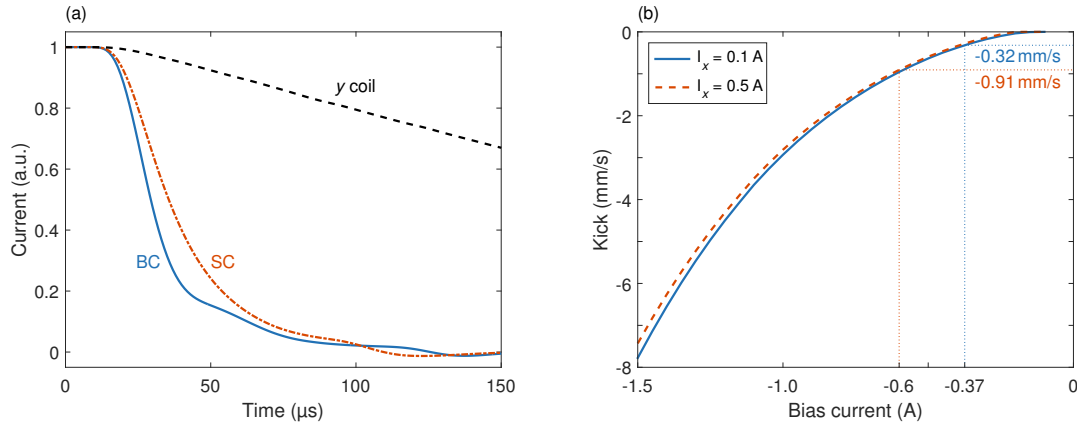


Figure 5.19: (a) shows a direct comparison of the step response functions of the BC (solid blue line), the SC (dash-dotted orange line) and the y coil (dashed black line) from Fig. 3.3 for the first 150 μs after switching the control to zero. The simulated kick imprinted on the atoms due to the mismatched switching in (a) is shown in (b) as a function of the initial bias current for $I_{\text{BC}} = 6 \text{ A}$, $I_{\text{SC}} = 2 \text{ A}$ and two different x coil currents [0.1 A (solid blue) and 0.5 A (dashed orange)], which are kept constant. The kicks for the two release positions are -0.32 mm/s and -0.91 mm/s . They are highlighted by the respective dotted lines.

corresponding release position is at $z = 209 \mu\text{m}$, the atoms can be expected to be very close to the chip. Indeed, this is observed. The predicted kick at release position B with $I_y = -0.37 \text{ A}$ is only -0.32 mm/s , which is well within the tuning range of the corresponding dipole oscillation [Fig. 5.18(a)]. Hence, this simple release protocol can be expected to suffice for the BC lens. The situation is different for the SC-BC lens. The predicted kick at release position A with $I_y = -0.6 \text{ A}$ is -0.91 mm/s and exceeds the corresponding tuning range of 0.5 mm/s (sigmoid ramp). A different switch-off protocol is favored over the excitation of such a strong dipole oscillation.

Two alternatives to the simple trap switch-off are depicted in Fig. 5.20. A trap motion can be suppressed by simultaneously ramping down all magnetic fields contributing to the trap. Since the bias coil is slowest, all other currents are matched to it. The simplest way is depicted in (a). The control of the bias coil (thin light blue line) is switched to zero and the remaining currents (dashed orange line) are matched to the y coil response (solid blue line) until $I_y = 0$ for the first time. The same procedure needs to be applied to the x coil, too (not shown). However, the required kink at zero current cannot be realized very well. The other alternative is shown in Fig. 5.20(b). The y coil control is switched to a finite value such that the overshoot is tangent to the abscissa. All other currents can be easily matched to such a smooth function and are kept at zero afterwards. The rampdown of the bias coil control reduces the subsequent oscillation of the y current. The ramp shapes for the chips and the x coil are calculated for a ramp time of 0.98 ms . If this time is changed without recalculating the ramp shape, the currents will no longer be matched. This can be used to tune the COMM after release. A longer ramp time leads to a reduced share of bias current and hence to a trap moving away from

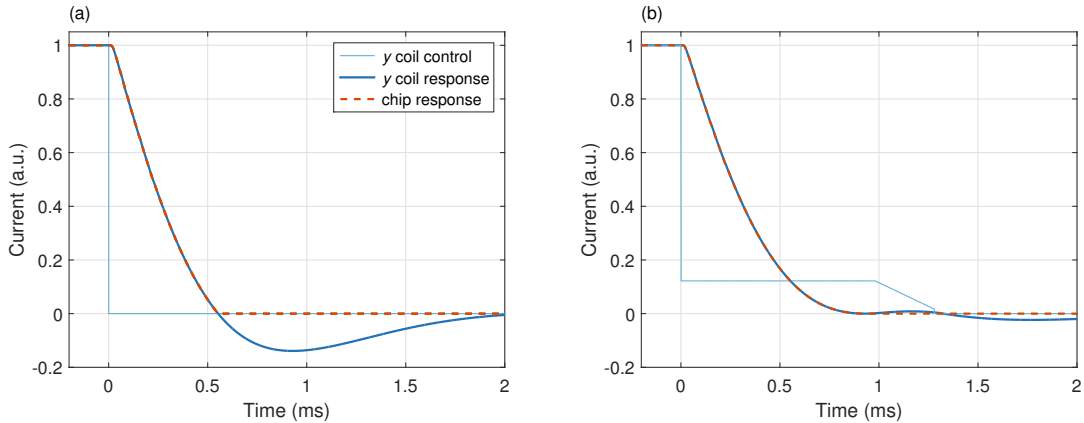


Figure 5.20: Comparison of two strategies for matching the chip currents to that of the y coil: (a) The y coil control (thin solid blue line) is switched to zero and the chip control (not shown) is chosen such that its response (dashed orange line) matches the y coil current (solid blue line) until it reaches zero for the first time. (b) The y coil control is switched to a finite value resulting in an overshoot tangent to the abscissa. The chip currents are matched accordingly.

the chip. In fact, a ramp time of 1.12 ms has to be used in order to minimize the COMM. A possible cause is a delayed magnetic field decay due to eddy currents. However, this effect could not be quantified so far.

5.3.3 Miscellaneous contributions to center of mass motion

The major control knobs for the COMM in the z direction are the hold time prior to release and the release itself. After release, the atoms are primarily accelerated by the magnetic field gradient and by changing coil currents. The air drag is small compared to these forces, which amount to several hundred μg (see Figs. 3.6 and 3.8). This magnetic field gradient could be mitigated by temporarily transferring the atoms from $m_F = 2$ into the $m_F = 0$ substate. Apart from that, a compensation by using the $m_F = -2$ substate is conceivable, too. The atoms would have to be transferred to the $m_F = -2$ substate after $1/4$ of the pre-TOF and transferred back to $m_F = 2$ after $3/4$. This cancels out the velocity as well as the position change due to the gradient. However, these schemes typically require coil switching for an efficient ARP, which also affects the atomic velocity. Still, an efficient state reversal is possible at smaller B -fields compared to the $m_F = 0$ transfer. Hence, this is an interesting prospect for the future.

The effect of B' during the pre-TOF can be calculated. As an example, the largest component of ∇B is used $\left[\frac{\partial B}{\partial x} \Big|_{I_x=0.5 \text{ A}} = 1.00(2) \frac{\text{G}}{\text{m}}, \text{ see Section 3.4} \right]$. The effect after 80 ms pre-TOF, which is used for the BC lens, is a velocity change of -0.5 mm/s and a displacement of $-21 \mu\text{m}$, both in the x direction. It should be mentioned that this combination was never used. This quantization field is used for the SC-BC lens campaigns with a pre-TOF of 33 ms. Unfortunately, no 3D information on

the gradient for $I_x = 0.1\text{ A}$ is available and the gradients are not equal, because the 2D components are different. On the other hand, the y' components differ by approximately 10% only. The observed velocity in the y' direction after the BC lens [Figs. 5.1(d) and (f)] is approximately 0.3 mm/s . The kick calculated above would have a component of $-(-0.5\text{ mm/s})/\sqrt{2} \approx 0.35\text{ mm/s}$ in this direction. The fitted initial y' -velocity after release is only $0.18(4)\text{ mm/s}$ [Fig. 3.8(b)]. Hence, a part of the observed COMM in the y' direction after the BC-lens could indeed be caused by the magnetic field gradient. However, this is only a hint rather than a proof, because the gradient is not fully known for this configuration.

A mismatch of magnetic lens center and atomic COM also leads to a kick. To a small degree, the lens position can be used to tune the COMM. Larger deviations can affect the collimation and should be avoided. The z coordinate of the COM is adjusted by the methods described above. The resulting positions are compared with the Detection 2 system in order to gain 3D information. The corresponding measured absorption images are shown in Fig. 5.21 for the SC-BC-lens and in Fig. 5.22 for the BC-lens. The left images (a) show the atomic cloud after the respective pre-TOF. The right ones (b) show an *in situ* image of atoms trapped in the respective lens trap. The dotted lines depict the grid of SC conductors as the coordinate reference. Figures 5.21 and 5.22 are plotted with the same scale. The two subclouds (left and right, see also Fig. 2.10) are further apart for the BC-lens, as expected from the larger distance from the chip. All positions are summarized in Table 5.3 with the corresponding fit uncertainties. The positions for a repeated measurement of the one in Fig. 5.21(a) is also given (D121b). The Q-2 coordinates are calculated from the Detection 2 coordinates by invoking Eq. (2.17). The results are given in the bottom three rows of the table. All deviations are on the order of $10\text{ }\mu\text{m}$. Dipole oscillations within the lens trap can falsify the *in situ* measurement. The transfer to the SC-BC lens trap was performed very smoothly such that oscillation amplitudes are assumed to be small. Still, this was not checked.

Chronologically, the SC-BC-lens campaign was completed before the second detection system became available. For this reason, the positions could only be checked but not improved based on the new information. On the other hand, the BC-lens could profit from it. Besides the COMM control, an optimally matched position simplifies the quantitative description of the lens, which is the subject of the next chapter. A mismatch Δx_i in the i direction leads to the velocity change

$$\Delta v_i = \omega_i^2 \Delta x_i \tau_{\text{lens}}, \quad (5.34)$$

where τ_{lens} is the lens duration ($\tau_{\text{BC-lens}} = 2.64\text{ ms}$) and ω_i is the respective trapping frequency of the lens trap [$\omega_{\text{BC-lens}} = 2\pi \cdot (3.0, 10.8, 10.8)\text{ Hz}$]. The resulting velocity change per micrometer position mismatch is $\Delta v_x = 1\text{ }\mu\text{m/s}/\mu\text{m}$ and $\Delta v_{y,z} = 12\text{ }\mu\text{m/s}/\mu\text{m}$. In the y direction, the positions differ by $9\text{ }\mu\text{m}$. Hence, this lens kick amounts to $12\text{ }\mu\text{m/s}/\mu\text{m} \cdot 9\text{ }\mu\text{m} = 108\text{ }\mu\text{m/s}$ in the y direction and cannot be responsible for the observed velocity of 0.3 mm/s in the y' direction, which was discussed above (x gradient). This position mismatch can be corrected by a different z current. According to the chip model, the lens trap moves by $\Delta y_0 = +14.7\text{ }\mu\text{m}/\text{mA}_z$. Therefore, the required correction is $\Delta I_z = 0.61\text{ mA}$. This needs to be compared to

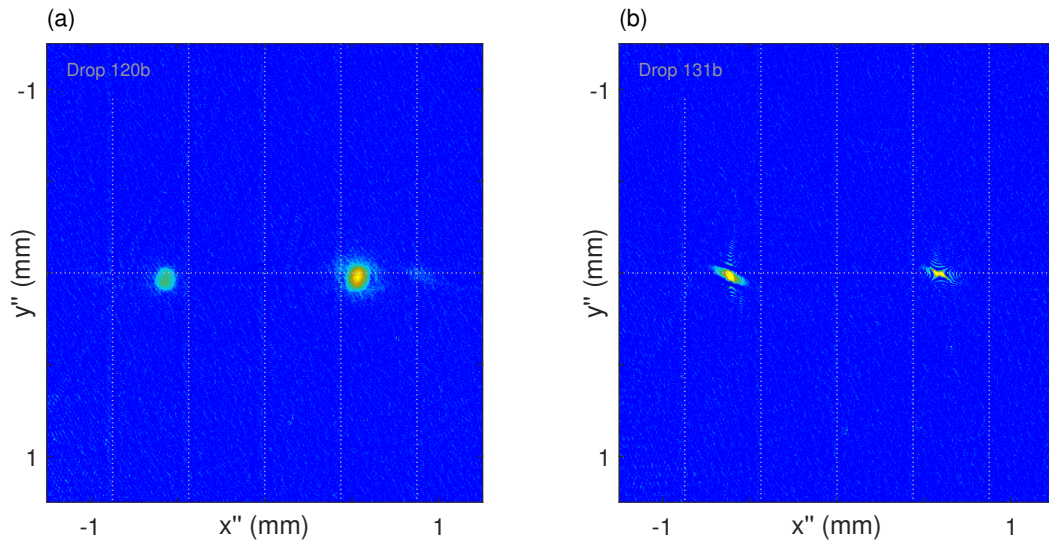


Figure 5.21: The position of the atoms at the time of the SC-BC magnetic lens [(a), 33 ms pre-TOF, release position A] is compared to the position of this lens by an *in situ* measurement of atoms in the lens trap (b). Both images are taken with Detection 2. The coordinate system is referenced to the grid defined by the SC conductors, which are depicted as the dotted gray lines.

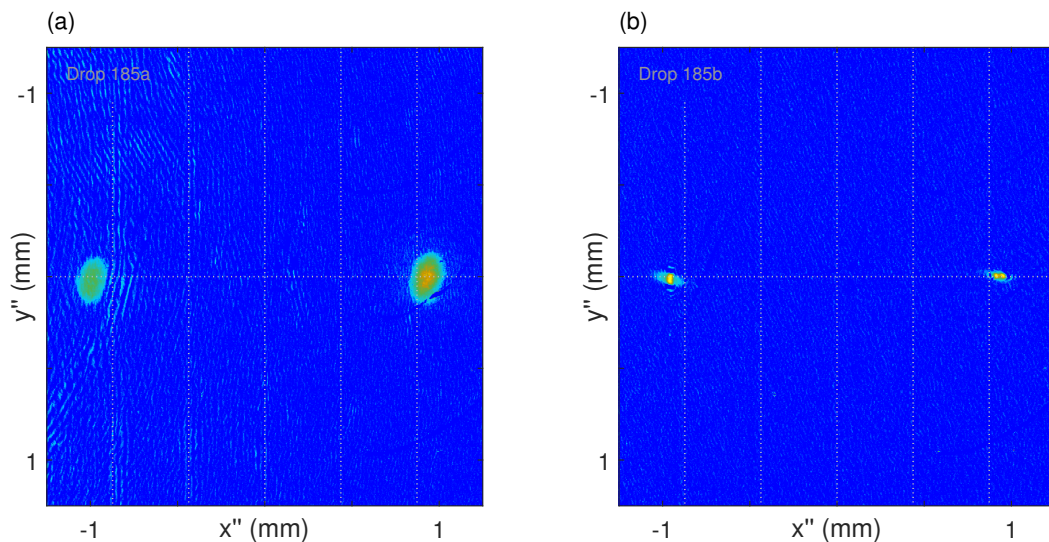


Figure 5.22: The position of the atoms at the time of the BC magnetic lens [(a), 80 ms pre-TOF, release position B] is compared to the position of this lens by an *in situ* measurement of atoms in the lens trap (b). Both images are taken with Detection 2. The coordinate system is referenced to the grid defined by the SC conductors, which are depicted as the dotted gray lines.

| (in μm) | SC-BC lens pre-TOF Drop 120b | SC-BC lens pre-TOF Drop 121b | SC-BC lens <i>in situ</i> Drop 131b | BC lens pre-TOF Drop 185a | BC lens <i>in situ</i> Drop 185b |
|---------------------|------------------------------------|------------------------------------|---|---------------------------------|--|
| x''_L | -558(1) | -562.0(8) | -601.4(3) | -977.5(9) | -942.6(3) |
| x''_R | 542.2(3) | 549.9(3) | 593(1) | 938.6(2) | 935.9(9) |
| y''_L | 45.3(6) | 43.8(6) | 26.3(2) | 32.1(4) | 21.1(3) |
| y''_R | 30.0(3) | 28.1(3) | 10.7(2) | 13.8(3) | 6.6(1) |
| x | -8.0(5) | -6.0(4) | -4.3(5) | -19.5(5) | -3.3(5) |
| y | 37.7(3) | 36.0(3) | 18.5(1) | 22.9(3) | 13.9(2) |
| z | 831.9(9) | 841.3(7) | 908.8(8) | 1501.8(8) | 1470.8(7) |

Table 5.3: Coordinates within the Detection 2 coordinate system of the left and right cloud in Figs. 5.21 and 5.22. D121b is a repeated measurement of D120b [Fig. 5.21(a)]. All errors are fit uncertainties. The Q-2 coordinates (x, y and z) are calculated using Eqs. (2.17a) to (2.17c).

the precision of the analog outputs. One bit is equivalent to 0.305 mA. The correction corresponds to almost 2 bits. It is just below the threshold, such that no unwanted bit change occurs. Based on this, the z current compensating the offset field [see Fig. 3.1(b)] is increased for the BC-lens campaigns. Unfortunately, this correction was based on the false assumption, that the *in situ* image [Fig. 5.22(b)] was taken at the center of the y oscillation. The *in situ* oscillation within the lens trap is shown in Fig. 5.23. Since only four data points are available, the simulated trap frequencies (chip model) are used for fitting. The center of the oscillation is plotted as the dashed black line. The expected position for the hold time of 24 ms, which was used for the *in situ* measurement in Fig. 5.22(b), is depicted as the dotted black line. The oscillation in (b) is due to a y oscillation. An x oscillation would occur at a frequency of 3 Hz and is not covered by the range of hold times. Such an oscillation would effectively result in an offset in the y' fit. As a matter of fact, the shift of $[-8\mu\text{m} - (-15\mu\text{m})] = 7\mu\text{m}$ in the y' direction corresponds to a shift of $7 \cdot \sqrt{2}\mu\text{m} \approx 10\mu\text{m}$ in the y direction. This is almost equal to the deviation found in Table 5.3 for the y coordinate. The x' oscillation in (a) reveals that the z coordinate of the BC-lens-trap is underestimated by $9\mu\text{m}$ in Table 5.3.

The COMM in the z direction after the BC-lens can be suppressed by shifting the lens trap. This is the difference between Set B and C in Fig. 5.1. The shift is realized by using $I_{\text{BC}} = 1.828\text{ A}$ (Set C) instead of $I_{\text{BC}} = 1.8\text{ A}$ (Set B) for the lens. This value was optimized experimentally and corresponds to a trap shift of $29\mu\text{m}$ according to the chip model. Hence, the remaining mismatch in z needs to be overcompensated. The reason is the additional kick by switching the lens trap on and off again. Invoking Eq. (5.34), the predicted velocity change due to the trap shift is $\Delta v_z = 0.35\text{ mm/s}$, which agrees reasonably well with the velocity $v_{x'} = -0.41(2)\text{ mm/s}$ in Fig. 5.1(c). The small difference is caused by the L_3 anharmonicity of the trap and the fact that the chip model tends to underestimate small trapping frequencies by a few percent (see Appendix C.2).

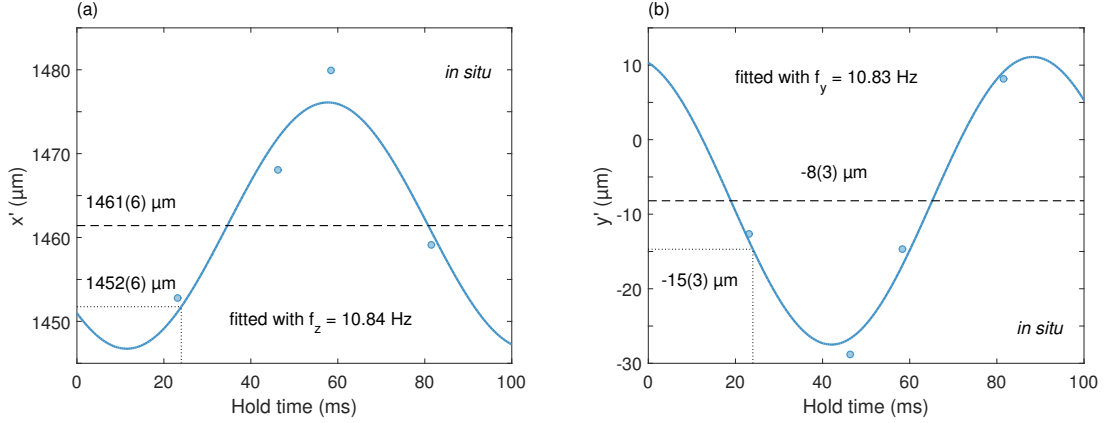


Figure 5.23: *In situ* position measurements of a BEC in the BC-lens-trap for different hold times in the trap. The data for the x' direction (a) and the y' direction (b) are fitted (solid blue line) assuming an oscillation at the corresponding frequency predicted by the chip model (f_z and f_y). The respective center of the oscillation is shown as the dashed black line. The hold time (24 ms) used for Fig. 5.22(b) with the related position is highlighted by the dotted black line.

After shifting the lens trap by $29\ \mu\text{m}$ for Set C, there is a position difference of approximately $\Delta z = 8\ \mu\text{m}$, which compensates all other contributions to v_z , for example, the kick due to switching the lens on and off. According to Eq. (5.34), this compensation amounts to

$$\Delta v_{z,\text{BC}} \approx 0.1\ \text{mm/s}. \quad (5.35)$$

It is illuminating to analyze the interplay of effects within the Detection 1 frame (Fig. 5.24). The release position was determined by an *in situ* measurement and is depicted as the black plus sign. The data set from Fig. 5.18 (100 ms TOF) is corrected for the oscillation and shown as the blue circles. The air drag effect is small for this TOF, as can be seen by comparing the open circles (uncorrected) to the full circles (corrected). The corrected center of the oscillation is highlighted as the dash-dotted blue lines for the x' and the y' oscillation, respectively. Without any velocity scatter, all blue points would overlap in this center. The position expected from the fits in Fig. 5.18 for 80 ms TOF (instead of 100 ms) and a hold time of $t_{\text{hold}} = 18.46\ \text{ms}$ is shown as the orange diamond. Still, the magnetic field gradient (see Fig. 3.8) is effective for this reduced time only. This shifts the expected position to the orange 'X'. The corresponding 1σ uncertainty in this position according to the fits is plotted as the dashed orange ellipse around this point. The position of the BC-lens according to Fig. 5.23 and including the y shift of $9\ \mu\text{m}$ is shown as the green ellipse. The radii correspond to the 1σ confidence bounds by the fits in Fig. 5.23. The position after the actual pre-TOF and hold time is measured three times (orange circles). The orange ellipse illustrates the scatter about the mean value. The measured position is further away from the chip than expected. This was already found by the measurement with the Detection 2 system. The shifted trap for Set C ($I_{\text{BC}} = 1.828\ \text{A}$) is located to the right of the orange ellipse and thus

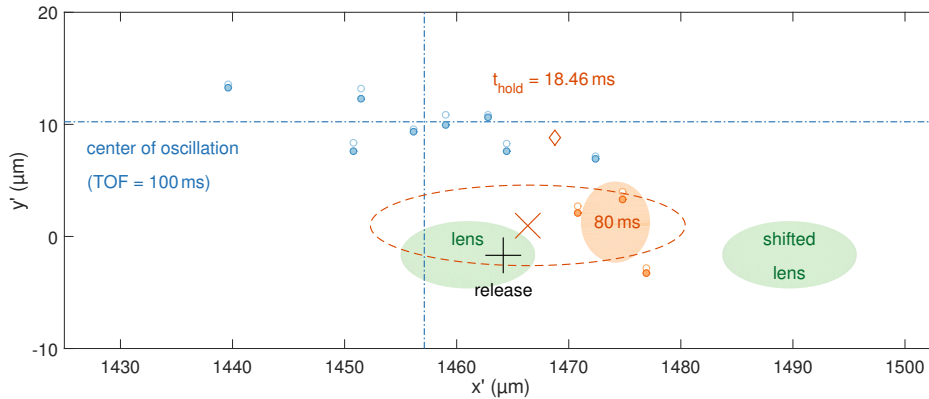


Figure 5.24: Comparison of the relevant positions for the BC magnetic lens within the frame of Detection 1. For all data points, the atoms were released from release position B (black plus sign). The blue circles show the data points of Fig. 5.18, but corrected for the actual dipole oscillation (center of oscillation at 100 ms TOF). Again, the open circles are raw data without air drag correction. The orange diamond depicts the position expected from the fit in Fig. 5.18 for a (pre-)TOF of 80 ms and a hold time $t_{\text{hold}} = 18.46$ ms. The reduced interaction time with the magnetic field gradient (see Fig. 3.8) shifts the expected position to the orange 'x' with the 1σ confidence bound shown as the dashed orange line. The measured position (for $t_{\text{hold}} = 18.46$ ms and 80 ms pre-TOF) is shown by the orange data points with the orange ellipse depicting the 1σ confidence bound. The measured *in situ* position of the BC lens with the 1σ confidence bound from the fit in Fig. 5.23 is shown as the left green ellipse. The shifted lens for Set C is located 29 μm further away from the chip.

further away from the chip than the BEC. A pre-compensation by a velocity of 0.41 mm/s in the z direction after release cannot reduce v_z in Set B, because the lens would compensate this additional velocity.

The number of data points that can be taken in microgravity is very limited. The velocity scatter complicates this even further because it limits the faith which can be put into a single data point. Still, it is comforting that the magnetic lens can be expected to reduce this velocity scatter for the same reason it can collimate an atomic ensemble. There exist six data sets which can be used for a comparison in Table 5.4. The first one is the set in Fig. 5.2 on the dipole oscillation after the sigmoid ramp. This set can be directly compared to the (lensed) Set A in Fig. 5.1. The scatter is one order of magnitude smaller. The scatter without lensing with the atoms released from position B can be obtained from the data sets in Fig. 5.16 for the release after the crane trick and from Fig. 5.18 for the trap decompression by the STA ramp. The values are comparable, but significantly smaller than for the first set. The reason for this can be the smaller trap frequencies at position B. However, the release mechanism is different, too. The two BC lens sets (Set B and C in Fig. 5.1) have a significantly reduced velocity scatter in the x' direction. The scatter in the y' direction is reduced only slightly, but it was low to start with. Both lens types feature a comparable post-lens scatter.

| release position | lens type | $\sigma_{v_{x'}} (\mu\text{m/s})$ | $\sigma_{v_{y'}} (\mu\text{m/s})$ |
|------------------|-----------------------|-----------------------------------|-----------------------------------|
| A | no lens (sigmoid) | 188 | 65 |
| | SC-BC (Set A) | 18 | 7 |
| B | no lens (crane trick) | 106 | 15 |
| | no lens (STA) | 100 | 23 |
| | BC (Set B) | 20 | 10 |
| | BC (Set C) | 9 | 14 |

Table 5.4: The velocity scatter in the x' ($\sigma_{v_{x'}}$) and the y' direction ($\sigma_{v_{y'}}$) is summarized for the data sets in Fig. 5.2 (no lens) and for the three different sets in Fig. 5.12 after a magnetic lens. The corresponding release position (A or B, see Fig. 2.12) is given.

Conclusions

The systematics affecting the center of mass motion in the Q-2 experiment were analyzed in detail. The dominant effect is caused by the residual air drag in the drop tower. It was shown how the center of mass motion can be controlled. The minimum residual speed was 0.3 mm/s in Set C with a minimum 1D component of 6(9) $\mu\text{m/s}$. For ultimate precision sensors, such as STE-QUEST, this is not yet sufficient. For example, the required relative velocity (K vs. Rb) is 0.3 nm/s [60]. Even though this is not a requirement on the common COM velocity, it can be anticipated that there is still a gap of a few orders of magnitude. A further reduction of the COMM in Q-2 requires many more data points in microgravity, but is straightforward: The atoms need to be released with a velocity opposite to the one caused by switching the lens on and off again. This is along the z direction and easily tunable by the hold time prior to the release or by the switch-off mechanism. The release position is a distance $v_z \cdot \text{pre-TOF}$ away from the lens center. The magnetic field gradient needs to be compensated by the state reversal scheme during the pre-TOF. The velocity change when changing the coil currents needs to be characterized further and reduced as far as possible, for example by a slow ramp-up of the current. As before, the atoms need to be transferred into the $m_F = 0$ substate quickly after the lens to prevent any further acceleration due to the gradient. With this simple recipe, the COM velocity can be reduced to the level of the velocity scatter, which is on the order of 10 $\mu\text{m/s}$. For a further reduction, this scatter must be understood and minimized. One possible source is the temperature of the experiment, especially of the atom chip and the copper mount. An increased temperature leads to an expansion of the material which affects the position of the BEC. Hence, equal temperatures might reduce the scatter. Furthermore, it will be interesting to study the differential scatter of two species, which might be suppressed.

Chapter 6

Magnetic lensing

This final chapter deals with manipulating the dynamics of a BEC. The first section describes the free expansion after release and introduces a formalism, which is applied throughout the chapter. The second part introduces the concept of magnetic lensing and discusses different strategies under the given experimental constraints. Section 6.3 deals with the rich *in situ* dynamics and its effect on the free expansion of a BEC. These collective modes are studied thoroughly because they have far reaching consequences for magnetic lensing. The concluding section shows several experimental realizations of magnetic lensing.

All data presented in this chapter were taken in microgravity. The author contributed equally in a team with Jan Rudolph, Alexander Grote, Christoph Grzeschik and Christian Deppner. Additional support was provided by Waldemar Herr. References for the theoretical framework are indicated in the main text. The evaluation and interpretation of the experimental data as well as the numerical simulations were performed by the author.

6.1 Free expansion

The dynamics of an atomic cloud is governed by Eq. (2.38). In the TF approximation, the stationary ground state is an inverted parabola in 3D with TF radii given by Eq. (2.39). In the single particle limit, the mean field term is negligible and the stationary solution is Gaussian. For the typical particle numbers and trap frequencies in Q-2, the TF approximation is a good approximation. Nevertheless, some dynamics of the atomic cloud can be calculated analytically if a Gaussian trial wave function is used. The Gaussian widths are determined by solving a set of differential equations that have been derived from the Gross-Pitaevskii equation by a variational principle [172]. Within this framework it is also possible to include an additional term, which is proportional to the square of the atomic density. This treatment is based on [172, 173] and facilitates to quantify the error by the TF approximation, because the kinetic energy term is not neglected. The Hamiltonian becomes:

$$H = -\frac{\hbar^2}{2m}\Delta + V(\vec{r}) + g_2 n(\vec{r}) + g_3 n(\vec{r})^2, \quad (6.1)$$

where $g_2 = 5\hbar \cdot 10^{-11} \text{ cm}^3/\text{s}$ and $g_3 = 4\hbar \cdot 10^{-26} \text{ cm}^6/\text{s}$ for ^{87}Rb [174]. The magnetic potential is assumed to be harmonic¹ and is conveniently reformulated as:

$$V(\vec{r}) = \frac{1}{2}m\bar{\omega}^2 (\tilde{\lambda}_x^2 x^2 + \tilde{\lambda}_y^2 y^2 + \tilde{\lambda}_z^2 z^2), \quad (6.2)$$

where $\omega_i = \bar{\omega}\tilde{\lambda}_i$ and $\tilde{\lambda}_x\tilde{\lambda}_y\tilde{\lambda}_z = 1$. The $\tilde{\lambda}_i$'s are dimensionless trap frequencies ($i = x, y, z$). Time and Gaussian ($e^{-1/2}$) widths w_i of the wave function are rescaled according to:

$$\tilde{t} = \bar{\omega}t, \quad w_i = a_{\text{osc}}u_i. \quad (6.3)$$

These widths are related to those of the atomic density distribution by

$$\sigma_i = w_i/\sqrt{2}. \quad (6.4)$$

The tilde notation is omitted for the u_i 's in favor of a better readability. A variational approach yields the following (dimensionless) set of differential equations:

$$\begin{aligned} \ddot{u}_x + \tilde{\lambda}_x^2 u_x &= \frac{1}{u_x^3} + \frac{\mathcal{P}}{u_x^2 u_y u_z} + \frac{\mathcal{K}}{u_x^3 u_y^2 u_z^2}, \\ \ddot{u}_y + \tilde{\lambda}_y^2 u_y &= \frac{1}{u_y^3} + \frac{\mathcal{P}}{u_x u_y^2 u_z} + \frac{\mathcal{K}}{u_x^2 u_y^3 u_z^2}, \\ \ddot{u}_z + \tilde{\lambda}_z^2 u_z &= \frac{1}{u_z^3} + \frac{\mathcal{P}}{u_x u_y u_z^2} + \frac{\mathcal{K}}{u_x^2 u_y^2 u_z^3}, \end{aligned} \quad (6.5)$$

with

$$\mathcal{P} = \sqrt{2/\pi}Na/a_{\text{osc}} \quad (6.6)$$

and

$$\mathcal{K} = g_3 \frac{4N^2}{9\sqrt{3}\pi^3\bar{\omega}\hbar a_{\text{osc}}^6}. \quad (6.7)$$

The first term on the right hand side of Eq. (6.5) corresponds to the kinetic energy term in the Hamiltonian. The \mathcal{P} - and \mathcal{K} -terms originate from the g_2 and g_3 interactions, respectively. The equilibrium widths can be obtained by numerically solving Eq. (6.5) with the \ddot{u}_i 's set to zero.

This variational approach allows for a study of the rich dynamics of a trapped condensate as well as the free expansion after release with $\tilde{\lambda}_i = 0$. However, all widths refer to Gaussian wave functions. In the TF regime, atomic density distributions are parabolic rather than Gaussian. For this reason, the variational approach is compared to the scaling approach, where the TF radii $R_i(t)$ are referenced to the initial equilibrium widths $R_i(0)$ by a set of scaling parameters λ_i [175]:

$$R_i(t) = \lambda_i(t)R_i(0). \quad (6.8)$$

¹This is only an approximation, but reasonable and necessary for a description of the *in situ* dynamics within this framework.

The physical interpretation is that the density profiles keep their parabolic shape, but at rescaled widths. The scaling parameters satisfy the non-dimensionless set of differential equations:

$$\ddot{\tilde{\lambda}}_i + \omega_i^2(t)\tilde{\lambda}_i = \frac{\omega_i^2(0)}{\lambda_i\lambda_1\lambda_2\lambda_3}, \quad (6.9)$$

which is similar to Eq. (6.5), except for the neglected kinetic energy term and the not included \mathcal{K} -term. Here, $\tilde{\lambda}_i$ (ω_i) plays the role of u_i ($\tilde{\lambda}_i$) in the variational approach.

Both approaches describe the temporal evolution of the same physical quantity, that is, the width of a Bose-Einstein condensate in three dimensions. Hence, if only the \mathcal{P} -term on the right hand side of Eq. (6.5) were considered, both approaches should concur, except for the different measure of width. In order to make them comparable, the equilibrium Gaussian widths [77]

$$w_i = \left(\frac{2}{\pi}\right)^{1/10} a_{\text{osc}} \frac{\bar{\omega}}{\omega_i} \left(\frac{Na}{a_{\text{osc}}}\right)^{1/5} \quad (6.10)$$

are related to the equilibrium TF radii [Eq. (2.39)]:

$$\frac{R_i}{w_i} = \frac{a_{\text{osc}} \frac{\bar{\omega}}{\omega_i} \left(\frac{15Na}{a_{\text{osc}}}\right)^{1/5}}{\left(\frac{2}{\pi}\right)^{1/10} a_{\text{osc}} \frac{\bar{\omega}}{\omega_i} \left(\frac{Na}{a_{\text{osc}}}\right)^{1/5}} = \frac{15^{1/5}}{\left(\frac{2}{\pi}\right)^{1/10}} \approx 1.798. \quad (6.11)$$

This ratio is independent of the trap frequencies and applies to all spatial directions. It is applicable during the free expansion, too, because of the scaling law in Eq. (6.8). Both approaches are compared on the basis of the free expansion of 10^5 atoms released from trap A. The widths expected from the variational approach with $g_3 = 0$ are converted using Eq. (6.11) and shown in Fig. 6.1(a). The initial confinement is stronger in the y and z directions than in the x direction, as expected from the trap frequencies $\omega_A = 2\pi \cdot (17.5, 61.1, 59.8)$ Hz of this trap [see also Eq. (2.39) and Fig. 2.13]. A stronger confinement leads to an increased expansion rate. During this expansion the atomic cloud changes its shape from elongated (cigar-like) to pancake-like. The shape is characterized by the aspect ratio, which is defined as the ratio of the axial to radial TF radii. This change in aspect ratio is a characteristic feature of BECs. The radii shown in Fig. 6.1(a) are not directly detectable due to the geometry of the imaging systems, except for the z direction (x') and the y direction (y''). For this reason, the projection of the atomic cloud, which is a three dimensional ellipsoid, onto the Detection 1 camera frame is exemplarily calculated and shown in Fig. 6.1(b) as the solid lines. The corresponding curves as predicted by the scaling approach are shown as the dashed lines in (b). The tiny difference is due to the kinetic term, which is intrinsically neglected in the scaling approach. If this term is also neglected in the variational approach, both curves overlap (g_3 was set to zero for comparison already). The effect of a nonzero value of g_3 is small and would partially counteract the kinetic term. Experimental data for various TOFs (integer multiples of 25 ms) after the release from trap A were taken during a single catapult flight. A nice visualization of these expanding condensates has been selected as the cover image of the 63rd volume (2015) of *Progress of Physics* and can be found

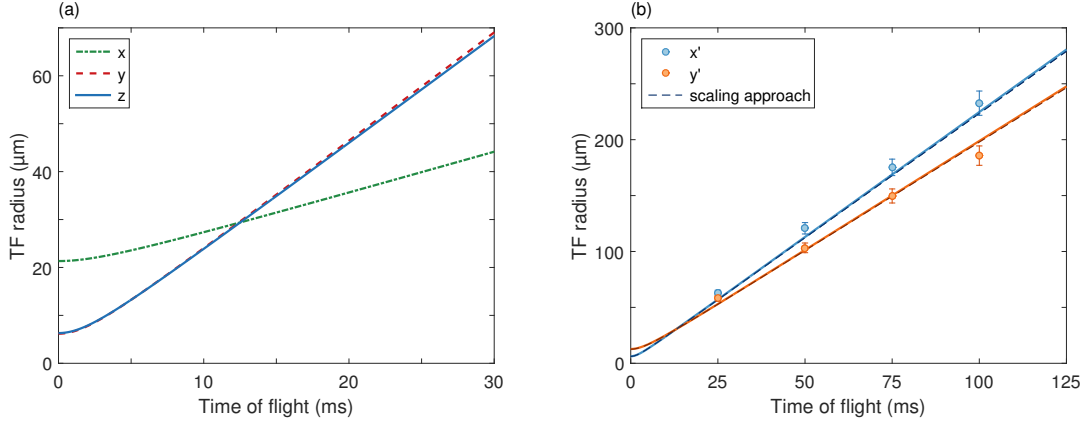


Figure 6.1: (a) TF radii of a BEC with $N = 10^5$ atoms released from an $\omega = 2\pi \cdot (17.5, 61.1, 59.8)$ Hz trap as predicted by the variational approach [Eq. (6.5)] with $\mathcal{K} = 0$ and converted using Eq. (6.11). (b) The solid lines show these predicted TF radii of the expanding BEC as seen by the Detection 1 imaging system. The predictions by the scaling approach are plotted as dashed lines. The circles show experimental data, rescaled to $N = 10^5$. The error bars refer to the uncertainty in the measured number of atoms.

here [176]. The TF radii in the respective directions are shown by the circles in Fig. 6.1(b). The measured radii depend on the number of atoms by an $N^{1/5}$ law [see Eq. (2.39)], which is preserved during the free expansion. Hence, a meaningful comparison is possible for the same number of atoms only. In fact, all data points are rescaled to $N = 10^5$ with the error bars indicating the uncertainty arising from the fitted number of atoms. In the trap, thermal and condensate fraction have a significant spatial overlap. For this reason, N is taken as the total number of atoms, as determined by two-dimensional bimodal fits (Gaussian + inverted parabola).

Both approaches, variational and scaling, can describe the free expansion of a BEC. They agree if the same approximations are made. In the following, only the TF radii are given as a measure of width. Despite this, the variational approach is used for numerical calculations of the dynamics, because it accounts for all terms in the Hamiltonian [Eq. (6.1)]. The widths are converted using Eq. (6.11). The g_3 contributions corresponds to three-body interactions. Scattering events involving more than three rubidium atoms and also atom loss are neglected.

The data points in Fig. 6.1(b) agree reasonably well with the theory. Nevertheless, all x' radii are slightly larger than the expected values. A simple explanation would be a differing actual trap frequency compared to the one simulated using the chip model, but this is ruled out by the measurement in Fig. 5.2(a), which was performed using the same release trap. The deviation cannot be explained by a differing number of atoms, either, because this would affect all directions. Having said that, the data set in Fig. 5.2 can be used for more statistics at 100 ms TOF. In addition, the $N^{1/5}$ scaling law can be checked by leaving the exponent as a fit parameter [N^x , Fig. 6.2(a)]. The fits for both directions yield $x = 0.21(1)$ in good agreement with $1/5$. Furthermore, this plot illustrates the scatter in the number of atoms ($\sigma_N = 46k$ at $\langle N \rangle = 84k$).

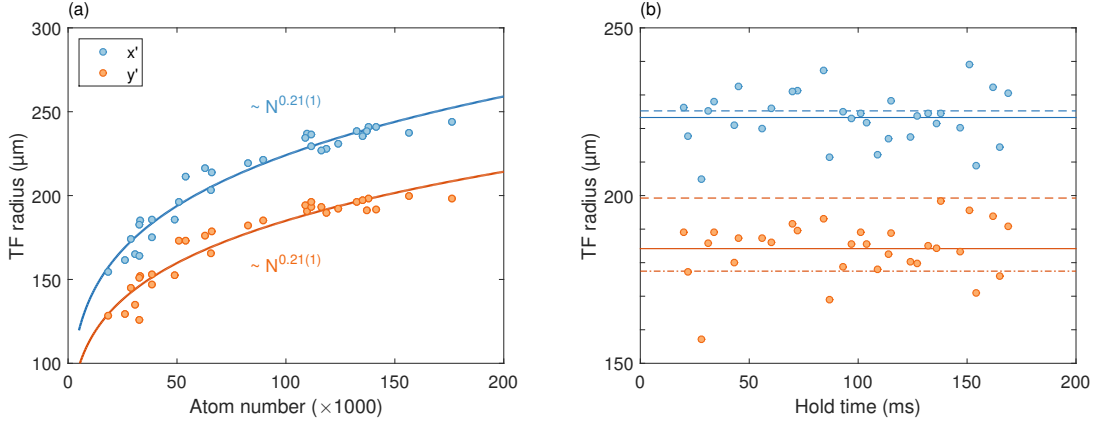


Figure 6.2: (a) The data points show the TF radii of the data set in Fig. 5.2 versus the number of atoms for the Detection 1 frame. The solid lines are fitted model functions of the form $a_1 N^{a_2}$ confirming the $N^{1/5}$ scaling law. (b) shows the data set from (a), but corrected for the scatter in the number of atoms by a rescaling to $N = 10^5$. The mean values (solid lines) are compared to the values expected from the chip model (dashed lines). The dash-dotted line is the expected y' radius if the trap axes coincide with the Q-2 coordinate system (no rotation).

Figure 6.2(b) shows the data points from (a), but rescaled to 10^5 atoms. Neither direction shows any signature of an oscillation. The histograms (not shown) are approximately Gaussian. This shows that collective excitations of the BEC, which are discussed in the next section, play no role for the SC-BC-lens with the preceding 250 ms sigmoid ramp to release position A.

The solid lines in (b) show the mean (rescaled) TF radii along with the expected values from the variational approach (dashed lines). The latter rely on the chip model. Only one out of three trap frequencies was measured (and confirmed) in microgravity (see Fig. 5.2). The other two, especially the weak one, might differ. In addition, the eigenvectors of the trap are rotated about the z axis. Typically, this rotation is on the order of 10° or below. Whenever radii, expansion rates etc. are given, they are referenced to the trap's eigensystem, but labelled according to the similar Q-2 coordinate system for clarity. According to the chip model, release trap A is rotated by 11.8° . This effect is considered in the figures above. Within the Detection 1 frame, it affects the y' direction only. Without this rotation, the expected y' TF radius ($177 \mu\text{m}$) is shown as the dash-dotted orange line in (b). The measured average value is $184(2) \mu\text{m}$. Accordingly, the 100 ms value for y' in Fig. 6.1(b) seems to be no outlier and the observed discrepancy can be explained by an incorrectly predicted rotation of the trap. However, no direct measurement of this rotation angle is possible with Q-2. In fact, also different frequencies in the x and y directions under the constraint of an unchanged geometric mean value is conceivable. The measured x' radius [$223(2) \mu\text{m}$] agrees with the predicted value ($225 \mu\text{m}$) and does not confirm the tendency observed in Fig. 6.1(b). Figure 6.2(b) shows the limits of the chip model. Nevertheless, it remains an invaluable tool, even for quantitative predictions.

6.2 Concept of magnetic lensing

It could be seen from Fig. 6.1 that the TF radii increase at a rate of approximately 2 mm/s. Such an ensemble containing 10^5 atoms is not detectable for much longer than 0.1 s TOF primarily due to the decreasing atomic density. Furthermore, the expansion rate is responsible for systematic errors in an atom interferometer, for example due to non-planar laser wave fronts. A significant reduction of the expansion rate is a key motivation of this work. Clearly, it seems possible to engineer slower expansion rates by using shallower traps in microgravity. Still, the time required for an adiabatic transfer to such a trap increases dramatically for ultrashallow traps. Hence, this is not an option for the drop tower. Even space-borne experiments would suffer from the reduced data rate.

In Q-2, expansion rates are reduced by the application of a magnetic lens, which is essentially a magnetic trap, too. The pre-TOF in between release and magnetic lens needs to be large enough such that the mean field energy is almost completely converted into kinetic energy. Ideally, there is a linear mapping between position and velocity. The 1D phase space representation of an atomic ensemble directly before the lens is depicted in Fig. 6.3(a). The application of a 1D potential with trap frequency ω_{lens} in the x direction results in the acceleration

$$a_{\text{lens}} = -\omega_{\text{lens}}^2 x.$$

Hence, the transient lens potential results in a position dependent velocity change Δv_{lens} , which is opposing the expansion velocity:

$$\Delta v_{\text{lens}} = -\omega_{\text{lens}}^2 x \tau_{\text{lens}},$$

where τ_{lens} is the lens duration. This is indicated by the white arrows in Fig. 6.3(a). It is equivalent to a rotation of the phase space distribution. If

$$\tau_{\text{lens}} = \frac{1}{\omega_{\text{lens}}^2 t_{\text{p}}}, \quad (6.12)$$

where t_{p} is the pre-TOF, the resulting phase space distribution is oriented along the position axis and the atomic ensemble is said to be collimated [Fig. 6.3(b)]. Its momentum distribution has a minimum width. The phase space distribution before the lens narrows down with increasing t_{p} and approaches a line. Hence, the minimum residual expansion rate that can be realized by the lens depends on t_{p} .

The equations above are valid for a perfectly harmonic lens potential only. Any deviation results in a deformed phase space distribution after the lens and increases the minimum velocity spread achievable with the respective lens. The effect of an L_3 anharmonicity on the velocity distribution was discussed in Section 5.2 in the context of the detection pseudo force.

It is worth mentioning that τ_{lens} is independent of the release trap. Still, shallower traps require a longer pre-TOF to establish the linear mapping. Hence, the lens time is indirectly affected by the release trap. In practice, τ_{lens} needs to be long compared to the characteristic switching time of the bias coil. This is a true limitation.

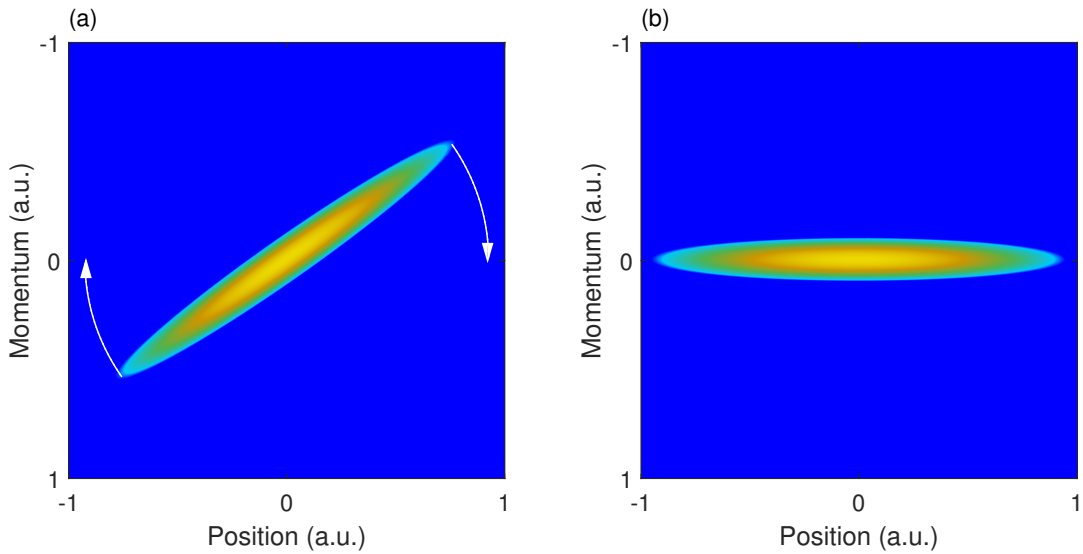


Figure 6.3: A 1D phase space distribution of an expanding BEC is shown before (a) and after (b) a magnetic lens. The action of the lens is a rotation of this distribution as indicated by the white arrows.

Equation (6.12) suggests to reduce ω_{lens} because of the quadratic dependence. On the other hand, shallow lens traps are strongly affected by residual fields and field gradients and the chip model is not calibrated in this regime. A direct measurement of the trap center and frequencies would require a sampling over a few periods of the *in situ* oscillation which can readily exceed the available microgravity time. Hence, the release trap frequency should be as high as possible for a short pre-TOF. For this reason, the release traps are not scaled down prior to the release.

Even though the above discussion is purely 1D, it can be directly transferred to a 3D lens. The only problem is that Eq. (6.12) cannot be satisfied for all dimensions when using an anisotropic lens potential. In a first step, the two radial directions with similar trap frequencies can be lensed. The axial direction is hardly affected by such a lens, but the large radial expansion rates are minimized. A further reduction is conceivable by the application of two lenses in analogy to a telescope in optics. A numerical simulation of such a matter-wave telescope is shown in Fig. 6.4. For simplicity, an axially symmetric release trap is assumed. The repeated application of the BC-lens during the shaded gray areas in (a) leads to a good collimation of the ensemble. As a consequence of the residual mean field energy, the TF radii increase at a rate of approximately $43 \mu\text{m/s}$ on long time scales (b). This expansion is isotropic by construction. The effect of neglecting the \mathcal{K} -term in Eq. (6.5) is an increased expansion rate in the radial directions and a reduced one in the axial direction, as visualized by the thin lines in (b). The origin of the deviation is the differing equilibrium size within the release trap rather than the focus in the radial directions. A similar absolute deviation can be observed during the free evolution over the full 10s, but the relative difference becomes important in this ultralow expansion regime only. In reality, the radial directions have differing release trap

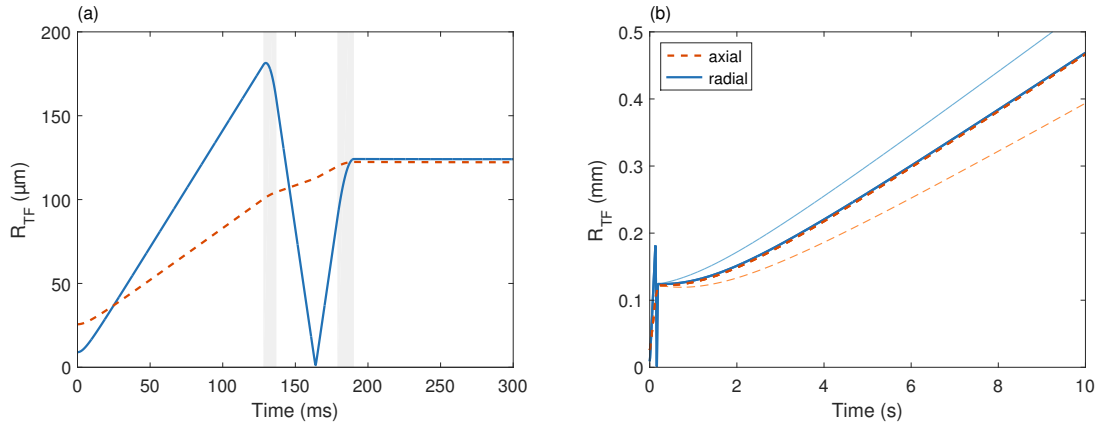


Figure 6.4: (a) shows a numerical simulation of the axial (solid blue line) and radial (dashed orange line) TF radii during a matter-wave telescope assuming an axially symmetric release trap with $\omega = 2\pi \cdot (9, 26, 26)$ Hz, which is similar to release trap B. The actual BC-lens trap is used for magnetic lensing twice as indicated by the shaded gray areas. (b) shows the long term evolution of the TF radii, which increase at a rate of $43 \mu\text{m}/\text{s}$ because of the residual interaction energy. The thin lines represent the same simulations, but with neglected \mathcal{K} -term.

frequencies, which lead to differing radial expansion rates. Furthermore, the cloud would be deformed due to the anharmonicities in the z direction, which cannot be neglected at this cloud size. Such a matter-wave telescope is not realized in this work. First of all, it would be more difficult to adjust. Aside from that, the high density in the focus gave rise to a significant loss of atoms.

The notion of temperature

Sometimes, magnetic lensing is referred to as 'delta-kick-cooling' in the literature [2, 56, 177]. This name suggests that the action of the lens happens instantaneously rather than over a period of a few milliseconds. In contrast to a free expansion time on the second scale this seems justified. Yet, the 'cooling' term within the name is misleading, because a magnetic lens is not actually cooling the atomic ensemble. The temperature is well defined for a thermal ensemble within the trap, where it affects the *in situ* width and the velocity spread [see Eqs. (2.24) to (2.27)]. Below T_c , the temperature is also a measure for the condensate fraction [see Eq. (2.32)]. As a matter of fact, the free expansion of the condensate fraction is governed almost entirely by the mean field energy. The temperature within the trap and prior to the release is no measure for the free expansion of a BEC. At some time after release, the expansion rates saturate, but the velocity distribution is not equal to that of a thermalized ensemble at any temperature. Hence, the temperature is not defined for expanding BECs. Despite this, it has become an intuitive and established measure for the expansion rate of a BEC [1, 2, 178]. To indicate the problems with this notion, these temperatures are called kinetic temperatures (T_{kin}). The lowest real temperature of an atomic ensemble reported so far is 350 pK [179].

For thermal atoms, the Maxwell-Boltzmann distribution of velocities in 3D is given by [180]:

$$f(v) = \sqrt{\frac{2}{\pi}} \frac{v^2}{\tilde{v}^3} \exp\left(-\frac{v^2}{2\tilde{v}^2}\right), \quad (6.13)$$

where

$$\tilde{v} = \sqrt{\frac{k_B T}{m}}. \quad (6.14)$$

According to the equipartition theorem, the temperature is related to the root mean square velocity v_{rms} by:

$$T = \frac{mv_{\text{rms}}^2}{3k_B} \quad (6.15)$$

with

$$v_{\text{rms}} = \sqrt{3}\tilde{v} = \sqrt{\frac{3k_B T}{m}} \quad (6.16)$$

for the distribution in Eq. (6.13). The key step in the definition of T_{kin} is the application of Eq. (6.15) to expanding BECs, because v_{rms} is still a well defined quantity. This equation implicitly assumes that the BEC exhibits no COMM.

The velocity distribution of an expanding BEC is changing because of the interactions during the initial free expansion phase. After a long TOF the distribution saturates and is referred to as the limiting velocity distribution. For lensed atoms, this saturation occurs at a much longer TOF compared an unlensed ensemble. In this work, 20s TOF are used to numerically calculate the limiting distribution. This is sufficient as can be anticipated from the expansion curve in Fig. 6.4(b). The blue line in Fig. 6.5(a) shows the limiting velocity distribution of a BEC with 10^5 atoms released from trap A. This distribution has a root mean square velocity of 1.25 mm/s. For comparison, a thermal distribution sharing the same v_{rms} is plotted as the dash-dotted orange line, which differs significantly. The thermal ensemble has a well defined temperature of $T = 5.45$ nK. The BEC is said to have the same kinetic temperature. The simulated ensemble in Fig. 6.4(b) has $v_{\text{rms}} = 28 \mu\text{m/s}$ corresponding to $T_{\text{kin}} = 3$ pK.

In addition to the ailing definition of T_{kin} , a comparison of the expansion rates of different atomic species' is not directly possible by comparing temperatures because of the mass dependence in Eq. (6.15). For these reasons, v_{rms} is a better measure for the expansion rate than T_{kin} . Nevertheless, this is only a matter of notation. The requirement for precision measurements is to keep the atomic ensemble reasonably small on long time scales without the application of trapping forces. In this work, 3D kinetic temperatures are given for a comparison with the state of the art. Many authors extend the temperature definition to the particular dimensions, in which they have succeeded to reduce the velocity spread [1, 44, 181–185]. However, no justification for the negligence of existing degrees of freedom is given.

The pre-TOF is a crucial parameter for magnetic lensing. If it is chosen too large, the atomic ensemble samples highly anharmonic regimes of the lens potential. If the pre-TOF is too short, on the other hand, there is still a residual mean field energy resulting in a re-emerging expansion of the atomic cloud. This expansion is equal

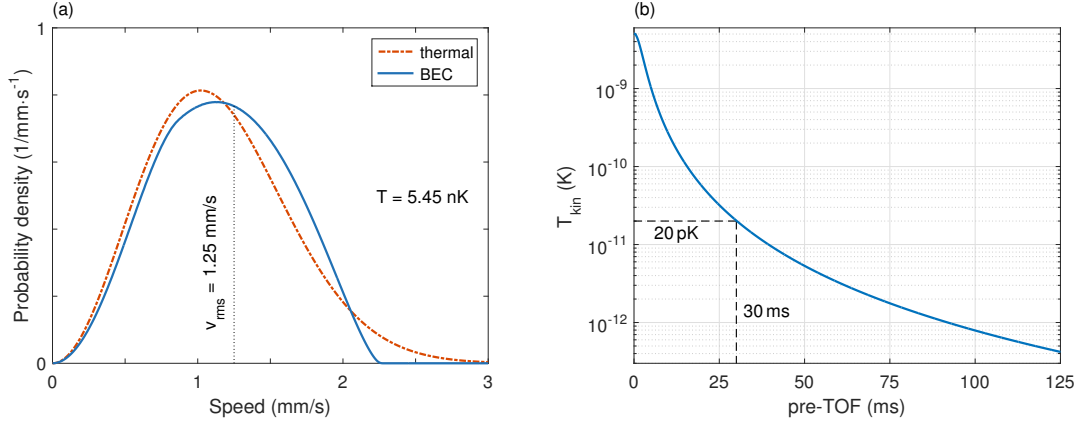


Figure 6.5: (a) compares the limiting velocity distribution of a BEC containing 10^5 atoms released from trap A (solid blue line) to a thermal distribution at a temperature of 5.45 nK (dash-dotted orange line). Both distributions share the same root mean square velocity $v_{\text{rms}} = 1.25$ mm/s. (b) shows the dependence of the minimum kinetic temperature, which can be achieved by applying a perfect 3D magnetic lens to the velocity distribution in (a), as a function of the pre-TOF. The value for the SC-BC-lens (30 ms) is highlighted by the dashed line with a limiting kinetic temperature of 20 pK.

to the one expected for atoms that are released from a hypothetical shallower trap with equilibrium TF radii equal to the pre-TOF values of the lensed BEC. Hence, the residual mean field energy E_{int} at the time of the lens is equal to the one in this hypothetical trap with a pre-TOF dependent $\bar{\omega}$. The corresponding mean field energy per particle is given by [77]:

$$\frac{E_{\text{int}}}{N} = \frac{1}{7} \hbar \bar{\omega} \left(\frac{15Na}{a_{\text{osc}}} \right)^{2/5}, \quad (6.17)$$

with the resulting rms velocity:

$$v_{\text{rms}} = \sqrt{\frac{2E_{\text{int}}}{Nm}} = \sqrt{\frac{2\hbar\bar{\omega}}{7m} \left(\frac{15Na}{a_{\text{osc}}} \right)^{1/5}}. \quad (6.18)$$

The equivalent kinetic temperature is plotted as a function of the pre-TOF in Fig. 6.5(b). This is a lower limit for perfectly lensed atoms (in 3D) released from trap A. This curve also depends on the number of atoms: Smaller BECs have a reduced kinetic energy per particle². For a pre-TOF of 30 ms, as used for the SC-BC-lens, the limit is 20 pK. Yet, this plot does not include the detrimental effects by anharmonicities. They would result in a minimum at a finite pre-TOF.

²Still, BECs containing more atoms are beneficial, because the atomic density scales as $N/v_{\text{rms}}^3 \sim N^{2/5}$.

6.3 Collective modes

Equation (6.5) was used to explain the free expansion of a BEC in Section 6.1. With nonzero $\tilde{\lambda}_i$ the equations describe the *in situ* dynamics, which is a collective excitation of all atoms in the BEC. Several kinds of these so called collective modes exist [77]. The low-frequency modes are illustrated in Fig. 6.6 for a cylindrically symmetric trap. The quadrupole mode (QM) is an in-phase oscillation of the radial TF radii in combination with an out-of-phase oscillation of the axial TF radius. In the radial quadrupole (RQ) mode, only the radial directions oscillate out-of-phase to each other while leaving the axial TF radius unaffected. Accordingly, the breathing mode (BM) is an in-phase oscillation of all three radii. In contrast, the scissors mode (SM) is an oscillating orientation of the BEC at a constant shape. In this spirit, it is fundamentally different from the other modes and cannot be described by Eq. (6.5). All these modes have been observed experimentally [186–193].

The mode frequencies primarily depend on the the trap frequencies. However, also the number of atoms and the oscillation amplitude affect the mode frequencies. Analytic results exist for simplified systems, for example using a cylindrically symmetric trap and invoking the TF approximation. The influence of these systematics on the mode frequencies is analyzed numerically and presented in this section. For definiteness, a cylindrically symmetric potential is given by:

$$V_{\text{cyl}}(\vec{r}) = \frac{1}{2}m\omega_r^2(\lambda^2x^2 + y^2 + z^2), \quad (6.19)$$

where ω_r is the radial trap frequency and

$$\lambda = \frac{\omega_x}{\omega_r}, \quad (6.20)$$

with axial trap frequency ω_x . The mode frequencies in this trap can be approximated by [194]:

$$w_{\text{QM,BM}} = \omega_r \left[2 + \frac{3}{2}\lambda^2 \mp \frac{1}{2}\sqrt{16 - 16\lambda^2 + 9\lambda^4} \right]^{1/2} \quad (6.21)$$

and

$$w_{\text{RQ}} = \sqrt{2}\omega_r. \quad (6.22)$$

The systematics are studied on the basis of release trap B with trap frequencies $\omega_B = 2\pi \cdot (9.1, 27.9, 24.6)$ Hz. For comparability, the time dependent TF radii can be rescaled by their respective equilibrium values R_{eq} , where the spatial index is omitted. This procedure is borrowed from the scaling approach, even though the time evolution is calculated using the variational approach. Without any collective excitations, all rescaled radii would be unity for all times. Figure 6.7(a) to Figure 6.9(a) show the rescaled TF radii for the QM, the RQ mode and the BM. The amplitude of the oscillations is arbitrarily chosen such that the maximum of all rescaled radii is 1.15. The largest relative oscillation amplitude occurs in the x direction for the QM and in the z (y) direction for the RQ mode (BM). The asymmetry for the latter two is a consequence of the violation of the cylindrical symmetry. The smaller initial

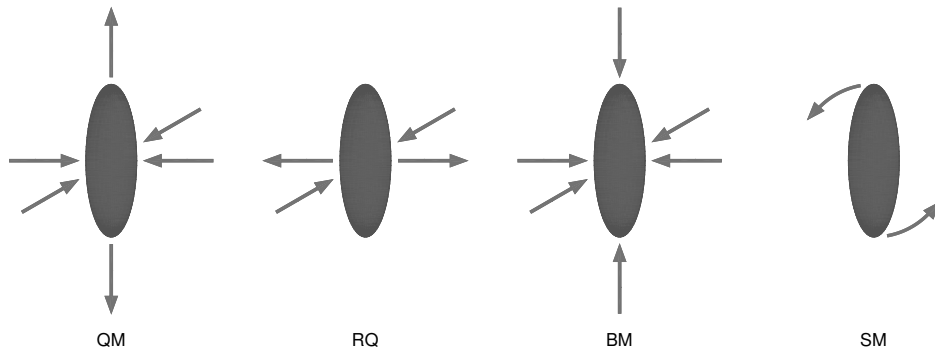


Figure 6.6: Four different collective excitations of a BEC in a cylindrically symmetric trap are illustrated. The QM is characterized by an in-phase oscillation of the TF radii in the radial direction in combination with an out-of-phase axial oscillation. The latter direction remains constant in the case of the RQ mode, where the radial directions are out of phase. For the BM, all three directions are in phase. The SM is a rotary motion oscillating about an equilibrium orientation. The size remains approximately constant.

amplitudes in the remaining directions are carefully chosen such that the amplitude spectrum exhibits no frequency components other than the actual mode frequency and its higher harmonics. The amplitude spectra for 20 s of the oscillation are shown in the respective (b) figures. The dotted lines indicate $f_{\text{QM}} = \omega_{\text{QM}}/2\pi$ and its higher harmonics. The dashed lines mark f_{RQ} (left) and f_{BM} (right). It can be seen that the actual QM frequency is in good agreement with f_{QM} while the other two mode frequencies are higher than the approximate values.

The dependence of the mode frequency on the number of atoms is shown in the (c) figures. The solid thick black line was calculated for the actual trap including all the systematics mentioned above. The oscillation amplitude is chosen like in (a). To illustrate the bare N dependence, the same simulation is repeated for a small amplitude oscillation in a cylindrically symmetric trap, which is similar to release trap B in the sense that they share the same ω_x and using $\omega_r = \sqrt{\omega_y \omega_z}$. In the following, this trap is referred to as the cylindrically symmetric trap equivalent to release trap B. The \mathcal{K} term is neglected for this simulation, but the kinetic term is still included. The resulting mode frequency is shown as the solid thin red line. It approaches the corresponding approximate frequency for large N . If the kinetic term were neglected, too, the simulated frequency would equal the approximate one for all N . Typical atom numbers are on the order of 10^5 in Q-2. If a BEC contained 10^4 atoms or even fewer, the data point would be neglected for any kind of measurement presented in this work. Hence, the maximum frequency shift due to variations in N is on the order of 2 Hz for the RQ mode and even smaller for the QM and the BM.

The amplitude dependence of the mode frequencies is shown in the (d) figures assuming $N = 10^5$ atoms in release trap B. A quantitative comparison of this dependence for the three modes is difficult, because every mode has three different amplitudes. In addition, their ratio is amplitude dependent, too. For definiteness,

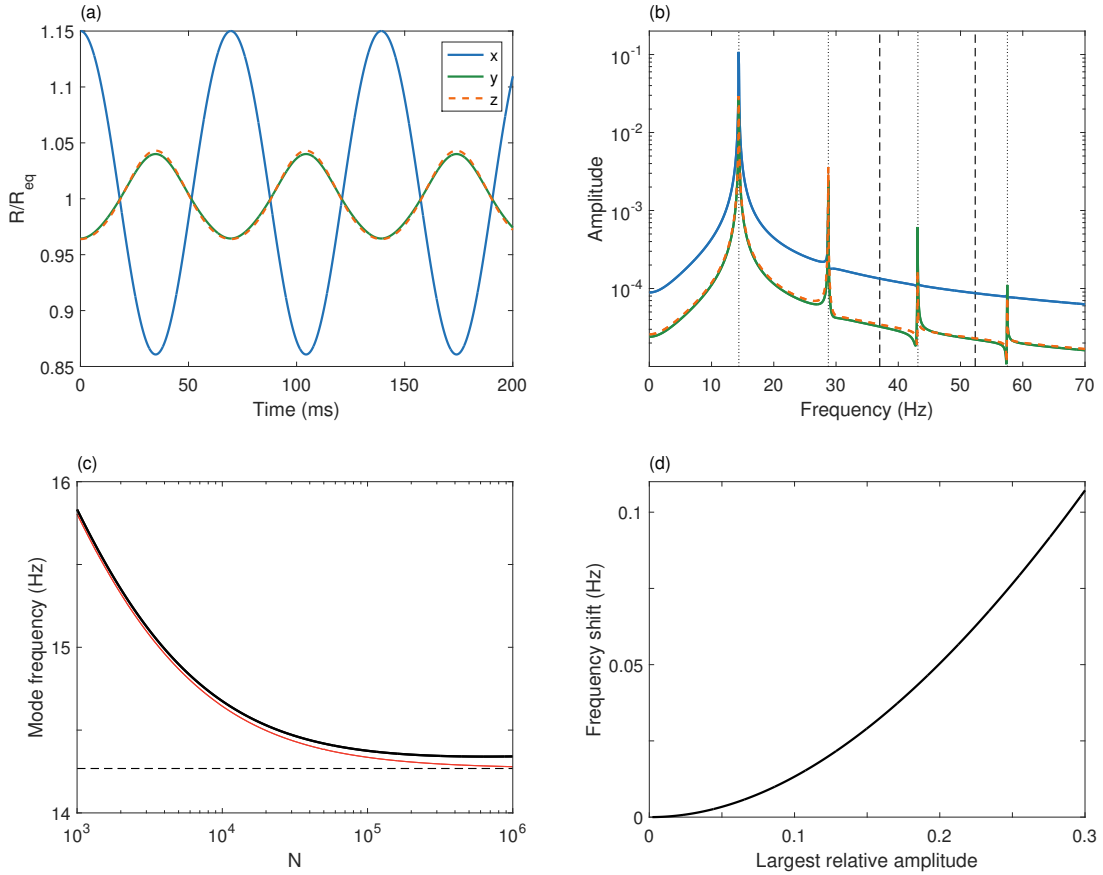


Figure 6.7: (a) shows a quadrupole mode oscillation of the TF radii within release trap B assuming $N = 10^5$. All radii are rescaled by their respective equilibrium values R_{eq} . The corresponding amplitude spectra are plotted in (b). The expected mode frequency f_{QM} [see Eq. (6.21)] and the higher harmonics are depicted by the dotted lines. The frequencies of the other two modes are indicated by the dashed black lines [see Eqs. (6.21) and (6.22)]. (c) shows the dependence of the mode frequency on the number of atoms for the oscillation in (a) [solid thick black line, release trap B] in comparison to a small amplitude QM oscillation in the equivalent cylindrically symmetric trap (solid thin red line). The \mathcal{K} -term was neglected for the latter curve to show the asymptotic behavior for large N . The amplitude dependence of the real trap QM frequency is shown in (d) for $N = 10^5$. The amplitude is taken as the amplitude of the rescaled R_x oscillation, which is almost 0.15 in (a).

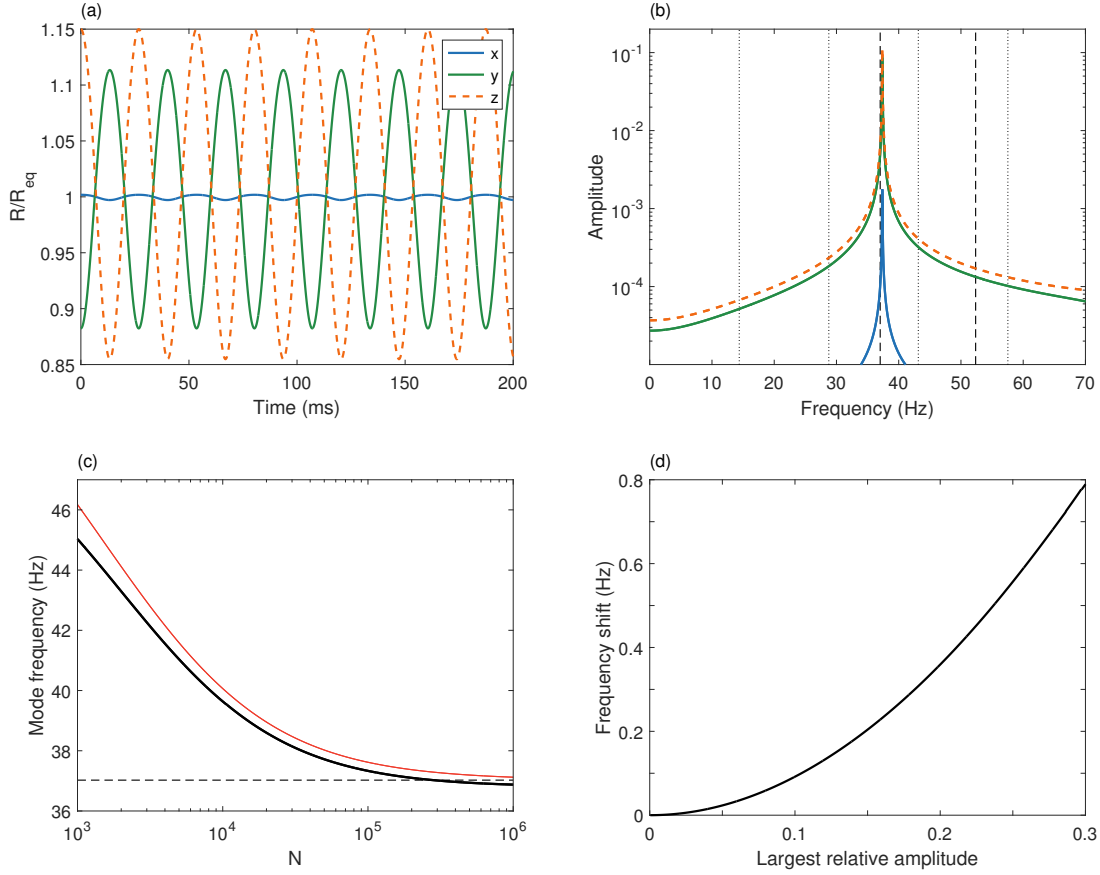


Figure 6.8: (a) shows a RQ mode oscillation of the TF radii within release trap B assuming $N = 10^5$. All radii are rescaled by their respective equilibrium values R_{eq} . The corresponding amplitude spectra are plotted in (b). The expected mode frequency f_{RQ} [see Eq. (6.22)] is depicted as the left dashed thin black line. The right one indicates f_{BM} and the dotted lines depict f_{QM} and its higher harmonics [see Eq. (6.21)]. (c) shows the dependence of the mode frequency on the number of atoms for the oscillation in (a) [solid thick black line, release trap B] in comparison to a small amplitude RQ mode oscillation in the equivalent cylindrically symmetric trap (solid thin red line). The \mathcal{K} -term was neglected for the latter curve to show the asymptotic behavior. The amplitude dependence of the real trap RQ mode frequency is shown in (d) for $N = 10^5$. The amplitude is taken as the amplitude of the rescaled R_z oscillation, which is almost 0.15 in (a).

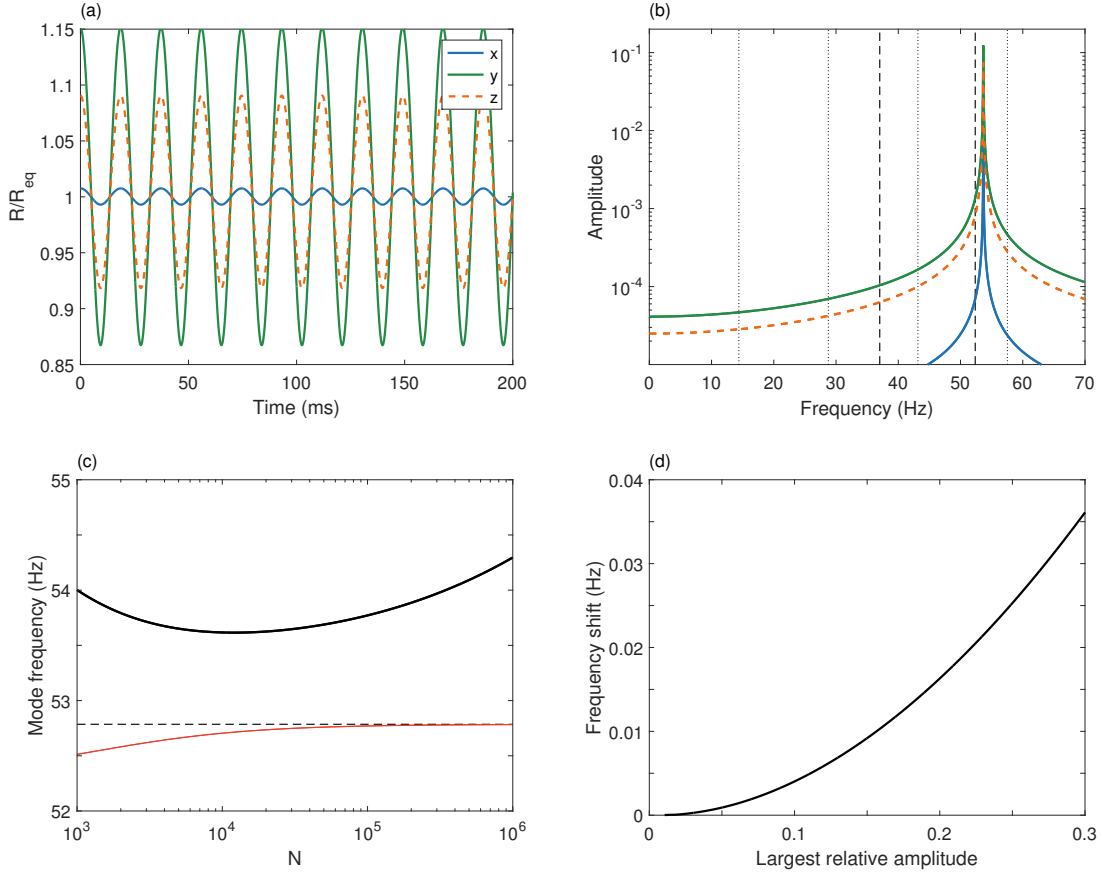


Figure 6.9: (a) shows a BM oscillation of the TF radii within release trap B assuming $N = 10^5$. All radii are rescaled by their respective equilibrium values R_{eq} . The corresponding amplitude spectra are plotted in (b). The expected mode frequency f_{BM} [see Eq. (6.21)] is depicted as the right dashed thin black line. The left one indicates f_{RQ} and the dotted lines depict f_{QM} and its higher harmonics [see Eqs. (6.21) and (6.22)]. (c) shows the dependence of the mode frequency on the number of atoms for the oscillation in (a) [solid thick black line, release trap B] in comparison to a small amplitude BM oscillation in the equivalent cylindrically symmetric trap (solid thin red line). The \mathcal{K} -term was neglected for the latter curve to show the asymptotic behavior. The amplitude dependence of the real trap BM frequency is shown in (d) for $N = 10^5$. The amplitude is taken as the amplitude of the rescaled R_y oscillation, which is almost 0.15 in (a).

the amplitude is defined as the largest of all three amplitudes. The observed frequency shifts are below 1 Hz for all modes and relative amplitudes below 0.3. For comparison, the amplitude in the respective (a) figures is almost 0.15 by construction.

In order to quantify the effect of a not perfectly cylindrically symmetric trap, the departure of the radial frequencies from their geometric mean ω_r is parametrized by the asymmetry parameter ϵ :

$$\begin{aligned}\omega_y &= \omega_r \cdot (1 + \epsilon), \\ \omega_z &= \omega_r / (1 + \epsilon).\end{aligned}\tag{6.23}$$

The resulting mode frequencies within the TF approximation and for small oscillation amplitudes are shown as a function of the asymmetry parameter in Fig. 6.10(a). The trap corresponding to $\epsilon = 0$ is the equivalent cylindrically symmetric trap for release trap B. Figure 6.10(b) shows the frequency difference with respect to $\epsilon = 0$. It can be seen, that the QM is hardly affected by the asymmetry, but the other two mode frequencies are shifted in opposite directions. The asymmetry parameter for release trap B is $\epsilon_B = 0.0645$ and highlighted by the vertical dotted line. Interchanging the roles of ω_y and ω_z in Eq. (6.23) has no effect, because neither direction is preferred.

The scissors mode

In contrast to the modes presented in Figs. 6.7 to 6.9, the SM cannot be analyzed in a similar fashion. The SM oscillation shown in Fig. 6.6 stays within the plane. Hence, the orientation of the BEC can be characterized by a single angle θ which is governed by a harmonic oscillator differential equation [195]:

$$\ddot{\theta} + 2\omega_{\text{SM}}^2 \theta = 0,\tag{6.24}$$

where

$$\omega_{\text{SM}} = \sqrt{\omega_x^2 + \omega_y^2}.\tag{6.25}$$

The plane of the oscillation is assumed to be the x - y plane, because the trap orientation is rotated about the z axis during the decompression phase from the evaporation trap to any release trap further away from the chip. A scissors mode in the x - z plane is possible, too, but it lacks a source of excitation in Q-2. In release trap B, the SM frequency is $\omega_{\text{SM}} = 2\pi \cdot 29.3$ Hz for the x - y plane. This frequency is independent from the number of atoms and the oscillation amplitude, but the scope of Eq. (6.24) is bound by a condition on the maximum amplitude:

$$\theta \ll 1,\tag{6.26}$$

beyond which the SM turns into a QM [195]. Indeed, numerical simulations confirm a strong coupling. As a matter of fact, these simulations cannot address Eqs. (6.5) and (6.24) separately, because a rotating BEC has a finite angular momentum, which needs to be conserved. This leads to an increasing angular velocity $\dot{\theta}$ for decreasing TF radii and vice versa. The strong coupling to the QM can be understood by

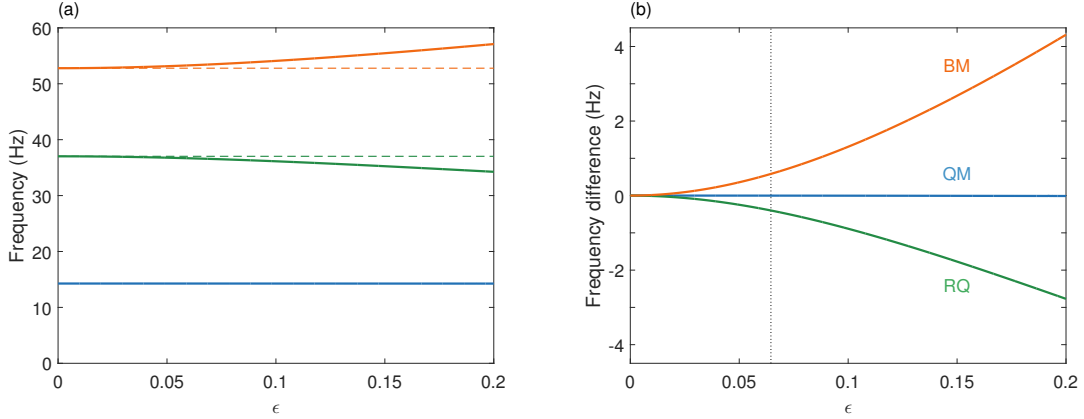


Figure 6.10: (a) The collective mode frequencies within the TF approximation are shown as a function of the asymmetry parameter ϵ [see Eq. (6.23)] for a set of magnetic traps similar to release trap B. The traps are similar in the sense that they share the same ω_x and $\omega_y \cdot \omega_z$, but at a variable asymmetry. The dashed lines are the asymptotes for a cylindrically symmetric trap. The deviation from these reference values are shown in (b). The dotted line indicates the actual asymmetry $\epsilon_B = 0.0645$ of release trap B.

recalling that the TF radius is largest in the x direction. This radius experiences the largest oscillation amplitude during a QM oscillation.

The moment of inertia Θ_{BEC} of a BEC is different from Θ_{rigid} of the equivalent rigid body. S. Stringari [196] has found that both are related by the trap frequencies:

$$\Theta_{\text{BEC}} = \left(\frac{\omega_y - \omega_x}{\omega_y + \omega_x} \right)^2 \Theta_{\text{rigid}}. \quad (6.27)$$

The rigid value considering a TF density distribution is calculated in a lengthy but straightforward calculation to be

$$\Theta_{\text{rigid}} = \frac{1}{7} m N (R_x^2 + R_y^2). \quad (6.28)$$

For comparison, the pre-factor for a homogeneous density distribution would be $1/5$.

6.3.1 Excitation of collective modes

An excitation of these collective modes is possible by changing the trap configuration faster than the BEC can adiabatically adapt to the new trap. The coils' step response limits the characteristic rate for trap changes to approximately 1 kHz, which is much higher than the mode frequencies in release trap B. Hence, all these modes can be excited in Q-2.

The rampout from the final evaporation trap to either of the release positions is such a changing trap configuration. The resulting dynamics are simulated using Eqs. (6.5) and (6.24) for the 250 ms sigmoid ramp to release trap A (see also Fig. 5.14) and for the 150 ms ramp to release trap B (see also Fig. 5.17). The local

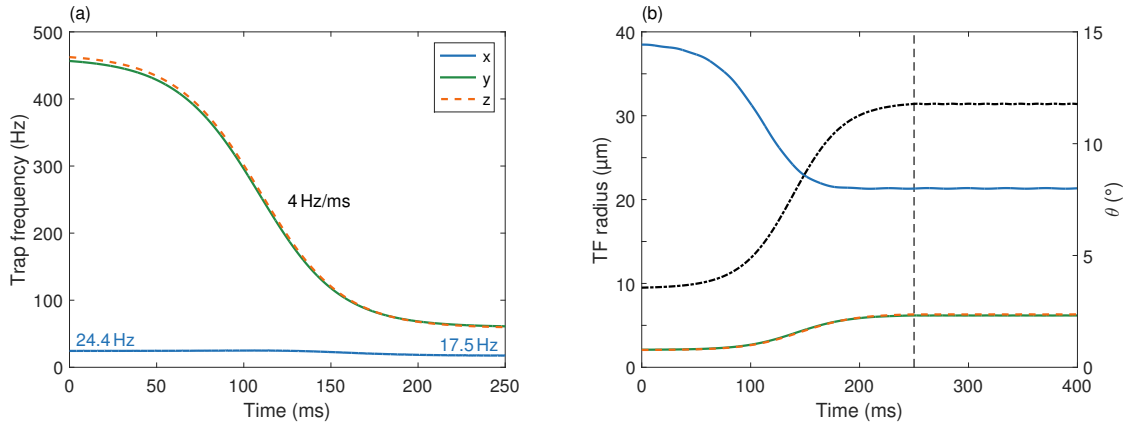


Figure 6.11: The course of the trap frequencies during the 250 ms sigmoid ramp to release trap A is shown in (a). The axial trap frequency changes from 24.4 Hz to 17.5 Hz while the radial frequencies decrease by up to 4 Hz/ms. (b) shows the corresponding TF radii during this ramp and for a subsequent hold time of 150 ms after the end of the ramp, which is highlighted by the dashed thin black line. A BEC containing $N = 10^5$ atoms is assumed. The rotation angle θ of the condensate's principal axes about the z axis is shown as the dash-dotted black line (right ordinate).

trap frequencies and the orientation during the rampout are obtained from the chip model. The results for the sigmoid ramp are presented in Fig. 6.11. The radial trap frequencies experience the largest decrease at a maximum rate of 4 Hz/ms, while the axial trap frequency decreases from 24.4 Hz to 17.5 Hz only. This change is adiabatic as can be seen by the absence of oscillations in the TF radii and in the orientation of the condensate [dash-dotted black line in (b)]. It is interesting that the axial radius decreases, even though the axial trap frequency decreases, too. This is due to the significant drop in $\bar{\omega}$ [see Eq. (2.39)]. A tiny QM oscillation is visible in R_x during the hold time after the end of the ramp, which is depicted as the vertical dashed black line. The amplitude would be larger for a reduced ramp time. This simulation agrees qualitatively with the data set shown in Fig. 6.2, which does not exhibit any signature of a shape oscillation.

The situation is different for the faster rampout to position B, as shown in Fig. 6.12. The trap frequencies need to decrease faster, because the final trap is shallower and the ramp time is reduced. In addition, the ramp shape is optimized for minimal dipole oscillations, which entails the rapid changes during the first third of the ramp. In order to gain more information on the magnetic field gradients within the chamber, a different magnetic quantization field was used for the BC-lens data sets, as discussed in Section 3.4. The required change of the x coil current from 0.5 A to 0.1 A was conducted directly before the rampout. This leads to an increase of the radial trap frequencies by approximately 100 Hz, as shown by the inset in (a).

This combination leads to the maximum rate of 29 Hz/ms at which the radial frequencies decrease, which is almost one order of magnitude larger compared to the sigmoid ramp. The effect is an excitation of all collective modes discussed

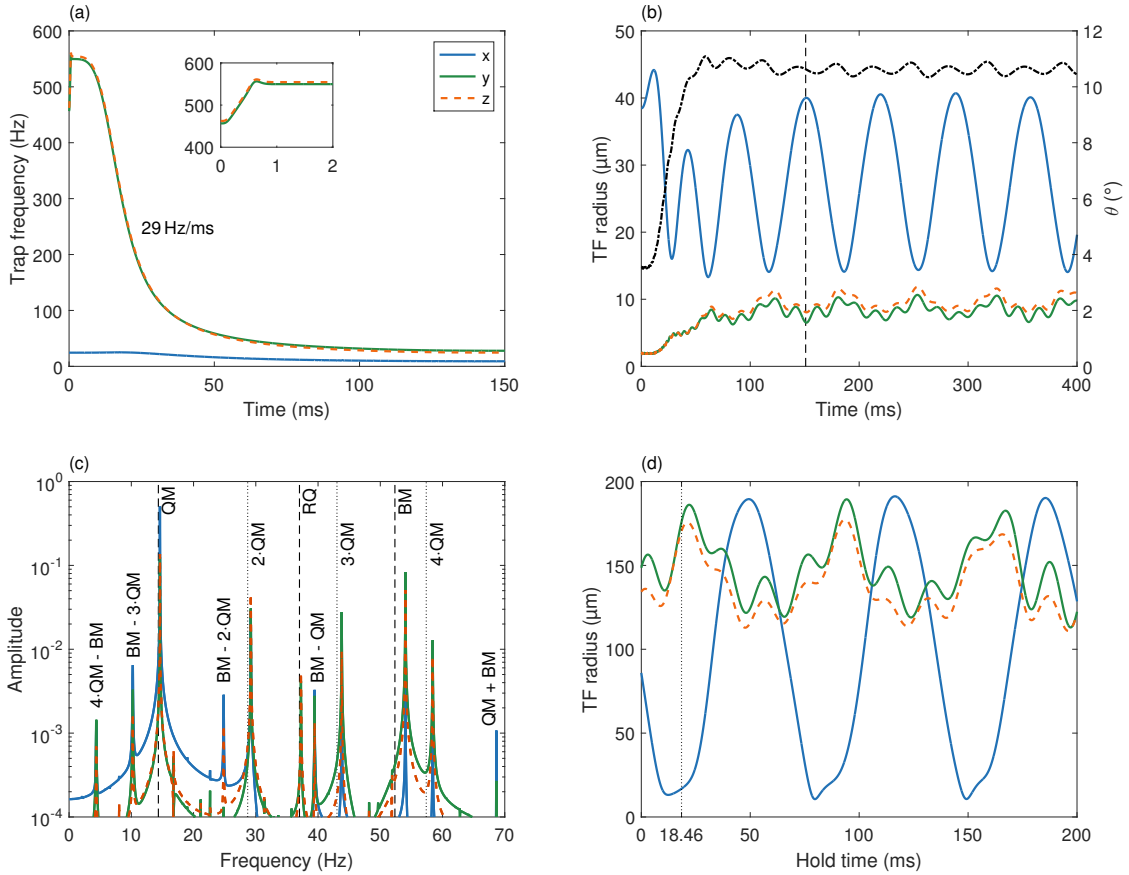


Figure 6.12: The course of the trap frequencies during the 150 ms ramp to release trap B is depicted in (a). The inset shows an increase of the radial trap frequencies by approximately 100 Hz right before the ramp due to the adjustment of the x coil current from 0.5 A to 0.1 A as used for the quantization field during the free expansion phase. In the course of the ramp, the radial frequencies decrease by up to 29 Hz/ms. (b) shows the corresponding TF radii during this ramp and for a subsequent hold time of 250 ms after the end of the ramp, which is highlighted by the dashed thin black line. A BEC containing $N = 10^5$ atoms is assumed. The rotation angle θ of the condensate's principal axes about the z axis is shown as the dash-dotted black line (right ordinate). (c) shows the amplitude spectrum of the normalized TF radii during the hold time. The normalization is comparable to Figs. 6.7 to 6.9. The peaks are attributed to the principal modes (QM, RQ, BM) and their harmonics. All remaining peaks can be attributed to sum and difference frequencies. The TF radii after 100 ms TOF are plotted in (d) assuming the oscillations in (b). The dotted line indicates the release time used for the BC-lens.

above. The dominant mode is the QM with the large amplitude oscillation of R_x , as shown in (b). The first point of excitation is directly at the beginning due to the changing x current within the first millisecond. This leads to the initial increase of R_x . The interval with rapidly decreasing radial frequencies excites the QM almost exclusively as proven by another simulation (not shown). The strong coupling of the SM to the QM leads to the deformed sine oscillation of the cloud's orientation. In order to identify the modes contributing to the disordered course of R_y and R_z , the amplitude spectrum is calculated and presented in (c). It is normalized and arranged like in Figs. 6.7 to 6.9 for comparison. As expected from (b), the dominant mode is indeed the QM. The BM is excited much stronger than the RQ mode. The spectrum exhibits many more peaks, all of which can be attributed to linear combinations of the mode frequencies. The corresponding sum and difference frequencies are indicated in the figure for the larger peaks.

All collective modes are *in situ* oscillations and cannot continue after the release. Despite this, there is a strong effect on the free expansion, caused by the time varying nonzero initial expansion rate in combination with the oscillating initial TF radii. The latter result in a time dependent interaction energy which is converted into kinetic energy during the initial free expansion phase. The effect of the particular excitation is shown in (d) for 100 ms TOF. Again, the largest amplitude occurs in the axial direction. The hold time used for the BC-lens is marked by the vertical dotted line. The axial radius is minimal at this time. The effect on the lens is discussed in the next subsection.

The TF radii themselves are not the first choice for the detection of these modes. This is due to the required rescaling to a reference particle number in combination with the uncertainties in the measurement of N . A better choice is the aspect ratio, because the scaling law drops out. Experimental data were sampled after 100 ms TOF using both detection systems. They are shown by the circles in Fig. 6.13(a) for the Detection 1 view and in (b) for Detection 2. The solid thin blue lines show the expectation according to the simulation in Fig. 6.12(d). The curves overestimate the signal, because no damping of the collective modes was included so far. This damping can be mediated, for example, by trap anharmonicities [192] and by thermal atoms [195], which are always present at $T > 0$. Within the simulation, the system of differential equation has to be extended by a term

$$-\frac{2\dot{u}_i}{\tau_{\text{damp}}\bar{\omega}},$$

where τ_{damp} is the damping time, which can be found by improving the overlap with the data in Fig. 6.13(a). A reasonable agreement is found for $\tau_{\text{damp}} = 300$ ms as shown by the solid thick blue line. In order to show the effect of a varying number of atoms, the simulation is repeated for $N = 3 \cdot 10^4$ (dotted blue line) and for $N = 3 \cdot 10^5$ (dash-dotted blue line). The differences are small. Their origin is the dependence of the mode frequencies on N .

The analysis of the Detection 2 data is more complex, because there are two images of the same cloud. This is encoded in the color using blue for the left cloud and orange for the right one. In any case, the expected aspect ratios are almost

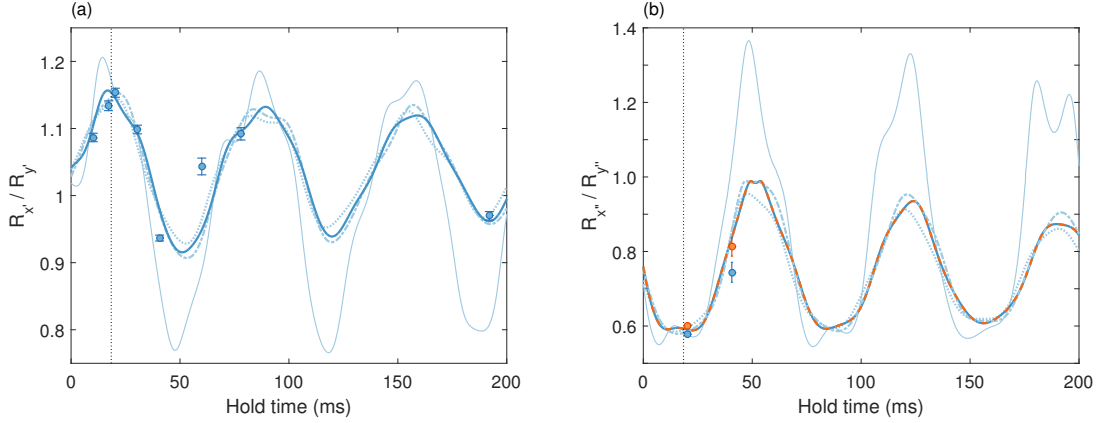


Figure 6.13: The simulated aspect ratio of a BEC after 100 ms TOF is shown as a function of the hold time in release trap B for the Detection 1 (a) and 2 (b) frame. The solid thin blue lines show the undamped case while all other lines are simulated with a characteristic damping time of 300 ms. All solid lines assume $N = 10^5$. The dotted (dash-dotted) lines are simulated for $N = 3 \cdot 10^4$ ($N = 3 \cdot 10^5$). The circles show data points measured in microgravity. The reflected and direct image for Detection 2 are expected to exhibit almost the same aspect ratio, as shown by the dashed orange line in (b) for $N = 10^5$. The measured aspect ratio is shown for the left (blue circles) and right cloud (orange circles) in the Detection 2 density images.

equal for both clouds. This is exemplarily shown by the dashed orange line in (b) for the damped case with $N = 10^5$.

The data set proves the excitation of collective modes prior to the BC-lens. However, there are not enough points for a reliable estimate of the damping time. Indeed, not a single point was reproduced so far. The simulations are in reasonable agreement with the data. The residual deviations could arise from uncertainties in the chip model.

As a matter of fact, it is possible to fit a single sinusoid to the data in (a) with a frequency of 19.5 Hz. The expected QM frequency is $f_{\text{QM}} \approx 14.5$ Hz only. This difference is significant and cannot be explained in terms of systematic effects arising from the number of atoms or the amplitude of the oscillation. Another systematic effect is an increase of f_{QM} due to a SM oscillation, during which the axial direction samples a part of the higher radial trap frequency f_y . Nevertheless, this effect is far too small to be responsible for such a shift. For example, an oscillation amplitude of 10° for the SM would increase f_{QM} by 0.3 Hz only. The remaining uncertainty is the chip model. The axial trap frequency was not measured for this particular trap. However, a relative difference of +36% would be required for a QM frequency of 19.5 Hz. This appears unlikely in the view of relative differences of 4% or below, which have been observed so far (see Figs. 5.2, 5.16 and 5.18), even though all frequencies measured in microgravity are systematically higher than the ones predicted by the chip model. This discrepancy can be reviewed in the overview of trap frequencies in Appendix C.2.

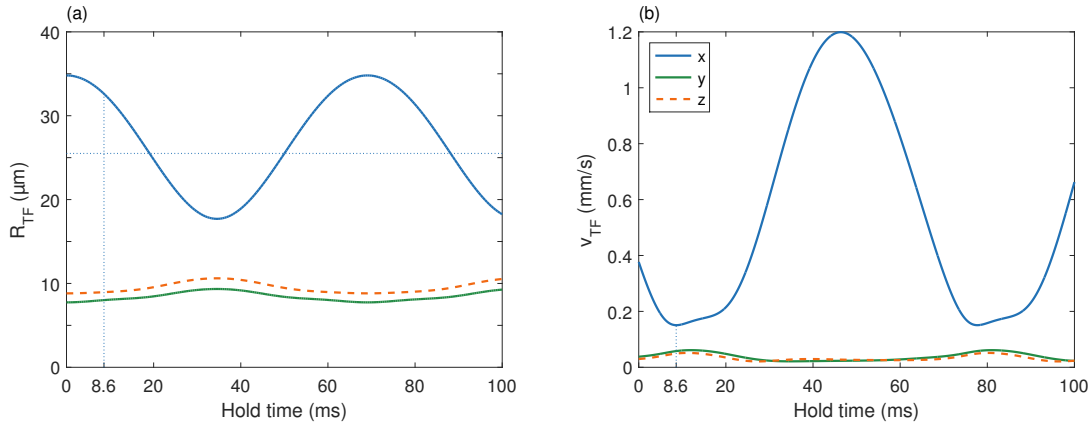


Figure 6.14: (a) shows a pure QM oscillation of 10^5 atoms in release trap B. The equilibrium TF radius in the x direction is $R_x = 25.5 \mu\text{m}$ and depicted as the horizontal dotted blue line. This QM affects the velocity v_{TF} , at which the TF radii increase. The limiting velocities after 80 ms pre-TOF, BC-lens (2.64 ms) and 20 s TOF are plotted in (b) as a function of the hold time. The smallest expansion rate in the axial direction is $v_{\text{TF},x} = 151 \mu\text{m/s}$ and can be observed after 8.6 ms of the oscillation assuming the initial phase shown in (a). The curves are periodic with the QM frequency.

6.3.2 Quadrupole mode excitations for magnetic lensing

A quadrupole mode excitation can be used to systematically improve a magnetic lens. The key idea is that the TF radius in the axial direction (R_x), which is hardly affected by the lens, should be as large as possible at the time of release. Ideally, this direction would be neither expanding due to the interaction energy nor is it lensed. The TF radius would remain approximately constant. For the further discussion, it is helpful to introduce a TF velocity as:

$$v_{\text{TF}} = \frac{d}{dt} R_{\text{TF}}. \quad (6.29)$$

This velocity increases during the free expansion due to the conversion of interaction energy into kinetic energy. For large BECs, v_{TF} saturates and the atomic cloud expands further with this limiting TF velocity.

As an example case, a pure QM is assumed in release trap B, as shown in Fig. 6.14(a). The axial radius (solid blue line) varies by almost $\pm 10 \mu\text{m}$ with respect to the equilibrium value of $R_x = 25.5 \mu\text{m}$ (horizontal dotted line). The phase of the QM oscillation can be adjusted with the hold time in the release trap. As an example, the resulting phase dependent performance of the BC-lens with 80 ms pre-TOF is analyzed. The limiting TF velocity in the three directions is shown in (b). It can be seen, that the optimum hold time is not at the peak of the axial QM oscillation (0 ms), but at a finite hold time (8.6 ms). This time depends on the QM amplitude. For larger amplitudes, the ideal case of an unaffected axial direction is fulfilled better. In this example case, however, a small negative initial TF velocity is beneficial, because it counteracts the emerging expansion of R_x while the radial

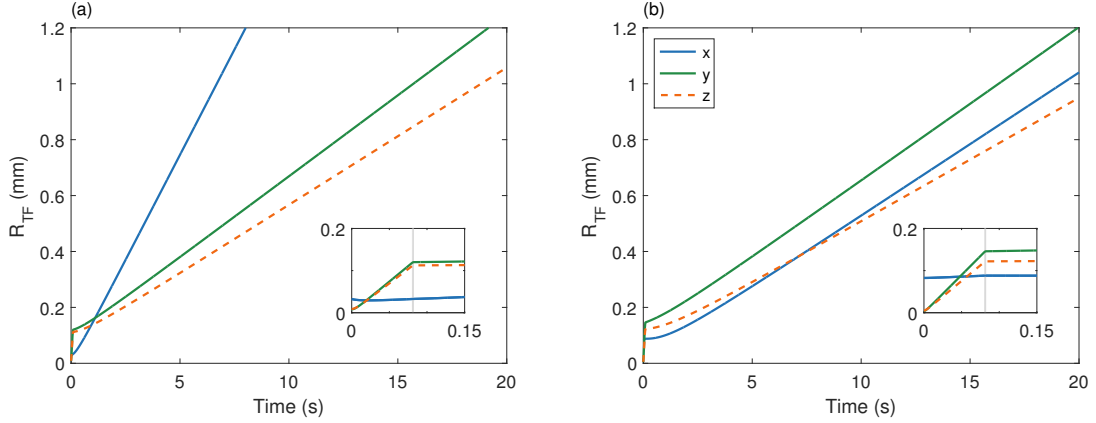


Figure 6.15: The expansion curves before, during and after the BC-lens are shown for two different initial states prior to the release from trap B. The initial state in (a) is the one depicted in Fig. 6.14(a) with a hold time of 8.6 ms. The inset is a magnified view of the initial expansion phase including the lens, which is indicated as the shaded area. (b) shows the equivalent curves for an even larger QM amplitude with initial $R_x = 82.6 \mu\text{m}$ and an optimum hold time of 0.2 ms.

directions are still compact. Nevertheless, the minimum axial expansion rate of $v_{\text{TF}} \approx 0.2 \text{ mm/s}$ still exceeds the radial ones. Obviously, it is also possible to deteriorate the lens performance by an unfortunate hold time. The expansion curves using the optimum hold time are plotted in Fig. 6.15(a). The inset shows a magnified view of the pre-TOF phase and the lens (shaded gray). The pre-compensation of the emerging axial expansion rate by means of a negative initial v_{TF} is clearly visible. Still, the axial direction dominates the expansion on long time scales. The limiting TF velocity is $(151, 58, 49) \mu\text{m/s}$ resulting in $v_{\text{rms}} = 64 \mu\text{m/s}$, which is equivalent to $T_{\text{kin}} = 14 \text{ pK}$.

The effect of an even larger QM amplitude is visualized in Fig. 6.15(b). The expansion curves show the TF radii of an almost perfectly collimated ensemble. The residual expansion rates are $v_{\text{TF}} = (51, 55, 44) \mu\text{m/s}$ and originate from the residual interaction energy at the pre-TOF size. The inset shows the huge initial axial radius $R_x = 86.6 \mu\text{m}$ (blue line), which remains approximately constant on this time scale. Neglecting the trap anharmonicity, this ensemble would be detectable for approximately 10 s TOF and exhibit $v_{\text{rms}} = 33 \mu\text{m/s}$ equivalent to $T_{\text{kin}} = 4 \text{ pK}$.

It is conceivable that collective modes can be utilized even further. One limitation of magnetic lensing is the constrained set of magnetic traps, that can be realized experimentally. The key motivation for the choice of the BC-lens is the axial symmetry at this and only this position. Traps further away from the chip are even less anharmonic, but no longer share the same radial trapping frequency. This problem could be relaxed by superimposing the QM with a RQ mode. Thinking further, it might even be possible to skirt the tail problem by using no lens at all, but rather engineer the quantum state in a way that it exhibits large initial TF radii and vanishing initial TF velocities. However, this would be highly nontrivial for several

reasons. For example, the particle number would have to be stabilized to avoid fluctuations of the mode phase. Furthermore, the scope of the system of differential equations [Eq. (6.5)] might be exceeded due to very high transient densities and the anharmonicities.

6.4 Experimental realization of magnetic lensing

Several coherent data sets after different lens types were measured in microgravity. The absorption images are shown in Appendices A and B. A lot of information can be extracted from these images. This was demonstrated in the previous chapters. For example, the magnetic field gradient was extracted from quadratic fits to the COM positions of data sets with atoms in the $m_F = 2$ substate (see Section 3.4). Data sets with atoms in the $m_F = 0$ substate were used for the air drag correction and the analysis of other systematics on the COMM (see Section 5.2). The ARP efficiency in microgravity could be measured, too (see Section 4.4). After the ARP, all atomic substates need to be separated in space by a SG kick, because the residual magnetic field gradient is too weak such that different substates partially overlap for almost 0.5 s. This overlap would falsify the lens evaluation and thus make these images useless.

The size information in these images is the subject of this chapter. The presentation of the data is subdivided into the two principal lens types, SC-BC-lens and pure BC-lens. The first one involves the 250 ms sigmoid ramp for the transport of the atomic ensemble to release position A. No collective mode is excited here, unlike for the BC-lens, for which the transport to release position B is realized by the 150 ms STA ramp. This transfer excites a QM that is advantageous for magnetic lensing, provided that the phase is chosen correctly. Two slightly different realizations of the BC-lens are presented. The differences are explained further in the corresponding subsection.

6.4.1 SC-BC-lens

The SC-BC-lens trap is very similar to release trap A, from which the atoms for this lens are released. It is derived from release trap A by scaling down all currents with the same factor. This lens scaling is not held constant during the lens, but is ramped up and down within 6 ms resembling a Gaussian. The maximum lens scaling is 0.244 and occurs after 3 ms at the center time of the lens. The control functions for the SC, BC and the y coil are calculated such that the currents follow the desired ramp, which was used as an example case in Section 3.3 (see Fig. 3.4). The x coil must not be rescaled accordingly, because a finite quantization field must be present at all times to avoid spin flips. The resulting lens trap frequencies are shown in Fig. 6.16(a) for the range of scalings used for SC-BC-lens. It can be seen, that the trap frequencies depend nonlinearly on the lens scaling. Below 0.065, the resulting potential no longer forms a trap in three dimensions. In addition, the trap rotates about the z axis and translates in all three directions, as shown in (b). One

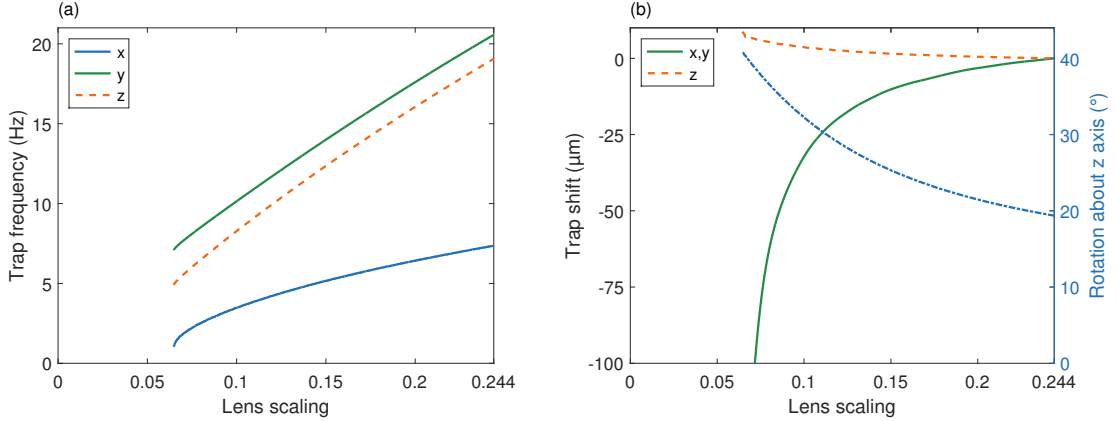


Figure 6.16: The behavior of the trap frequencies as predicted by the chip model when reducing the currents for release trap A to a certain factor (lens scaling) is shown in (a). A lens scaling of 0.244 corresponds to the maximum trap strength used during the SC-BC-lens. Below 0.065, the chip model predicts no traps. In between, the trap center shifts as a function of the scaling as shown in (b). The trap’s principal axes rotate about the z axis, as depicted by the dash-dotted blue line (right axis).

reason for this is the constant x current. The effect is mitigated already by starting the y coil ramp at 5 mA rather than zero. This list of effects makes it practically impossible to evaluate the expansion after the lens by means of Eq. (6.5). For this reason, 3D numerical simulations are performed and compared to the data, as will be discussed below.

Measured data set

A subset of the acquired absorption images is shown in Fig. 6.17. The two pre-TOF images show the input state for the lens as detected by the respective cameras. The Detection 2 images show the right cloud only. The left one (mirror image) looks similar, but is much fainter. The reason for this is the different polarization of the detection light. The magnetic field direction is optimized for the cycling transition of the Detection 1 system using σ^+ -polarized light. The Detection 2 laser beam is σ^- -polarized, which is converted into σ^+ after the reflection at the chip surface. This reflected light is responsible for the right cloud in the image. The σ^- -polarized direct light responsible for the mirror image is detuned from resonance due to the magnetic quantization field. This field is reduced for all BC-lens data sets such that both clouds are clearly visible.

The most prominent feature in the Detection 1 image series is the comet like tail due to the L_3 anharmonicity, which was discussed above. The optical analog to this effect is comatic aberration. This tail is not pointing exactly into the x' direction, which would be expected. This deviation can be understood by a mismatch in the y position of the atoms with respect to the lens center at maximum lens scaling.

Within Fig. 6.17, the atoms are in the $m_F = 0$ substate in the images for 102 ms TOF and for all images with 500 ms TOF or more. The other atoms are in $m_F = 2$.

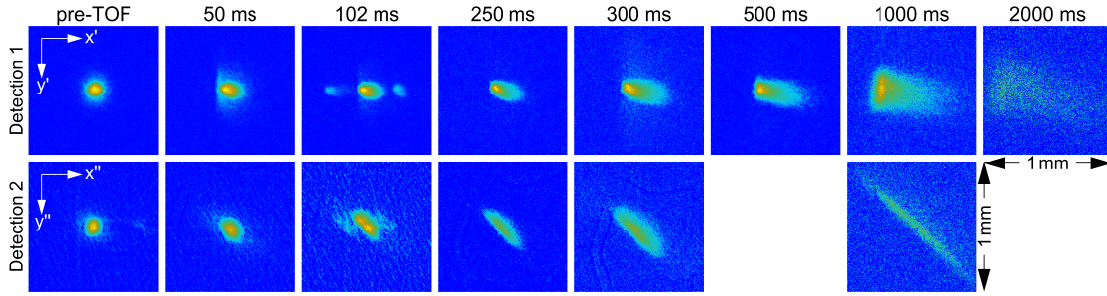


Figure 6.17: The image series shows the measured shape of the atomic cloud directly before the application of the SC-BC-lens (pre-TOF, leftmost column) and for various TOFs after this lens as detected by the two imaging systems Detection 1 (upper row) and Detection 2 (lower row). The respective camera coordinate systems are exemplarily given in the pre-TOF images. The lower row shows only the right cloud (direct image). The mirror image is similar, but much fainter because of an unfavorably high magnetic offset field used for the cycling transition (see Section 2.1).

In both 102 ms TOF images, three clouds are visible. The two fainter ones are atoms in the $m_F = +1$ substate (right) and in the $m_F = -1$ substate (left). The Gaussian background is visible in the Detection 1 images for short TOFs. It is much larger and fainter compared to the condensate fraction and exhibits a sharp and almost vertical edge to the left. This edge is a consequence of the L_3 anharmonicity, too.

It is worth mentioning that the extent in the y' direction is much smaller than expected from the 45° projection of the practically unlensed x direction. This is a consequence of the translating and rotating lens trap due to the Gaussian ramp. The cloud's extent along the weak principal trap axis is still large, but a shear is imprinted onto the cloud resulting in a rotation of approximately 45° in the Detection 2 frame. The elongated atomic cloud is then almost co-aligned with the Detection 1 laser beam that is propagating from the bottom right to the top left within the Detection 2 frame. This results in the reduced size seen by the Detection 1 camera.

3D ray tracing simulation

The exact shape of the measured density distribution after the lens can be understood with the help of a 3D numerical ray tracing simulation. For this simulation, $N = 84 \cdot 10^3$ atoms are assumed, which is the average atom number for release trap A (see also Fig. 6.2). The input state, as seen in the pre-TOF images in Fig. 6.17, is well known: Each atom exhibits a TF distributed position. The TF radii and velocities 80 ms after release are calculated using the variational approach. The set of $k = \{1, \dots, N\}$ atomic velocities v_i^k is related to the atomic positions r_i^k by:

$$v_i^k = v_{\text{TF},i} \frac{r_i^k}{R_{\text{TF},i}}, \quad (6.30)$$

where $i = \{x, y, z\}$. These velocities are changed by the time dependent lens potential. This already includes the translation and rotation of the lens trap, because the

effect of the local potential gradient is evaluated for each of the N atoms at the respective position. The problem of describing the lens action for scalings smaller than 0.065 is also solved by this method. The free expansion during the TOF, that is after the lens, is determined by the post-lens position and velocity distribution. This ray tracing simulation neglects any residual mean field interactions of the atoms, which is justified, because the weak axis grows rapidly such that the densities are small. The interactions during the pre-TOF were intrinsically accounted for in the calculation of the input state by the variational approach.

The results of this simulation are shown in Appendix A as the first column of images for both detection systems. The corresponding TOF is given in every image. The measured density distributions are plotted next to the simulated ones. The measured images show the drop number in the top left corner and the information about the Zeeman state in the top right corner. The simulation agrees with the measured data. The shape, size and orientation of the simulated density distributions match the measured ones for both detection systems. However, it must be assumed that the lens potential is in fact stronger than predicted by the chip model. This is implemented as a global factor resulting in trap frequencies that are 7% higher. It is conceivable, that the chip model is inaccurate for shallow traps, because the model was not calibrated in this regime, but for stronger traps within ground-based measurements. Furthermore, magnetic offset fields and field gradients have a stronger effect on shallower traps. In fact, the assumption of a stronger trap is supported by the overview in Appendix C.2. Having said that, the stronger potential is equivalent to the application of the non-enhanced one at a later or for a longer time. This could actually happen if the magnetic field was delayed with respect to the coil current. Indeed, similar observations were made for the release protocol of this release trap, where the chip currents had to be ramped down a factor 1.14 more slowly than expected to reduce the COMM [see Fig. 5.20(b)]. However, the same enhancement factor has to be assumed for the simulation of the BC-lens below, where the coil current is not changed during the lens. Hence, the assumption of an enhanced potential compared the chip model's prediction is justified.

One free parameter in the simulation is the position of the atoms with respect to the lens. Both positions were measured (see Table 5.3) and the y offset of +18 μm leads to a correct prediction of the tail direction. In contrast, a z offset of -30 μm was used in the simulations instead of the measured average offset of -72 μm . Further away from the chip, the local trap frequency ω_z is smaller as a consequence of the L_3 anharmonicity. This effectively introduces a reduced chip model correction factor in this direction. As another consequence of this anharmonicity, the simulation predicts an extremely sharp left edge of the atomic cloud, which is not observed to this extent in the measured images for two reasons. First of all, a high local density tends to disperse due to atomic interactions. Second, the detection system cannot resolve such sharp features. These effects are not distinguishable in the images. They are accounted for in the simulation by a normally distributed position noise with a standard deviation of 10 μm .

The numerical simulation does not discriminate between different Zeeman states. In fact, a background magnetic field curvature would change the size of an $m_F = 2$

ensemble after some TOF. Such a curvature could not be ruled out by any measurement so far. However, a comparison of the measured images for different Zeeman states does not suggest the existence of such a curvature. Examples are the Detection 1 images for 0.3 s and all images for 1 s TOF. In fact, the statistical fluctuations from shot to shot are much larger, as can be seen in the Detection 1 images for 1 s TOF. These fluctuations can arise from a scatter in the position or in the number of atoms, for example.

Results

The application of the SC-BC-lens significantly reduces the expansion rate of the atomic ensemble and allows for its detection after a long TOF. Without the lens, the ensemble would exceed the image boundaries in Fig. 6.17 for the 250 ms images already. The longest free evolution time of a BEC observed in Q-2 is 2.7 s, which is equal to the current record [1]. The density images are also shown in Appendix A, but they are very dilute. Spatial filtering is required to see the atomic cloud at all. Still, the spatial density profiles of the absorption images show the characteristic shape expected from the previous images.

The measured density distributions were described by a 3D ray tracing simulation. The good agreement for the different TOFs allows for the conclusion that the simulated velocity distribution must be comparable to that of the real atomic ensemble. This is extremely useful, because the root mean square velocity can be obtained directly from this simulation. It is $v_{\text{rms}} = 330 \mu\text{m/s}$, which is equivalent to $T_{\text{kin}} = 378_{-30}^{+60} \text{pK}$. These values increase with N . For the standard reference number of $N = 10^5$ the result is $v_{\text{rms}} = 342 \mu\text{m/s}$ ($T_{\text{kin}} = 408 \text{pK}$). These results are well above the limit of 20 pK for an ideal harmonic 3D lens after this pre-TOF (Fig. 6.5). This discrepancy is primarily caused by the anharmonicity and the fact that the lens is collimating in two dimensions only. The given uncertainty in T_{kin} is estimated from the sensitivity of the simulated value to parameter changes.

6.4.2 BC-lens

The previous SC-BC-lens did not involve any collective excitation and was thus effectively a 2D lens. The transport of the atomic ensemble to release position B, as required for the BC-lens, does involve a collective behavior. It is primarily a QM, as discussed above. The excitation mechanism is well understood now, but was not known at the time the data sets were acquired. It was really a lucky coincidence that the hold time, which was determined by the phase of the *in situ* dipole oscillation, was also optimizing the phase of the QM. This is in no way clear because they propagate at different frequencies.

The SC-BC-lens was selected and optimized under the constraint of a release position that is accessible in a ground-based measurement, too. The strategy for the BC-lens was the opposite. The chip model predicts an axially symmetric trap with $\omega_{\text{BC-lens}} = 2\pi \cdot (3.0, 10.8, 10.8) \text{ Hz}$ at $z = 1449 \mu\text{m}$ with $I_{\text{BC}} = 1.8 \text{ A}$ and $I_y = -75.4 \text{ mA}$. The remaining sequence is adjusted accordingly, as described in the previous chapter.

The lens trap is switched on and off rather than ramped to avoid trap translations and rotations. A pre-TOF of 80 ms is chosen as a trade off between residual interactions and the sampling of anharmonicities. According to Eq. (6.12), the required lens time is $\tau_{\text{lens}} = 2.64 \text{ ms}$, which is not much longer than the characteristic switching time of the bias coil. For this reason, the coil current is switched on before the lens and only the BC current is used for the fast switching of the potential. The homogeneous magnetic field alone is not affecting the atoms.

Measured data sets

Three data sets were measured with the BC-lens. For the first one, the atoms remained in the $m_F = 2$ substate. This data set was also used to determine the magnetic field gradient in Section 3.4 with $I_x = 0.1 \text{ A}$ for the quantization field (Fig. 3.8). The second one was Set B in the COMM measurements (Fig. 5.1) with atoms in the $m_F = 0$ substate. This is the only data set with images from the Detection 2 system. A third data set was measured with a slightly different lens configuration using $I_{\text{BC}} = 1.828 \text{ A}$ and corresponds to Set C in (Fig. 5.1). This change successfully eliminated the COMM in the x' direction. The different BC current is responsible for slightly different trap frequencies and a shifted trap center, which is $29 \mu\text{m}$ further away from the chip. Hence, the data sets can be grouped by the BC current that is used for the lens. The differences regarding the lens performance are small. Still, they are considered in the analysis below. To keep track of the key parameters, they are summarized here:

I) $I_{\text{BC}} = 1.8 \text{ A}$, $m_F = 2$

II) $I_{\text{BC}} = 1.8 \text{ A}$, $m_F = 0$, Set B

III) $I_{\text{BC}} = 1.828 \text{ A}$, $m_F = 0$, Set C

Data Set B gives the best overview of the lens performance because of the information from both cameras. The measured images are shown in Fig. 6.18, which is arranged like Fig. 6.17. The only differences are the additional information from the left cloud in the Detection 2 images and the different scale. The absorption images exhibit some characteristic differences compared to the SC-BC-lens image series. First of all, the tail in the Detection 1 images is pointing in the x' direction, indicating a good overlap of atoms and lens in the y direction. Another evident feature is the anchor like shape for long TOFs. Furthermore it can be seen that the lens is not perfectly collimating the atomic ensemble. There is a focus around 400 ms. Again, the principal axes of the clouds in the Detection 2 images are rotated, but not as much as for the SC-BC-lens. The comet like tail is visible in these images, too. It points towards the left for the left cloud and towards the right for the right one, as expected. This is clearly visible after 200 ms TOF. After 1 s, the anchor like shape destroys this correlation.

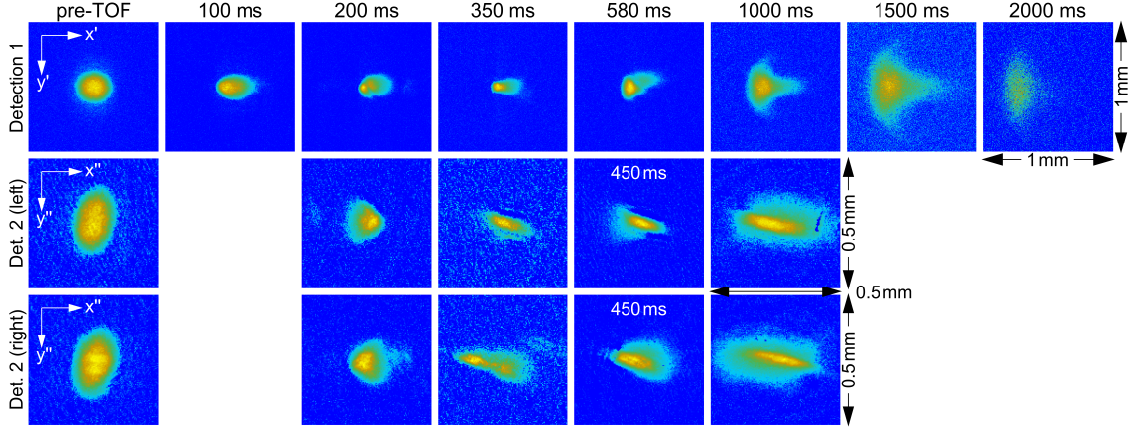


Figure 6.18: The image series shows the measured shape of the atomic cloud directly before the application of the BC-lens (pre-TOF, leftmost column) and for various TOFs after this lens as detected by the two imaging systems Detection 1 (upper row) and Detection 2 (lower two rows). The respective camera coordinate systems are exemplarily given in the pre-TOF images, which are common to all BC-lens data sets. The remaining images belong to Data Set B.

Analysis using the variational approach

The variational approach was used to describe the *in situ* dynamics of the condensate during the transfer to release position B. The shape during the free expansion was then calculated by a subsequent time evolution of Eq. (6.5) with the $\tilde{\lambda}_i = 0$. It is possible to extend this analysis to the lens by choosing the $\tilde{\lambda}_i$ according to the respective BC-lens frequencies for the duration of the lens. This strategy was applied for the numerical simulation of the matter-wave telescope in Fig. 6.4, too. An analysis of the SC-BC-lens using this approach was not possible because the lens trap frequencies were not defined at all times. In contrast, the BC-lens frequencies are constant during the lens. The contributions from the short switching processes are neglected. Hence, it is possible to partially evaluate the BC-lens performance using this approach. The density profiles in the y' direction are still more or less TF distributed, but the x' direction cannot be analyzed in the same way because of the tail. The TF radius is fitted for the Detection 2 images within a coordinate system co-rotated with the eigensystem of the measured atomic cloud. The resulting values are falsified by the tail, too, but not as much as for the Detection 1 images.

$I_{BC} = 1.8 \text{ A}$

The simulated time dependence of the TF radii for both data sets using $I_{BC} = 1.8 \text{ A}$ is plotted in Fig. 6.19(a). These curves assume $N = 10^5$. The lens ends at $\text{TOF} = 0$ and the pre-TOF is the interval with negative TOF values. The *in situ* dynamics prior to the release was shown in Fig. 6.12(b) and is not reprinted here. The behavior of R_x , which leads to a collimation in this direction, is visible, too (see also Figs. 6.14 and 6.15). A focus in the y direction is predicted after approximately 750 ms. The projection of the TF radii in (a) onto the Detection 1 system is shown in (b). Here,

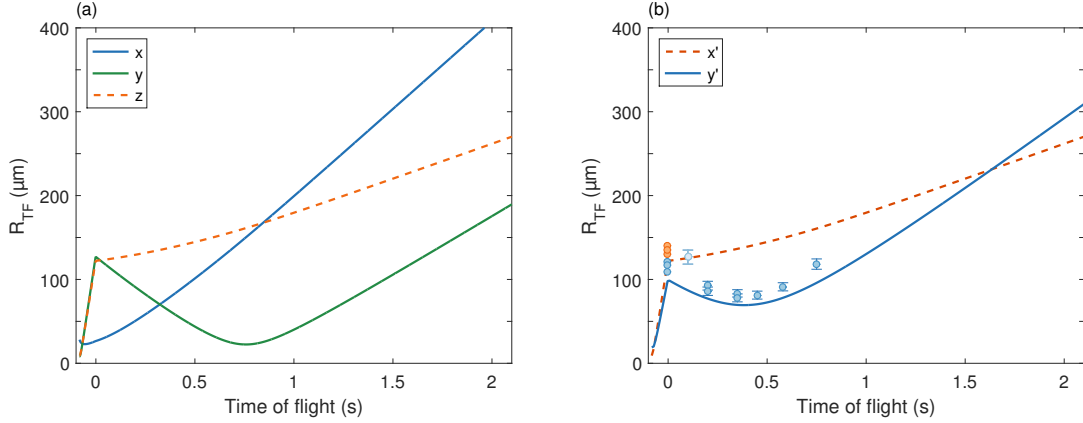


Figure 6.19: (a) shows the simulated time evolution of the TF radii before (TOF < 0) and after (TOF > 0) the BC-lens with $I_{\text{BC}} = 1.8 \text{ A}$ assuming the initial state predicted in Fig. 6.12(d) and a characteristic damping time of 300 ms. (b) depicts the projection of the curves from (a) onto the Detection 1 frame (x' and y') in comparison to experimental data using the same color code. The atoms are in the $m_F = 2$ substate. In the x' direction, the TF radius is not defined after the lens because of the comet-like tail. All curves and data are rescaled to $N = 10^5$. The error bars are calculated assuming 30% relative uncertainty in the fitted number of atoms. The data point for 100 ms is plotted in a lighter blue, because the measured atomic cloud exhibits an artifact (see D187a in Appendix B.1.1).

the focus occurs earlier at 400 ms due to the geometry of the imaging system. This focus is no desired feature, but a consequence of a lens action that is underestimated by 7% like for the SC-BC-lens. The circles show the measured data points. The ones at TOF = 0 are the pre-TOF data and common to all three BC-lens data sets. The remaining data points were sampled after the lens and belong to the data set in the $m_F = 2$ substate. All data points are rescaled to $N = 10^5$ for comparison. This step is only an approximation when collective modes are involved, because the mode frequencies depend on N . Still, this effect is small, as shown in the previous section. Having said that, all these data points are slightly above the predicted curve. Even the measured pre-TOF size, for which $R_{y'}$ is still well defined, exceeds the prediction. One possible explanation is that the actual collective excitation differs from the simulated one, for example due to uncertainties in the chip model. However, an underestimation of the respective measured number of atoms for each data point would result in an overestimation of the measured size, too, because of the rescaling. Twice as many atoms would be required to explain the discrepancy for the pre-TOF images, which is a rather large difference. The error bars indicate the effect of a 30% relative uncertainty in N . Despite this, the model correctly predicts the course of $R_{y'}$. Some absorption images, for example the Detection 1 image for 200 ms in Fig. 6.18, exhibit artifacts that are not yet understood. These data points are plotted in a lighter blue because the artifacts can affect the measured size as well as the number of atoms.

Data Set B in $m_F = 0$ is the second set with $I_{\text{BC}} = 1.8 \text{ A}$ and shares the same expected curves. The measured TF radii within the Detection 1 frame are shown

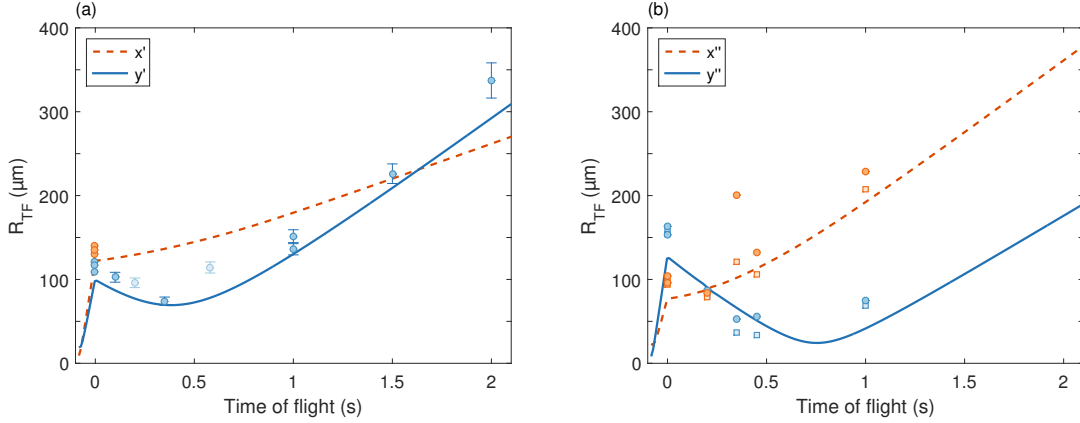


Figure 6.20: (a) shows the same curves like in Fig. 6.19(b), but with experimental data points using atoms prepared in the $m_F = 0$ substate after the lens with $I_{BC} = 1.8 \text{ A}$ (Data Set B, see Fig. 6.18). The three data points at -3 ms are the pre-TOF images with atoms still in the $m_F = 2$ substate. Again, data points in light blue exhibit artifacts. The corresponding projection onto the Detection 2 frame is depicted in (b). The circles show the TF radii of the direct image (right cloud) and the squares correspond the mirror image (left cloud). All curves and the data points in (a) are rescaled to $N = 10^5$. The error bars are calculated assuming 30% relative uncertainty in the fitted number of atoms. In (b), error bars are omitted, because there is no information on the number of atoms.

in Fig. 6.20(a). Again, all data points are slightly above the predicted curve for the Detection 1 view, but there is no systematic difference compared to the previous data set in $m_F = 2$. This would have been a hint to an existing background magnetic field curvature. In (b), the circles represent the right cloud in the Detection 2 absorption images and the fitted radii for the left clouds are given by the squares. These radii are not rescaled, because no information on the number of atoms exists for these data points. The projected TF radii can be different for the direct and mirror image, respectively. This would be the case if the eigensystem of the trap were rotated about the y axis. The effect would be, for example, a rotation of the anisotropic atomic cloud into the reflected detection laser beam for the direct image and correspondingly out of the direct beam for the reflected image. As a consequence, the two shadows cast onto the CCD by the anisotropic cloud would differ. However, such a rotation is negligible according to the chip model such that the expected curves overlap for both images. The principal course of the data points follows these curves, even though the pre-TOF radii are still systematically larger. Actually, the data points do exhibit a small systematic difference when comparing the radii of the direct and mirror image. Still, this is no evidence for a rotation about the y axis because of the dissimilar polarization and magnetic field orientation relative to the laser beam for the two clouds.

$I_{BC} = 1.828 \text{ A}$

The expected course of the TF radii after the shifted BC-lens with $I_{BC} = 1.828 \text{ A}$ for Data Set C is slightly different and depicted by the thick lines in Fig. 6.21(a).

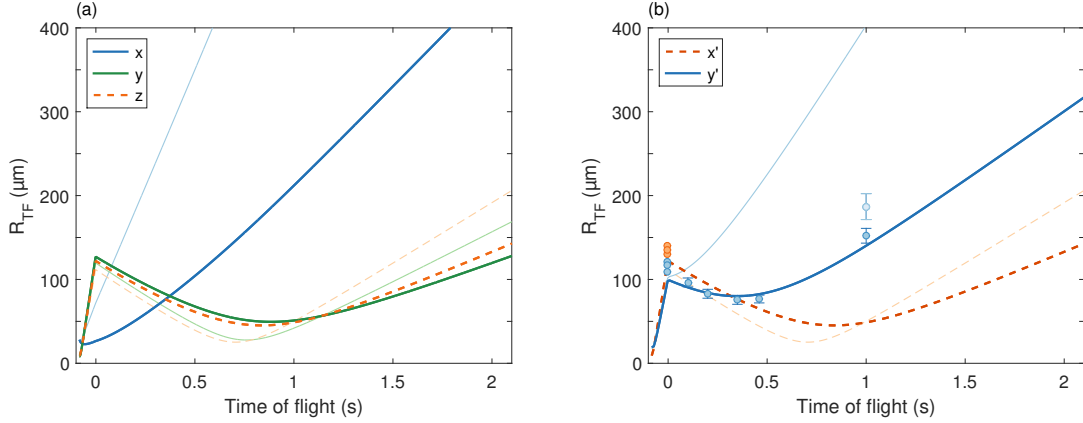


Figure 6.21: The thick lines in (a) show the simulated time evolution of the TF radii before (TOF < 0) and after (TOF > 0) the shifted BC-lens with $I_{BC} = 1.828 \text{ A}$ assuming the initial state predicted in Fig. 6.12(d) and a characteristic damping time of 300 ms. The thin lines depict the expected expansion without any collective excitation. (b) depicts the projection of the curves from (a) onto the Detection 1 frame (x' and y') in comparison to experimental data using the same color code. The atoms are in the $m_F = 0$ substate and belong to Data Set C, except for the three pre-TOF data points common to all BC-lens data sets. Again, data points in light blue exhibit artifacts. The error bars are calculated assuming 30% relative uncertainty in the fitted number of atoms.

The largest difference compared to Fig. 6.19(a) can be seen in the z direction. The thin lines visualize the action of the lens if no collective mode of the BEC is excited. The radial directions are hardly affected by the mode, but the expansion rate in the x direction is significantly higher without the QM. However, its amplitude is still insufficient for a perfect collimation in this direction. These thin lines are plotted in the Detection 1 view (b), too. This is another strong confirmation of the simulated collective excitation, because the data points (blue circles) are well described by the corresponding predicted curve (thick blue line).

3D ray tracing simulation

Like for the SC-BC-lens, a 3D ray tracing simulation can help to understand the dynamics after the lens. The details of this simulation were described above such that only the differences are mentioned here. The biggest difference is the input state for the lens because of the collective excitation. As a consequence, R_x is not expanding quickly. This is exactly the goal that should be reached, but it leads to a larger residual density and accordingly to stronger interactions during the TOF. Hence, they may no longer be neglected. However, a full 3D simulation of the Gross-Pitaevskii equation with a reasonable spatial resolution requires a massive amount of computational power. For this reason, the interactions are considered in an approximate manner by calculating the root mean square size and using this value to determine the effect of the interactions by the variational approach. This strategy reproduces the expansion of a TF distributed cloud, but can be an approximation

only for distorted clouds as measured with Q-2.

Apart from that, no offset needs to be assumed in the x and y directions, but a z offset of $31\ \mu\text{m}$ is required for the $I_{\text{BC}} = 1.8\ \text{A}$ data sets. The adapted BC current shifts the lens by $29\ \mu\text{m}$ away from the chip and towards the atoms leaving a negligible position difference. The measured pre-TOF orientation of the atomic ensemble deviates from the predicted one. A rotation of the atomic cloud by -5° about the z axis has to be assumed to meet the measured input state for the lens. All these effects also affect the dynamics after the lens as expected from the variational approach. They were accounted for in Figs. 6.19 to 6.21.

An analogous comparison of this ray tracing simulation to the experimental data is given in Appendix B for the three BC-lens data sets. The tail points in the x' direction, which confirms the good overlap of atoms and lens in the y direction. The anchor like shape can be reproduced by the simulation. This is particularly promoted by the small rotation and the enhanced potential. Furthermore, the anchor is more pronounced for a larger number of atoms. The overall shape of the measured clouds in the Detection 1 view can be reproduced very well, but the size tends to be underestimated. This effect was observed in the previous analysis based on the variational approach, too. One big problem is the varying number of atoms in the measured ensembles. The 3D simulation assumes $N = 10^5$, but the measured values can be different. In principle, it is possible to leave the atom number as a parameter that is to be optimized for every data point. However, this also involves a re-calculation of the collective excitation. This step takes more than an hour and is too slow to be part of a fit routine. The simulated Detection 2 view agrees with the measured data except for the lagging orientation.

Results

The BC-lens realized with Q-2 shows the fruitful interplay of a QM collective excitation with an axially symmetric magnetic lens to achieve a collimation in three spatial dimensions. This was understood with the help of numerical simulations. Table 6.1 summarizes the results of all BC-lens simulations that were presented in this chapter. The three components of the TF velocity, the root mean square velocity and the kinetic temperature are listed for $N = 10^5$. The results in the upper part of the table are based on the variational approach. The velocity spread that was calculated using the 3D ray tracing simulation is shown in the lower part of the table for the three BC-lens data sets. This simulation can be seen as a fit to the experimental data.

The first row in the upper part of the table quantifies the free expansion out of release trap B if neither a lens is applied nor a collective mode is excited. This ensemble would grow in size with a few mm/s, which is equivalent to a kinetic temperature of approximately 2 nK. This can be considered hot in the scope of this work. The largest reduction of the velocity spread is possible with the BC-lens alone (second row), even without any collective excitation. Still, the lens itself hardly affects $v_{\text{TF},x}$, as discussed. Only the QM can lead to a significant reduction of this velocity, even though at the cost of a small increase in the radial directions.

| | $v_{\text{TF},x} \left(\frac{\mu\text{m}}{\text{s}} \right)$ | $v_{\text{TF},y} \left(\frac{\mu\text{m}}{\text{s}} \right)$ | $v_{\text{TF},z} \left(\frac{\mu\text{m}}{\text{s}} \right)$ | $v_{\text{rms}} \left(\frac{\mu\text{m}}{\text{s}} \right)$ | $T_{\text{kin}} \text{ (pK)}$ |
|------------------|---|---|---|--|-------------------------------|
| No lens/mode | 625 | 1451 | 1343 | 784 | 2139 |
| No mode | 566 | 29 | 24 | 214 | 160 |
| Sim. mode | 175 | 61 | 48 | 72 | 18 |
| Fig. 6.15(a) | 160 | 58 | 49 | 64 | 14 |
| Fig. 6.15(b) | 51 | 55 | 44 | 33 | 4 |
| Set in $m_F = 2$ | - | - | - | 117 | 48 |
| Set B | - | - | - | 117 | 48 |
| Set C | - | - | - | 126 | 55 |

Table 6.1: Comparison of the three components of the TF velocity, the root mean square velocity and the kinetic temperature assuming $N = 10^5$ for different numerical simulations. The upper part is based on the variational approach. The first row lists the values for the free expansion without any lens or collective excitation as a reference. The remaining rows of the upper part quantify the dependence of the post-BC-lens expansion on the collective excitation. The simulated mode (sim. mode) is the expected one in Q-2. The lower part lists the results of a 3D simulation of the measured data sets. These simulations assume the simulated mode as the input state for the respective lens.

The net effect is a significantly reduced velocity spread. This was analyzed for three different collective excitations. The first one is the simulated mode (third row) that is excited during the transfer of the atoms to their release position. This actually excited mode is not a pure QM, in contrast to the bottom two rows of the upper part in the table. They would quantify the expansion if a pure QM of a similar amplitude (a) or an optimized amplitude (b) had been excited. This shows the great potential of the QM plus lens combination. The 4 pK are no fundamental limit but rather a consequence of the chosen combination of release trap and pre-TOF.

The 3D simulation of the three BC-lens data sets yields significantly larger values compared to the variational approach including the simulated collective mode. This is a consequence of the anharmonic potential resulting in the anchor like shape after a long TOF. The first two rows are equal, because the lens is unchanged. Set C, on the other hand, exhibits a slightly larger velocity spread. The uncertainty in the values for T_{kin} is on the order of 10 pK estimated like for the SC-BC-lens. The measured ensemble, however, is systematically larger than the simulated one. This can result in a systematic underestimation of the velocity spread by the 3D simulation. There can be different reasons for the mismatch. First of all, the chip model is used for the 3D simulation and for the simulation of the collective excitation, where the coarse of the trap frequencies is required. Hence, any uncertainty in this model directly affects all lens simulations. Aside from that, the simulation of the collective excitation assumes a harmonic potential and a certain damping time of the excitation. It is conceivable that the anharmonicity does have a small effect on the mode. In addition, there may be different damping times for the different modes such that the actual mode slightly differs from the simulated one. These effects would change the input state for the lens and thus the subsequent expansion. Further uncertainties

are the approximate treatment of the interactions, the neglected switching process of the BC current and the number of atoms. Still, there is no good alternative to the 3D simulation for the determination of the velocity spread. The reason is that some classical atomic trajectories converge after the lens. This destroys the linear mapping of position and velocity for intermediate TOFs. After a long TOF, that is more than 2 s, the linear mapping re-establishes such that the rms size of the atomic ensemble is indeed a measure for the rms velocity. However, the limited detection efficiency would systematically reduce this size in that TOF regime, such that this is not an option. In order to derive an estimate on how much the 3D simulation underestimates the velocity spread, the post-lens density and velocity distribution is adjusted in a separate simulation to match the rms size of simulated and measured density profiles for all TOFs. This is meaningful for Set B only, because the density profiles can be checked for both detection views. The changes are kept small enough to preserve the overall shape of the simulated clouds. Based on this approach, the estimate for the kinetic temperature is $T_{\text{kin}} = 70_{-10}^{+20}$ pK equivalent to $v_{\text{rms}} \approx 140$ $\mu\text{m/s}$.

These BC-lens data sets are the first experimental realization of a collimation in three spatial dimensions. This is a huge step towards precision measurements in space. The velocity spread of 140 $\mu\text{m/s}$ almost satisfies the extremely ambitious STE-QUEST requirements, even though neither the mode amplitude nor the lens duration are fully optimized yet.

Chapter 7

Summary and discussion

The Q-2 experiment can provide a flux of $2.5 \cdot 10^5$ condensed atoms per second. This benchmark figure is competitive with the best lab-sized setups and is unprecedented among mobile devices. The compact and robust design of Q-2 allows for its operation in the drop tower and paves the way for various applications as well as tests of fundamental physics. The high flux and repetition rates exceeding 1 Hz could be achieved by the combination of the double MOT setup in combination with the atom chip, which facilitates high frequency traps for fast evaporative cooling to quantum degeneracy.

Precision sensors using light-pulse atom interferometry benefit from this high flux because of the rapid suppression of statistical errors. This may even be the decisive factor whether or not a scientific goal can be reached within the operating time of, for example, a satellite or even the experiment itself. Still, systematic errors are the major limitation. For example, the measurement of the acceleration in a gravimeter is directly falsified by spurious non-gravitational accelerations. The magnetic field gradient can have an overwhelming contribution if the atoms are in any of the magnetic substates. For this reason, an efficient transfer to the $m_F = 0$ substate is inevitable.

This transfer was realized by an adiabatic rapid passage with 91% efficiency. The detrimental effect of transverse decoherence on this efficiency was explained. A protocol for measuring the dephasing time using spin-echos was demonstrated and a mitigation strategy for this loss mechanism was proposed. There are two main reasons that justify the quest for a passage efficiency close to unity. First of all, the flux of cold atoms is deteriorated by an inefficient transfer, especially if multiple passages are performed. Aside from that, atoms in the unwanted Zeeman states need to be separated in space by a transient magnetic field gradient. This takes a finite time and makes it practically impossible to evaluate the post-lens density distribution for short TOFs. In addition, the transient gradient can lead to additional systematics on the ultimate precision level. The detailed description of the adiabatic rapid passage that was given in this work can be transferred to other atomic species, for example potassium. This will involve a different Hamiltonian and thus different numbers, but the methods and qualitative conclusions remain the same.

Systematic errors

The residual acceleration in the $m_F = 0$ substate is proportional to the magnetic field and its gradient. This is the reason why the STE-QUEST requirements demand $B = 1$ mG besides a gradient of less than $83 \mu\text{G}/\text{m}$. The magnetic field could indeed be measured with a 1 mG precision in Q-2 by using rf spectroscopy, limited by the stability of the system. The gradient was found to be approximately $1 \text{ G}/\text{m}$, even though extensive care was taken to select non-magnetic materials within the magnetic shield. Still, the source of this gradient is either the shield itself or a component within, because the shielding factor is high enough to suppress even the fields from the strong magnets of, for example, the ion getter pump that is located outside the shield. A gradient that is too strong cannot be healed by an arbitrarily small offset field because it would change over the spatial extent of the atomic ensemble. Hence, this gradient must be either reduced or well characterized such that the related systematic errors can be accounted for in the error budget. A suppression of the gradient at least in the sensitive interferometer axis at the cost of the remaining directions is conceivable by means of active compensation. In any case, the magnetic field gradient must be well characterized, either to include it in an error correction or to prove that the gradient is below a certain level. The components of the magnetic field gradient were measured to a precision of almost $10 \text{ mG}/\text{m}$ in Q-2 within 1 s time of flight. The limitation is the atomic ensemble leaving the detection zone because of the accelerated motion in the $m_F = 2$ substate. The time interval can be extended, for example, by adapting the magnification of the imaging system, using the $m_F = 1$ substate or by an initial velocity of the atoms opposing the acceleration. This would reduce the uncertainty in the gradient significantly. For space missions with an available TOF exceeding 10 s, a characterization of the magnetic field gradient to a few $10 \mu\text{G}/\text{m}$ seems feasible.

Several further systematics that can lead to spurious non-gravitational accelerations within $m_F = 0$ were characterized. The largest of them was the residual air drag, which is not a specific problem of the drop tower, but an issue for all micro-gravity platforms. Fortunately, this contribution is a common effect in a differential measurement. This alleviation also applies to the centrifugal and the Coriolis force, provided that the differences in the center of mass position and velocity between the two atomic species are small. This is only one reason why a good level of control over the center of mass motion is so important. The atomic motion through distorted laser wave fronts or in a gravity gradient is responsible for further systematic errors.

It was demonstrated in this work how the COMM can be predicted and systematically reduced. The largest contributions to the atomic velocity are the dipole oscillation within the release trap and the release. It was explained how this oscillation amplitude can be minimized. The residual oscillation was used to tune the initial velocity after release by choosing an appropriate hold time in the trap. This can become problematic if a different hold time is required by the quadrupole mode oscillation for magnetic lensing. This was not the case in Q-2, but the initial velocity after release can just as well be controlled by the release mechanism. For example, a hard switch-off leads to a motion towards the atom chip and can be

compensated by a Stern-Gerlach kick. Alternatively, the release can be conducted in a more controlled manner by ramping down the currents for the trap. The ability to calculate a control function for the current drivers based on the respective step response function is important in this respect. In between release and adiabatic rapid passage, the predominant effects on the atomic velocity are the static magnetic field gradient, the transient gradient when switching a coil and a kick by the lens if it is displaced with respect to the atomic center of mass. These contributions were investigated and minimized as far as possible.

Owing to this thorough treatment, a residual velocity of $6(9) \mu\text{m/s}$ was realized in one spatial direction. The scheme for a reduction of the COMM in the remaining directions to the same level was discussed and can be realized with Q-2. A further suppression of this residual motion to a nm/s level is currently limited by slightly different initial velocities from one shot to another. This velocity scatter applies to rubidium. The differential velocity of two atomic species can be much lower than their common motion.

Velocity spread

The key for atom interferometry with a pulse separation time of several seconds is the realization of ultralow expansion rates of the atomic ensemble. There is a broad agreement that the necessary velocity spread, which is below 0.1 mm/s , is not feasible by an adiabatic decompression of the trap if a high flux of atoms shall be maintained. For comparison, the lowest reported thermodynamic temperature for rubidium atoms is 350 pK and took several minutes [179]. Still, the velocity spread is larger than 0.3 mm/s . Lensing the atoms is more efficient. The best collimation in 2D is equivalent to a kinetic temperature of 50 pK [1]. This could be realized by a multiple lensing scheme using a combination of a collective excitation and an optical dipole lens with a total time exceeding 1 s . These authors used the concept of collective excitations in a different and less controlled way such that no efficient collimation in the third dimension was possible. The equivalent 3D kinetic temperature is in the nK regime.

Different experimental realizations of magnetic lensing were demonstrated in this work. The 3D kinetic temperatures are as low as 378 pK for the SC-BC-lens and 70 pK for the BC-lens, both for a single lens. The latter corresponds to an unprecedented velocity spread of $140 \mu\text{m/s}$. It is difficult to extract these numbers from the measured absorption images because of the highly asymmetric clouds. In this work, a 3D numerical ray tracing simulation was conducted to describe the post-lens expansion. This simulation exhibits several advantages compared to an analysis based on fitted TF radii. First of all, the velocity spread can be directly extracted. Aside from that, the 3D analysis allows for a deeper understanding of the effects. For example, the strong shear after the SC-BC-lens that led to a compact density distribution within one camera frame could be quantitatively understood. Another advantage is the fact that a numerical simulation is not losing any atoms. This is fundamentally different for the measured density images, because atoms in the high

energy tail can no longer be detected after some time. The effect is an underestimated expansion rate. This was not properly accounted for in [80] which claims a kinetic temperature of 50 pK based on the same BC-lens data set.

The performance of a magnetic lens suffers from its anisotropy, which is common to most neutral atoms traps. It was demonstrated how a quadrupole mode excitation within the release trap can solve this problem. The mode is excited during the transport of the BEC from the high frequency trap used for evaporative cooling to the shallower release trap further away from the atom chip. This could be understood by a numerical simulation using the variational approach and confirmed by the measured aspect ratio after release as well as the measured expansion after the magnetic lens. The only free parameters in this simulation are the number of atoms and the damping time of the excitation. The phase is predicted correctly. It could be proven that a varying atom number, which is the experimental reality, only has a small effect on the mode. The measured expansion rates are close to the optimum for the used combination of release trap, pre-TOF and lens. Apart from the quadrupole mode, other types of collective modes exist. They were characterized on the basis of the actual release trap. It was no coincidence that exactly the quadrupole mode was the dominant one after the transfer of the BEC, because this mode exhibits the smallest frequency and is thus the easiest to excite.

Outlook

The minimization of the COMM is conceptually simple: All contributions to the atomic velocity either have to vanish or sum up to zero. There are at least two contributions that cannot vanish, that are the kick towards the chip by switching the lens potential on and off and the kick during the action of the lens due to the anharmonicity. The latter is directed away from the chip, but is much smaller than the first effect. This means that this sum has to be either compensated by a small offset of the lens center with respect to the atoms or the velocity just before the lens must be adjusted to cancel the overall lens kick. The pre-compensation is to be preferred, because a shifted anharmonic lens affects the collimation, too. Another big effect on the COMM is the switching process of the coils. This effect needs to be studied further because it is limiting the control over the atomic ensemble. The coil switching cannot be avoided during the free expansion because it is required for the lens and the adiabatic rapid passage. The additional kick is particularly bothersome since it is not limited to the z direction, which is easily controlled by means of the trap switch-off or a Stern-Gerlach kick. Aside from this coil kick, there is only one more effect of a similar significance and with components in the x and y directions. It is the acceleration due to the magnetic field gradient in between release and ARP. A compensation scheme for this effect was proposed in this work: The ensemble has to be transferred from $m_F = 2$ to $m_F = -2$ after a quarter of the time and back after three quarters. Indeed, this double passage can be realized using the standard quantization field and does not require equally strong magnetic field like the transfer to $m_F = 0$. Hence, it does not involve any additional kicks. Actually,

another tuning option arises by shifting the time of transfer. The sensitive direction is that of the magnetic field gradient, which is primarily the x direction. In addition, this direction can be changed by a different quantization field during the TOF. The remaining COMM will be small enough such that it can be fully suppressed in three dimensions by a small adjustment of the lens center with negligible effects on the collimation.

It was shown in this work that the dominant contribution to the measured atomic motion after the lens is the residual air drag in the drop tower. Unfortunately, this effect could be characterized least accurately and thus deserves further attention. A reasonable improvement would be the implementation of a commercial accelerometer that is capable of measuring the capsule accelerations to a $1\ \mu\text{g}$ accuracy every 0.1 s. Such sensors are not easy to find and very expensive. Still, the drop tower operators did offer to provide a suitable accelerometer such that this problem can be investigated further [197].

A reduction of the velocity scatter would allow for an even more enhanced control over the COMM. This must be achieved when aiming at ultimate precision measurements. The observed scatter was based on data sets involving several drops. Hence, it is basically a drop-to-drop scatter with a different temperature of the atom chip, the vacuum chamber and possibly of the reference resistors in the current drivers. Space missions exhibit a thermalized experiment in continuous operation. Hence, the observed velocity scatter can be a drop tower specific problem which is not limiting a space mission. Still, this particular issue was not addressed so far. For this reason, there can be a great potential for further improvements within Q-2, for example by a temperature stabilization or by warm-up measurements.

Q-2 is the first experiment that demonstrated the great potential of collective excitations for magnetic lensing. The foundations are laid in this work. Still, it is possible to gain further insight by extensive ground-based measurements. For this purpose, the free expansion time needs to be prolonged significantly beyond the standard TOF of 22 ms. This can be realized by a rotation of the entire capsule by 45° such that the atoms are falling along the Detection 1 laser beam. This involves adjusting the experimental sequence and the detection system, but is straightforward. In this way, a ground-based TOF exceeding 100 ms is possible, which assures a good signal to noise ratio in the detection of the collective excitations. This allows for an extended study of the damping time of the various modes and its dependence on the trap anharmonicity as well as the thermal fraction within the trap. Furthermore, protocols for a resonant excitation of certain modes can be tested.

The demonstrated post-lens velocity spread of the atomic ensemble is unprecedented. Nevertheless, a small improvement is still possible, because the lens is slightly too strong resulting in a focus after 750 ms. In addition, the amplitude of the quadrupole mode was insufficient for a perfect collimation in the weak trap direction. An optimized amplitude can reduce the velocity spread by approximately $10\ \mu\text{m/s}$. The amplitude can be controlled in two different ways. The first one is to distribute the required change in the x coil current over the transfer time to the release position. This will lead to a smaller, but cleaner quadrupole mode oscillation. The amplitude can then be increased by a resonant excitation prior to this transfer.

A further reduction of the velocity spread is limited by the anharmonicity of the experimentally viable magnetic potentials, which is responsible for the comet like tail. If the trap was harmonic, a velocity spread of $33 \mu\text{m/s}$ equivalent to a kinetic temperature of only 4 pK would be possible with a matched quadrupole mode. An increased pre-TOF would then allow for fK kinetic temperatures.

This anharmonicity is a drawback of chip traps. It can be mitigated by using lens traps even further away from the chip, which are less anharmonic. Without any modification of the experimental setup the distance to the chip can be doubled. In addition, only a small part of the atom chip – that is the outer Z structures – is actually used. A utilization of more structures might allow for more harmonic lens traps, but this requires either more current drivers or a distribution matrix for them, because the chip structures are electrically interconnected within the BC and SC. Yet, this can only mitigate rather than fully solve the tail problem. More advanced protocols can be developed to compensate for the velocity profile imprinted on the atoms by the lens potential, for example multiple lensing schemes involving other Zeeman states. Small modifications of the experimental setup are an alternative, too. For example, if the magnetic lens is replaced by an optical one, which exhibits no L_3 anharmonicity. An interesting minor change is the implementation of an auxiliary chip opposite to the atom chip. This can be a single wire in parallel to the SC-I to reduce the anharmonicity. In addition, it might be possible to engineer a quantum state, for example a strong breathing mode excitation superimposed with the quadrupole mode, such that the magnetic lens with its anharmonicity is no longer necessary. With these strategies, fK kinetic temperatures actually come in reach. It is important to note that the current limitation is the drop tower rather than the Q-2 experiment. If it were operated on the ISS, for example, it would be straightforward to characterize much shallower lens traps. They would, in turn, allow for shallower release traps, too, because the minimum lens time is limited by the switching characteristics of the base chip. The corresponding smaller expansion rate entails a longer pre-TOF to reach the same size, but also requires a smaller velocity change by the lens. This reduces the tail, too, and can be realized with the methods described in this work.

The next upgrade of the Q-2 experiment will be the potassium laser system and a potassium oven. This will allow for dual species atom interferometry. The concept of collective excitations can be transferred to potassium. A simultaneous quadrupole mode excitation of both species is expected to be unproblematic. The only disparity is the different mode frequency, such that it might be required to introduce a certain hold time in order to optimize the phase for both species.

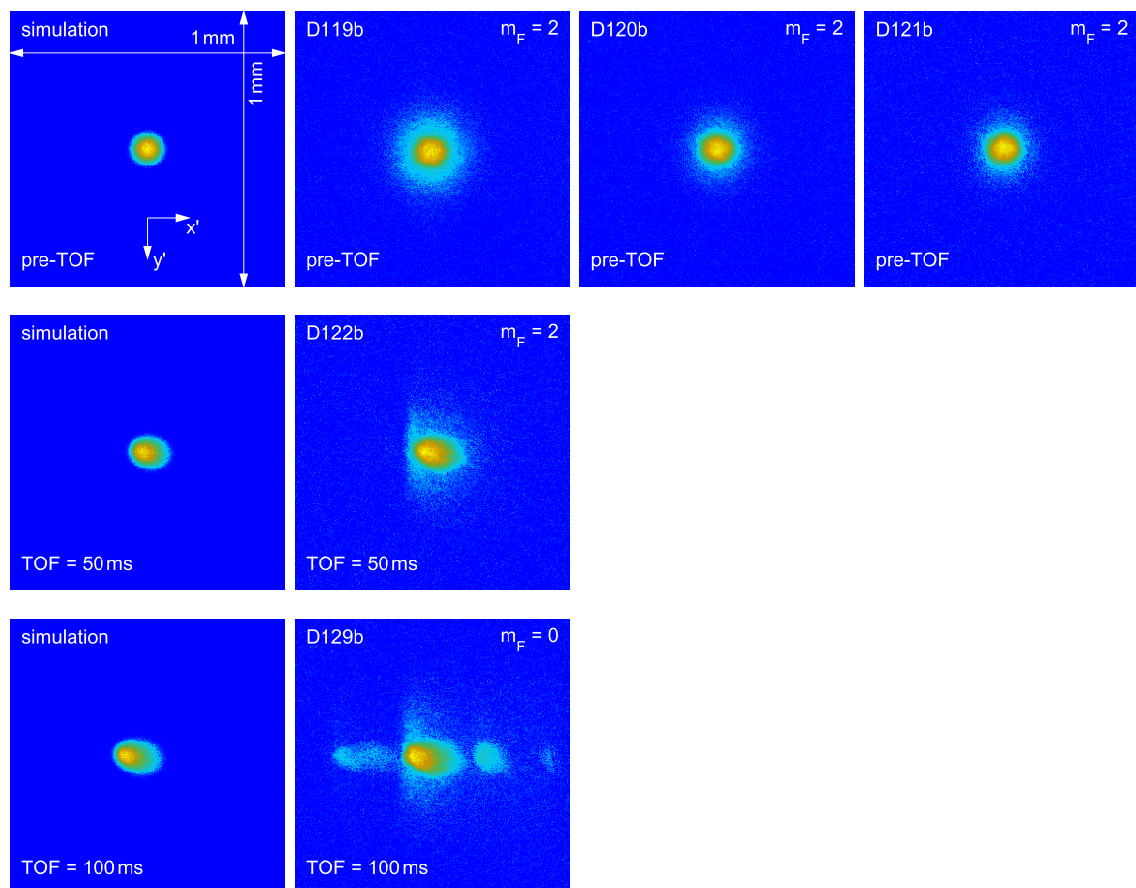
The STE-QUEST proposal is frequently used as a reference because it aims high. Even if these requirements are not met completely, precision measurements are still possible. For example, Q-2 can test the UFF after the potassium upgrade. In catapult mode, an interferometer time of $2T = 7 \text{ s}$ is possible. The systematics that become important on these time scales were discussed in this work. Besides this interesting perspective, Q-2 lays the foundations for the remaining two MAIUS missions and other space missions such as CAL and BEC-CAL on the ISS. The ability to predict and even to engineer a particular collective excitation of the BEC

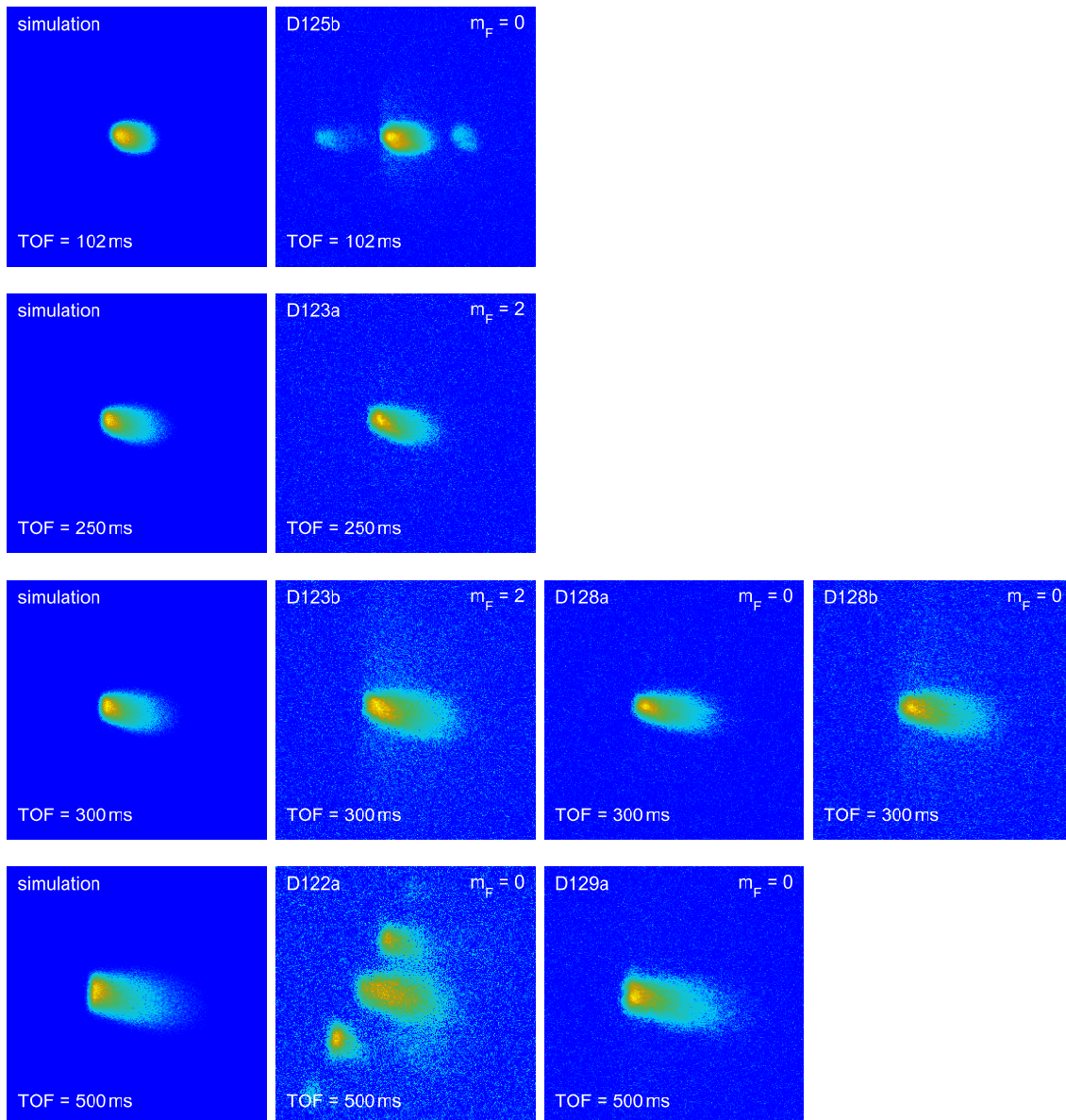
only based on a ground-based characterization is invaluable for all these missions, especially for MAIUS with its very limited microgravity time. An impact on a multitude of other experiments testing fundamental effects is conceivable, too. For example, the quantum reflection of BECs differs from the single particle theory in the low velocity regime [198]. Furthermore, ultracold atoms can be used to investigate Anderson localization of matter waves [199]. Aside from that, atom interferometry is sensitive to general relativistic effects. On the ultimate precision level, this facilitates a measurement of these effects, for example the Lense-Thirring effect [200] or gravitational waves, which have been observed recently [201]. The technologies and methods described in this work also find applications beyond tests of fundamental physics. For example, the collaborative research center geo-Q is assembling a cold atom based gravimeter for field applications, which is based on the same technology as Q-2.

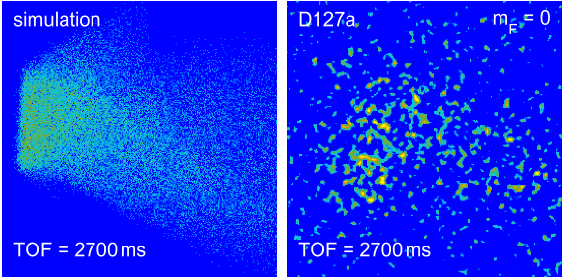
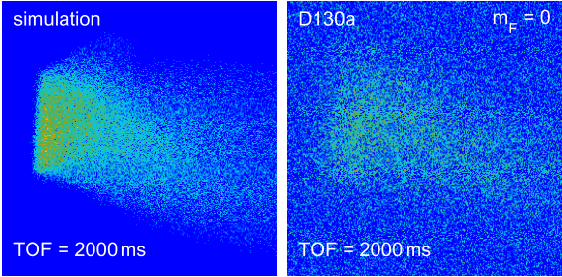
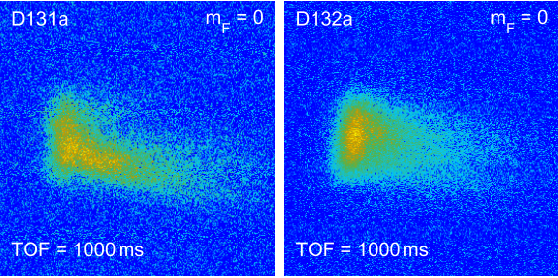
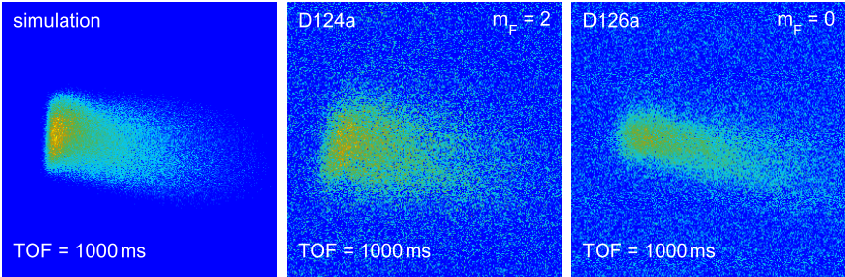
Appendix A

SC-BC-lens

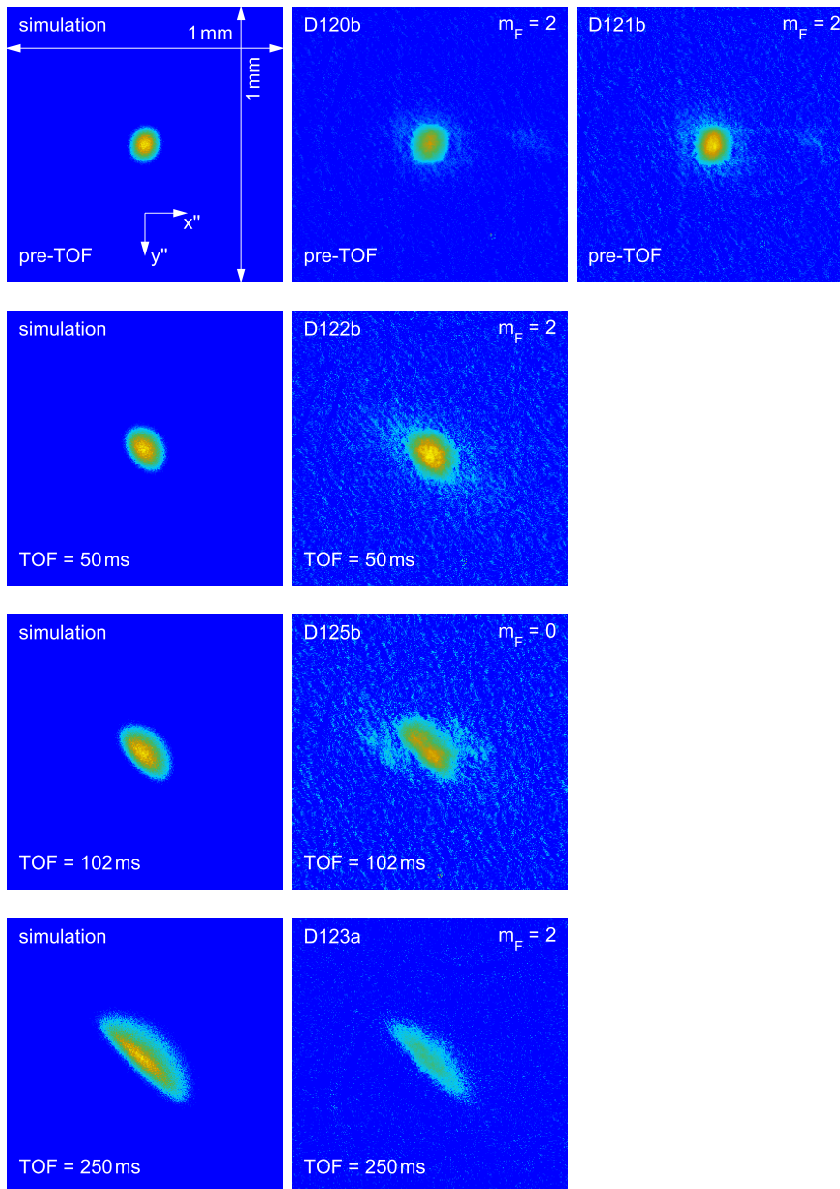
A.1 Detection 1 view

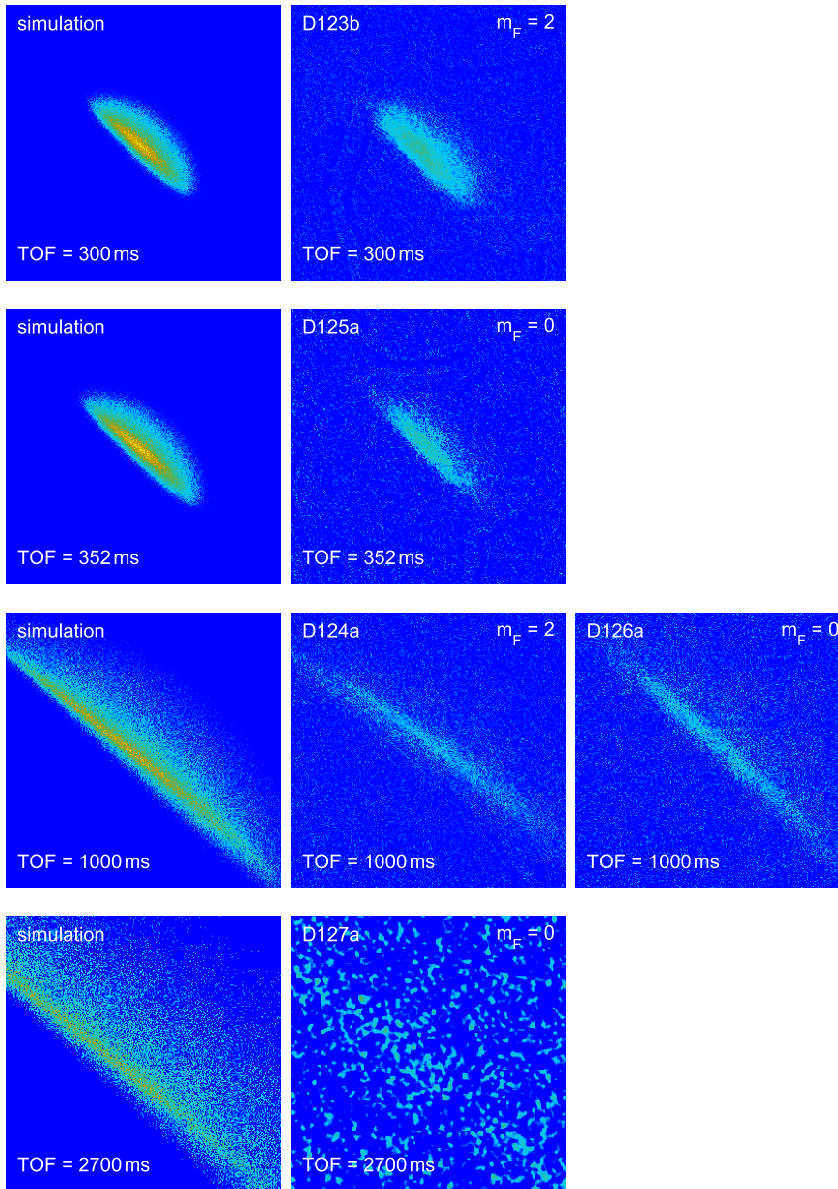






A.2 Detection 2 view (right cloud)



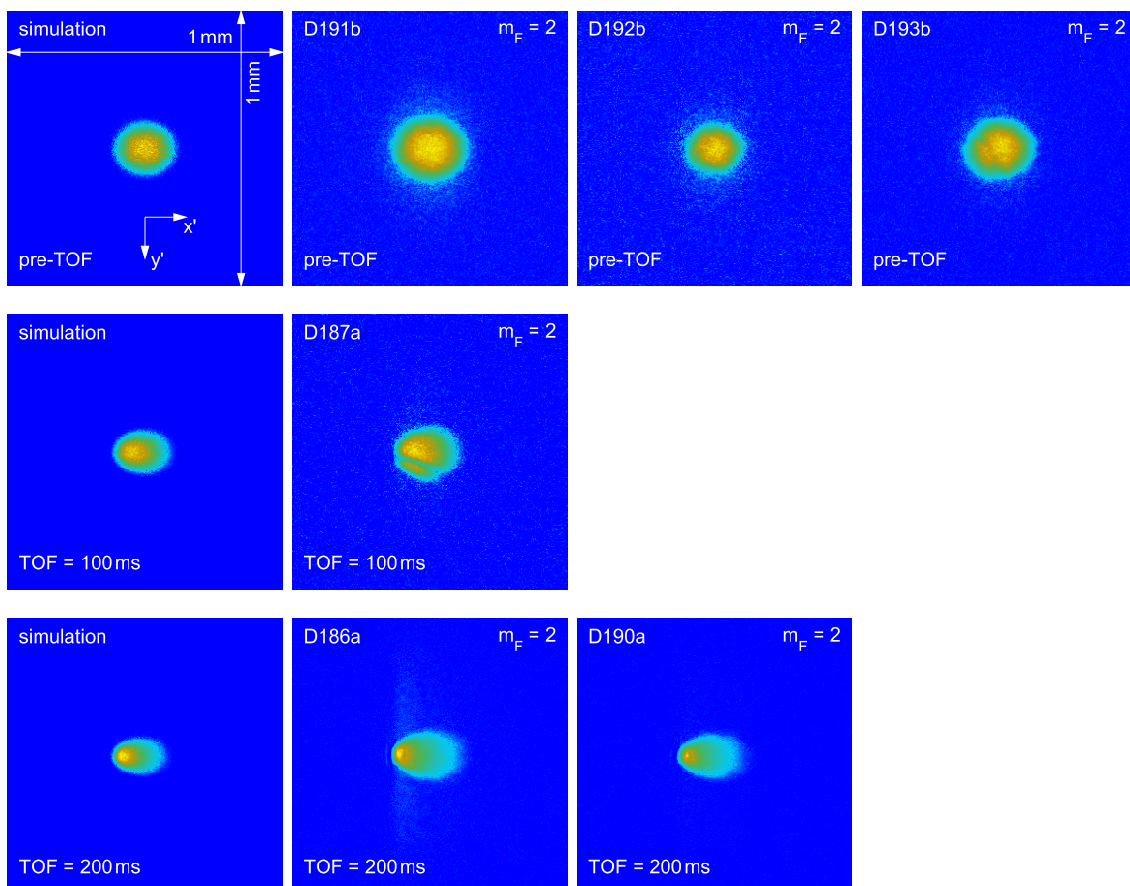


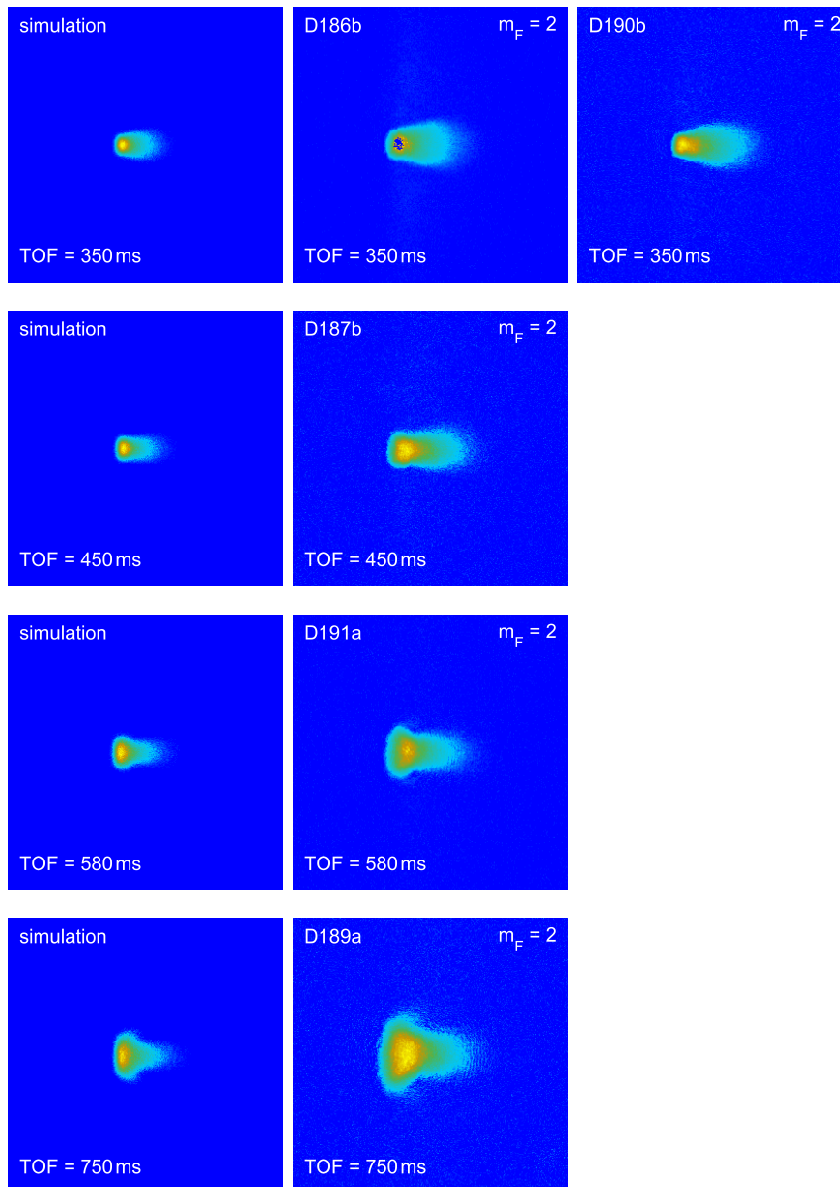
Appendix B

BC-lens

B.1 Data set in $m_F = 2$

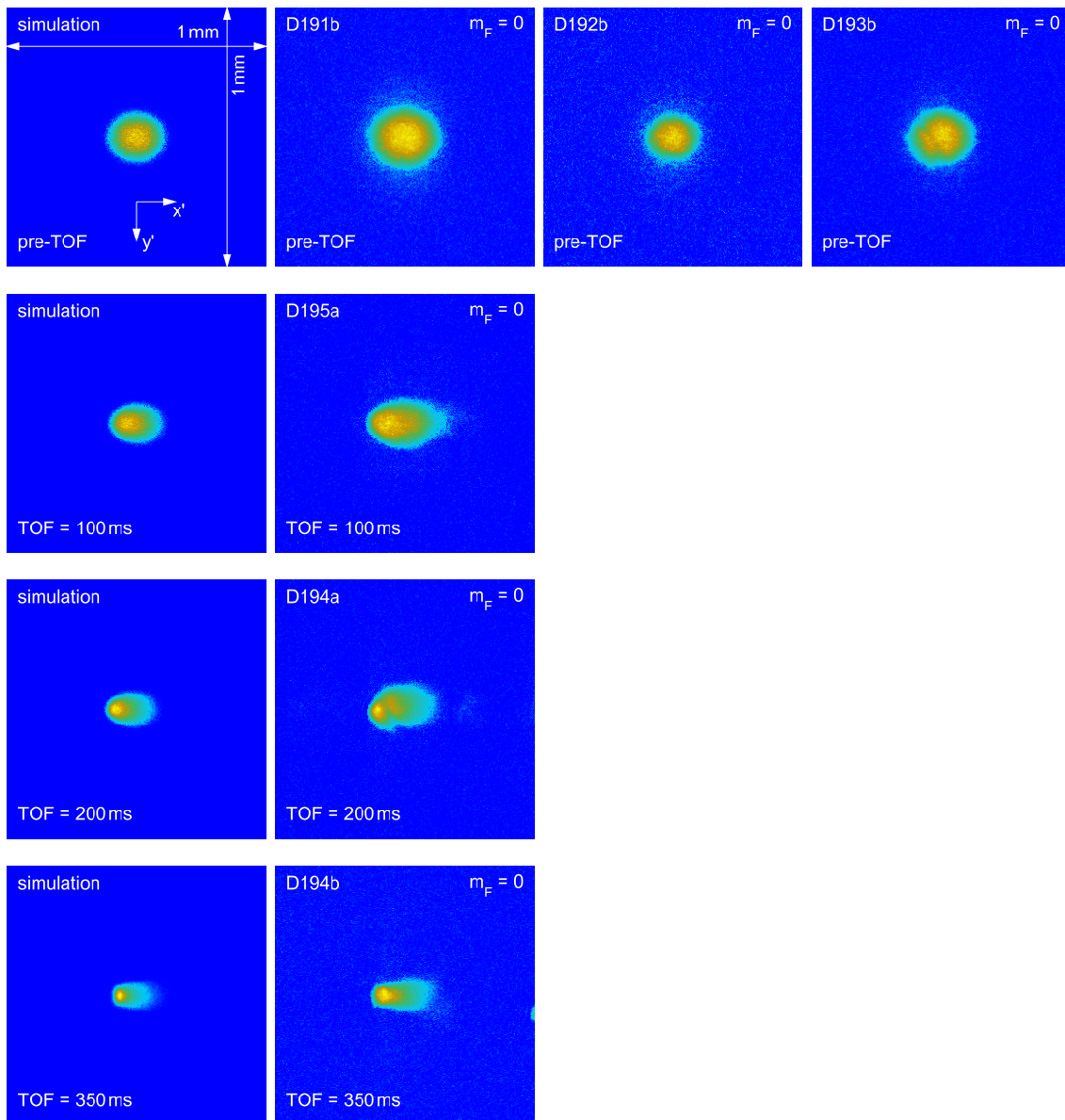
B.1.1 Detection 1 view

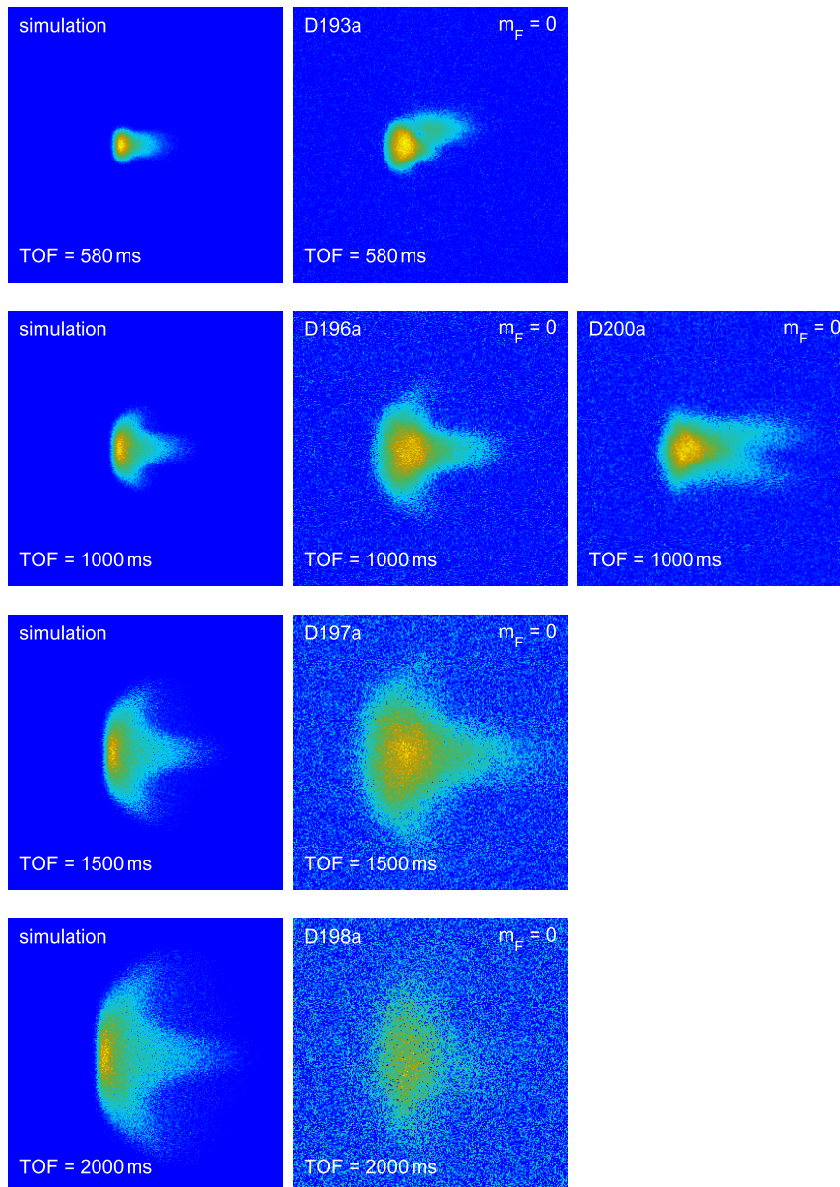




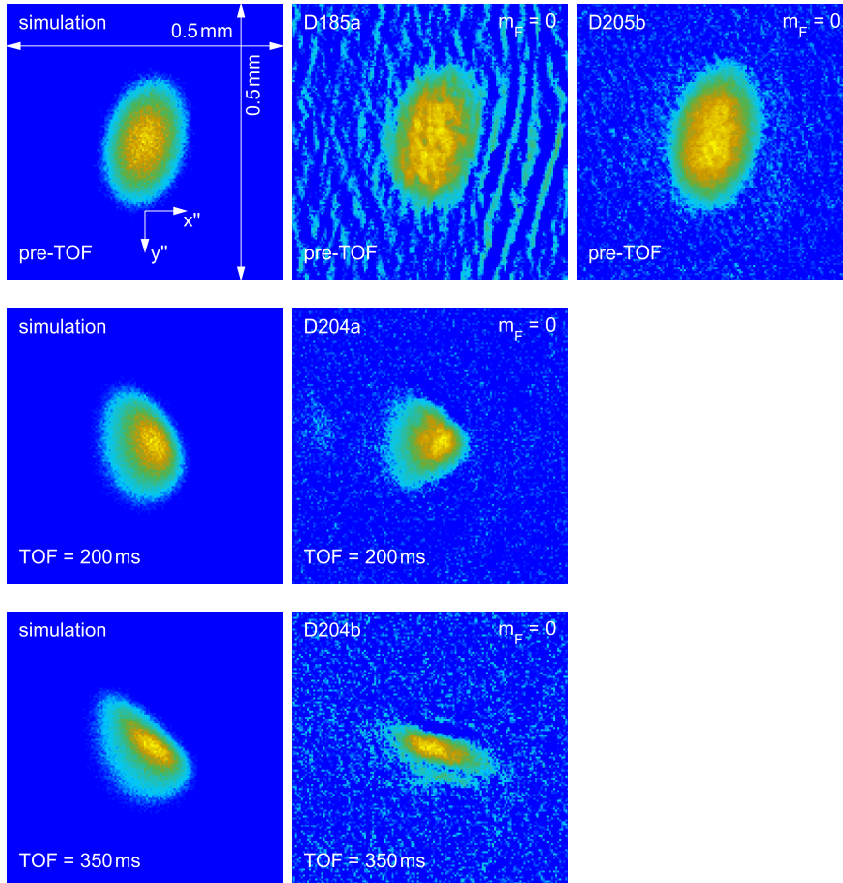
B.2 Data set in $m_F = 0$ (Set B)

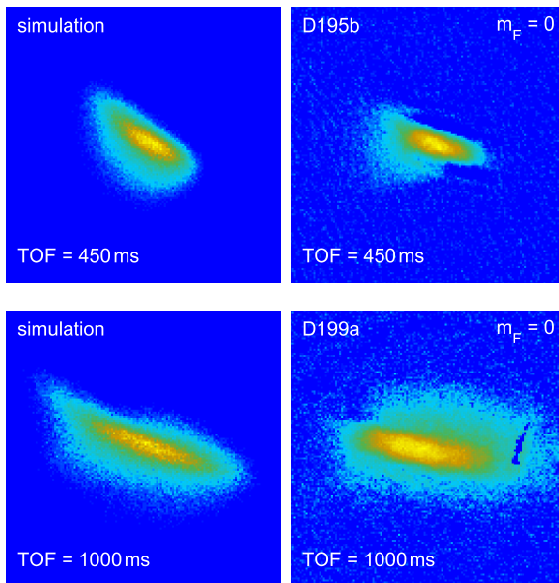
B.2.1 Detection 1 view



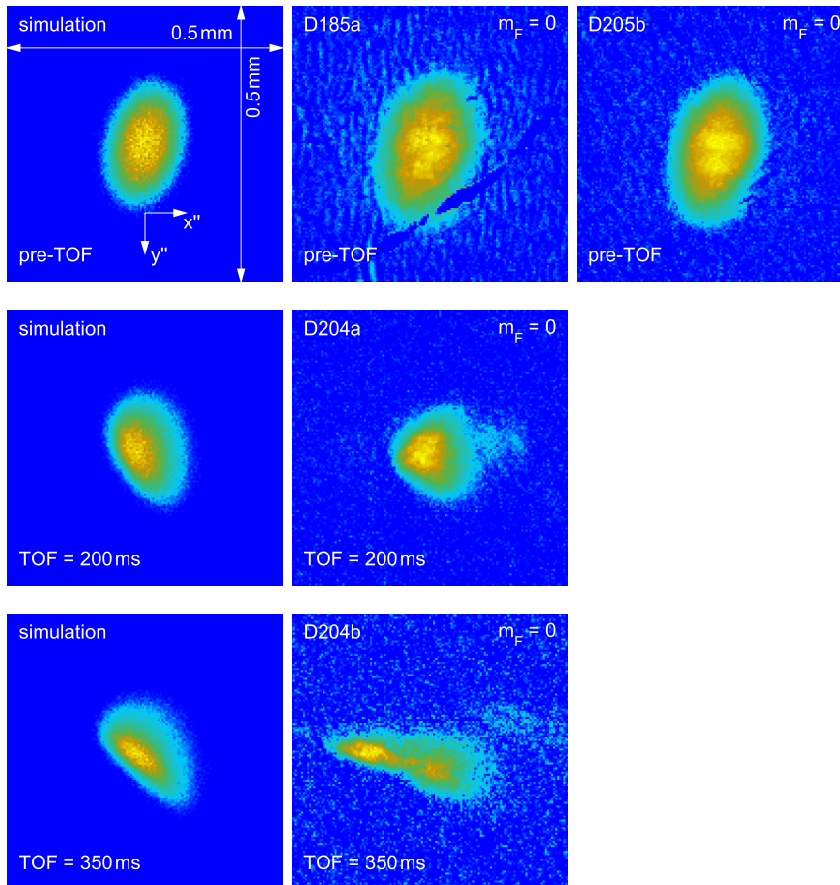


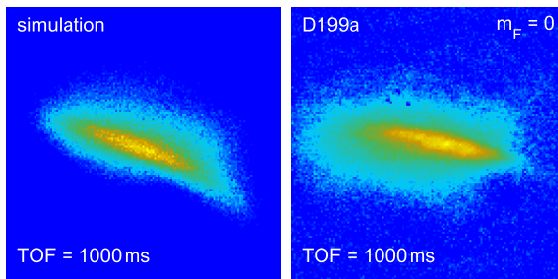
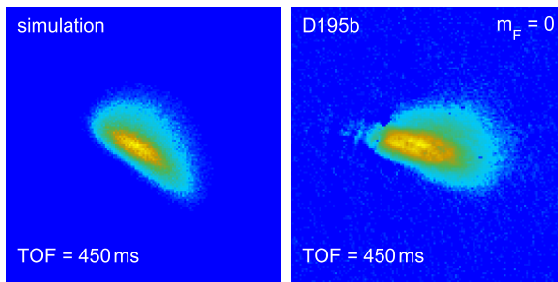
B.2.2 Detection 2 view (left cloud)





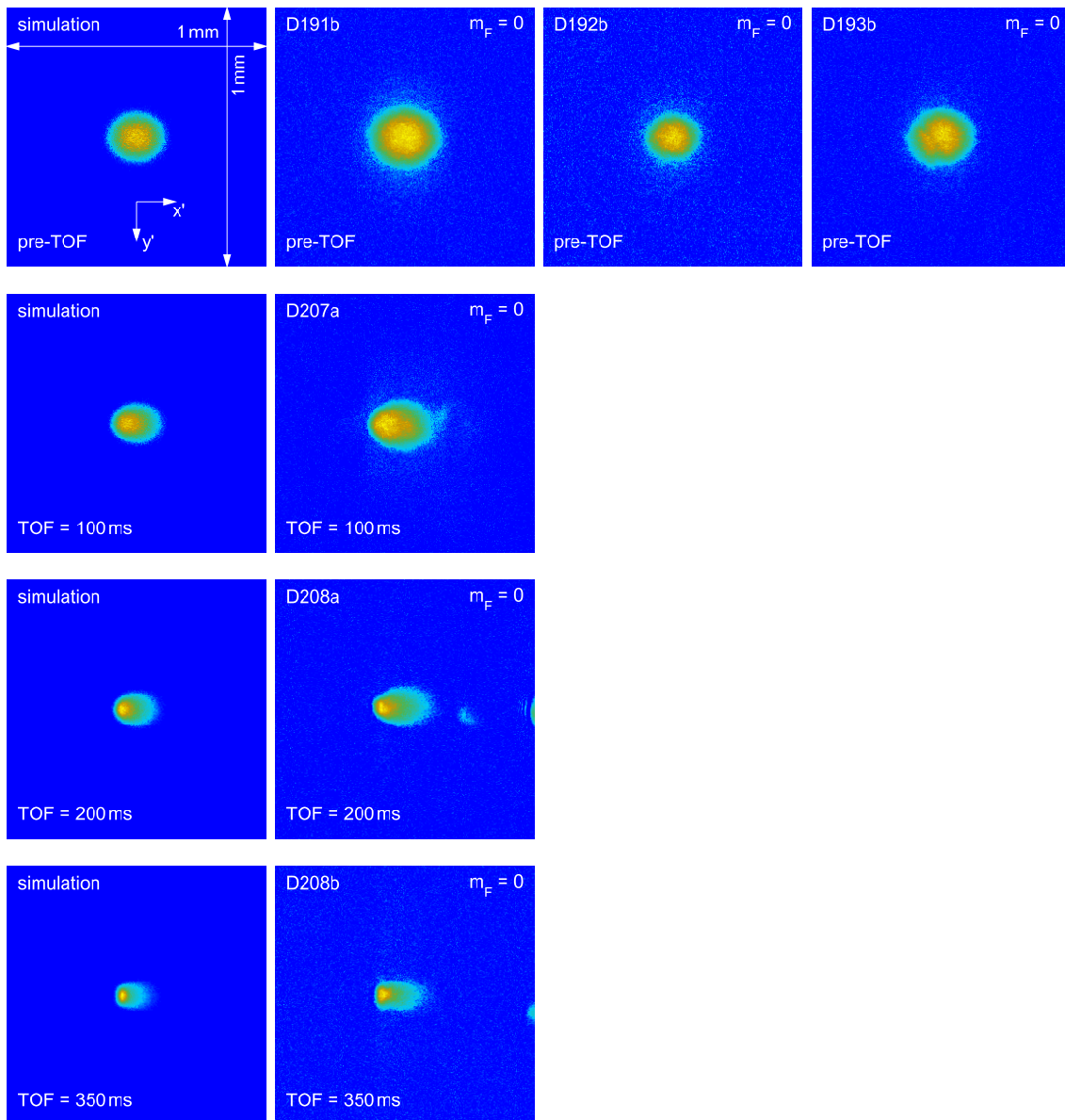
B.2.3 Detection 2 view (right cloud)

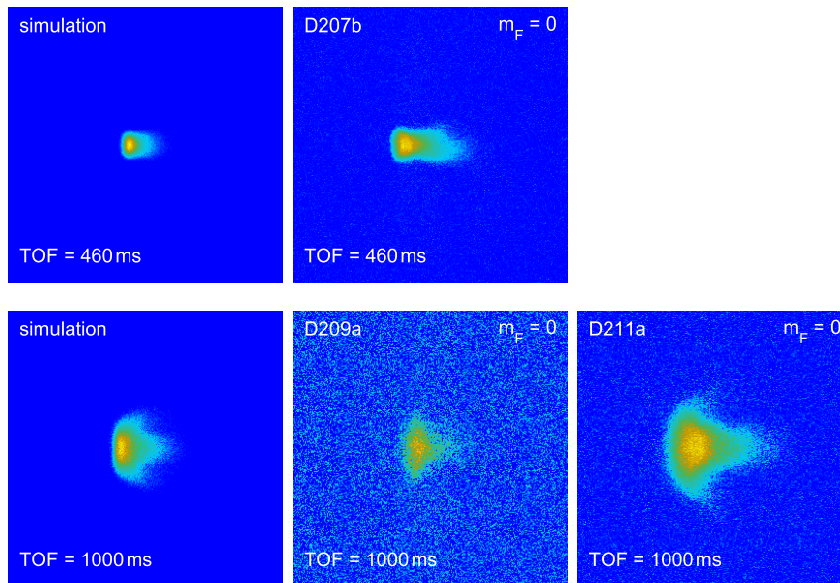




B.3 Data set in $m_F = 0$ (Set C)

B.3.1 Detection 1 view





Appendix C

Characteristic data

C.1 Rubidium data

| | | | |
|--|-------------------------|---|-------|
| Atomic number | Z | 37 | |
| Total nucleons | $Z + N$ | 87 | |
| Atomic mass | m | $1.443\,160\,648(72) \cdot 10^{-25}$ kg | [92] |
| Nuclear angular momentum | I | $3/2$ | |
| Nuclear g-factor | g_I | $-0.000\,995\,141\,4(10)$ | [202] |
| Fine structure Landé-factor of $5^2S_{1/2}$ | g_J | $2.002\,331\,13(20)$ | [203] |
| Hyperfine Landé-factor of $5^2S_{1/2}$, $F = 2$ | g_F | $0.499\,836\,43(5)$ | |
| Ground state hyperfine splitting | ΔE_{hfs} | $h \cdot 6\,834\,682\,610.9043$ Hz | [155] |
| Linear Zeeman shift ($5^2S_{1/2}$, $F = 2$) | ω_L | $2\pi \cdot 0.69958$ MHz/G | |
| Ground state polarizability | α_0 | $h \cdot 0.0794(16)$ Hz/(V/cm) ² | [92] |
| Natural linewidth (D ₂ line) | Γ | $2\pi \cdot 6.0666(18)$ MHz | |
| Recoil velocity (D ₂ line) | v_r | 5.8845 mm/s | |
| Saturation intensity (σ^+) $ F = 2, m_F = \pm 2\rangle \rightarrow F' = 3, m_{F'} = \pm 3\rangle$ | I_{sat} | $1.669\,33(35)$ mW/cm ² | |
| Scattering length | a | $100a_0$ | [204] |

Table C.1: ⁸⁷Rb Physical Properties

C.2 Trap frequencies

| Trap | $\vec{f}_{\text{chip model}} = \vec{\omega}/2\pi$ (Hz) | $\vec{f}_{\text{measured}}$ (Hz) | relative error |
|-------------------------|--|----------------------------------|----------------|
| Evap. cooling (initial) | $f_x = 21.88$ | - | - |
| | $f_y = 1099.90$ | - | - |
| | $f_z = 1104.73$ | - | - |
| Evap. cooling (final) | $f_x = 24.43$ | - | - |
| | $f_y = 456.54$ | - | - |
| | $f_z = 462.34$ | - | - |
| Release trap A | $f_x = 17.48$ | - | - |
| | $f_y = 61.10$ | - | - |
| | $f_z = 59.83$ | $f_z = 60.4(3)$ | 1.0(5) % |
| Release trap B | $f_x = 9.10$ | - | - |
| | $f_y = 27.87$ | $f_y = 28(1)$ | 0(4) % |
| | $f_z = 24.59$ | $f_z = 25.7(3)$ | 5(1) % |
| Crane tricked trap | $f_x = 8.33$ | $f_x = 8.6(2)$ | 3(2) % |
| | $f_y = 26.54$ | $f_y = 27.2(7)$ | 2(3) % |
| | $f_z = 23.77$ | $f_z = 24.44(4)$ | 3(2) % |
| BC-lens (1.8 A) | $f_x = 2.95$ | - | - |
| | $f_y = 10.83$ | - | - |
| | $f_z = 10.83$ | - | - |
| BC-lens (1.828 A) | $f_x = 2.96$ | - | - |
| | $f_y = 10.68$ | - | - |
| | $f_z = 10.66$ | - | - |

Table C.2: This table gives an overview of the trap frequencies for the different traps used in this work. The frequencies simulated by the chip model are compared to experimental data, where possible. All values refer to microgravity.

Appendix D

Appendix to ARP

D.1 Derivation of the dressed-state Hamiltonian

In this appendix, the matrix elements of the Schrödinger picture Hamiltonian are derived. This is done by standard means of quantum mechanics. Similar solutions can be found elsewhere [205]. For convenience, Eqs. (4.31), (4.32) and (4.35) are reprinted here

$$i\hbar \frac{\partial}{\partial t} |\Psi(t)\rangle = [\hat{H}_0 + \hat{H}_{\text{rf}}(t)] |\Psi(t)\rangle,$$

$$\hat{H}_0 = \hbar (\omega_L \hat{F}_{\bar{z}} + \omega_Q \hat{Q}_{\bar{z}}),$$

$$\hat{H}_{\text{rf}}(t) = g_F \mu_B B_{\text{rf}} \cos(\omega_{\text{rf}} t) \hat{F}_{\bar{x}}.$$

For the solution of the Schrödinger equation, the following ansatz is used

$$|\Psi(t)\rangle = \sum_{m_F} c_{m_F} e^{-im_F \omega_{\text{rf}} t} |m_F\rangle. \quad (\text{D.1})$$

First of all, the three terms are solved separately

$$i\hbar \frac{\partial}{\partial t} |\Psi(t)\rangle = i\hbar \sum_{m_F} \frac{\partial c_{m_F}}{\partial t} e^{-im_F \omega_{\text{rf}} t} |m_F\rangle + \hbar \omega_{\text{rf}} \sum_{m_F} m_F c_{m_F} e^{-im_F \omega_{\text{rf}} t} |m_F\rangle,$$

$$\begin{aligned} \hat{H}_0 |\Psi(t)\rangle &= \hbar (\omega_L \hat{F}_{\bar{z}} + \omega_Q \hat{Q}_{\bar{z}}) \sum_{m_F} c_{m_F} e^{-im_F \omega_{\text{rf}} t} |m_F\rangle \\ &= \hbar \omega_L \sum_{m_F} c_{m_F} e^{-im_F \omega_{\text{rf}} t} \hat{F}_{\bar{z}} |m_F\rangle + \hbar \omega_Q \sum_{m_F} c_{m_F} e^{-im_F \omega_{\text{rf}} t} \hat{Q}_{\bar{z}} |m_F\rangle \\ &= \hbar \omega_L \sum_{m_F} c_{m_F} e^{-im_F \omega_{\text{rf}} t} m_F |m_F\rangle + \hbar \omega_Q \sum_{m_F} c_{m_F} e^{-im_F \omega_{\text{rf}} t} Q_{m_F} |m_F\rangle, \end{aligned}$$

$$\begin{aligned} \hat{H}_{\text{rf}}(t) |\Psi(t)\rangle &= g_F \mu_B B_{\text{rf}} \cos(\omega_{\text{rf}} t) \hat{F}_{\bar{x}} \sum_{m_F} c_{m_F} e^{-im_F \omega_{\text{rf}} t} |m_F\rangle \\ &= g_F \mu_B B_{\text{rf}} \frac{1}{2} (e^{i\omega_{\text{rf}} t} + e^{-i\omega_{\text{rf}} t}) \sum_{m_F} c_{m_F} e^{-im_F \omega_{\text{rf}} t} \frac{1}{2} (\hat{F}_+ + \hat{F}_-) |m_F\rangle. \end{aligned}$$

Multiplication of all three equations from the left with $\langle m'_F |$ yields

$$\begin{aligned}
\langle m'_F | i\hbar \frac{\partial}{\partial t} \Psi(t) \rangle &= i\hbar \sum_{m_F} \frac{\partial c_{m_F}}{\partial t} e^{-im_F \omega_{\text{rf}} t} \langle m'_F | m_F \rangle + \hbar \omega_{\text{rf}} \sum_{m_F} m_F c_{m_F} e^{-im_F \omega_{\text{rf}} t} \langle m'_F | m_F \rangle \\
&= i\hbar \frac{\partial c_{m'_F}}{\partial t} e^{-im'_F \omega_{\text{rf}} t} \delta_{m'_F m_F} + \hbar \omega_{\text{rf}} m'_F c_{m'_F} e^{-im'_F \omega_{\text{rf}} t} \delta_{m'_F m_F}, \\
\langle m'_F | \hat{H}_0 \Psi(t) \rangle &= \hbar \omega_L \sum_{m_F} c_{m_F} e^{-im_F \omega_{\text{rf}} t} m_F \langle m'_F | m_F \rangle \\
&\quad + \hbar \omega_Q \sum_{m_F} c_{m_F} e^{-im_F \omega_{\text{rf}} t} Q_{m_F} \langle m'_F | m_F \rangle \\
&= \hbar \omega_L c_{m'_F} e^{-im'_F \omega_{\text{rf}} t} m'_F \delta_{m'_F m_F} + \hbar \omega_Q c_{m'_F} e^{-im'_F \omega_{\text{rf}} t} Q_{m'_F} \delta_{m'_F m_F}, \\
\langle m'_F | \hat{H}_{\text{rf}}(t) \Psi(t) \rangle &= \frac{1}{4} g_F \mu_B B_{\text{rf}} (e^{i\omega_{\text{rf}} t} + e^{-i\omega_{\text{rf}} t}) \sum_{m_F} c_{m_F} e^{-im_F \omega_{\text{rf}} t} \langle m'_F | \hat{F}_+ + \hat{F}_- | m_F \rangle \\
&= \frac{1}{4} g_F \mu_B B_{\text{rf}} (e^{i\omega_{\text{rf}} t} + e^{-i\omega_{\text{rf}} t}) \sum_{\pm} c_{m'_F \mp 1} e^{-i(m'_F \mp 1) \omega_{\text{rf}} t} \langle m'_F | \hat{F}_{\pm} | m'_F \mp 1 \rangle \\
&= \frac{1}{4} g_F \mu_B B_{\text{rf}} (e^{i\omega_{\text{rf}} t} + e^{-i\omega_{\text{rf}} t}) \\
&\quad \cdot \sum_{\pm} c_{m'_F \mp 1} e^{-i(m'_F \mp 1) \omega_{\text{rf}} t} \sqrt{F(F+1) - (m'_F \mp 1)((m'_F \mp 1) \pm 1)} \delta_{m'_F m_F \mp 1} \\
&= \frac{1}{4} g_F \mu_B B_{\text{rf}} (e^{i\omega_{\text{rf}} t} + e^{-i\omega_{\text{rf}} t}) \cdot \sum_{\pm} c_{m'_F \mp 1} e^{-i(m'_F \mp 1) \omega_{\text{rf}} t} \sqrt{6 - (m'_F \mp 1)m'_F} \delta_{m'_F m_F \mp 1},
\end{aligned}$$

with the Kronecker delta $\delta_{m'_F m_F}$. Putting all three partial equations together $[\langle m'_F | i\hbar \frac{\partial}{\partial t} \Psi(t) \rangle = \langle m'_F | \hat{H}_0 + \hat{H}_{\text{rf}}(t) | \Psi(t) \rangle]$

$$\begin{aligned}
i\hbar \frac{\partial c_{m'_F}}{\partial t} e^{-im'_F \omega_{\text{rf}} t} \delta_{m'_F m_F} &= \hbar (\omega_L - \omega_{\text{rf}}) m'_F c_{m'_F} e^{-im'_F \omega_{\text{rf}} t} \delta_{m'_F m_F} \\
&\quad + \hbar \omega_Q c_{m'_F} e^{-im'_F \omega_{\text{rf}} t} Q_{m'_F} \delta_{m'_F m_F} + \frac{1}{4} g_F \mu_B B_{\text{rf}} (e^{i\omega_{\text{rf}} t} + e^{-i\omega_{\text{rf}} t}) \\
&\quad \cdot \sum_{\pm} c_{m'_F \mp 1} e^{-i(m'_F \mp 1) \omega_{\text{rf}} t} \sqrt{6 - (m'_F \mp 1)m'_F} \delta_{m'_F m_F \mp 1},
\end{aligned}$$

multiplying with $e^{im'_F \omega_{\text{rf}} t}$ and substituting the identities $\Delta_{\text{r}} = \omega_{\text{rf}} - \omega_L$ and $\hbar \Omega_{\text{r}} = g_F \mu_B B_{\text{rf}}$ results in

$$\begin{aligned}
i\hbar \frac{\partial c_{m'_F}}{\partial t} \delta_{m'_F m_F} &= -\hbar \Delta_{\text{r}} m'_F c_{m'_F} \delta_{m'_F m_F} + \hbar \omega_Q c_{m'_F} Q_{m'_F} \delta_{m'_F m_F} \\
&\quad + \frac{1}{4} \hbar \Omega_{\text{r}} (e^{i\omega_{\text{rf}} t} + e^{-i\omega_{\text{rf}} t}) \cdot \sum_{\pm} c_{m'_F \mp 1} e^{\pm i\omega_{\text{rf}} t} \sqrt{6 - (m'_F \mp 1)m'_F} \delta_{m'_F m_F \mp 1} \\
&= \hbar (\omega_Q Q_{m'_F} - \Delta_{\text{r}} m'_F) c_{m'_F} \delta_{m'_F m_F} \\
&\quad + \frac{1}{4} \hbar \Omega_{\text{r}} \cdot \sum_{\pm} c_{m'_F \mp 1} (1 + e^{\pm 2i\omega_{\text{rf}} t}) \sqrt{6 - (m'_F \mp 1)m'_F} \delta_{m'_F m_F \mp 1} \\
&\approx \hbar (\omega_Q Q_{m'_F} - \Delta_{\text{r}} m'_F) c_{m'_F} \delta_{m'_F m_F} \\
&\quad + \frac{1}{4} \hbar \Omega_{\text{r}} \cdot \sum_{\pm} c_{m'_F \mp 1} \sqrt{6 - (m'_F \mp 1)m'_F} \delta_{m'_F m_F \mp 1},
\end{aligned}$$

where the terms with $e^{\pm 2i\omega_r t}$ have been neglected (rotating wave approximation). The time dependence is eliminated by the Ansatz $c_{m'_F} = \tilde{c}_{m'_F} e^{-iE_{m'_F} t/\hbar}$

$$\begin{aligned} E_{m'_F} \tilde{c}_{m'_F} \delta_{m'_F m_F} &= \hbar (\omega_Q Q_{m'_F} - \Delta_r m'_F) \tilde{c}_{m'_F} \delta_{m'_F m_F} \\ &+ \frac{1}{4} \hbar \Omega_r \cdot \sum_{\pm} \tilde{c}_{m'_F \mp 1} \sqrt{6 - (m'_F \mp 1)m'_F} \delta_{m'_F m_F \mp 1}. \end{aligned}$$

Applying the relation $Q_{m_F} = 1 - (\frac{m_F}{2})^2$ the possible values of Q_{m_F} are $Q_{\pm 2} = 0$, $Q_{\pm 1} = \frac{3}{4}$ and $Q_0 = 1$. Hence the nonzero matrix elements are

$$\begin{aligned} \langle \pm 2 | \hat{H} | \pm 2 \rangle &= \hbar (\omega_Q Q_2 \mp 2\Delta_r) = \mp 2\hbar \Delta_r, \\ \langle \pm 1 | \hat{H} | \pm 1 \rangle &= \hbar (\omega_Q Q_1 \mp 1\Delta_r) = \hbar (\frac{3}{4}\omega_Q \mp \Delta_r), \\ \langle 0 | \hat{H} | 0 \rangle &= \hbar (\omega_Q Q_0 + 0\Delta_r) = \hbar \omega_Q, \end{aligned}$$

$$\begin{aligned} \langle 2 | \hat{H} | 1 \rangle &= \frac{\hbar \Omega_r}{4} \sqrt{6 - (2-1)(2)} = \frac{\hbar \Omega_r}{4} \sqrt{6-2} = \frac{1}{2} \hbar \Omega_r, \\ \langle 1 | \hat{H} | 2 \rangle &= \frac{\hbar \Omega_r}{4} \sqrt{6 - (1+1)(1)} = \frac{\hbar \Omega_r}{4} \sqrt{6-2} = \frac{1}{2} \hbar \Omega_r, \\ \langle 1 | \hat{H} | 0 \rangle &= \frac{\hbar \Omega_r}{4} \sqrt{6 - (1-1)(1)} = \frac{\hbar \Omega_r}{4} \sqrt{6} = \sqrt{\frac{3}{8}} \hbar \Omega_r, \\ \langle 0 | \hat{H} | 1 \rangle &= \frac{\hbar \Omega_r}{4} \sqrt{6 - (0+1)(0)} = \frac{\hbar \Omega_r}{4} \sqrt{6} = \sqrt{\frac{3}{8}} \hbar \Omega_r, \\ \langle 0 | \hat{H} | -1 \rangle &= \frac{\hbar \Omega_r}{4} \sqrt{6 - (0-1)(0)} = \frac{\hbar \Omega_r}{4} \sqrt{6} = \sqrt{\frac{3}{8}} \hbar \Omega_r, \\ \langle -1 | \hat{H} | 0 \rangle &= \frac{\hbar \Omega_r}{4} \sqrt{6 - (-1+1)(-1)} = \frac{\hbar \Omega_r}{4} \sqrt{6} = \sqrt{\frac{3}{8}} \hbar \Omega_r, \\ \langle -1 | \hat{H} | -2 \rangle &= \frac{\hbar \Omega_r}{4} \sqrt{6 - (-1-1)(-1)} = \frac{\hbar \Omega_r}{4} \sqrt{6-2} = \frac{1}{2} \hbar \Omega_r, \\ \langle -2 | \hat{H} | -1 \rangle &= \frac{\hbar \Omega_r}{4} \sqrt{6 - (-2+1)(-2)} = \frac{\hbar \Omega_r}{4} \sqrt{6-2} = \frac{1}{2} \hbar \Omega_r. \end{aligned}$$

The respective second lines could also be derived directly from the Hermitian conjugate of the previous (transposed) one, for example, $\langle 1 | \hat{H} | 2 \rangle = \langle 2 | \hat{H} | 1 \rangle^\dagger = \frac{1}{2} \hbar \Omega_r^* = \frac{1}{2} \hbar \Omega_r$. (Rabi frequency is real in the chosen coordinate system.) Choosing the basis

$$|2\rangle = \begin{pmatrix} 1 \\ 0 \\ 0 \\ 0 \\ 0 \end{pmatrix}, \quad \dots \quad |-2\rangle = \begin{pmatrix} 0 \\ 0 \\ 0 \\ 0 \\ 1 \end{pmatrix}, \quad (\text{D.2})$$

the corresponding matrix representation of \hat{H} is

$$H = \hbar \begin{pmatrix} -2\Delta_r & \frac{1}{2}\Omega_r & 0 & 0 & 0 \\ \frac{1}{2}\Omega_r & \frac{3}{4}\omega_Q - \Delta_r & \sqrt{\frac{3}{8}}\Omega_r & 0 & 0 \\ 0 & \sqrt{\frac{3}{8}}\Omega_r & \omega_Q & \sqrt{\frac{3}{8}}\Omega_r & 0 \\ 0 & 0 & \sqrt{\frac{3}{8}}\Omega_r & \frac{3}{4}\omega_Q + \Delta_r & \frac{1}{2}\Omega_r \\ 0 & 0 & 0 & \frac{1}{2}\Omega_r & 2\Delta_r \end{pmatrix}. \quad (\text{D.3})$$

D.2 Power series of systematic shifts

The deviation of the resonance frequencies from the unperturbed values (at $\Omega_r = 0$) can be approximated by

$$\Delta_{\text{error}}(x) = 2\pi \cdot 1000 \cdot (a_1x + a_2x^2 + a_3x^3 + a_4x^4 + a_5x^5 + a_6x^6 + a_7x^7 + a_8x^8) \cdot B^2.$$

Also, the Rabi frequency of the two crossings $m_F = 2 \leftrightarrow 1$ and $m_F = 1 \leftrightarrow 0$ can be described by a similar power series

$$\Omega_{i,j}(x) = 2\pi \cdot 1000 \cdot (b_1x + b_2x^2 + b_3x^3 + b_4x^4 + b_5x^5 + b_6x^6 + b_7x^7 + b_8x^8).$$

The corresponding coefficients are printed in the table below.

| | $\Delta_{2,1} + 3/4\omega_Q$ | $\Delta_{1,0} + 1/4\omega_Q$ | | $\Omega_{2,1}$ | $\Omega_{1,0}$ |
|-------|------------------------------|------------------------------|-------|----------------|----------------|
| a_1 | -0.007 273 3 | 0.000 690 2 | b_1 | 1 | $\sqrt{3/2}$ |
| a_2 | -2.2022 | -1.0519 | b_2 | 0.062 879 | -0.027 461 |
| a_3 | -7.9043 | 9.5271 | b_3 | -12.9951 | -16.295 |
| a_4 | 367.7681 | -38.7487 | b_4 | 89.5151 | -73.137 |
| a_5 | -3028.5316 | 0 | b_5 | -338.0677 | 1534.4766 |
| a_6 | 12 041.2347 | 0 | b_6 | 753.2573 | -6900.2602 |
| a_7 | -23 980.4269 | 0 | b_7 | -922.799 | 10 480.542 |
| a_8 | 19 242.2217 | 0 | b_8 | 477.0381 | 0 |

Table D.1: Coefficients of powers series expansions. The coefficient's dimensions are $[a_n] = (\text{G}^2/\text{kHz})^{n-1}$ and $[b_n] = \text{G}^{2n}/\text{kHz}^{n-1}$ with $[x] = \text{kHz}/\text{G}^2$ and $[B] = \text{G}^2$. The valid range is $0 \leq x \leq 0.175 \text{ kHz}/\text{G}^2$.

The same coefficients are also valid for the crossings $m_F = -2 \leftrightarrow -1$ and $m_F = -1 \leftrightarrow 0$, but with a change of sign for Δ_{error} .

D.3 ARP code

The solutions obtained from Eq. (4.45) are equivalent to numerical solutions of the time dependent Schrödinger equation. However, the latter require considerably more computation time. Furthermore, this time scales with τ , whereas the time to solve Eq. (4.45) is independent of τ . The data shown in Fig. 4.19 were computed on a 3000×5000 grid on twelve parallel cores on a computing cluster within 30 hours, equivalent to 7.3 ms/point. In principle, it could be done on a state of the art personal computer, too. In contrast, solving the time dependent Schrödinger equation takes 2.5 s/point using Runge Kutta (4th order) and a step size of 10 ns (for $\tau = 9$ ns). The same job would have taken two weeks with that scheme on the computing cluster. The software package is provided under the following link: <https://www.dropbox.com/s/i8oemj7q3uv8dcw/simulations.7z?dl=0>

Bibliography

- [1] T. Kovachy, J. M. Hogan, A. Sugarbaker, S. M. Dickerson, C. A. Donnelly, C. Overstreet and M. A. Kasevich. *Matter Wave Lensing to Picokelvin Temperatures*. Physical Review Letters **114**(14):143004 (2015).
doi:10.1103/PhysRevLett.114.143004
- [2] H. Müntinga, H. Ahlers, M. Krutzik, A. Wenzlawski, S. Arnold, D. Becker, K. Bongs, H. Dittus, H. Duncker, N. Gaaloul, C. Gherasim, E. Giese, C. Grzeschik, T. W. Hänsch, O. Hellmig, W. Herr, S. Herrmann, E. Kajari, S. Kleinert, C. Lämmerzahl, W. Lewoczko-Adamczyk, J. Malcolm, N. Meyer, R. Nolte, A. Peters, M. Popp, J. Reichel, A. Roura, J. Rudolph, M. Schiemangk, M. Schneider, S. T. Seidel, K. Sengstock, V. Tamma, T. Valenzuela, A. Vogel, R. Walser, T. Wendrich, P. Windpassinger, W. Zeller, T. van Zoest, W. Ertmer, W. P. Schleich and E. M. Rasel. *Interferometry with Bose-Einstein Condensates in Microgravity*. Physical Review Letters **110**(9):093602 (2003).
doi:10.1103/PhysRevLett.110.093602
- [3] A. D. Cronin, J. Schmiedmayer and D. E. Pritchard. *Optics and interferometry with atoms and molecules*. Review of Modern Physics **81**(3):1051 (2009).
doi:10.1103/RevModPhys.81.1051
- [4] F. Hasselbach. *Progress in electron- and ion-interferometry*. Reports on Progress in Physics **73**(1):016101 (2010).
doi:10.1088/0034-4885/73/1/016101
- [5] D. A. Pushin, M. G. Huber, M. Arif, C. B. Shahi, J. Nsofini, C. J. Wood, D. Sarenac and D. G. Cory. *Neutron Interferometry at the National Institute of Standards and Technology*. Advances in High Energy Physics **2015**(687480) (2015).
doi:10.1155/2015/687480
- [6] A. Wicht, J. M. Hensley, E. Sarajlic and S. Chu. *A Preliminary Measurement of the Fine Structure Constant Based on Atom Interferometry*. Physica Scripta **2002**(T102):82 (2002).
<http://iopscience.iop.org/article/10.1238/Physica.Topical.102a00082/meta>
- [7] R. Bouchendira, P. Cladé, S. Guellati-Khélifa, F. Nez and F. Biraben. *New Determination of the Fine Structure Constant and Test of the Quantum Elec-*

- trodynamics*. Physical Review Letters **106**(8):080801 (2011).
doi:10.1103/PhysRevLett.106.080801
- [8] A. Bertoldi, G. Lamporesi, L. Cacciapuoti, M. de Angelis, M. Fattori, T. Petelski, A. Peters, M. Prevedelli, J. Stuhler and G. M. Tino. *Atom interferometry gravity-gradiometer for the determination of the Newtonian gravitational constant G*. The European Physical Journal D **40**(2):271 (2006).
doi:10.1140/epjd/e2006-00212-2
- [9] J. B. Fixler, G. T. Foster, J. M. McGuirk and M. A. Kasevich. *Atom Interferometer Measurement of the Newtonian Constant of Gravity*. Science **315**(5808):74 (2007).
doi:10.1126/science.1135459
- [10] G. Lamporesi, A. Bertoldi, L. Cacciapuoti, M. Prevedelli and G. M. Tino. *Determination of the Newtonian Gravitational Constant Using Atom Interferometry*. Physical Review Letters **100**(5):050801 (2008).
doi:10.1103/PhysRevLett.100.050801
- [11] G. Rosi, F. Sorrentino, L. Cacciapuoti, M. Prevedelli and G. M. Tino. *Precision measurement of the Newtonian gravitational constant using cold atoms*. Nature **510**(7506):518 (2014).
doi:10.1038/nature13433
- [12] C. R. Ekstrom, J. Schmiedmayer, M. S. Chapman, T. D. Hammond and D. E. Pritchard. *Measurement of the electric polarizability of sodium with an atom interferometer*. Physical Review A **51**(5):3883 (1995).
doi:10.1103/PhysRevA.51.3883
- [13] A. Miffre, M. Jacquy, M. Büchner, G. Tréneç and J. Vigué. *Atom interferometry measurement of the electric polarizability of lithium*. The European Physical Journal D **38**(2):353 (2006).
doi:10.1140/epjd/e2006-00015-5
- [14] S. Dimopoulos, P. W. Graham, J. M. Hogan, M. A. Kasevich and S. Rajendran. *Atomic gravitational wave interferometric sensor*. Physical Review D **78**(12):122002 (2008).
doi:10.1103/PhysRevD.78.122002
- [15] S. Dimopoulos, P. W. Graham, J. M. Hogan, M. A. Kasevich and S. Rajendran. *Gravitational wave detection with atom interferometry*. Physics Letters B **678**(1):37 (2009).
doi:10.1016/j.physletb.2009.06.011
- [16] W. Chaibi, R. Geiger, B. Canuel, A. Bertoldi, A. Landragin and P. Bouyer. *Low frequency gravitational wave detection with ground-based atom interferometer arrays*. Physical Review D **93**(2):021101 (2016).
doi:10.1103/PhysRevD.93.021101

- [17] S. Fray, C. A. Diez, T. W. Hänsch and M. Weitz. *Atomic Interferometer with Amplitude Gratings of Light and Its Applications to Atom Based Tests of the Equivalence Principle*. Physical Review Letters **93**(24):240404 (2004).
doi:10.1103/PhysRevLett.93.240404
- [18] K.-Y. Chung, S.-w. Chiow, S. Herrmann, S. Chu and H. Müller. *Atom interferometry tests of local Lorentz invariance in gravity and electrodynamics*. Physical Review D **80**(1):016002 (2009).
doi:10.1103/PhysRevD.80.016002
- [19] A. Bonnin, N. Zahzam, Y. Bidel and A. Bresson. *Simultaneous dual-species matter-wave accelerometer*. Physical Review A **88**(4):043615 (2013).
doi:10.1103/PhysRevA.88.043615
- [20] D. Schlippert, J. Hartwig, H. Albers, L. L. Richardson, C. Schubert, A. Roura, W. P. Schleich, W. Ertmer and E. M. Rasel. *Quantum Test of the Universality of Free Fall*. Physical Review Letters **112**(20):203002 (2014).
doi:10.1103/PhysRevLett.112.203002
- [21] M. G. Tarallo, T. Mazzoni, N. Poli, D. V. Sutyryn, X. Zhang and G. M. Tino. *Test of Einstein Equivalence Principle for 0-Spin and Half-Integer-Spin Atoms: Search for Spin-Gravity Coupling Effects*. Physical Review Letters **113**(2):023005 (2014).
doi:10.1103/PhysRevLett.113.023005
- [22] L. Zhou, S. Long, B. Tang, X. Chen, F. Gao, W. Peng, W. Duan, J. Zhong, Z. Xiong, J. Wang, Y. Zhang and M. Zhan. *Test of Equivalence Principle at 10^{-8} Level by a Dual-Species Double-Diffraction Raman Atom Interferometer*. Physical Review Letters **115**(1):013004 (2015).
doi:10.1103/PhysRevLett.115.013004
- [23] B. Barrett, L. Antoni-Micollier, L. Chichet, B. Battelier, T. Lévèque, A. Landragin and P. Bouyer. *Dual matter-wave inertial sensors in weightlessness*. Nature Communications **7**:13786 (2016).
doi:10.1038/ncomms13786
- [24] M. Arndt and K. Hornberger. *Testing the limits of quantum mechanical superpositions*. Nature Physics **10**(4):271 (2014).
doi:10.1038/nphys2863
- [25] T. Kovachy, P. Asenbaum, C. Overstreet, C. A. Donnelly, S. M. Dickerson, A. Sugarbaker, J. M. Hogan and M. A. Kasevich. *Quantum superposition at the half-metre scale*. Nature **528**(7583):530 (2015).
doi:10.1038/nature16155
- [26] A. Peters, K. Y. Chung and S. Chu. *Measurement of gravitational acceleration by dropping atoms*. Nature **400**(6747):849 (1999).
doi:10.1038/23655

- [27] A. Louchet-Chauvet, T. Farah, Q. Bodart, A. Clairon, A. Landragin, S. Merlet and F. P. D. Santos. *The influence of transverse motion within an atomic gravimeter*. New Journal of Physics **13**(6):065025 (2011).
doi:10.1088/1367-2630/13/6/065025
- [28] J. E. Debs, P. A. Altin, T. H. Barter, D. Döring, G. R. Dennis, G. McDonald, R. P. Anderson, J. D. Close and N. P. Robins. *Cold-atom gravimetry with a Bose-Einstein condensate*. Physical Review A **84**(3):033610 (2011).
doi:10.1103/PhysRevA.84.033610
- [29] H. J. McGuinness, A. V. Rakholia and G. W. Biedermann. *High data-rate atom interferometer for measuring acceleration*. Applied Physics Letters **100**(1):011106 (2012).
doi:10.1063/1.3673845
- [30] P. A. Altin, M. T. Johnsson, V. Negnevitsky, G. R. Dennis, R. P. Anderson, J. E. Debs, S. S. Szigeti, K. S. Hardman, S. Bennetts, G. D. McDonald, L. D. Turner, J. D. Close and N. P. Robins. *Precision atomic gravimeter based on Bragg diffraction*. New Journal of Physics **15**(2):023009 (2013).
doi:10.1088/1367-2630/15/2/023009
- [31] M. Hauth, C. Freier, V. Schkolnik, A. Senger, M. Schmidt and A. Peters. *First gravity measurements using the mobile atom interferometer GAIN*. Applied Physics B **113**(1):49 (2013).
doi:10.1007/s00340-013-5413-6
- [32] Z.-K. Hu, B.-L. Sun, X.-C. Duan, M.-K. Zhou, L.-L. Chen, S. Zhan, Q.-Z. Zhang and J. Luo. *Demonstration of an ultrahigh-sensitivity atom-interferometry absolute gravimeter*. Physical Review A **88**(4):043610 (2013).
doi:10.1103/PhysRevA.88.043610
- [33] Y. Bidet, O. Carraz, R. Charrière, M. Cadoret, N. Zahzam and A. Bresson. *Compact cold atom gravimeter for field applications*. Applied Physics Letters **102**(14):144107 (2013).
doi:10.1063/1.4801756
- [34] S. Abend, M. Gebbe, M. Gersemann, H. Ahlers, H. Müntinga, E. Giese, N. Gaaloul, C. Schubert, C. Lämmerzahl, W. Ertmer, W. P. Schleich and E. M. Rasel. *Atom-Chip Fountain Gravimeter*. Physical Review Letters **117**(20):203003 (2016).
doi:10.1103/PhysRevLett.117.203003
- [35] M. J. Snadden, J. M. McGuirk, P. Bouyer, K. G. Haritos and M. A. Kasevich. *Measurement of the Earth's Gravity Gradient with an Atom Interferometer-Based Gravity Gradiometer*. Physical Review Letters **81**(5):971 (1998).
doi:10.1103/PhysRevLett.81.971

- [36] J. M. McGuirk, G. T. Foster, J. B. Fixler, M. J. Snadden and M. A. Kasevich. *Sensitive absolute-gravity gradiometry using atom interferometry*. Physical Review A **65**(3):033608 (2002).
doi:10.1103/PhysRevA.65.033608
- [37] T. L. Gustavson, P. Bouyer and M. A. Kasevich. *Precision Rotation Measurements with an Atom Interferometer Gyroscope*. Physical Review Letters **78**(11):2046 (1997).
doi:10.1103/PhysRevLett.78.2046
- [38] D. S. Durfee, Y. K. Shaham and M. A. Kasevich. *Long-Term Stability of an Area-Reversible Atom-Interferometer Sagnac Gyroscope*. Physical Review Letters **97**(24):240801 (2006).
doi:10.1103/PhysRevLett.97.240801
- [39] J. K. Stockton, X. Wu and M. A. Kasevich. *Bayesian estimation of differential interferometer phase*. Physical Review A **76**(3):033613 (2007).
doi:10.1103/PhysRevA.76.033613
- [40] A. Gauguet, B. Canuel, T. Lévêque, W. Chaibi and A. Landragin. *Characterization and limits of a cold-atom Sagnac interferometer*. Physical Review A **80**(6):063604 (2009).
doi:10.1103/PhysRevA.80.063604
- [41] J. K. Stockton, K. Takase and M. A. Kasevich. *Absolute Geodetic Rotation Measurement Using Atom Interferometry*. Physical Review Letters **107**(13):133001 (2011).
doi:10.1103/PhysRevLett.107.133001
- [42] G. Tackmann, P. Berg, C. Schubert, S. Abend, M. Gilowski, W. Ertmer and E. M. Rasel. *Self-alignment of a compact large-area atomic Sagnac interferometer*. New Journal of Physics **14**(1):015002 (2012).
doi:10.1088/1367-2630/14/1/015002
- [43] H. Xue, Y. Feng, S. Chen, X. Wang, X. Yan, Z. Jiang and Z. Zhou. *A continuous cold atomic beam interferometer*. Journal of Applied Physics **117**(9):094901 (2015).
doi:10.1063/1.4913711
- [44] A. Peters, K. Y. Chung and S. Chu. *High-precision gravity measurements using atom interferometry*. Metrologia **38**(1):25 (2001).
doi:10.1088/0026-1394/38/1/4
- [45] M. de Angelis, A. Bertoldi, L. Cacciapuoti, A. Giorgini, G. Lamporesi, M. Prevedelli, G. Saccorotti, F. Sorrentino and G. M. Tino. *Precision gravimetry with atomic sensors*. Measurement Science and Technology **20**(2):022001 (2009).
doi:10.1088/0957-0233/20/2/022001

- [46] O. Carraz, C. Siemes, L. Massotti, R. Haagmans and P. Silvestrin. *A Spaceborne Gravity Gradiometer Concept Based on Cold Atom Interferometers for Measuring Earth's Gravity Field*. *Microgravity Science and Technology* **26**(3):139 (2014).
doi:10.1007/s12217-014-9385-x
- [47] E. Gibney. *Billion-euro boost for quantum tech*. *Nature* **532**(7600):426 (2016).
https://www.nature.com/polopoly_fs/1.19796!/menu/main/topColumns/topLeftColumn/pdf/nature.2016.19796.pdf
- [48] European Union. *Quantum Manifesto* (2016).
http://qurope.eu/system/files/u7/93056_Quantum%20Manifesto_WEB.pdf
- [49] AtomSensors. Website (2017).
<http://www.atomsensors.com/index.php/en/>
- [50] AOSense. Website (2017).
<http://aosense.com/>
- [51] μ QUANS. Website (2017).
<https://www.muquans.com/>
- [52] M. A. Kasevich and S. Chu. *Measurement of the gravitational acceleration of an atom with a light-pulse atom interferometer*. *Applied Physics B* **54**(5):321 (1992).
doi:10.1007/BF00325375
- [53] S. S. Zsigeti, J. E. Debs, J. J. Hope, N. P. Robins and J. D. Close. *Why momentum width matters for atom interferometry with Bragg pulses*. *New Journal of Physics* **14**(2):023009 (2012).
doi:10.1088/1367-2630/14/2/023009
- [54] J. G. Williams, S. G. Turyshev and D. H. Boggs. *Progress in Lunar Laser Ranging Tests of Relativistic Gravity*. *Physical Review Letters* **93**(26):261101 (2004).
doi:10.1103/PhysRevLett.93.261101
- [55] S. Schlamminger, K.-Y. Choi, T. A. Wagner, J. H. Gundlach and E. G. Adelberger. *Test of the Equivalence Principle Using a Rotating Torsion Balance*. *Physical Review Letters* **100**(4):041101 (2008).
doi:10.1103/PhysRevLett.100.041101
- [56] J. Hartwig, S. Abend, C. Schubert, D. Schlippert, H. Ahlers, K. Posso-Trujillo, N. Gaaloul, W. Ertmer and E. M. Rasel. *Testing the universality of free fall with rubidium and ytterbium in a very large baseline atom interferometer*. *New Journal of Physics* **17**(3):035011 (2015).
doi:10.1088/1367-2630/17/3/035011

- [57] G. Rosi, G. D'Amico, L. Cacciapuoti, F. Sorrentino, M. Prevedelli, M. Zych, Č. Brukner and G. Tino. *Quantum test of the equivalence principle for atoms in coherent superposition of internal energy states*. Nature Communications **8**:15529 (2017).
doi:10.1038/ncomms15529
- [58] M. A. Hohensee, H. Müller and R. B. Wiringa. *Equivalence Principle and Bound Kinetic Energy*. Physical Review Letters **111**(15):151102 (2013).
doi:10.1103/PhysRevLett.111.151102
- [59] T. Damour. *Theoretical aspects of the equivalence principle*. Classical and Quantum Gravity **29**(18):184001 (2012).
doi:10.1088/0264-9381/29/18/184001
- [60] C. Schubert, J. Hartwig, H. Ahlers, K. Posso-Trujillo, N. Gaaloul, U. Velte, A. Landragin, A. Bertoldi, B. Battelier, P. Bouyer, F. Sorrentino, G. M. Tino, M. Krutzik, A. Peters, S. Herrmann, C. Lämmerzahl, L. Cacciapuoti, E. Rocco, K. Bongs, W. Ertmer and E. M. Rasel. *Differential atom interferometry with 87 Rb and 85 Rb for testing the UFF in STE-QUEST*. arXiv **1312.5963v1** (2013).
<https://arxiv.org/abs/1312.5963>
- [61] D. N. Aguilera, H. Ahlers, B. Battelier, A. Bawamia, A. Bertoldi, R. Bondarescu, K. Bongs, P. Bouyer, C. Braxmaier, L. Cacciapuoti, C. Chaloner, M. Chwalla, W. Ertmer, M. Franz, N. Gaaloul, M. Gehler, D. Gerardi, L. Gesa, N. Gürlebeck, J. Hartwig, M. Hauth, O. Hellmig, W. Herr, S. Herrmann, A. Heske, A. Hinton, P. Ireland, P. Jetzer, U. Johann, M. Krutzik, A. Kubelka, C. Lämmerzahl, A. Landragin, I. Lloro, D. Massonnet, I. Mateos, A. Milke, M. Nofrarias, M. Oswald, A. Peters, K. Posso-Trujillo, E. Rasel, E. Rocco, A. Roura, J. Rudolph, W. Schleich, C. Schubert, T. Schuldt, S. Seidel, K. Sengstock, C. F. Sopena, F. Sorrentino, D. Summers, G. M. Tino, C. Trenkel, N. Uzunoglu, W. von Klitzing, R. Walser, T. Wendrich, A. Wenzlawski, P. Weßels, A. Wicht, E. Wille, M. Williams, P. Windpassinger and N. Zahzam. *STE-QUEST - test of the universality of free fall using cold atom interferometry*. Classical and Quantum Gravity **31**(11):115010 (2014).
doi:10.1088/0264-9381/31/11/115010
- [62] B. Altschul, Q. G. Bailey, L. Blanchet, K. Bongs, P. Bouyer, L. Cacciapuoti, S. Capozziello, N. Gaaloul, D. Giulini, J. Hartwig, L. Iess, P. Jetzer, A. Landragin, E. Rasel, S. Reynaud, S. Schiller, C. Schubert, F. Sorrentino, U. Sterr, J. D. Tasson, G. M. Tino, P. Tuckey, and P. Wolf. *Quantum tests of the Einstein Equivalence Principle with the STE-QUEST space mission*. Advances in Space Research **55**(1):501 (2015).
doi:10.1016/j.asr.2014.07.014
- [63] S. M. Dickerson, J. M. Hogan, A. Sugarbaker, D. M. S. Johnson and M. A. Kasevich. *Multiaxis Inertial Sensing with Long-Time Point Source Atom In-*

- terferometry*. Physical Review Letters **111**(8):083001 (2013).
doi:10.1103/PhysRevLett.111.083001
- [64] L. Zhou, Z. Y. Xiong, W. Yang, B. Tang, W. C. Peng, K. Hao, R. B. Li, M. Liu, J. Wang and M. S. Zhan. *Development of an atom gravimeter and status of the 10-meter atom interferometer for precision gravity measurement*. General Relativity and Gravitation **43**(7):1931 (2011).
doi:10.1007/s10714-011-1167-9
- [65] S. T. Seidel. *Eine Quelle für die Interferometrie mit Bose-Einstein-Kondensaten auf Höhenforschungsraketen*. Ph.D. thesis, Gottfried Wilhelm Leibniz Universität Hannover (2014).
https://www.iqo.uni-hannover.de/uploads/tx_tkpublikationen/Doktorarbeit_Stephan_Seidel__Version_1.1_kompremiert.pdf
- [66] N. J. Penley, C. P. Schafer and J.-D. F. Bartoe. *The international space station as a microgravity research platform*. Acta Astronautica **50**(11):691 (2002).
doi:10.1016/S0094-5765(02)00003-6
- [67] U. Kaczmarczik. *Deputy Technical Director of ZARM-FABmbH*. private communication (2016)
- [68] B. V. Tryggvason, R. F. Redden, R. A. Herring, W. M. B. Duval, R. W. Smith, K. S. Rezkallah and S. Varma. *The vibration environment on the international space station: its significance to fluid-based experiments*. Acta Astronautica **48**(2-3):59 (2001).
doi:10.1016/S0094-5765(00)00140-5
- [69] T. van Zoest, N. Gaaloul, Y. Singh, H. Ahlers, W. Herr, S. T. Seidel, W. Ertmer, E. Rasel, M. Eckart, E. Kajari, S. Arnold, G. Nandi, W. P. Schleich, R. Walser, A. Vogel, K. Sengstock, K. Bongs, W. Lewoczko-Adamczyk, M. Schiemangk, T. Schuldt, A. Peters, T. Könemann, H. Müntinga, C. Lämmerzahl, H. Dittus, T. Steinmetz, T. W. Hänsch and J. Reichel. *Bose-Einstein Condensation in Microgravity*. Science **328**(5985):1540 (2010).
doi:10.1126/science.1189164
- [70] J. Grosse, S. T. Seidel, D. Becker, M. D. Lachmann, M. Scharringhausen, C. Braxmaier and E. M. Rasel. *Design and qualification of an UHV system for operation on sounding rockets*. Journal of Vacuum Science & Technology A **34**(3):031606 (2016).
doi:10.1116/1.4947583
- [71] V. Schkolnik, O. Hellmig, A. Wenzlawski, J. Grosse, A. Kohfeldt, K. Döringshoff, A. Wicht, P. Windpassinger, K. Sengstock, C. Braxmaier, M. Krutzik and A. Peters. *A compact and robust diode laser system for atom interferometry on a sounding rocket*. Applied Physics B **122**(8):217 (2016).
doi:10.1007/s00340-016-6490-0

- [72] A. Kubelka-Lange, S. Herrmann, J. Grosse, C. Lämmerzahl, E. M. Rasel and C. Braxmaier. *A three-layer magnetic shielding for the MAIUS-1 mission on a sounding rocket*. *Review of Scientific Instruments* **87**(6):063101 (2016). doi:10.1063/1.4952586
- [73] C. van Harmelen and M. Soriano. *Development of the Science Data System for the International Space Station Cold Atom Lab*. In *IEEE Aerospace Conference*, pp. 1–7 (2015). doi:10.1109/AERO.2015.7118928
- [74] J. M. Hogan, D. M. S. Johnson, S. Dickerson, T. Kovachy, A. Sugarbaker, S. wey Chiow, P. W. G. M. A. Kasevich, B. Saif, S. Rajendran, P. Bouyer, B. D. Seery and L. F. R. Keski-Kuha. *An Atomic Gravitational Wave Interferometric Sensor in Low Earth Orbit (AGIS-LEO)*. *General Relativity and Gravitation* **43**(7):1953 (2011). doi:10.1007/s10714-011-1182-x
- [75] Novespace. Website (Performances) (2015). <http://www.novespace.fr/en,novespace,client.html>
- [76] Drop Tower Operation and Service Company (ZARM FABmbH). *ZARM Drop Tower Bremen User Manual* (2011). https://www.zarm.uni-bremen.de/fileadmin/images/droptower/downloads/Users_Manual_0611.pdf
- [77] C. J. Pethick and H. Smith. *Bose-Einstein Condensation in Dilute Gases*. Cambridge University Press, 2nd edn. (2008). ISBN 978-0-521-84651-6. www.cambridge.org/9780521846516
- [78] J. Rudolph, W. Herr, C. Grzeschik, T. Sternke, A. Grote, M. Popp, D. Becker, H. Müntinga, H. Ahlers, A. Peters, C. Lämmerzahl, K. Sengstock, N. Gaaloul, W. Ertmer and E. M. Rasel. *A high-flux BEC source for mobile atom interferometers*. *New Journal of Physics* **17**(6):065001 (2015). doi:10.1088/1367-2630/17/7/079601
- [79] W. Herr. *Eine kompakte Quelle quantenentarteter Gase hohen Flusses für die Atominterferometrie unter Schwerelosigkeit*. Ph.D. thesis, Technische Informationsbibliothek und Universitätsbibliothek Hannover (TIB) (2013). https://www.tib.eu/de/suchen/id/TIBKAT%3A746945310/Eine-kompakte-Quelle-quantenentarteter-Gase-hohen/?tx_tibsearch_search%5Bsearchspace%5D=tn
- [80] J. Rudolph. *Matter-Wave Optics with Bose-Einstein Condensates in Microgravity*. Ph.D. thesis, Gottfried Wilhelm Leibniz Universität Hannover (2016). https://www.iqo.uni-hannover.de/uploads/tx_tkpublikationen/Doktorarbeit_Jan_Rudolph.pdf

- [81] C. Grzeschik. *Experiments with Bose-Einstein Condensates in Microgravity*. Ph.D. thesis, Humboldt-Universität zu Berlin (2017).
doi:10.18452/18037
- [82] A. Grote. *Ultracold 87Rb : from quantum metrology to two-photon ionization*. Ph.D. thesis, Universität Hamburg (2016).
https://www.physnet.uni-hamburg.de/services/biblio/dissertation/dissfbPhysik/___Kurzfassungen/Alexander___Grote
- [83] E. L. Raab, M. P. Prentiss, A. Cable, S. Chu and D. E. Pritchard. *Trapping of Neutral Sodium Atoms with Radiation Pressure*. Physical Review Letters **59**(23):2631 (1987).
doi:10.1103/PhysRevLett.59.2631
- [84] A. L. Migdall, J. V. Prodan, W. D. Phillips, T. H. Bergeman and H. J. Metcalf. *First Observation of Magnetically Trapped Neutral Atoms*. Physical Review Letters **54**(24):2596 (1985).
doi:10.1103/PhysRevLett.54.2596
- [85] W. Petrich, M. H. Anderson, J. R. Ensher and E. A. Cornell. *Stable, Tightly Confining Magnetic Trap for Evaporative Cooling of Neutral Atoms*. Physical Review Letters **74**(17):3352 (1995).
doi:10.1103/PhysRevLett.74.3352
- [86] S. Chu, J. E. Bjorkholm, A. Ashkin and A. Cable. *Experimental Observation of Optically Trapped Atoms*. Physical Review Letters **57**(3):314 (1986).
doi:10.1103/PhysRevLett.57.314
- [87] A. Ashkin. *Acceleration and Trapping of Particles by Radiation Pressure*. Physical Review Letters **24**(4):156 (1970).
doi:10.1103/PhysRevLett.24.156
- [88] G. Cennini, G. Ritt, C. Geckeler and M. Weitz. *Bose-Einstein condensation in a CO_2 -laser optical dipole trap*. Applied Physics B **77**(8):773 (2003).
doi:10.1007/s00340-003-1333-1
- [89] W. H. Wing. *On neutral particle trapping in quasistatic electromagnetic fields*. Progress in Quantum Electronics **8**(3–4):181 (1984).
doi:10.1016/0079-6727(84)90012-0
- [90] C. V. Sukumar and D. M. Brink. *Spin-flip transitions in a magnetic trap*. Physical Review A **56**(3):2451 (1997).
doi:10.1103/PhysRevA.56.2451
- [91] D. M. Brink and C. V. Sukumar. *Majorana spin-flip transitions in a magnetic trap*. Physical Review A **74**(3):035401 (2006).
doi:10.1103/PhysRevA.74.035401

- [92] D. A. Steck. *Rubidium 87 D Line Data* (2015).
<http://steck.us/alkalidata>, revision 2.1.5
- [93] J. Fortágh and C. Zimmermann. *Magnetic microtraps for ultracold atoms*. *Reviews of Modern Physics* **79**(1):235 (2007).
doi:10.1103/RevModPhys.79.235
- [94] G. Reinaudi, T. Lahaye, Z. Wang and D. Guéry-Odelin. *Strong saturation absorption imaging of dense clouds of ultracold atoms*. *Optics Letters* **32**(21):3143 (2007).
doi:10.1364/OL.32.003143
- [95] S. Spießberger, M. Schiemangk, A. Sahm, A. Wicht, H. Wenzel, A. Peters, G. Erbert and G. Tränkle. *Micro-integrated 1 Watt semiconductor laser system with a linewidth of 3.6 kHz*. *Optics Express* **19**(8):7077 (2011).
doi:10.1364/OE.19.007077
- [96] M. Schiemangk, K. Lampmann, A. Dinkelaker, A. Kohfeldt, M. Krutzik, C. Kürbis, A. Sahm, S. Spießberger, A. Wicht, G. Erbert, G. Tränkle and A. Peters. *High-power, micro-integrated diode laser modules at 767 and 780 nm for portable quantum gas experiments*. *Applied Optics* **54**(17):5332 (2015).
doi:10.1364/AO.54.005332
- [97] M. Schiemangk. *Entwicklung ultrastabiler Lasersysteme für Experimente mit Quantengasen*. Diploma Thesis (2007).
https://www.physics.hu-berlin.de/en/qom/publications/pdfs/DA_Max_Schiemangk.pdf
- [98] O. Brox, F. Bugge, A. Mogilatenko, E. Luvsandamdin, A. Wicht, H. Wenzel and G. Erbert. *Distributed feedback lasers in the 760 to 810 nm range and epitaxial grating design*. *Semiconductor Science and Technology* **29**(9):095018 (2014).
doi:10.1088/0268-1242/29/9/095018
- [99] T.-P. Nguyen, M. Schiemangk, S. Spießberger, H. Wenzel, A. Wicht, A. Peters, G. Erbert and G. Tränkle. *Optimization of 780 nm DFB diode lasers for high-power narrow linewidth emission*. *Applied Physics B* **108**(4):767 (2012).
doi:10.1007/s00340-012-5131-5
- [100] M. Popp. *Compact, low-noise current sources for efficient creation of Bose-Einstein condensates employing the atom-chip technology*. Ph.D. thesis, Technische Informationsbibliothek und Universitätsbibliothek Hannover (TIB) (2017)
- [101] E. Baum and J. Bork. *Systematic design of magnetic shields*. *Journal of Magnetism and Magnetic Materials* **101**(1–3):69 (1991).
doi:10.1016/0304-8853(91)90682-Z

- [102] F. Thiel. *Demagnetization of Layered Ferromagnetic Structures for Magnetically Shielding: Frequency Considerations*. IEEE Transactions on Magnetics **45**(12):5307 (2009).
doi:10.1109/TMAG.2009.2022935
- [103] T. Könemann. *Konzeption, Entwicklung und Umsetzung von atomoptischen Fallturmentperimenten für den Einsatz unter Schwerelosigkeit am Fallturm Bremen*. Ph.D. thesis, Universität Bremen (2009).
<https://www.deutsche-digitale-bibliothek.de/binary/532SZM76NALNE3LNDCM4K4DGTL67IF5W/full/1.pdf>
- [104] E. A. Burt and C. R. Ekstrom. *Optimal three-layer cylindrical magnetic shield sets for scientific applications*. Review of Scientific Instruments **73**(7):2699 (2002).
doi:10.1063/1.1487892
- [105] A. Kubelka-Lange. *Entwicklung einer hocheffektiven Magnetfeldabschirmung für die Forschungsraketenmission MAIUS-1*. Ph.D. thesis, Universität Bremen (2017)
- [106] Q. Wang, P. Ping, X. Zhao, G. Chu, J. Sun and C. Chen. *Thermal runaway caused fire and explosion of lithium ion battery*. Journal of Power Sources **208**:210 (2012).
doi:10.1016/j.jpowsour.2012.02.038
- [107] G. Chen and T. J. Richardson. *Thermal instability of Olivine-type LiMnPO_4 cathodes*. Journal of Power Sources **195**(4):1221 (2010).
doi:10.1016/j.jpowsour.2009.08.046
- [108] M. Safari and C. Delacourt. *Modeling of a Commercial Graphite/ LiFePO_4 Cell*. Journal of The Electrochemical Society **158**(5):562 (2011).
doi:10.1149/1.3567007
- [109] B. Scrosati and J. Garche. *Lithium batteries: Status, prospects and future*. Journal of Power Sources **195**(9):2419 (2010).
doi:10.1016/j.jpowsour.2009.11.048
- [110] Z. Li, D. Zhang and F. Yang. *Developments of lithium-ion batteries and challenges of LiFePO_4 as one promising cathode material*. Journal of Materials Science **44**(10):2435 (2009).
doi:10.1007/s10853-009-3316-z
- [111] E. Prada, D. D. Domenico, Y. Creff, J. Bernard, V. Sauvant-Moynot and F. Huet. *Simplified Electrochemical and Thermal Model of LiFePO_4 -Graphite Li-Ion Batteries for Fast Charge Applications*. Journal of The Electrochemical Society **159**(9):A1508 (2012).
doi:10.1149/2.064209jes

- [112] Lipopower. Website (December 2nd, 2016).
<http://shop.lipopower.de/A123-Systems-AMP20M1HD-A-20Ah-Folienzelle-Sonderposten>
- [113] A. Ritchie and W. Howard. *Recent developments and likely advances in lithium-ion batteries*. Journal of Power Sources **162**(2):809 (2006).
doi:10.1016/j.jpowsour.2005.07.014
- [114] X. Hu, S. Li and H. Peng. *A comparative study of equivalent circuit models for Li-ion batteries*. Journal of Power Sources **198**:359 (2012).
doi:10.1016/j.jpowsour.2011.10.013
- [115] C. Weng, J. Sun and H. Peng. *An Open-Circuit-Voltage Model of Lithium-Ion Batteries for Effective Incremental Capacity Analysis*. In *Proceedings of the AMSE* (2013).
doi:10.1115/DSCC2013-3979
- [116] M. Popp. *Institute of Quantum Optics, Hanover*. private communication (2016)
- [117] W. Ketterle and N. V. Druten. *Evaporative Cooling of Trapped Atoms*. Advances in Atomic Molecular and Optical Physics **37**:181 (1996).
doi:10.1016/S1049-250X(08)60101-9
- [118] D. M. Farkas, E. A. Salim and J. Ramirez-Serrano. *Production of Rubidium Bose-Einstein Condensates at a 1 Hz Rate*. arXiv **1403.4641** (2014).
<https://arxiv.org/abs/1403.4641>
- [119] D. M. Farkas, K. M. Hudek, E. A. Salim, S. R. Segal, M. B. Squires and D. Z. Anderson. *A compact, transportable, microchip-based system for high repetition rate production of Bose-Einstein condensates*. Applied Physics Letters **96**(9):093102 (2010).
doi:10.1063/1.3327812
- [120] M. Horikoshi and K. Nakagawa. *Atom chip based fast production of Bose-Einstein condensate*. Applied Physics B **82**(3):363 (2006).
doi:10.1007/s00340-005-2083-z
- [121] M. H. T. Extavour, L. J. LeBlanc, T. Schumm, B. Cieslak, S. Myrskog, A. Stummer, S. Aubin and J. H. Thywissen. *Dual-Species Quantum Degeneracy of 40K and 87Rb on an Atom Chip*. AIP Conference Proceedings **869**(1):241 (2006).
doi:10.1063/1.2400654
- [122] T. Kinoshita, T. Wenger and D. S. Weiss. *All-optical Bose-Einstein condensation using a compressible crossed dipole trap*. Physical Review A **71**(1):011602 (2005).
doi:10.1103/PhysRevA.71.011602

- [123] J.-F. Clément, J.-P. Brantut, M. Robert-de Saint-Vincent, R. A. Nyman, A. Aspect, T. Bourdel and P. Bouyer. *All-optical runaway evaporation to Bose-Einstein condensation*. Physical Review A **79**(6):061406 (2009).
doi:10.1103/PhysRevA.79.061406
- [124] K. Yamashita, K. Hanasaki, A. Ando, M. Takahama and T. Kinoshita. *All-optical production of a large Bose-Einstein condensate in a double compressible crossed dipole trap*. Physical Review A **95**(1):013609 (2017).
doi:10.1103/PhysRevA.95.013609
- [125] E. W. Streed, A. P. Chikkatur, T. L. Gustavson, M. Boyd, Y. Torii, D. Schneble, G. K. Campbell, D. E. Pritchard and W. Ketterle. *Large atom number Bose-Einstein condensate machines*. Review of Scientific Instruments **77**(2):023106 (2006).
doi:10.1063/1.2163977
- [126] Y.-J. Lin, A. R. Perry, R. L. Compton, I. B. Spielman and J. V. Porto. *Rapid production of ^{87}Rb Bose-Einstein condensates in a combined magnetic and optical potential*. Physical Review A **79**(6):063631 (2009).
doi:10.1103/PhysRevA.79.063631
- [127] D. Halliday, R. Resnick and J. Walker. *FUNDAMENTALS OF PHYSICS*. Wiley, 7th extended edn. (2005). ISBN 0-471-23231-9. Page 834
- [128] F. Bloch, W. W. Hansen and M. Packard. *The Nuclear Induction Experiment*. Physical Review **70**(7-8):474 (1946).
doi:10.1103/PhysRev.70.474
- [129] W. R. Janzen, T. J. R. Cyr and B. A. Dunell. *Adiabatic Rapid-Passage Experiments in Some Solids*. The Journal of Chemical Physics **48**(3):1246 (1968).
doi:10.1063/1.1668789
- [130] D. J. McCarron, H. W. Cho, D. L. Jenkin, M. P. Köppinger and S. L. Cornish. *Dual-Species Bose-Einstein condensate of ^{87}Rb and ^{133}Cs* . Physical Review A **84**(1):011603 (2011).
doi:10.1103/PhysRevA.84.011603
- [131] D. Jenkin, D. McCarron, M. Köppinger, H. Cho, S. Hopkins and S. Cornish. *Bose-Einstein condensation of ^{87}Rb in a levitated crossed dipole trap*. The European Physical Journal D **65**(11-18):11 (2011).
doi:10.1140/epjd/e2011-10720-5
- [132] W. Peng-Jun, F. Zheng-Kun, C. Shi-Jie and Z. Jing. *Feshbach resonances in an ultracold mixture of ^{87}Rb and ^{40}K* . Chinese Physics B **20**(10):103401 (2011).
doi:10.1088/1674-1056/20/10/103401

- [133] G. K. Büning. *Lange Kohärenzzeit optisch gefangener Ensembles*. Ph.D. thesis, Gottfried Wilhelm Leibniz Universität Hannover (2011).
<https://www.tib.eu/de/suchen/id/TIBKAT%3A664556140/Lange-Koh%C3%A4renzzeit-optisch-gefangener-Ensembles/>
- [134] J. C. Camparo and R. P. Frueholz. *Parameters of Adiabatic rapid passage in the 0-0 hyperfine transition of ^{87}Rb* . *Physical Review A* **30**(2):803 (1984).
doi:10.1103/PhysRevA.30.803
- [135] M. M. T. Loy. *Observation of Population Inversion by Optical Adiabatic Rapid Passage*. *Physical Review Letters* **32**(15):814 (1974).
doi:10.1103/PhysRevLett.32.814
- [136] M. M. T. Loy. *Two-Photon Adiabatic Inversion*. *Physical Review Letters* **41**(7):473 (1978).
doi:10.1103/PhysRevLett.41.473
- [137] S. Nakanishi, T. Endo, T. Muramoto and T. Hashi. *Optical adiabatic rapid passage by linear frequency chirping in ruby*. *Optics Communications* **38**(5-6):419 (1981).
doi:10.1016/0030-4018(81)90080-8
- [138] J. S. Melinger, S. R. Gandhi, A. Hariharan, J. X. Tull and W. S. Warren. *Generation of Narrowband Inversion with Broadband Laser Pulses*. *Physical Review Letters* **68**(13):2000 (1992).
doi:10.1103/PhysRevLett.68.2000
- [139] J. S. Melinger. *Adiabatic population transfer with frequency-swept laser pulses*. *The Journal of Chemical Physics* **101**(8):6439 (1994).
doi:10.1063/1.468368
- [140] J. C. Camparo and R. P. Frueholz. *A dressed atom interpretation of Adiabatic rapid passage*. *Journal of Physics B* **17**(20):4169 (1984).
<http://iopscience.iop.org/article/10.1088/0022-3700/17/20/015/meta>
- [141] E. Jaynes and F. Cummings. *Comparison of Quantum and Semiclassical Radiation Theories with Application to the Beam Maser*. *Proceedings of the IEEE* **51**(1):89 (1963).
doi:10.1109/PROC.1963.1664
- [142] S. Haroche and J.-M. Raimond. *Exploring the Quantum*. Oxford University Press (2006). ISBN 0-19-850914-6
- [143] P. Meystre and M. S. III. *Elements of Quantum Optics*. Springer (2007). ISBN 978-3-540-74209-8
- [144] S. M. Barnett and P. M. Radmore. *Methods in Theoretical Quantum Optics*. Clarendon Press - Oxford (1997). ISBN 0-19-856362-0

- [145] I. I. Rabi. *Space Quantization in a Gyating Magnetic Field*. Physical Review **51**(8):652 (1937).
doi:10.1103/PhysRev.51.652
- [146] C. Zener. *Non-Adiabatic Crossing of Energy Levels*. Proceedings of the Royal Society A **137**(833):696 (1932).
<http://rspa.royalsocietypublishing.org/content/royprsa/137/833/696.full.pdf>
- [147] F. Bloch. *Nuclear Induction*. Physical Review **70**(7-8):460 (1946).
doi:10.1103/PhysRev.70.460
- [148] S. Reynaud and C. Cohen-Tannoudji. *Dressed atom approach to collisional redistribution*. Journal de Physique **43**(7):1021 (1982).
doi:10.1051/jphys:019820043070102100
- [149] L. M. K. Vandersypen and I. L. Chuang. *NMR techniques for quantum control and computation*. Review of Modern Physics **76**(4):1037 (2004).
doi:10.1103/RevModPhys.76.1037
- [150] E. L. Hahn. *Spin Echos*. Physical Review **80**(4):580 (1950).
doi:10.1103/PhysRev.80.580
- [151] H. Y. Carr and E. M. Purcell. *Effects of Diffusion on Free Precession in Nuclear Magnetic Resonance Experiments*. Physical Review **94**(3):630 (1954).
doi:10.1103/PhysRev.94.630
- [152] J. G. Powles. *The Adiabatic Fast Passage Experiment in Magnetic Resonance*. Proceedings of the Physical Society **71**(3):497 (1958).
<http://iopscience.iop.org/article/10.1088/0370-1328/71/3/424/meta>
- [153] G. Breit and I. I. Rabi. *Measurement of Nuclear Spin*. Physical Review **38**(11):2082 (1931).
doi:10.1103/PhysRev.38.2082.2
- [154] R.-B. Li, L. Zhou, J. Wang and M.-S. Zhan. *Measurement of the quadratic Zeeman shift of ^{85}Rb hyperfine sublevels using stimulated Raman transitions*. Optics Communications **282**(7):1340 (2009).
doi:10.1016/j.optcom.2008.12.034
- [155] S. Bize, Y. Sortais, M. S. Santos, C. Mandache, A. Clairon and C. Salomon. *High-accuracy measurement of the 87Rb ground-state hyperfine splitting in an atomic fountain*. Europhysics Letters **45**(5):558 (1999).
<http://stacks.iop.org/0295-5075/45/i=5/a=558>
- [156] D. Harting and P. Klinkenberg. *The quadratic Zeeman-effect in the principal series of caesium, rubidium and potassium*. Physica **14**(10):669 (1949).
doi:10.1016/0031-8914(49)90010-5

- [157] O. Halpern. *Zur Quantentheorie des normalen Zeemaneffektes*. Zeitschrift für Physik **18**(1):352 (1923).
doi:10.1007/BF01327715
- [158] T. Fließbach. *Mechanik: Lehrbuch zur Theoretischen Physik I*. Spektrum, 5th edn. (2006). ISBN 978-3-8274-1683-4. Page 44
- [159] Institut für Wetter- und Klimakommunikation GmbH. Website (July 27th, 2016).
<http://www.wetterspiegel.de/de/europa/deutschland/bremen/13610w102240x23.html>
- [160] W. Raith. *Lehrbuch der Experimentalphysik: Elektromagnetismus*. Bergmann Schaefer. de Gruyter, 8th edn. (1999). ISBN 3-11-016097-8. Page 74
- [161] J. D. Jackson. *Klassische Elektrodynamik*. de Gruyter, 4th edn. (2006). ISBN 978-3-11-018970-4. Page 171
- [162] D. R. Lide. *Handbook of chemistry and physics*. CRC Press, 84th edn. (2003-2004). Page 10-165
- [163] H. Selig, H. Dittus and C. Lämmerzahl. *Drop Tower Microgravity Improvement Towards the Nano-g Level for the MICROSCOPE Payload Tests*. Microgravity Science and Technology **22**(4):539 (2010).
doi:10.1007/s12217-010-9210-0
- [164] F. M. White. *Fluid Mechanics*. McGraw-Hill, 7th edn. (2011). ISBN 978-0-07-352934-9. Page 483.
<https://drive.google.com/file/d/0B9JtpWUzKcwkNC110C1mQ0NzZjg/view>
- [165] P. Touboul, E. Willemenot, B. Foulon and V. Josselin. *Accelerometers for CHAMP, GRACE and GOCE space missions: synergy and evolution*. BOLL. LETTINO DI GEOFISICA TEORICA ED APPLICATA **40**(3-4):321 (1999).
http://www3.ogs.trieste.it/bgta/pdf/bgta40.3.4_TOUBOUL.pdf
- [166] Z. Wei, H. Houtse, Z. Min, Y. Mei-Juan, Z. Xu-Hua and P. Bi-Bo. *Influence of the Adjusted Accuracy of Center of Mass Between GRACE Satellite and SuperSTAR Accelerometer on the Accuracy of Earth's Gravitational Field*. Chinese Journal of Geophysics **52**(3):564 (2009).
doi:10.1002/cjg2.1378
- [167] S. Bremer and M. List. *Modelling of the MICROSCOPE Mission*. Space Science Reviews **151**(1):39 (2010).
doi:10.1007/s11214-009-9599-1
- [168] H. Selig. *Deputy Project Manager MICROSCOPE-ZARM*. private communication (2016)

- [169] L. Verlet. *Computer "Experiments" on Classical Fluids. I. Thermodynamical Properties of Lennard-Jones Molecules*. Physical Review **159**(1):98 (1967).
doi:10.1103/PhysRev.159.98
- [170] W. C. Swope, H. C. Andersen, P. H. Berens and K. R. Wilson. *A computer simulation method for the calculation of equilibrium constants for the formation of physical clusters of molecules: Application to small water clusters*. The Journal of Chemical Physics **76**(1):637 (1982).
doi:10.1063/1.442716
- [171] W. Herr. *Institute of Quantum Optics, Hanover*. private communication (2015)
- [172] V. M. Pérez-García, H. Michinel, J. I. Cirac, M. Lewenstein and P. Zoller. *Low Energy Excitations of a Bose-Einstein Condensate: A Time-Dependent Variational Analysis*. Physical Review Letters **77**(27):5320 (1996).
doi:10.1103/PhysRevLett.77.5320
- [173] H. J. H. Al-Jibbouri. *Collective Excitations in Bose-Einstein Condensates*. Ph.D. thesis, Freie Universität Berlin (2013).
http://www.diss.fu-berlin.de/diss/receive/FUDISS_thesis_000000095270
- [174] A.-X. Zhang and J.-K. Xue. *Band structure and stability of Bose-Einstein condensates in optical lattices with two- and three-atom interactions*. Physical Review A **75**(1):013624 (2007).
doi:10.1103/PhysRevA.75.013624
- [175] Y. Castin and R. Dum. *Bose-Einstein Condensates in Time Dependent Traps*. Physical Review Letters **77**(27):5315 (1996).
doi:10.1103/PhysRevLett.77.5315
- [176] J. Rudolph and H. Ahlers. *Progress of Physics*. cover page (2015).
doi:10.1002/prop.201570001
- [177] H. Ammann and N. Christensen. *Delta Kick Cooling: A New Method for Cooling Atoms*. Physical Review Letters **78**(11):2088 (1997).
doi:10.1103/PhysRevLett.78.2088
- [178] A. E. Leanhardt, T. A. Pasquini, M. Saba, A. Schirotzek, Y. Shin, D. Kielpinski, D. E. Pritchard and W. Ketterle. *Cooling Bose-Einstein Condensates Below 500 Picokelvin*. Science **301**(5639):1513 (2003).
doi:10.1126/science.1088827
- [179] P. Medley, D. M. Weld, H. Miyake, D. E. Pritchard and W. Ketterle. *Spin Gradient Demagnetization Cooling of Ultracold Atoms*. Physical Review Letters **106**(19):195301 (2011).
doi:10.1103/PhysRevLett.106.195301

- [180] H. J. Metcalf and P. v. d. Straten. *Laser Cooling and Trapping*. Springer (1999). ISBN 978-0-387-98728-6
- [181] R. Geiger, V. Ménot, G. Stern, N. Zahzam, P. Cheinet, B. Battelier, A. Villing, F. Moron, M. Lours, Y. Bidet, A. Bresson, A. Landragin and P. Bouyer. *Detecting inertial effects with airborne matter-wave interferometry*. Nature Communications **2**(474) (2011).
doi:10.1038/ncomms1479
- [182] M. Kasevich and S. Chu. *Laser cooling below a photon recoil with three-level atoms*. Physical Review Letters **69**(12):1741 (1992).
doi:10.1103/PhysRevLett.69.1741
- [183] A. Dunning, R. Gregory, J. Bateman, M. Himsforth and T. Freearge. *Interferometric Laser Cooling of Atomic Rubidium*. Physical Review Letters **115**(7):073004 (2015).
doi:10.1103/PhysRevLett.115.073004
- [184] J. Reichel, F. Bardou, M. B. Dahan, E. Peik, S. Rand, C. Salomon and C. Cohen-Tannoudji. *Raman Cooling of Cesium below 3 nK: New Approach Inspired by Lévy Flight Statistics*. Physical Review Letters **75**(25):4575 (1995).
doi:10.1103/PhysRevLett.75.4575
- [185] B. Saubaméa, T. W. Hijmans, S. Kulin, E. Rasel, E. Peik, M. Leduc and C. Cohen-Tannoudji. *Direct Measurement of The Spatial Correlation Function of Ultracold Atoms*. Physical Review Letters **79**(17):3146 (1997).
doi:10.1103/PhysRevLett.79.3146
- [186] D. S. Jin, J. R. Ensher, M. R. Matthews, C. E. Wieman and E. A. Cornell. *Collective Excitations of a Bose-Einstein Condensate in a Dilute Gas*. Physical Review Letters **77**(3):420 (1996).
doi:10.1103/PhysRevLett.77.420
- [187] M.-O. Mewes, M. R. Andrews, N. J. van Druten, D. M. Kurn, D. S. Durfee, C. G. Townsend and W. Ketterle. *Collective Excitations of a Bose-Einstein Condensate in a Magnetic Trap*. Physical Review Letters **77**(6):988 (1996).
doi:10.1103/PhysRevLett.77.988
- [188] M. Edwards, P. A. Ruprecht, K. Burnett, R. J. Dodd and C. W. Clark. *Collective Excitations of Atomic Bose-Einstein Condensates*. Physical Review Letters **77**(9):1671 (1996).
doi:10.1103/PhysRevLett.77.1671
- [189] O. M. Maragò, S. A. Hopkins, J. Arlt, E. Hodby, G. Hechenblaikner and C. J. Foot. *Observation of the Scissors Mode and Evidence for Superfluidity of a Trapped Bose-Einstein Condensed Gas*. American Physical Society **84**(10):2056 (2000).
doi:10.1103/PhysRevLett.84.2056

- [190] F. Chevy, V. Bretin, P. Rosenbusch, K. W. Madison and J. Dalibard. *Transverse Breathing Mode of an Elongated Bose-Einstein Condensate*. Physical Review Letters **88**(25):250402 (2002).
doi:10.1103/PhysRevLett.88.250402
- [191] C. Fort, F. S. Cataliotti, L. Fallani, F. Ferlaino, P. Maddaloni and M. Inguscio. *Collective Excitations of a Trapped Bose-Einstein Condensate in the Presence of a 1D Optical Lattice*. Physical Review Letters **90**(14):140405 (2003).
doi:10.1103/PhysRevLett.90.140405
- [192] G. Bismut, B. Pasquiou, E. Maréchal, P. Pedri, L. Vernac, O. Gorceix and B. Laburthe-Tolra. *Collective Excitations of a Dipolar Bose-Einstein Condensate*. Physical Review Letters **105**(4):040404 (2010).
doi:10.1103/PhysRevLett.105.040404
- [193] C. J. E. Straatsma, V. E. Colussi, M. J. Davis, D. S. Lobser, M. J. Holland, D. Z. Anderson, H. J. Lewandowski and E. A. Cornell. *Collapse and revival of the monopole mode of a degenerate Bose gas in an isotropic harmonic trap*. Physical Review A **94**(4):043640 (2016).
doi:10.1103/PhysRevA.94.043640
- [194] S. Stringari. *Collective Excitations of a Trapped Bose-Condensed Gas*. Physical Review Letters **77**(12):2360 (1996).
doi:10.1103/PhysRevLett.77.2360
- [195] D. Guéry-Odelin and S. Stringari. *Scissors Mode and Superfluidity of a Trapped Bose-Einstein Condensed Gas*. Physical Review Letters **83**(22):4452 (1999).
doi:10.1103/PhysRevLett.83.4452
- [196] S. Stringari. *Moment of Inertia and Superfluidity of a Trapped Bose Gas*. Physical Review Letters **76**(9):1405 (1996).
doi:10.1103/PhysRevLett.76.1405
- [197] U. Kaczmarczik. *Deputy Technical Director of ZARM-FABmbH*. private communication (2017)
- [198] T. A. Pasquini, M. Saba, G.-B. Jo, Y. Shin, W. Ketterle, D. E. Pritchard, T. A. Savas and N. Mulders. *Low Velocity Quantum Reflection of Bose-Einstein Condensates*. Physical Review Letters **97**(9):093201 (2006).
doi:10.1103/PhysRevLett.97.093201
- [199] G. Roati, C. D'Errico, L. Fallani, M. Fattori, C. Fort, M. Zaccanti, G. Modugno, M. Modugno and M. Inguscio. *Anderson localization of a non-interacting Bose-Einstein condensate*. Nature **453**(7197):895 (2008).
doi:10.1038/nature07071

- [200] S. Dimopoulos, P. W. Graham, J. M. Hogan and M. A. Kasevich. *General relativistic effects in atom interferometry*. Physical Review D **78**(4):042003 (2008).
doi:10.1103/PhysRevD.78.042003
- [201] B. P. Abbott et al. *Observation of Gravitational Waves from a Binary Black Hole Merger*. Physical Review Letters **116**(6):061102 (2016).
doi:10.1103/PhysRevLett.116.061102
- [202] E. Arimondo, M. Inguscio and P. Violino. *Experimental determinations of the hyperfine structure in the alkali atoms*. Review of Modern Physics **49**(1):31 (1977).
doi:10.1103/RevModPhys.49.31
- [203] G. P. Barwood, P. Gill and W. R. C. Rowley. *Optically narrowed Rb-stabilized GaAlAs diode laser frequency standards with 1.5×10^{-10} absolute accuracy*. Proceedings of the SPIE **1837**:262 (1992).
doi:10.1117/12.143699
- [204] E. G. M. van Kempen, S. J. J. M. F. Kokkelmans, D. J. Heinzen and B. J. Verhaar. *Interisotope Determination of Ultracold Rubidium Interactions from Three High-Precision Experiments*. Physical Review Letters **88**(9):093201 (2002).
doi:10.1103/PhysRevLett.88.093201
- [205] S. T. Seidel. *Manipulation von Bose-Einstein-Kondensaten unter Schwereelosigkeit*. Diploma Thesis (2009)

Glossary

atom chip Three layers of conducting structures for magnetic trapping of rubidium atoms. The chip comprises mesoscopic wires, the BC and the SC.

crane trick Protocol for the suppression of a residual dipole oscillation in the magnetic trap, reminiscent of quickly moving a load suspended by a rope on a crane.

pre-TOF Time between release and beginning of the magnetic lens.

release position A/B The release positions corresponding to release traps A and B, that are $812\ \mu\text{m}$ and $1476\ \mu\text{m}$ away from the atom chip, respectively.

release trap A/B These are the two specific release traps used for all measurements presented in this work. The two traps differ in their trap frequencies and in the trap position. The respective positions are called release position A/B.

T-Bus Communication bus for the T-Stack.

T-Stack Electronics stack for the laser system.

TOF Time between end of magnetic lens and detection. If no lens is applied, the TOF is the time between release and detection.

velocity spread A measure for the spreading of an atomic ensemble defined as the root mean square velocity of the velocity distribution, which exhibits a zero mean velocity.

Acronyms

1D one dimensional.

2D two dimensional.

3D three dimensional.

AOM acousto-optical modulator.

ARP adiabatic rapid passage.

AWG arbitrary waveform generator.

BC base chip.

BEC Bose-Einstein condensate.

BEC-CAL BEC Cold Atom Lab.

BM breathing mode.

BMS battery management system.

CAL Cold Atom Lab.

CCS capsule control system.

cMOT compressed magneto-optical trap.

COM center of mass.

COMM center of mass motion.

EEP Einstein's equivalence principle.

FEM finite element method.

FPGA field programmable gate array.

HF HighFinesse.

- ICE** Interférométrie atomique à sources Cohérentes pour l'Espace.
- IMU** inertial measurement unit.
- IP** Ioffe-Pritchard.
- IR** impulse response.
- ISS** International Space Station.
- MAIUS** MAteriewellen Interferometrie Unter Schwerelosigkeit.
- MO** master oscillator.
- MOPA** master oscillator power amplifier.
- MOT** magneto-optical trap.
- NI** National Instruments.
- NMR** nuclear magnetic resonance.
- PA** power amplifier.
- PSD** power spectral density.
- Q-1** QUANTUS-1 experiment.
- Q-2** QUANTUS-2 experiment (this work).
- QM** quadrupole mode.
- QUANTUS** QUANTengase Unter Schwerelosigkeit.
- rf** radio frequency.
- RQ** radial quadrupole.
- SC** science chip.
- SG** Stern-Gerlach.
- SM** scissors mode.
- SOC** state of charge.
- SR** step response.
- STA** shortcut to adiabaticity.
- STE-QUEST** Space-Time Explorer and QUantum Equivalence principle Space Test.

TEC thermoelectric cooler.

TF Thomas-Fermi.

TOF time of flight.

TRL technology readiness level.

UFF universality of free fall.

ZARM Center of Applied Space Technology and Microgravity.

Acknowledgments

First of all I want to thank Claus Lämmerzahl for supervising my thesis and for giving me the opportunity to work on such an exciting experiment within a landmark of Bremen. He was always there for counsel and assistance, especially in view of the project as a whole. I am also grateful for the journeys to many amazing places in the world, where I could present my results or participate in a summer school.

My interest in quantum optics emerged to a great extent from a joint theory/experimental lecture given by Christoph Weiss and Christoph Lienau. Aside from that, I want to thank Christoph Lienau for his work as a referee of my rather long thesis and for many valuable discussions in earlier years during my studies.

A special thank goes to Ernst M. Rasel for organizing the QUANTUS project and for his perpetual dedication to this amazing field of research.

I also want to thank many of my colleagues. First of all, Waldemar Herr for acquainting me with the various experimental techniques and theoretical foundations in my early days with the project and also for proof-reading my thesis later on - thank you. I want to appreciate my colleagues Jan Rudolph, Alexander Grote and Christoph Grzeschik from the core experimental team for a great time and many inspiring moments during our research. We had an exciting, challenging and labor-intensive time with ups and downs. Two major setbacks were a complete electrical damage of the T-Stack and a water damage with an ankle-deep water level in the lab. Both occurred still in Hanover and delayed the prospect of the first drop further into the future. Still, the team was bonded by that and we could motivate each other. I thank Alexander Grote in particular for many motivating discussions that helped me to stay focused at the time just before I started writing this thesis.

I want to thank Sven Herrmann for his continuous support and for proof-reading my thesis, even with a baby in his arms. Aside from that, Sven was always the first person to speak to regarding organizational aspects and also for fundamental physical questions.

The contributions of Hauke Müntinga and Holger Ahlers from the Q-1 team should be mentioned here as well. They laid many foundations for mobile BEC machines and created an invaluable toolbox called 'muchbetterbecfit' for a pre-evaluation of the absorption density images. Hauke also assisted the Q-2 team in the preparations for the first drop, especially regarding the interplay of the different computers and networks involved in a drop.

Many people at the drop tower deserve gratitude: The drop tower operators for their solution-oriented attitude and their willingness to work overtime, even for a third drop on a Friday evening. All the people from the mechanics workshop, who can build practically everything, even on a short notice. Last but not least, also Ronald Mairose and Marcus Stadlander from the electronics workshop, who contributed with some customized circuits to the experiment and also enabled me to design and build them on my own. Thank you all.

I want to thank Brynle Barrett from the group of Philippe Bouyer for the vibration spectrum of the A310 during parabolic flight. I received the raw data of that french research group only an hour after sending my e-mail, which is really amazing.

Special thanks also go to the DLR for funding the QUANTUS project, that could gain international reputation. It was a long way to go, which would not have been possible without the dedication of Rainer Kuhl, Thomas Driebe and Rainer Forke from DLR. The success of Q-2 and MAIUS really triggered the international cooperation on BEC-CAL.

I also want to thank my family and friends for supporting me throughout all the years and for the precious time I could share with them. Finally, I also want to thank my girlfriend for her patience and support during the final months of writing.

Selbstständigkeitserklärung

Hiermit erkläre ich, das ich diese Arbeit selbstständig verfasst und nur die angegebenen Hilfsmittel verwendet habe. Teile der Dissertation wurden bereits in [78] veröffentlicht.

Tammo Sterneke

Bremen, den 30. Oktober 2017